DESIGN AND OPTIMIZATION OF GRAPHITIC-CARBON NITRIDE HYBRID NANOSTRUCTURES FOR ENHANCED PHOTOCATALYTIC ACTIVITY

A thesis submitted in partial fulfilment of the requirements for the award of the degree of

DOCTOR OF PHILOSOPHY

by

V P MADHURIMA

[ROLL NO: 717055]

Under the supervision of

Prof. KUSUM KUMARI

Associate Professor,
Dept. of Physics,
NIT Warangal

Dr. P. K. JAIN

Associate Director,
ARCI, Hyderabad

DEPARTMENT OF PHYSICS

NATIONAL INSTITUTE OF TECHNOLOGY WARANGAL

WARANGAL-506004, TELANGANA, INDIA

NOVEMBER 2023

Dedicated to my parents

Shri. Vattem Ajoy Babu

&

Smt. Girija

DECLARATION

This is to certify that the work prepared in the thesis entitled "**DESIGN AND OPTIMIZATION OF GRAPHITIC-CARBON NITRIDE HYBRID NANOSTRUCTURES FOR ENHANCED PHOTOCATALYTIC ACTIVITY**" is a bonafide work done by me under the supervision of Prof. Kusum Kumari and Dr. P.K. Jain, and was not submitted elsewhere for the award of any degree.

I declare that this written submission represents my ideas in my own words and where others' ideas or words have been included, I have adequately cited and referenced the original sources. I also declare that I have adhered to all principles of academic honesty and integrity and have not misrepresented or fabricated or falsified any idea/data/fact/source in my submission. I understand that any violation of the above will be a cause for disciplinary actions by the institute and can also evoke penal action from the sources which have thus not been properly cited or from whom proper permission has not been taken when needed.

V P Madhurima

(Roll No. 717055)

Date: 29.11.2023

CERTIFICATE

This is to certify that the work presented in the thesis entitled "**DESIGN AND OPTIMIZATION OF GRAPHITIC-CARBON NITRIDE HYBRID NANOSTRUCTURES FOR ENHANCED PHOTOCATALYTIC ACTIVITY**" is a bonafide work carried out by **Ms. V P Madhurima (Roll No. 717055)** under our supervision and was not submitted elsewhere for the award of any degree.

Dr. P K. JAIN
Research Supervisor,
Associate Director,
ARCI, Hyderabad

Prof. KUSUM KUMARI
Research Supervisor,
Associate Professor,
Dept. of Physics, NITW

Date: 29.11.2023

ACKNOWLEDGEMENTS

First and foremost, I would like to express my sincere gratitude to my supervisors, Prof. Kusum Kumari, Associate Professor, Physics Dept., NIT – Warangal and Dr. P. K. Jain, Associate Director, ARCI, Hyderabad, for their unlimited support and unconditional guidance during my PhD Journey. Their constant motivation and valuable suggestions always helped me to get going and achieve the purpose of this study. A special thanks to the head of the physics department, Prof. T.V. Appa Rao for his support and also to the members of the Doctoral Scrutiny Committee (DSC) committee for their invaluable suggestions during all the DSC meetings. I would like to extend my sincere thanks to all the staff and students of Dept. of Physics, NITW for their constant support during my PhD journey.

I thank Prof. Bidyadhar Subudhi, Director, NITW for allowing me to pursue my PhD in this premier institute. I express my heartfelt gratitude to Dr. Tata Narasinga Rao, Director, ARCI – Hyderabad and former Director, (Late) Dr. G. Padmanabham for giving me an opportunity to pursue my PhD research work and providing the state-of-art characterization and processing facilities. I was very fortunate to get a chance to work at the Centre for Carbon Materials, ARCI, Hyderabad. My special thanks goes to Dr. Balaji Padya, Dr. Ravi Kali, and Dr. Sanjay Dhage for always being there when I needed their support. I would also like to thank Mr. D. P. Surya Prakash Rao, Mr. E. Konda, and Mr. P Anjaiah for their kind assistance while operating the equipments. Besides, a special thanks to E&I centre scientist and staff (Dr. Nirmala, Mr. Ch. Sambasiva Rao & Ms. Aruna) for their constant support during instrument troubleshoot. In addition, I would like to thank the members of Centre for Material Characterizations and Testing, Dr. G. Ravi Chandra, Dr. K. Suresh, Mr. K. Ramesh Reddy, and others for helping me with various characterization facilities. I am grateful to other scientific staff of ARCI – Hyderabad, Dr. P. H. Borse, Dr. Neha Hebalkar, Dr. B.V. Sharada, Dr. S. Anandan, and Dr. S. Sakthivel, for their valuable advice, encouragement, and timely help in accessing various characterization facilities at their centres.

Having Mr. N. Ravi Kiran, Dr. M. Sagar, Dr. A. Harish, Dr. Aniruddha Karati, Dr. M. Nagaraju, Mr. B. Ramesh, Ms. Mahalakshmi, Mr. Rohit, and Ms. Riya Davis as my research colleagues during my PhD journey provided me the confidence and support to overcome my hard times. I would also like to thank all the cleaning staff who used to keep our labs and seating places clean and tidy.

I express sincere gratitude to all my professors at Dept. of Physics, Osmania University for encouraging me to pursue PhD especially Prof. G. Prasad. His knowledge and insights towards the subject always inspired me to pursue higher studies. Also, a special thanks to Mr. Nityananda Ghosh, Physics Lecturer, Loyola Academy Degree and PG College, Hyderabad, and Ms. V. Jayalakshmi, my school teacher, for believing in me and constantly motivating me to pursue higher studies. In addition, I must thank Dr. M. Manasa, Ms. V. Jaya, and Ms. T. Spandana for giving me emotional strength during my tough times.

I am infinitely indebted to my parents Ms. V. Girija and Mr. V. Ajoy Babu, without their motivation and hard work, I would not been having what I am today. Their constant motivation and unconditional love always helped me in overcoming my obstacles and strengthened my determination. I would like to thank my brother, Mr. V.S. Dharma Teja, for being my mentor, inspiration, and role model since my childhood. I am also grateful to all my friends, relatives and well-wishers who always encouraged, supported, and prayed for me.

V P Madhurima

(Roll No. 717055)

Date: 29.11.2023

ABSTRACT

Carbon nanomaterials (CNMs), ever since their discovery have gained widespread attention due to their remarkable properties like high tensile strength, Young's modulus, surface area to volume ratio, thermal and electrical conductivities, carrier mobility and many more. Due to their phenomenal features, CNMs have catered to several fields of research ranging from aerospace to drug delivery applications. The present study was an effort to develop and understand the photocatalytic behaviour of CNMs-based graphitic carbon nitride (g-C_3N_4) hybrid photocatalyst materials for effective degradation of rhodamine B (RhB) dye. Hence, the overall objective of this thesis work was to develop g-C_3N_4 photocatalyst material by optimizing the synthesis parameters and study its photocatalytic dye degradation property. Further, to enhance the photocatalytic performance of g-C_3N_4 by synergistically coupling with the CNMs and finally to compare & study the photocatalytic property and eventually propose a degradation mechanism based on morphology of the developed photocatalyst materials.

In this thesis work, 2D g-C_3N_4 was synthesized using a conventional thermal decomposition process using melamine as the precursor material. The synthesis parameters like reaction temperature and atmosphere were optimized to obtain the near-ideal g-C_3N_4 material. This optimized photocatalyst was further improved by incorporating ammonium chloride (NH_4Cl) during the synthesis process. The role of NH_4Cl was to act as a bubbling agent and provide porous and thin sheets of g-C_3N_4. The structure, morphology, and optical properties of the developed photocatalyst materials were investigated using XRD, SEM, TEM, UV-DRS, FTIR, PL, BET and XPS techniques. The photocatalytic behaviour was evaluated with the help of an in-house fabricated reactor taking RhB as the target dye. It was observed that the improved g-C_3N_4 removed 94% of the RhB dye (Conc. = 10 mg/L) in 30 minutes whereas the initially prepared g-C_3N_4 showed only 35% efficiency.

Further, various CNMs like carbon nanotubes (CNTs) and carbon soot nanoparticles (CS) were prepared using the arc discharge technique. It is a conventional physical method of preparing CNMs where two graphite rods are brought near and a high current is applied in an inert atmosphere. The sublimation of one of the graphite electrodes and deposition on the cooler surfaces results in the formation of the CNTs and CS. Besides, graphene nanoplatelets (GNP) were synthesized through microwave exfoliation of graphite intercalated compound followed by sheer mixing in a solvent mixture (DMSO & DI water). The obtained CNMs were coupled

with g-C_3N_4 to attain higher degradation efficiencies. It was observed that CS coupled g-C_3N_4hybrid photocatalyst showed 97% degradation of RhB (conc. = 20 mg/L) in 90 minutes however, pristine g-C_3N_4 showed 88% in similar conditions. Moreover, the CNT-coupled g-C_3N_4 hybrid photocatalyst also showed 97% degradation in 90 minutes under visible light irradiation. Further, the 2D/2D hybrid photocatalysts showed the highest performance. Here, GNP-coupled g-C_3N_4hybrid photocatalyst showed 96% degradation in 60 minutes whereas pristine g-C_3N_4 showed 55% efficiency.

The enhanced performance of CNMs coupled hybrid photocatalyst was essentially due to the effective charge separation of photogenerated charge carriers resulting in reduced recombination rates. It was discovered that the 2D/2D coupling showed faster degradation rates than 1D/2D and other coupling systems. This was further proved by developing another 2D/2D system using commercial hexagonal boron nitride (hBN) coupled g-C_3N_4. It was observed that 91% of RhB was removed in 60 minutes under the visible light source. Therefore, the morphology played a significant role in deciding the overall performance of the materials.

Keywords: Graphitic Carbon Nitride (g-C_3N_4), Carbon Nanotubes (CNT), Carbon Soot, Graphene Nanoplatelets (GNPs), Hexagonal Boron Nitride (hBN), Rhodamine B (RhB), Visible - light Photocatalysis.

TABLE OF CONTENTS

LIST OF ABBREVIATIONS AND SYMBOLS

ABBREVIATIONS	DESCRIPTION
3D	Three dimensional
2D	Two dimensional
1D	One dimensional
0D	Zero dimensional
CNMs	Carbon Nanomaterials
C_{60}	Fullerenes
C_{70}	Larger Fullerenes
T_c	Critical Temperature
CO	Carbon Onions
CNTs	Carbon Nanotubes
CVD	Chemical Vapour Deposition
ITO	Indium Tin Oxide
FTO	Fluorine doped Tin Oxide
g-C_3N_4 or CN	Graphitic Carbon Nitride
RhB	Rhodamine B
MO	Methyl Orange
AR	Acid Red
AOP	Advanced Oxidative Process
CB	Conduction Band
VB	Valence Band
•OH	Hydroxyl Radical
$\bullet O_2^-$	Superoxide Radical
h	Planck's Constant
ν	Frequency of the incident energy
h^+	Hole vacancy
e^-	Electron
λ	Wavelength
CO_2	Carbon Dioxide
TiO_2	Titanium Dioxide
ZnO	Zinc Oxide

CeO_2	Ceric Oxide
Fe_2O_3	Ferric Oxide
CuO	Cupric Oxide
Bi_2O_3	Dibismuth Trioxide
MoS_2	Molybdenum Dioxide
ZnS	Zinc Sulphide
WS_2	Tungsten Disulphide
eV	Electron volts
LED	Light Emitting Diode
CQDs	Carbon Quantum Dots
HT	Hydrothermal
CNFs	Carbon Nanofibers
MB	Methylene Blue
SF	Sodium Fluorescein
rGO	Reduced Graphene Oxide
GO	Graphene Oxide
CMC	Carboxy Methyl Cellulose
BG 4	Basic Green 4
BB 9	Basic Blue 9
BPA	Bisphenol A
hBN	Hexagonal Boron Nitride
XRD	X-ray diffraction
FESEM	Field Emission Scanning Electron Microscopy
HRTEM	High Resolution Transmission Electron Microscopy
TGA	Thermogravimetric Analyser
RS	Raman Spectroscopy
UV-DRS	Ultraviolet-Visible diffuse reflectance spectroscopy
PL	Photoluminescence Spectroscopy
FT-IR	Fourier transform infrared spectroscopy
XPS	X-ray photoelectron spectroscopy
BET	Braunner-Emmett-Teller
SSA or S_{BET}	Specific Surface Area
GF	Graphite Flakes
NH_4Cl	Ammonium Chloride

H_2O_2	Hydrogen Peroxide
H_2SO_4	Sulphuric Acid
BQ	para - Benzoquinone
AO	Ammonium Oxalate
IPA	Isopropanol
DMSO	Dimethyl Sulfoxide
GCN	Graphitic Carbon Nitride
NGCN	Improved Graphitic Carbon Nitride
cpm	Centigrade per minute
DC	Direct Current
K	Kelvin
CD	Cathode deposit
CS	Carbon Soot
GIC	Graphite Intercalated Compound
EG	Exfoliated Graphite
DI	Deionized
rpm	Rotations per minute
min	Minutes
SC	Carbon soot incorporated in graphitic carbon nitride
CC	CNTs incorporated in graphitic carbon nitride
GC	GNPs incorporated in graphitic carbon nitride
BC	hBN incorporated in graphitic carbon nitride
d	Interlayer distance
D	Crystallite Size
A	Absorbance
ε	Molar Absorptivity
b	Length of the cuvette
C	Concentration of the solution
KE	Kinetic Energy
BE	Binding Energy
ϕ	Work Function
ZP	Zeta Potential
η (%)	Total amount of dye degraded
C_0	UV absorbance of RhB dye solution at time 0 minute

C_t	UV absorbance of RhB dye solution at time t minutes
mg	Milligram
gm	Gram
λ_{max}	Maximum absorbance wavelength
mg/L	Milligrams per litre
mg/ mL	Milligram per millilitre
mL	Millilitre
nm	Nanometre
cm	Centimetre

LIST OF FIGURES

CHAPTER-3

CHAPTER-4

CHAPTER-5

Figure 6.18 *Possible mechanism for RhB degradation in BC2 sample.*

LIST OF TABLES

Chapter 1

Introduction

1.1 The element carbon

The word carbon is derived from the Latin word “carbo” which means charcoal. In the present day, carbon is, of course much more than charcoal. The element carbon is symbolized as ‘C’ and has an atomic number of 6 with the following electronic configuration; $1s^2 2s^2 2p^2$. Carbon due to its versatile structure and properties holds top priority as the starting material in all the major industries across the globe. Unlike most elements, carbon has various material forms which are known as polymorphs or allotropes. They are entirely composed of carbon but have different physical structures. These very diverse materials, with such large differences in properties, all have the same building block- the element carbon, which is the thread that ties the various constituents of this chapter and gives its unity.

1.1.1 Various forms of natural carbon

Carbon materials have always played a crucial role for mankind; for instance, shiny and slippery natural graphite powder as pencil lead, soot in black ink in the printing industry, charcoal as an adsorbent, diamond in jewellery and ornaments, carbon fibres for reinforced composites, graphite electrode in steel industries, carbon electrode in Li-ion batteries, activated carbon in water purification systems, etc. So far, various carbon materials have been developed and more will be developed in the future [1]. Some of the naturally available carbon materials, their chemical structure and other salient features are discussed below:

1.1.1.1 Diamond

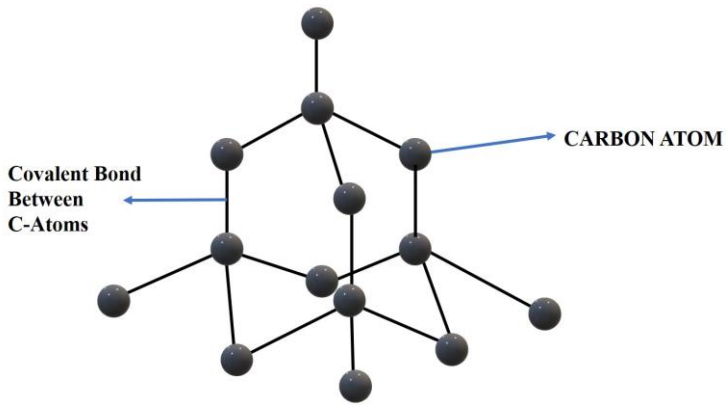

Figure 1.1 *Structure of diamond.*

Diamond is a 3D carbon allotrope with a tetrahedral crystal structure and contains sp^3-bonded carbon. The ideal diamond structure has the characteristic property that every carbon atom is surrounded by four other carbon atoms at the corners of a regular tetrahedron (Fig.1.1). Diamond has some outstanding properties; it has the highest thermal conductivity at room temperature, it is the hardest naturally occurring material, it has extremely high strength and rigidity, its semiconducting and optical properties are remarkable. In the last few years, breakthrough discoveries occurred when diamond thin films were successfully grown by various chemical and physical vapour deposition techniques at moderate temperatures and pressures [2]. With this discovery, a broad range of applications have opened for diamond and its derivates materials. Diamond is extensively used as micro tips in cutting, drilling, and grinding tools. Due to low electrical conductivity, diamond offers many advantages over other wide-bandgap materials and can be used in high-speed electronics and response systems as well as high-power laser windows, protective coatings and many more.

1.1.1.2 Graphite

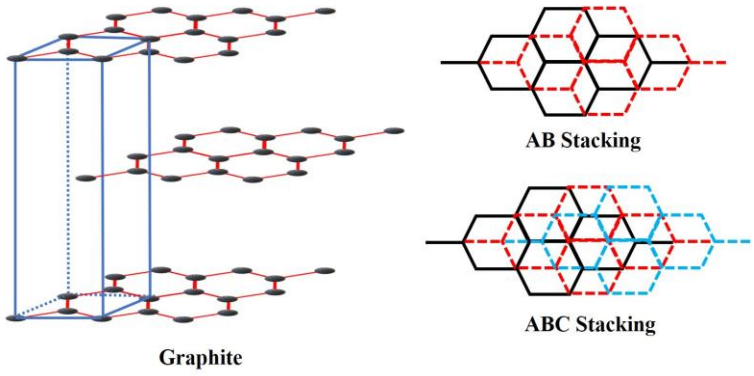

Figure 1.2 *Structure of graphite with various stacking arrangements.*

The most common form of carbon material that has been produced on an industrial scale is graphite. It is a 2D form of carbon with a hexagonal crystal structure and contains sp^2-bonded carbon in its structure. Its fundamental structure consists of a stack of layers of hexagonal carbon moieties. These layers have strong anisotropy due to the sp^2 covalent bonding in the layer (ab-plane) but weak van der Waals forces between π-electron clouds of the stacked layers (c-axis). The stacking layers possess a specific regularity based on which the crystal system can be determined as shown in Fig. 1.2: if it follows ABAB stacking then the graphite crystals have a hexagonal arrangement and if it is ABCABC stacking then the graphite crystals have rhombohedral crystal system. When the layers are too small and there is no stacking regularity even though they stack in parallel, in such case the graphite is called turbostratic stacking [3].

Ideal graphite has some remarkable physical, thermal, electrical, mechanical and chemical properties; its anisotropy when measured along the ab-direction and c-direction, graphite sublimes when the temperature reaches 4000 K at 1 atm pressure, high heat of vaporization, high thermal conductivity in the ab-direction, low electrical resistivity along ab-axis and high along c-axis, the anisotropy of graphite is reflected in its chemical behaviour as well, reaction with gases or vapours occurs preferentially at active sites that is, the end of the basal planes of the crystal and at the defect sites such as dislocations, vacancies and steps [4]. Besides these commendable properties, graphite also has a myriad of applications ranging from household aspects like pencil tips, and adsorbents to industrial aspects like brakes and clutch plates, linings, gaskets, lubricants, carbon brushes for electric motors, fire retardants and insulation and reinforcement products.

1.2 Carbon at nanoscale

The word nanoscience or nanotechnology has become the most commonly used terminology by the scientific community after the breakthrough discovery of new forms of nanocarbon materials which led the inventors to receive the Noble Prize. In the last couple of decades, 0D, 1D and 2D CNMs have gained tremendous momentum due to their exclusive thermal, optical, electrical, and chemical properties [5]. In particular, fullerenes, carbon onions, carbon nanotubes, graphene, graphene oxide and graphitic carbon nitride became the epitome of research and development in the nanotechnology sector. These carbon nanostructures have been explored and continue to experiment with in a wide spectrum of applications ranging from life sciences to aerospace as depicted in Fig. 1.3 [6]. These materials compete and outstand other materials due to their following inherent properties:

- A high surface-to-volume ratio leads to better performance.
- A high percentage of surface atoms or molecules results in unique properties.
- Size effect: It is the characteristic size of the building block that is reduced to a point where the mean free path of the electrons or phonons become comparable with the characteristic size of the building block of the material, then the material is said to have spatial confinement of electrons along that direction. If one dimension of the material is in the nanoscale range then such nanomaterials are called 2D nanomaterials. Similarly, if two and three dimensions of the material are at the nanoscale then such nanomaterials are called 1D and 0D nanomaterials respectively. The quantum confinement effect in carbon nanomaterials has produced unique optical and electronic properties with respect to its bulk counterparts.

- High electrical and thermal conductivities.
- High chemical activity.
- Extraordinary mechanical properties like high tensile strength and Young's Modulus.
- High carrier mobility and optical transparency.

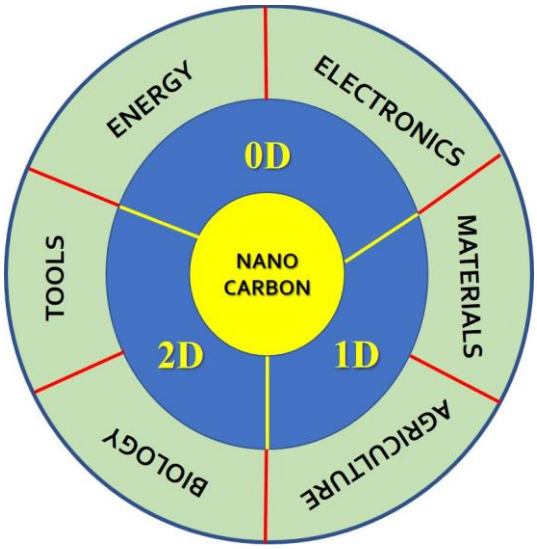

Figure 1.3 *Applications of multi-dimensional carbon nanomaterials in various fields.*

Some of the majorly researched carbon nanomaterials based on their dimensionality are discussed below:

1.2.1 Fullerenes and carbon onions

0D CNMs are majorly dominated by fullerenes and carbon onions. Fullerenes are large clusters of carbon atoms arranged in a stable geodesic structure in the form of a cage-like spheroid, consisting of a network of pentagonal and hexagonal formation of carbon atoms (Fig.1.4). The fullerene structure, in order to close into a spheroid must have exactly 12 pentagons and can have a variable number of hexagons. This result follows Euler's theorem of polyhedral [7]. To have a symmetrical structure and thermodynamical stability, it is important that the fullerene molecule satisfy the isolated pentagon rule where it is energetically unfavourable for two pentagons to be adjacent as this would result in higher curvature on the fullerene ball and thus more strain. For this reason, the smallest possible fullerene to satisfy the above rule consists of 60 carbon atoms (C_{60}) and the next possible largest fullerene is C_{70} [8].

Fullerenes are formed from the carbon-rich vapours that can be obtained in several ways like; resistive heating of carbon electrodes in a vacuum, plasma discharge between carbon

electrodes in an inert atmosphere, laser ablation and oxidative combustion of benzene/Ar gas mixture. Most of the synthesis methods result in a mixture of stable fullerenes, and impurity molecules like polyaromatic hydrocarbons and carbon soot. Therefore, the synthesis of fullerenes is generally followed by purification and extraction techniques [9]. Fullerene aggregates are exceptionally strong and have high impact strength and resilience. Theoretical calculations indicate the C_{60} could be a direct bandgap semiconductor similar to GaAs and can more readily act as an electron acceptor than that of an electron donor [10].

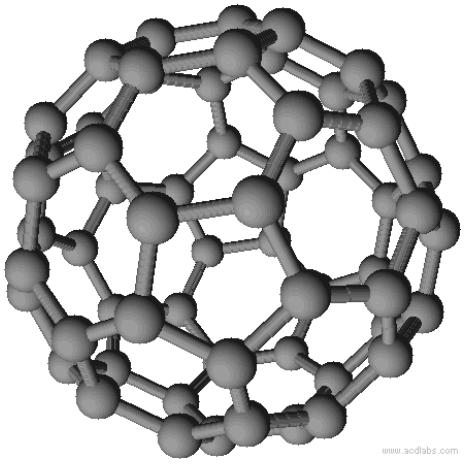

Figure 1.4 *Structure of C60 fullerene.*

Some of the potential applications of fullerenes and their derivates are listed below:

- Fullerenes when combined with Cs or K or Rb show superconductivity. Especially Cs_3C_{60} exhibits superconductivity below T_c= 38 K and at room temperature it acts as an insulator.
- Development of polymer-fullerene solar cells. The most effective cell has been made from bulk heterojunction in which a donor-type conjugated polymer is blended with an acceptor fullerene.
- Fullerene and its derivatives are extensively studied in biomedical and personal care sectors for toxicity, biocompatibility, molecular imaging, etc.

Recently, enormous attention has been received towards morphological variations in fullerene-like carbon nanostructures. Within this new class of carbons, carbon-onions (CO) or onion-like layered structures came into the spotlight. CO typically consists of hollow spherical fullerenes covered with graphene layers with increasing radii and maintaining an interlayer distance of 0.335nm attributing to the van der Waals interactions between the layers. CO have a cage-inside-cage structure similar to that of Russian dolls. CO is synthesized by similar techniques as that for fullerenes. It was observed that when an intense electron beam in TEM

was irradiated on carbon soot particles and tubular graphitic structures, a quasi-spherical CO was formed. Graphitization of nanodiamond particles at high temperatures under high vacuum results in concentric polyhedral graphitic shell structures [11]. Another unique technique which does not require a vacuum is under water direct current arc discharge process. Although it is economical, the output product efficiency is quite low and contains several nanocarbon impurities [12]. The physicochemical properties of CO depend on its structure, number of layers and their distance. The properties also depend on the method of synthesis and operating conditions. Similar to that of fullerenes, CO also have widespread applications in electrochemical, energy storage devices, electromagnetic shielding, biomedical applications and many more [13].

1.2.2 Carbon Nanotubes

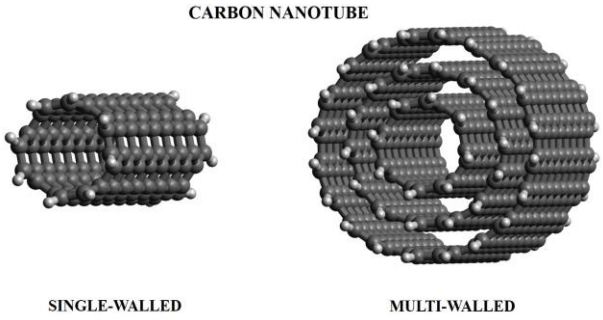

Figure 1.5 *Types of carbon nanotubes.*

CNTs were discovered by S. Iijima in 1991 and as the name suggests, it is a 1D CNM having tube-like morphology (Fig.1.5). CNTs are available in various forms like single-walled or multi-walled, of different types like armchair or zigzag or chiral and any nature like metallic or semiconducting [14]. CNTs production majorly comprises several techniques like arc discharge, laser ablation and chemical vapour deposition (CVD) [15]. However, numerous other routes have been developed but the overall yield is comparatively low. The first two methods *i.e.*, arc discharge and laser ablation are physical methods, where the precursor is essentially a graphite electrode which is evaporated either by passing current or by laser. These carbon vapours travel in an inert medium and get deposited on a relatively cooler surface. This solidification process results in CNTs formation. The latter method, CVD is a chemical process where the volatile precursors are used as a carbon feed source to a catalyst. Here catalyst acts as a nucleation site onto which CNTs growth takes place.

CNTs have tremendous electronic, optical, and structural properties that are largely determined by their nearly 1D structure. The chemical reactivity of CNTs is high due to their curvature and is directly proportional to the pi-orbital mismatch caused by an increased curvature. Covalent chemical modification on CNT structure multifold its chemical reactivity [16]. The elongated structure of CNTs results in remarkable electrical and electronic properties. The conductivity of smaller-diameter CNTs depends on their chiral vector. Even the optical properties are greatly influenced by their chirality. With increasing diameter, the optical properties of CNTs disappear [17]. Young's Modulus of CNTs in the axial direction is very high. Thus, making them potential materials for applications that need anisotropic properties [18].

Due to their high anisotropy and chemical reactivity CNTs have a vast array of applications. CNTs are highly preferred filler material in polymer nanocomposite preparation. CNTs are used to make high-strength materials in automobiles and aerospace industries [19]. CNTs are proactively used as electrode material for electrochemical devices due to their large specific surface area and porosity combined with high electrical conductivity [20]. Few research groups have primarily focused on using CNTs as field emission electron sources for flat panel displays, discharge tubes, lamps and X-ray and microwave generators [21]. Apart from these, CNTs are also used in sensing and probing devices because of their high sensitivity towards electron movement [22]. Post-pandemic CNTs are widely tested in biological sensors and drug delivery systems [23].

1.2.3 Graphene

With the discovery of graphene in the early 2000s, a breakthrough in the field of nanotechnology took place. A single layer of graphite is called graphene. It is the thinnest object ever created (thickness ~ 0.34 nm). Graphene is a 2D CNM with sp^2 hybridized carbon atoms all around as shown in Fig. 1.6. These sp^2 carbons consist of out-of-plane π-bonds and in-plane σ-bonds. This imparts the delocalization of an array of electrons on the surface of the graphene sheet resulting in electron conduction by providing weak interactions between graphene layers or between graphene and the substrate [24]. Various synthesis techniques have emerged in recent years. However, exfoliation of graphite flakes and thermal CVD are predominantly preferred. Exfoliation involves the separation of graphite sheets either by chemical or mechanical routes. It is a top-down approach [25]. Meanwhile, CVD is a bottom-up approach where the carbon precursors are made to deposit on a substrate, preferably a transition metal

substrate [26]. Besides, these techniques, some other methods are also tried and explored like unzipping CNTs, chemical synthesis and microwave synthesis [27].

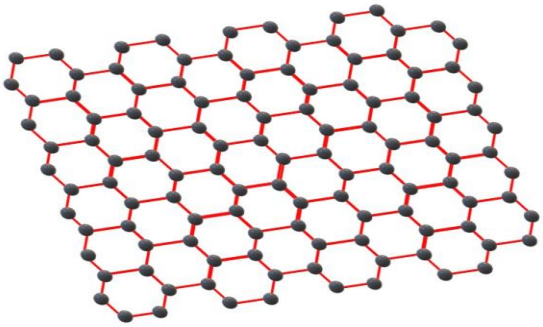

Figure 1.6 *Structural schematic of graphene.*

Graphene dominates several properties in terms of electrical conductivity, mechanical strength, optical transparency, and thermal conductivity. Studies reveal that by varying the thickness of graphene, excellent optical properties can be achieved and when combined with its remarkably high electrical conductivity, graphene becomes a top competitor in the transparent conductive membrane which could replace conventional membranes like Indium Tin Oxide (ITO) ad Fluorine doped Tin Oxide (FTO) [28]. Electron mobility is another interesting property of graphene. It is the most conductive material so far at room temperature, with a conductivity of 10^6 S/m and sheet resistance of 31 Ω/sq. The thermal conductivity and mechanical strength of graphene are also very high. The elastic modulus and tensile strength of graphene are 1.1 TPa and 125 GPa respectively [29]. Therefore, this can be considered as a typical 2D enhancement for potential applications in composite materials. The thermal conductivity of graphene at room temperature is $5x10^3$ W/m-K [30], which is almost 10 times higher than that of copper (401 W/m-K). Also, the specific surface area reaches 2630 m^2/g in the case of graphene [31]. This property can be explored in micro-detectors for gas sensing, by monitoring minute resistance changes during gas adsorption and desorption [32]. Due to the above-discussed exceptional properties, graphene has become a new dimension in the field of nanomaterial-based applications. Graphene is majorly applied in display systems, as transparent and flexible conductive films, conductive inks for printed electronics, graphene-based separation membranes, and graphene as biosensors and biomarkers in biomedical applications and energy storage devices [33].

1.2.4 Graphitic Carbon Nitride

Another class of 2D CNMs recently became popular due to their opto-electronic properties is g-C_3N_4. It is a metal-free compound having a structure similar to that of graphite hence, the name graphitic carbon nitride. It is a polymeric semiconductor material having a layered structure and consists of repeating motifs of a C-N heterocyclic array. Two different condensation states have been explained as the primary building blocks in a single layer of g-C_3N_4 (Fig. 1.7): (a) s-triazine units (C_3N_3) periodic moieties; (b) tri-s-triazine or heptazine units (C_6N_7) connected through planar tertiary amino groups. However, experimental, and theoretical studies demonstrate that heptazine-based g-C_3N_4 structure was energetically more stable than s-triazine structure and therefore, heptazine-based g-C_3N_4 structure is the most widely accepted basic building unit for g-C_3N_4 [34,35].

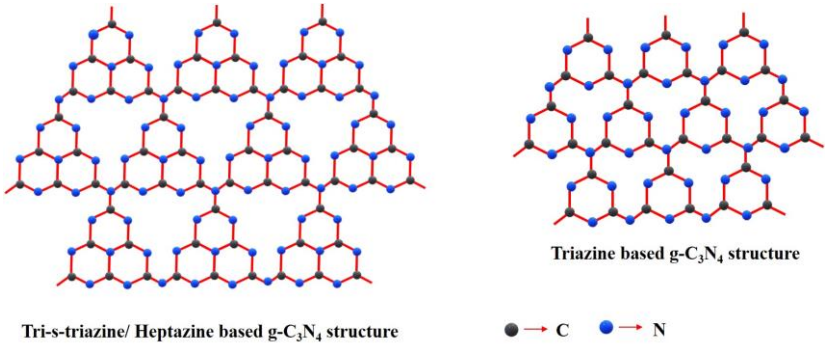

Figure 1.7 *Structural schematic of graphitic carbon nitride with two different building blocks.*

g-C_3N_4 can be readily fabricated in a cost-effective, eco-friendly approach with non-toxic carbon and nitrogen-rich precursors like melamine and urea through a conventional thermal condensation approach. Besides, thiourea, cyanamide, dicyandiamide and guanidine hydrochloride are also used [36]. Apart from this conventional synthesis method, a few other techniques are also explored like ionothermal synthesis, molecular self-assembly, microwave irradiation and ionic liquid strategy [37]. Owing to its graphitic structure, g-C_3N_4 has several properties in resemblance with 2D structures like high specific surface area, decent thermal stability up to 600 °C and many more [38]. The chemical reactivity of g-C_3N_4 is also appreciable due to the uncondensed amino groups at the edges which act as the reactive site for chemical reactions [39]. Since the material is semiconducting, it has a bandgap of around 2.7 eV which makes it a visible-light active material and hence this material finds major applications due to its optical properties [40]. The major areas of g-C_3N_4 material research lie in and around heterogeneous photocatalysis where it acts as a visible-light-driven photocatalyst for H_2

evolution, CO_2 reduction and organic pollutant degradation [41]. Besides, g-C_3N_4 is also explored in electrochemical energy devices due to its surface properties [42]. Recently, g-C_3N_4 has also made its footprint in the anti-bacterial application where photosensitization of bacteria is done by g-C_3N_4 in the presence of visible light [43]. Moreover, g-C_3N_4 has been explored in areas other than photocatalysis like device fabrication, biomedical applications, etc. [44].

1.3 Carbon nanomaterials in wastewater treatment

As we know, about three-quarters of the earth's surface is covered with water and the increasing demand for freshwater due to the exponential growth in the industrial sector and population has become a threat to the natural water resources for future generations. Therefore, there is an urgent need to treat industrial wastewater so that it can be reused by industries thus leaving the freshwater sources conserved for upcoming generations. In this context of wastewater treatment, significant breakthroughs have been achieved by nanomaterial-based wastewater treatment systems. The special contribution of CNMs for their unique promising features has generated tremendous interest among material researchers. Recent studies indicate extensive research of CNMs in wastewater treatment applications and were found with extremely positive outcomes. Majority of the industrial wastewater consists of heavy metal ions, organic matter, hazardous textile dyes and similar products. Therefore, the most common technique employed for wastewater treatment is adsorption onto the adsorbent. Apart from this method, few studies have used CNMs in disinfection, membrane filtration and heterogeneous photocatalysis techniques. the following section deals with each of the above-mentioned techniques in detail.

1.3.1 Adsorption

Adsorption is one of the most conventional and impressive wastewater treatment techniques employed for removing organic and inorganic water pollutants. It can be defined as the process in which liquid and gaseous solutes accumulate on the adsorbent material which is usually a solid molecule [45]. Broadly, absorption can be classified into two categories, physisorption and chemisorption. Physisorption is the phenomenon in which the adsorbate and the adsorbent are attracted and attached by the van der Waals forces while chemisorption happens when the respective molecules are attached through a strong chemical bond [46]. The overall performance of the adsorption process depends on the total percentage removal of the contaminant from the wastewater and it is directly proportional to the adsorption capability of the material being used. This essentially depends on the specific surface area, surface active

sites and the affinity towards the pollutant. Thus, CNMs prove to be an essential adsorbent due to their high specific surface area and abundant active sites [47,48]. However, CNMs do have some limitations in their pristine form due to the defects and other carbonaceous impurities generated during the synthesis process. So, to enhance its overall performance, surface functionalization in the presence of acid and alkali solution is preferred [49–51]. Some of the major contaminants removed by CNMs via the adsorption technique are heavy metal ions such as Zn, Cd, Pb and Cr, natural organic matters such as trihalomethane and synthetic dyes such as Rhodamine B (RhB), methyl orange (MO), acid red (AR) and many [52–56].

1.3.2 Disinfection

Another impressive decontamination technology was found to be the disinfection technique. This method mainly focuses on the elimination of pathogens and other microorganisms from the drinking water. A higher quality of purified water is needed when we are dealing with drinking water. It is a difficult task to remove bacterial contaminants as the concentration of the pathogens keeps fluctuating as also the type of pathogens. Conventional disinfectants such as chlorine and ozone-based disinfectants from toxic by-products become a challenge later for further removal. Therefore, to avoid the formation of these toxic by-products and improve the quality of treated water, nanotechnology came up as the solution provider for this issue [57]. In the past few years, several nanomaterial-engineered systems proved to be excellent and extraordinary disinfectants including silver nanoparticles [58], Ag-fullerenes n-C_{60} [59] and CNTs [60]. However, the poor dispersion stability of CNTs limits their application and still research is going to further improve the material by surface functionalization [61]. Similar is the case for the other CNMs, where the employment of fullerenes for antimicrobial studies is still budding and further material modifications are under research [62].

1.3.3 Membrane Filtration

Membrane filtration is another wastewater treatment technique that recently picked momentum. It is a physical separation method characterized by the ability to separate contaminants of different sizes or concentration levels. Membrane filters act as a barrier to separate contaminants from water. The overall performance of a membrane is decided by two crucial factors, membrane permeability and selectivity. In general, a high permeability and selectivity membrane is always preferred [63]. Such a type of membrane improves the overall purity of the water and also consumes lower energies which becomes an important aspect of this pressure-driven process. On that note, successful studies have proved that the incorporation

of CNMs into a membrane (mostly polymer-based membranes) enhances the overall purity of the output water [64–66].

1.3.4 Heterogeneous Photocatalysis

In the last few years, heterogeneous photocatalysis got tremendous attention from material science researchers because conventional water treatment techniques are too slow, ineffective, generate toxic by-products and are not eco-friendly. To overcome these problems, new and facile strategies have been developed and tested. One such method is heterogeneous photocatalysis. It is an advanced oxidative process (AOP) which consists of oxidation-reduction reactions in water and air. AOP's overall performance depends on the production and utilization of hydroxyl radicals [67]. Therefore, the term photocatalysis can be defined as a photon-assisted chemical reaction in the presence of a semiconductor photocatalyst [68].

1.3.4.1 Basic principle and mechanism

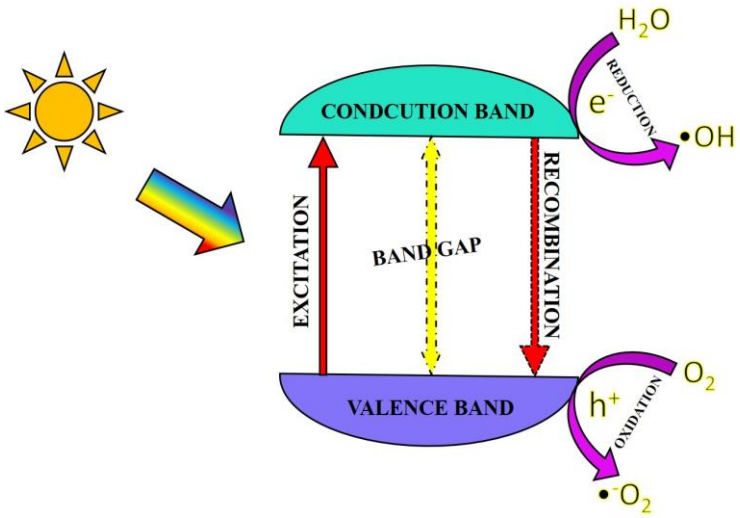

Figure 1.8 *Schematic of photocatalysis degradation mechanism.*

The photocatalytic process majorly involves three processes as shown in Fig. 1.8: photon absorption, electron-hole pair (exciton) generation and separation and surface catalytic reactions. Therefore, improvement in any of these processes simultaneously enhances photocatalytic performance [69]. (1) When the semiconductor is irradiated with energy equal to or greater than the bandgap of the semiconductor material, electrons get pulled out of the valence band (VB) and go to the conduction band (CB), leaving behind a hole vacancy in the VB. This whole process can be summarized as photon absorption and exciton generation. (2) The charge separation process involves the disengagement of the photo-generated charge

carriers. This happens by the migration of charge carriers towards the surface. Meanwhile, a large portion of these electrons and holes recombine due to the electrostatic force of interactions resulting in photon generation or heat. (3) Then, the electrons in the CB initiate the reduction reaction and reduce the target pollutant. Similarly, the holes in the VB oxidize the adsorbed toxic pollutant. Here, the oxidation and reduction reactions take place in the presence of the radical reactive species namely hydroxyl radical (•OH) and superoxide radicals ($\bullet O_2^-$). These radicals are formed due to the following reactions in the aqueous medium loaded with the catalyst and the pollutant in the presence of the light:

$$\textbf{Semiconductor} + h\nu \rightarrow h^+ + e^- \quad \text{---------- 1.1}$$

$$h^+ + H_2O \rightarrow \bullet OH + H^+ \quad \text{---------- 1.2}$$

$$e^- + O_2 \rightarrow \bullet O_2^- \quad \text{---------- 1.3}$$

$$Pollutant + (\bullet OH,\ h^+, \bullet O_2^-) \rightarrow Pollutant\ degradation \quad \text{--------- 1.4}$$

From the above discussion, it is clear that •OH radicals have strong oxidising power and $\bullet O_2^-$ radicals have strong reducing power and can be used to degrade several organic pollutants.

1.3.4.2 Photocatalytic degradation of rhodamine B dye

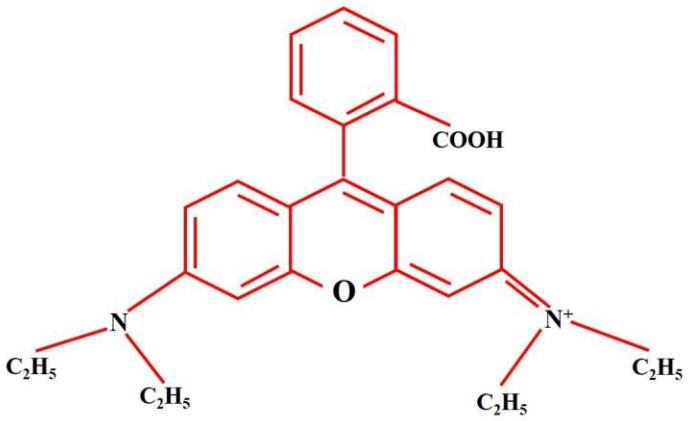

Figure 1.9 *Rhodamine B (RhB) chemical structure.*

RhB is a cationic xanthene dye with a bright pink colour having an absorption maximum at λ=554 nm. RhB is one of the most explored dyes in photocatalysis applications. The chemical structure of RhB essentially consists of ethyl groups on the edge of the benzene rings (Fig. 1.9) and upon prolonged light illumination, the absorption spectrum undergoes a blue shift due to the de-ethylation of the RhB dye molecule eventually leading to chromophore cleavage and

hence, de-colouration of the dye solution is achieved [70]. Chromophore is that part of the molecule which when exposed to light will absorb and reflect a certain colour.

Besides, pollutant degradation, photocatalysis is employed for several other applications like CO_2 reduction, water splitting, disinfection and many more [71].

1.4 Literature review on materials for photocatalytic degradation

Photocatalysis is a vast subject dealing with a wide variety of environmental applications. As previously discussed, a material must satisfy a few basic criteria to become an efficient photocatalyst. These include a suitable bandgap, a decent specific surface area and appropriate energy band levels for surface redox reactions to take place. Apart from carbon-based photocatalysts, there are several metal-based oxides, sulphides, nitrides, etc that are proven to be excellent photocatalysts. This section deals with a brief literature review of the current trends in photocatalytic dye degradation studies. Broadly, this section can be classified into two categories: one that deals with only carbon-based photocatalytic material and the other with all non-carbon-based photocatalytic materials.

1.4.1 Non-carbonaceous photocatalytic materials

The most commonly employed material for dye degradation studies is transition metal-based photocatalysts. Due to their suitable band gaps and band edge potentials, transition metal-based photocatalysts are widely preferred. TiO_2 is the highest preferred and proven photocatalyst material [72]. It has an ideal bandgap of 3.2 eV, which essentially falls in the ultraviolet region of the solar spectrum. To utilize the visible light which mostly reaches the earth's surface, bandgap tuning is employed where heterostructures or hybrids are formed by coupling or doping with other suitable materials thereby enhancing the TiO_2 photodegradation efficiency [73]. Other metal oxides that are widely used are ZnO, CeO_2, Fe_2O_3, CuO, Bi_2O_3, etc. [74,75]. Besides, metal sulphides like MoS_2, ZnS, WS_2, etc are applied for dye degradation studies [76]. Due to their excellent physical, chemical and optical properties, they have received great research interest [77]. For example, MoS_2 is a layered material having a bandgap between 1.1-1.3 eV. Upon exfoliation, MoS_2 nanosheets are formed and formed and present a bandgap of 1.7-1.9 eV [78]. Notably, several properties of this material can be altered by varying the number of layers and morphology [79]. Apart from these metal oxides and sulphides, metal-halides, selenides, phosphates, and nitrides are actively used for dye degradation studies. A

summary of this section can be tabulated where all the various photocatalyst materials, the target dye and other results are discussed in one place (Table 1.1).

Table 1.1 Literature review on non-carbonaceous photocatalyst materials for dye degradation studies.

Target Dye	Photocatalyst	Irradiation		Dye Conc. (mg/L)	Photo-catalyst Conc. (mg/L)	Efficiency (%)	Ref. No.
		Source	Time (min)				
MB	ZnO NPs	11W UV lamp	120	-	50	80	[80]
MG	$CdS/CdWO_4$	1kW Xe lamp	100	100	600	97	[81]
MO	$BiFeO_3/CuS/SiO_2$	LED	60	-	500	99	[82]
MG	CdS	9W LED	120	20	20000	95	[83]
RhB	hBN/BiOBr	300W Xe lamp	30	10	100	99	[84]
MB	$ZnWO_4/CdS$	350W Xe lamp	105	20	200	95.7	[85]
MB	CdS/Mg-Al	300W Xe lamp	90	10	400	94.78	[86]
MB	BiOCl	15W UV lamp	240	5	500	80	[87]
MB	CuS	70W Hg lamp	120	5	1600	100	[88]
RR141	ZnO/CdS	UV lamp	240	10	250	80	[89]
MB	ZnO/Mn	8W Hg lamp	120	-	300	99	[90]
MB	hBN/PANI	UV source	90	10	200	93	[91]
MO						95	
MO	$ZnO/ZnSe/MoSe_2$	Visible source	180	30	600	91.5	[92]
MO	$ZnO/ZNFe_2/NG$	10W LED lamp	140	10	333.33	99	[93]
MB	CuO/ZnO	500W halogen lamp	85	10	4000	97	[94]
RhB	ZnO/Ag	300W Xe lamp	20	10	1500	100	[95]

RB203	ZnO/CNT	8W UV lamp	20	20	5	99.1	[96]
MB	MoS_2	Sunlight	20	32	100	99.3	[97]
MB	$MnTiO_3/TiO_2$	Sunlight	240	-	100	75	[98]
RhB	Ce-Sm/TiO_2	250W Xe lamp	30	10	-	98	[99]
RhB	CeO_2/TiO_2	Xe lamp	180	-	-	82	[100]

1.4.2 Carbonaceous photocatalytic materials

The current section deals with photocatalytic degradation studies based on CNMs coupled with graphitic carbon nitride. From earlier discussions, it can be inferred that the properties of carbon materials are deeply associated with their dimensions and morphology. Accordingly, C/g-C_3N_4 materials usually show different physicochemical characteristics. Therefore, these functional CNMs can be roughly categorised into three groups; 0D, 1D and 2D. Each of the types is discussed in detail.

1.4.2.1 0D CNMs based g-C_3N_4 photocatalysts

0D CNMs typically include carbon quantum dots (CQDs), fullerenes, etc. and generally possess the following advantages: (1) it has significant surface effects and quantum confinement effect due to their tiny size. (2) the photo-generated carriers have powerful redox capability compared with other dimensional CNMs. (3) the operability of 0D CNMs is high including tuneable optoelectronic properties, suitable functionalization, etc. that can promote their photoluminescence activity. Also, it has excellent solubility, chemical reactivity and so on, making these materials promising in the field of photocatalysis and other photochemical applications.

Some of the reports that worked on the photocatalytic degradation of 0D CNMs/g-C_3N_4 are discussed here. Fang. S and co-workers designed C-dots modified g-C_3N_4 modified hybrids for RhB degradation studies [101]. They used a novel strategy for synthesis where the C-dots were hydrothermally prepared by taking carbon soot as the raw material. Further, the obtained C-dots stock solution was mixed with 10g of dicyandiamide and the dried mixture was pyrolyzed at 823 K for 3 hrs. The resultant yellow product was milled into powder for further use. The photocatalytic studies were carried out on RhB under a 3W LED lamp. The C-dot/g-C_3N_4 photocatalyst concentration was fixed at 1mg/L and the dye concentration was $1x10^{-5}$

mole/L. It was observed that 0.25 wt.% of C-dot modified g-C_3N_4 showed the highest photocatalytic activity which was 3 times higher than pristine g-C_3N_4. Another group Liu. H et.al has made N-doped CQD-modified g-C_3N_4 through the impregnation method and achieved 100% degradation of RhB under a visible light source [102]. Xu. Z and group employed a simple and fast hydrothermal (HT) process where C-dots were dispersed in between the layers of g-C_3N_4 without hampering its original structure [103]. This technique has resulted in a better version of the material with an enlarged specific surface area by 356 times and showed improved photodegradation performance on RhB. A similar type of work with various other pollutants and synthesis methodology has been reported and can be summarized in the table given below (Table 1.2).

Table 1.2 Literature review on 0D CNMs/ g-C_3N_4 photocatalyst materials for pollutant degradation studies.

Target Pollutant	**Photocatalyst**	**Synthesis Methodology**	**Efficiency (%)**	**Irradiation**		**Ref. No.**
				Source	**Time (min)**	
Phenol	C-dot/g-C_3N_4	Impregnation-Thermal method	100	300W Xe lamp	200	[104]
BPA	CQD/ Exf. g-C_3N_4	Hydrothermal	90	64W LED	240	[105]
RhB	GO/g-C_3N_4/C-dots	Hydrothermal	99	Visible Source	35	[106]
CV			99		60	
RhB	C_{60}/g-C_3N_4	Adsorption	97	500W Xe lamp	60	[107]
RhB	CQD/g-C_3N_4	Thermal decomposition	100	300W Xe lamp	80	[108]
MB			100		20	
MO	S-CQDs/g-C_3N_4	Co-polymerization	94.3	300W Xe lamp	80	[109]
MB	N-CQDs	Hydrothermal	97	Sunlight	160	[110]

1.4.2.2 1D CNMs based g-C_3N_4 photocatalyst

The 1D functional CNMs commonly used for g-C_3N_4 modification are mainly CNTs and carbon nanofibers (CNFs). These materials usually possess these features: (1) 1D materials can be easily functionalized with hydroxyl and carboxyl groups which can increase the surface chemical activity of the material as a whole. (2) The 1D linear channel provides an easy path for the direct transfer of electrons. (3) The 1D tubular structure provides a higher specific

surface area thus, providing more active sites. Some of the recent works published on 1D CNMs/g-C_3N_4 material for photocatalytic studies are discussed herewith. Shi. L and co-workers designed CNTs modified porous g-C_3N_4 using single step thermal polycondensation method and successfully prepared this hybrid structure [111]. The CNTs used were of commercial-grade quality. The obtained photocatalyst was studied over RhB degradation under a 300 W Xe lamp visible light source where 30 mg of the catalyst was added to 50 mL of the dye solution having a concentration of 5 mg/L. To obtain adsorption equilibrium, the solution was stirred for 60 min in aphotic conditions. After 40 min of irradiation under light, the hybrid composite degraded by almost 99%. However, pristine material could perform up to 81%. Hence, the addition of CNTs leads to the enhancement of the photodegradation performance by efficiently restricting the recombination of the charge carriers. Another group Ma. T, et.al, synthesized CNFs modified g-C_3N_4 through electrospinning technique, high-temperature pyrolysis, and gas-solid phase method [112]. Herein, the authors first prepared g-C_3N_4 via thermal pyrolysis of melamine at 550 °C for 4hrs. followed by an electrospinning technique where the precursor solution was the mixture of g-C_3N_4+PAN dissolved DMF solution. Finally, the CNF/g-C_3N_4 was prepared through a facile gas-solid method where a high-pressure and temperature autoclave was utilised as the reaction chamber. The prepared photocatalyst was employed for the degradation of different organic dyes, especially, methyl orange (MO), acid red 18 (AR 18), methylene blue (MB), sodium fluorescein (SF) and ethyl rhodamine B (ER B) under a UV light (500W Hg lamp) and a visible source (300 W Xe lamp). The initial concentration of all the target pollutants was 5mg/L and the catalyst loading was 1mg/ml in the dye solution. It was observed that under UV light except for MB, all other dyes were degraded above 90 % in 6 hrs. However, under visible light even after 9 hrs except for AR18 and SF, other dyes could barely perform. Therefore, the role of CNFs was to increase the adsorption sites thereby increasing the photocatalytic efficiency. Besides, dye degradation studies CNTs/g-C_3N_4 model is highly employed for H_2 generation [113–116], oxygen evolution reactions [117], CO_2 reduction [118], electrochemical sensors [119,120] and many more. Some of the works are listed in Table 1.3.

Table 1.3 Literature review on 1D CNMs/ g-C_3N_4 photocatalyst materials for pollutant degradation studies.

Target Pollutant	Photocatalyst	Synthesis Methodology	Efficiency (%)	Irradiation		Ref. No.
				Source	Time (min)	
MB	MWCNT/White g-C_3N_4	Hydrothermal	100	300W Xe lamp	180	[121]
MO	NCNT/mpg-C_3N_4	Pyrolysis	88	300W Xe lamp	300	[122]
RhB			95		30	
RhB	MWCNT/g-C_3N_4	Supramolecular Assembly	100	300W Xe lamp	60	[123]
RhB	CNT/g-C_3N_4	Hydrothermal	100	150W Xe lamp	80	[124]
RhB	CNTg-C_3N_4	Thermal decomposition	91.7	Visible light	300	[125]
RhB	CNT/g-C_3N_4	Water bath method	98.1	300W Xe lamp	60	[126]
RhB	CNF/g-C_3N_4	Dip coating + pyrolysis	98	300W Xe lamp	60	[127]

1.4.2.3 2D CNMs based g-C_3N_4 photocatalyst

The 2D functional CNMs typically include graphene, graphene oxide (GO) or reduced graphene oxide (rGO), g-C_3N_4 nanosheets and their derivates essentially consisting of abundant sp^2 hybridizations. These 2D structures possess some of the following features: (1) the excellent covalent bond on their surface resulting in powerful in-plane conductivity, (2) the vast surface of 2D materials renders abundant surface sites that help in faster photoelectrochemical reactions. (3) the pi-pi interactions are superior in 2D structures thus coupling with g-C_3N_4 is highly favourable. Some of the major works based on 2D CNMs/ g-C_3N_4 material for dye degradation are discussed here. One of the reports by Li. Y and group [128] were about cross-linked rGO/g-C_3N_4 nanocomposite fabricated via pyrolysis of a mixture of cyanamide and GO with different weight ratios. The photodegradation study was carried out on RhB dye and 4-nitrophenol under visible light illumination. After 75 min of irradiation, RhB was completely degraded by GCN/rGO-2.5. However, other samples moderately performed. This improved performance of the nanocomposite could be attributed to visible light utilization, efficient electron transportation and oxidation power which is due to the positive shift in the VB

potential, narrow bandgap, and improved electronic conductivity. Another group Christy. E. J. S and Pius. A synthesized carboxymethyl cellulose (CMC) based g-C_3N_4/GO/CMC bio-composite through a solution blending method where CMC solution and GO solution were mixed in an ultrasonic bath to get a homogeneous suspension. Later, 20 mL of $NH_3.H_2O$ was added to the above suspension and heated at 90 °C under continuous stirring for 60min to obtain GO/CMC composite. Further, g-C_3N_4 solution was mixed to attain a homogeneous solution which was heated at 80 °C and calcined at 250 °C for 2 hrs to obtain a g-C_3N_4/GO/CMC composite. This novel composite was applied to basic green 4 (BG 4) and basic blue 9 (BB 9) dye degradation under direct sunlight. It was observed that 94% of BG 4 was degraded in 60min whereas 98% of BB 9 was degraded in 50 min. Besides dye degradation studies, these 2D/2D structures are applied for Bisphenol A (BPA) degradation [129]. Jilani. A and group prepared sulfonated polyaniline graphene-modified C_3N_4 for BPA degradation under UV radiation [130]. H_2 evolution studies have also been tested using 2D CNMs/g-C_3N_4 hybrid structure [131–134]. Further, CO_2 reduction [135,136], antibacterial studies [137,138] and electrochemical sensing studies [139,140] are also carried out using this novel material. A summary of various 2D/2D CNMs models for photodegradation application is tabulated below (Table 1.4).

Table 1.4 Literature review on 2D CNMs/ g-C_3N_4 photocatalyst materials for pollutant degradation studies.

Target Pollutant	**Photocatalyst**	**Synthesis Methodology**	**Efficiency (%)**	**Irradiation**		**Ref. No.**
				Source	**Time (min)**	
RhB	GO/g-C_3N_4	Sono-chemical	94.2	300W Xe lamp	150	[141]
2,4-dichlorophenol			87.1		240	
MB	GO/g-C_3N_4	Ultrasonication	99	LED source	180	[142]
MO	rGO/g-C_3N_4	Solvent method	97.5	300W Xe lamp	60	[143]
RhB	rGO/g-C_3N_4	Thermal decomposition	95	350W Xe lamp	60	[144]
MO	rGO/g-C_3N_4	Thermal decomposition + hydrothermal	92.3	500W Xe lamp	120	[145]
RhB	rGO/g-C_3N_4	Microwave Irradiation	97.2	300W Xe lamp	30	[146]

From the above literature survey, it was observed that there is an urgent need for a visible-light active photocatalyst in the market which is environmentally benignant, inexpensive and shows excellent photocatalytic performance. Further, the performance of the currently available g-C_3N_4 photocatalyst was enhanced by coupling with metal-based oxides, sulphides, etc. This leads to an additional task of removal of these metal-based photocatalysts from the water which otherwise would result in polluting the marine ecosystem. To overcome this problem, carbon nanomaterials-based g-C_3N_4 hybrid photocatalyst materials have been developed which showed remarkable performance as discussed in the literature review. However, the studied literature showed higher efficiencies when either the CNMs loading amount was higher or the light illumination time was longer. Therefore, the present thesis work was carefully curated by aiming at the voids currently present in this field of research and the following objectives were developed.

1.5 Objectives of the present thesis work

The key objectives of this thesis work are as follows:

- To optimize the synthesis parameters of pristine g-C_3N_4 photocatalyst material and study its photocatalytic dye degradation property.
- To enhance the photocatalytic performance of g-C_3N_4 by improving the surface area via templating technique.
- To enhance the photocatalytic performance of g-C_3N_4 by synergistically coupling with carbon nanomaterials such as CS, CNT and GNP prepared by arc discharge and microwave exfoliation techniques.
- To compare & study the photocatalytic property and eventually propose a degradation mechanism based on the morphology of the developed photocatalyst materials.

1.6 Structure of the thesis

This thesis presents an organised compilation of the work carried out over the years. On this note, the thesis has been divided into six chapters.

Chapter 1 deals with an overview of the carbon element and its structures, its basic properties, and applications. Based on the morphology CNMs have been categorised and briefly discussed. This chapter also discusses the contribution of CNMs in wastewater treatment and various other methods employed using CNMs focusing more on the heterogenous

photocatalysis, basic principle and mechanism. In addition, a literature study has been included on various types of photocatalytic materials employed for the decontamination of wastewater. In particular, graphitic carbon nitride and CNMs-based hybrid photocatalysts for dye degradation application are discussed. A summarized format of some of the recent reports is tabulated at the end. Finally, the objectives are discussed in bullet points in this chapter.

Chapter 2 describes detailed information about materials synthesis and characterization techniques used in the present study. It involves the synthesis of g-C_3N_4 through the thermal decomposition method. Followed by CNTs and CS synthesis via conventional arc discharge technique. This chapter also speaks about GNP synthesis via shear force-dominated exfoliation of exfoliated graphite. Also, the synthesis of g-C_3N_4/CNMs hybrid photocatalysts is discussed. Further, the details of the characterization techniques and photodegradation studies carried out in this work have been explained in this chapter. Structural and morphological investigations were done by X-ray diffraction (XRD), field-emission scanning electron microscopy (FE-SEM), high-resolution transmission electron microscopy (HR-TEM), thermogravimetric analyser (TGA) and Raman spectroscopy (RS). Optical studies by UV-Vis diffuse reflectance spectroscopy (UV-DRS), photoluminescence spectroscopy (PL), Fourier transform infrared spectroscopy (FT-IR) and X-ray photoelectron spectroscopy (XPS) techniques. Surface studies were carried out using N2 adsorption-desorption measurements (BET) and a zeta potential analyser. The photocatalytic degradation studies were carried out using a UV-Vis spectrophotometer instrument.

Chapter 3 is divided into two parts. The first part describes the structural, morphological, optical, and photocatalytic studies of pristine g-C_3N_4 photocatalysts synthesized via the pyrolysis process. In this section, the optimization of reaction temperature and atmosphere has been done and all the samples were applied to RhB degradation studies. It was observed that the *650Air* sample showed the best performance compared to other samples by degrading 96% of dye (conc. = 10mg/L) in 90 min. The second part deals with the improvement of the photocatalytic performance of the pristine g-C_3N_4 through a facile green templating technique where a porous and expanded g-C_3N_4 was achieved with enhanced photodegradation efficiency. Here, a certain amount of NH_4Cl was added to the precursor material during the pyrolysis process. The NH_4Cl at elevated temperature starts bubbling and gets decomposed leaving behind a porous and expanded g-C_3N_4 photocatalyst. It was observed that the expanded

g-C_3N_4 showed a 2.4 times higher photodegradation rate than its counterpart and degraded around 94% in just 30 min.

Chapter 4 is subdivided into three parts. The first part deals with the optimization of process parameters of arc discharge setup for high yields of CNTs and C-Soot. The obtained samples were analysed using XRD, FE-SEM, HR-TEM, RS, and TGA techniques. with the help of these results, the optimum process parameters were chosen. The second part deals with the structural, morphological, optical, and photocatalytic studies of the C-Soot/g-C_3N_4 hybrid photocatalyst. Here different weight ratios of C-Soot from 0.1% to 1% with respect to g-C_3N_4 were considered. The obtained samples were applied for 20 mg/L RhB dye degradation performance. It was observed that 0.1% weight of C-Soot in g-C_3N_4 showed the best performance with around 96% of dye getting removed as compared to pristine g-C_3N_4 which showed 88% degradation in 90 min. The third part describes the structural, morphological, optical, and photocatalytic activity of the CNT/g-C_3N_4 hybrid photocatalyst. Here also, a similar sample set was considered as in the previous case. Here, 97% of the dye was degraded in 90 min whereas the pristine g-C_3N_4moderately performed.

Chapter 5 too is categorised into two parts. The first part describes the structural, morphological, optical, and photocatalytic studies of GNP/g-C_3N_4 hybrid photocatalyst. Here too, different weight ratios were considered and RhB degradation performance was observed. It was observed that 96% of the dye was eliminated in 60 min. However, pristine g-C_3N_4 barely performed. The reason for faster degradation is the morphology of GNP and this hybrid forms a 2D/2D heterostructure where the charge separation and transportation rates are much higher as compared to 0D/2D or 1D/2D structures. As an extension to this 2D/2D structure, another non-carbon-based 2D structure was incorporated within g-C_3N_4. The second part deals with the h-BN/g-C_3N_4 hybrid. h-BN also called white graphene was commercially procured and used in this work as it is. h-BN has a similar structure as that of g-C_3N_4. This hybrid structure was applied for RhB degradation studies and it was observed that 0.5% loading of h-BN in g-C_3N_4 showed the best results. Here, 91% of the dye was removed in 60 min however, pristine g-C_3N_4 showed 55% degradation after 60 min.

Chapter 6 gives the summary and conclusions of the present thesis work. Besides, the future scope of this work is also discussed and suggestions are made for the extension of this work.

References

[1] M. Inagaki, F. Kang, M. Toyoda, H. Konno, Advanced materials science, and engineering of carbon, n.d.

[2] J.C. Angus, C.C. Hayman, Low-Pressure, Metastable Growth of Diamond and "Diamondlike" Phases, n.d. www.sciencemag.org.

[3] S.M. Lee, D.S. Kang, J.S. Roh, Bulk graphite: Materials and manufacturing process, Carbon Letters. 16 (2015) 135–146. https://doi.org/10.5714/CL.2015.16.3.135.

[4] H.O. Pierson, Handbook of carbon, graphite, diamond, and fullerenes: properties, processing, and applications, Noyes Publications, 1993.

[5] D. Luo, S.R. Schricker, W. Sigmund, S. Zauscher, Handbook of Nanomaterials Properties, n.d.

[6] O.A. Shenderova, V. V. Zhirnov, D.W. Brenner, Carbon nanostructures, Critical Reviews in Solid State and Materials Sciences. 27 (2002) 227–356. https://doi.org/10.1080/10408430208500497.

[7] H.S. Nalwa, Encyclopedia of nanoscience and nanotechnology. v. 1-10., American Scientific Publishers, 2004.

[8] EMERGY ("energy memory" and "emergent property of energy use") and its unit the "emjoule" for our embodied energy concept, EMERGY-defined "emdollar" for foreign trade, and "empower" for rate of EMERGY use Polunin suggested a different spelling "enmergy" used by H. T. Odum, in Ecosystem Theory, n.d. www.sciencemag.org.

[9] L.D. Lamb, D.R. Huffman, FULLERENE PRODUCTION, 1993.

[10] CARBON NANOMATERIALS SYNTHESIS, STRUCTURE, PROPERTIES AND APPLICATIONS, n.d.

[11] Takeshi. Akasaka, Fred. Wudl, Shigeru. Nagase, Chemistry of nanocarbons, Wiley, 2010.

[12] H. Lange, M. Sioda, A. Huczko, Y.Q. Zhu, H.W. Kroto, D.R.M. Walton, Nanocarbon production by arc discharge in water, Carbon N Y. 41 (2003) 1617–1623. https://doi.org/10.1016/S0008-6223(03)00111-8.

[13] K.D. Sattler, Carbon nanomaterials sourcebook. Volume 1, Graphene, fullerenes, nanotubes, and nanodiamonds, n.d.

[14] S. Rathinavel, K. Priyadharshini, D. Panda, A review on carbon nanotube: An overview of synthesis, properties, functionalization, characterization, and the application, Mater Sci Eng B Solid State Mater Adv Technol. 268 (2021). https://doi.org/10.1016/j.mseb.2021.115095.

[15] A. Szabó, C. Perri, A. Csató, G. Giordano, D. Vuono, J.B. Nagy, Synthesis methods of carbon nanotubes and related materials, Materials. 3 (2010) 3092–3140. https://doi.org/10.3390/ma3053092.

[16] D. Tasis, N. Tagmatarchis, A. Bianco, M. Prato, Chemistry of carbon nanotubes, Chem Rev. 106 (2006) 1105–1136. https://doi.org/10.1021/cr050569o.

[17] P.G.A. Janssen, K. Schouteden, M.A.J. Veld, (St, The Wondrous World of Carbon Nanotubes "a review of current carbon nanotube technologies," 2003.

[18] H. Qiu, J. Yang, Structure and Properties of Carbon Nanotubes, in: Industrial Applications of Carbon Nanotubes, Elsevier Inc., 2017: pp. 47–69. https://doi.org/10.1016/B978-0-323-41481-4.00002-2.

[19] B. Ribeiro, E.C. Botelho, M.L. Costa, C.F. Bandeira, Carbon nanotube buckypaper reinforced polymer composites: A review, Polimeros. 27 (2017) 247–255. https://doi.org/10.1590/0104-1428.03916.

[20] C. Gao, Z. Guo, J.H. Liu, X.J. Huang, The new age of carbon nanotubes: An updated review of functionalized carbon nanotubes in electrochemical sensors, Nanoscale. 4 (2012) 1948–1963. https://doi.org/10.1039/c2nr11757f.

[21] Y. Saito, S. Uemura, Field emission from carbon nanotubes and its application to electron sources, 2000.

[22] R.H. Baughman, A.A. Zakhidov, W.A. De Heer, Carbon nanotubes - The route toward applications, Science (1979). 297 (2002) 787–792. https://doi.org/10.1126/science.1060928.

[23] M.H.M. Hatta, J. Matmin, N.A.N.N. Malek, F.H. Kamisan, A. Badruzzaman, K. Batumalaie, S. Ling Lee, R. Abdul Wahab, COVID-19: Prevention, Detection, and Treatment by Using Carbon Nanotubes-Based Materials, ChemistrySelect. 8 (2023). https://doi.org/10.1002/slct.202204615.

[24] M.S.A. Bhuyan, M.N. Uddin, M.M. Islam, F.A. Bipasha, S.S. Hossain, Synthesis of graphene, Int Nano Lett. 6 (2016) 65–83. https://doi.org/10.1007/s40089-015-0176-1.

[25] K.E. Whitener, P.E. Sheehan, Graphene synthesis, Diam Relat Mater. 46 (2014) 25–34. https://doi.org/10.1016/j.diamond.2014.04.006.

[26] W. Mu, Y. Fu, S. Sun, M. Edwards, L. Ye, K. Jeppson, J. Liu, Controllable and fast synthesis of bilayer graphene by chemical vapor deposition on copper foil using a cold wall reactor, Chemical Engineering Journal. 304 (2016) 106–114. https://doi.org/10.1016/j.cej.2016.05.144.

[27] K. Edward, K. Mamun, S. Narayan, M. Assaf, D. Rohindra, U. Rathnayake, State-of-the-Art Graphene Synthesis Methods and Environmental Concerns, Appl Environ Soil Sci. 2023 (2023). https://doi.org/10.1155/2023/8475504.

[28] K.S. Kim, Y. Zhao, H. Jang, S.Y. Lee, J.M. Kim, K.S. Kim, J.H. Ahn, P. Kim, J.Y. Choi, B.H. Hong, Large-scale pattern growth of graphene films for stretchable transparent electrodes, Nature. 457 (2009) 706–710. https://doi.org/10.1038/nature07719.

[29] Z. Zhen, H. Zhu, Structure and properties of graphene, in: Graphene: Fabrication, Characterizations, Properties and Applications, Elsevier, 2017: pp. 1–12. https://doi.org/10.1016/B978-0-12-812651-6.00001-X.

[30] A.A. Balandin, Thermal properties of graphene and nanostructured carbon materials, Nat Mater. 10 (2011) 569–581. https://doi.org/10.1038/nmat3064.

[31] M.D. Stoller, S. Park, Z. Yanwu, J. An, R.S. Ruoff, Graphene-Based ultracapacitors, Nano Lett. 8 (2008) 3498–3502. https://doi.org/10.1021/nl802558y.

[32] F. Schedin, A.K. Geim, S. V. Morozov, E.W. Hill, P. Blake, M.I. Katsnelson, K.S. Novoselov, Detection of individual gas molecules adsorbed on graphene, Nat Mater. 6 (2007) 652–655. https://doi.org/10.1038/nmat1967.

[33] H. Nguyen Bich, H. Nguyen Van, Promising applications of graphene and graphene-based nanostructures, Advances in Natural Sciences: Nanoscience and Nanotechnology. 7 (2016). https://doi.org/10.1088/2043-6262/7/2/023002.

[34] B. Jürgens, E. Irran, J. Senker, P. Kroll, H. Müller, W. Schnick, Melem (2,5,8-triamino-tri-s-triazine), an important intermediate during condensation of melamine rings to graphitic carbon nitride: Synthesis, structure determination by x-ray powder diffractometry, solid-state NMR, and theoretical studies, J Am Chem Soc. 125 (2003) 10288–10300. https://doi.org/10.1021/ja0357689.

[35] J. Sehnert, K. Baerwinkel, J. Senker, Ab initio calculation of solid-state NMR spectra for different triazine and heptazine based structure proposals of g-C_3N_4, Journal of Physical Chemistry B. 111 (2007) 10671–10680. https://doi.org/10.1021/jp072001k.

[36] S. Cao, J. Low, J. Yu, M. Jaroniec, Polymeric Photocatalysts Based on Graphitic Carbon Nitride, Advanced Materials. 27 (2015) 2150–2176. https://doi.org/10.1002/adma.201500033.

[37] J. Wen, J. Xie, X. Chen, X. Li, A review on g-C_3N_4-based photocatalysts, Appl Surf Sci. 391 (2017) 72–123. https://doi.org/10.1016/j.apsusc.2016.07.030.

[38] M. Fronczak, Adsorption performance of graphitic carbon nitride-based materials: Current state of the art, J Environ Chem Eng. 8 (2020). https://doi.org/10.1016/j.jece.2020.104411.

[39] Y. Gong, M. Li, H. Li, Y. Wang, Graphitic carbon nitride polymers: Promising catalysts or catalyst supports for heterogeneous oxidation and hydrogenation, Green Chemistry. 17 (2015) 715–736. https://doi.org/10.1039/c4gc01847h.

[40] G. Dong, Y. Zhang, Q. Pan, J. Qiu, A fantastic graphitic carbon nitride (g-C_3N_4) material: Electronic structure, photocatalytic and photoelectronic properties, Journal of Photochemistry and Photobiology C: Photochemistry Reviews. 20 (2014) 33–50. https://doi.org/10.1016/j.jphotochemrev.2014.04.002.

[41] J. Zhu, P. Xiao, H. Li, S.A.C. Carabineiro, Graphitic carbon nitride: Synthesis, properties, and applications in catalysis, ACS Appl Mater Interfaces. 6 (2014) 16449–16465. https://doi.org/10.1021/am502925j.

[42] W. Niu, Y. Yang, Graphitic carbon nitride for electrochemical energy conversion and storage, ACS Energy Lett. 3 (2018) 2796–2815. https://doi.org/10.1021/acsenergylett.8b01594.

[43] X. Kong, X. Liu, Y. Zheng, P.K. Chu, Y. Zhang, S. Wu, Graphitic carbon nitride-based materials for photocatalytic antibacterial application, Materials Science and Engineering R: Reports. 145 (2021). https://doi.org/10.1016/j.mser.2021.100610.

[44] J. Liu, H. Wang, M. Antonietti, Graphitic carbon nitride “reloaded”: Emerging applications beyond (photo)catalysis, Chem Soc Rev. 45 (2016) 2308–2326. https://doi.org/10.1039/c5cs00767d.

[45] K. Kaneko, Determination of pore size and pore size distribution 1. Adsorbents and catalysts, 1994.

[46] R. Rashid, I. Shafiq, P. Akhter, & Muhammad, J. Iqbal, M. Hussain, A state-of-the-art review on wastewater treatment techniques: the effectiveness of adsorption method, (n.d.). https://doi.org/10.1007/s11356-021-12395-x/Published.

[47] C.P. Bergmann, F. Machado, M. Editors, Carbon Nanostructures Carbon Nanomaterials as Adsorbents for Environmental and Biological Applications, n.d. http://www.springer.com/series/8633.

[48] V.K. Gupta, T.A. Saleh, Sorption of pollutants by porous carbon, carbon nanotubes and fullerene- An overview, Environmental Science and Pollution Research. 20 (2013) 2828–2843. https://doi.org/10.1007/s11356-013-1524-1.

[49] M. Sajid, M. Asif, N. Baig, M. Kabeer, I. Ihsanullah, A.W. Mohammad, Carbon nanotubes-based adsorbents: Properties, functionalization, interaction mechanisms, and applications in water purification, Journal of Water Process Engineering. 47 (2022). https://doi.org/10.1016/j.jwpe.2022.102815.

[50] Z. Yin, C. Cui, H. Chen, Duoni, X. Yu, W. Qian, The Application of Carbon Nanotube/Graphene-Based Nanomaterials in Wastewater Treatment, Small. 16 (2020). https://doi.org/10.1002/smll.201902301.

[51] L.Y. Jun, N.M. Mubarak, M.J. Yee, L.S. Yon, C.H. Bing, M. Khalid, E.C. Abdullah, An overview of functionalised carbon nanomaterial for organic pollutant removal, Journal of Industrial and Engineering Chemistry. 67 (2018) 175–186. https://doi.org/10.1016/j.jiec.2018.06.028.

[52] J.R.M. Barbosa, A.S.G.G. Santos, A.T. Viana, A.G. Gonçalves, O.C. Nunes, M.F.R. Pereira, O.S.G.P. Soares, Carbon-based materials for water disinfection and heavy metals removal, Environmental Technology (United Kingdom). (2022). https://doi.org/10.1080/09593330.2022.2154173.

[53] R. Gusain, N. Kumar, S.S. Ray, Recent advances in carbon nanomaterial-based adsorbents for water purification, Coord Chem Rev. 405 (2020). https://doi.org/10.1016/j.ccr.2019.213111.

[54] D. Kumar Yadav, S. Srivastava, Carbon nanotubes as adsorbent to remove heavy metal ion (Mn^{+7}) in wastewater treatment, 2017. https://doi.org/10.1016/j.matpr.2017.02.312.

[55] F. Mashkoor, A. Nasar, Inamuddin, Carbon nanotube-based adsorbents for the removal of dyes from waters: A review, Environ Chem Lett. 18 (2020) 605–629. https://doi.org/10.1007/s10311-020-00970-6.

[56] M.A. AlSaadi, A. Al Mamun, M.Z. Alam, M.K. Amosa, M.A. Atieh, Removal of Cadmium from Water by CNT-PAC Composite: Effect of Functionalization, Nano. 11 (2016). https://doi.org/10.1142/S1793292016500119.

[57] Q. Li, S. Mahendra, D.Y. Lyon, L. Brunet, M. V. Liga, D. Li, P.J.J. Alvarez, Antimicrobial nanomaterials for water disinfection and microbial control: Potential applications and implications, Water Res. 42 (2008) 4591–4602. https://doi.org/10.1016/j.watres.2008.08.015.

[58] J.R. Morones, J.L. Elechiguerra, A. Camacho, K. Holt, J.B. Kouri, J.T. Ramírez, M.J. Yacaman, The bactericidal effect of silver nanoparticles, Nanotechnology. 16 (2005) 2346–2353. https://doi.org/10.1088/0957-4484/16/10/059.

[59] D.Y. Lyon, L.K. Adams, J.C. Falkner, P.J.J. Alvarez, Antibacterial activity of fullerene water suspensions: Effects of preparation method and particle size, Environ Sci Technol. 40 (2006) 4360–4366. https://doi.org/10.1021/es0603655.

[60] S.M. Al-Hakami, A.B. Khalil, T. Laoui, M.A. Atieh, Fast disinfection of escherichia coli bacteria using carbon nanotubes interaction with microwave radiation, Bioinorg Chem Appl. 2013 (2013). https://doi.org/10.1155/2013/458943.

[61] M. Maas, Carbon nanomaterials as antibacterial colloids, Materials. 9 (2016). https://doi.org/10.3390/ma9080617.

[62] M. Azizi-Lalabadi, H. Hashemi, J. Feng, S.M. Jafari, Carbon nanomaterials against pathogens; the antimicrobial activity of carbon nanotubes, graphene/graphene oxide, fullerenes, and their nanocomposites, Adv Colloid Interface Sci. 284 (2020). https://doi.org/10.1016/j.cis.2020.102250.

[63] B.D. Freeman, Basis of permeability/selectivity tradeoff relations in polymeric gas separation membranes, Macromolecules. 32 (1999) 375–380. https://doi.org/10.1021/ma9814548.

[64] M. Jani, J.A. Arcos-Pareja, M. Ni, Engineered Zero-Dimensional Fullerene/Carbon Dots-Polymer Based Nanocomposite Membranes for Wastewater Treatment, Molecules. 25 (2020). https://doi.org/10.3390/molecules25214934.

[65] S. Ali, S.A.U. Rehman, H.Y. Luan, M.U. Farid, H. Huang, Challenges, and opportunities in functional carbon nanotubes for membrane-based water treatment and desalination, Science of the Total Environment. 646 (2019) 1126–1139. https://doi.org/10.1016/j.scitotenv.2018.07.348.

[66] U. Chadha, S.K. Selvaraj, S. Vishak Thanu, V. Cholapadath, A.M. Abraham, M. Zaiyan M, M. Manoharan, V. Paramsivam, A review of the function of using carbon nanomaterials in membrane filtration for contaminant removal from wastewater, Mater Res Express. 9 (2022). https://doi.org/10.1088/2053-1591/ac48b8.

[67] J.L. Wang, L.J. Xu, Advanced oxidation processes for wastewater treatment: Formation of hydroxyl radical and application, Crit Rev Environ Sci Technol. 42 (2012) 251–325. https://doi.org/10.1080/10643389.2010.507698.

[68] G. Palmisano, V. Augugliaro, M. Pagliaro, L. Palmisano, Photocatalysis: A promising route for 21st century organic chemistry, Chemical Communications. (2007) 3425–3437. https://doi.org/10.1039/b700395c.

[69] A.L. Linsebigler, G. Lu, J.T. Yates, Photocatalysis on TiOn Surfaces: Principles, Mechanisms, and Selected Results, 1995.

[70] M. Pica, S. Calzuola, A. Donnadio, P.L. Gentili, M. Nocchetti, M. Casciola, De-ethy lation and cleavage of rhodamine b by a zirconium phosphate/silver bromide composite photocatalyst, Catalysts. 9 (2019). https://doi.org/10.3390/catal9010003.

[71] J. Yi-Junnxu Editors, Green Chemistry and Sustainable Technology Heterogeneous Photocatalysis: From Fundamentals to Green Applications, n.d. https://doi.org/10.1007/978-3-662-48719-8.

[72] D. Chen, Y. Cheng, N. Zhou, P. Chen, Y. Wang, K. Li, S. Huo, P. Cheng, P. Peng, R. Zhang, L. Wang, H. Liu, Y. Liu, R. Ruan, Photocatalytic degradation of organic pollutants using TiO2-based photocatalysts: A review, J Clean Prod. 268 (2020). https://doi.org/10.1016/j.jclepro.2020.121725.

[73] N. Madkhali, C. Prasad, K. Malkappa, H.Y. Choi, V. Govinda, I. Bahadur, R.A. Abumousa, Recent update on photocatalytic degradation of pollutants in waste water using TiO2-based heterostructured materials, Results in Engineering. 17 (2023). https://doi.org/10.1016/j.rineng.2023.100920.

[74] P. Ahuja, S.K. Ujjain, R. Kanojia, P. Attri, Transition metal oxides and their composites for photocatalytic dye degradation, Journal of Composites Science. 5 (2021). https://doi.org/10.3390/jcs5030082.

[75] R. Gusain, K. Gupta, P. Joshi, O.P. Khatri, Adsorptive removal, and photocatalytic degradation of organic pollutants using metal oxides and their composites: A comprehensive review, Adv Colloid Interface Sci. 272 (2019). https://doi.org/10.1016/j.cis.2019.102009.

[76] D. Ayodhya, G. Veerabhadram, A review on recent advances in photodegradation of dyes using doped and heterojunction-based semiconductor metal sulfide nanostructures for environmental protection, Mater Today Energy. 9 (2018) 83–113. https://doi.org/10.1016/j.mtener.2018.05.007.

[77] S. Zhang, X. Ou, Q. Xiang, S.A.C. Carabineiro, J. Fan, K. Lv, Research progress in metal sulfides for photocatalysis: From activity to stability, Chemosphere. 303 (2022). https://doi.org/10.1016/j.chemosphere.2022.135085.

[78] L.O. Amaral, A.L. Daniel-da-Silva, MoS2 and MoS2 Nanocomposites for Adsorption and Photodegradation of Water Pollutants: A Review, Molecules. 27 (2022). https://doi.org/10.3390/molecules27206782.

[79] Y. Yuan, R. tang Guo, L. fei Hong, X. yin Ji, Z. sheng Li, Z. dong Lin, W. guo Pan, Recent advances and perspectives of MoS2-based materials for photocatalytic dyes degradation: A review, Colloids Surf A Physicochem Eng Asp. 611 (2021). https://doi.org/10.1016/j.colsurfa.2020.125836.

[80] S.M. Tabrizi Hafez Moghaddas, B. Elahi, V. Javanbakht, Biosynthesis of pure zinc oxide nanoparticles using Quince seed mucilage for photocatalytic dye degradation, J Alloys Compd. 821 (2020). https://doi.org/10.1016/j.jallcom.2019.153519.

[81] H. Cui, B. Li, Z. Li, X. Li, S. Xu, Z-scheme based CdS/CdWO 4 heterojunction visible light photocatalyst for dye degradation and hydrogen evolution, Appl Surf Sci. 455 (2018) 831–840. https://doi.org/10.1016/j.apsusc.2018.06.054.

[82] V. Dutta, S. Sharma, P. Raizada, A. Hosseini-Bandegharaei, J. Kaushal, P. Singh, Fabrication of visible light active BiFeO3/CuS/SiO2 Z-scheme photocatalyst for efficient dye degradation, Mater Lett. 270 (2020). https://doi.org/10.1016/j.matlet.2020.127693.

[83] S. Anju Devi, K. Jugeshwar Singh, K. Nomita Devi, Visible light driven photocatalytic activities of metal sulfides synthesized by simple co-precipitation method, Mater Today Proc. 65 (2022) 2819–2824. https://doi.org/10.1016/j.matpr.2022.06.270.

[84] J. Di, J. Xia, M. Ji, B. Wang, S. Yin, Q. Zhang, Z. Chen, H. Li, Advanced photocatalytic performance of graphene-like BN modified BiOBr flower-like materials for the removal of pollutants and mechanism insight, Appl Catal B. 183 (2016) 254–262. https://doi.org/10.1016/j.apcatb.2015.10.036.

[85] Q. Wang, Y. Shi, T. Niu, J. He, H. She, B. Su, Preparing $ZnWO_4$–CdS composite with excellent visible light photocatalytic activity under mild conditions, J Solgel Sci Technol. 83 (2017) 555–566. https://doi.org/10.1007/s10971-017-4434-8.

[86] Z. Li, M. Chen, Z. Ai, L. Wu, Q. Zhang, Mechanochemical synthesis of CdS/MgAl LDH-precursor as improved visible-light driven photocatalyst for organic dye, Appl Clay Sci. 163 (2018) 265–272. https://doi.org/10.1016/j.clay.2018.07.037.

[87] G.K. Macedo, E.H. Dias, C. Ribeiro, O.F. Lopes, Development of Bismuth Oxyhalides for Organic Pollutant Photodegradation and Water Oxidation: Effect of Synthesis Parameter and Halide Species, J Braz Chem Soc. 33 (2022) 948–957. https://doi.org/10.21577/0103-5053.20220047.

[88] P.A. Ajibade, A.E. Oluwalana, Enhanced photocatalytic degradation of ternary dyes by copper sulfide nanoparticles, Nanomaterials. 11 (2021). https://doi.org/10.3390/nano11082000.

[89] T. Senasu, T. Chankhanittha, K. Hemavibool, S. Nanan, Visible-light-responsive photocatalyst based on ZnO/CdS nanocomposite for photodegradation of reactive red azo dye and ofloxacin antibiotic, Mater Sci Semicond Process. 123 (2021). https://doi.org/10.1016/j.mssp.2020.105558.

[90] L. Anju Chanu, W. Joychandra Singh, K. Jugeshwar Singh, K. Nomita Devi, Effect of operational parameters on the photocatalytic degradation of Methylene blue dye solution using manganese doped ZnO nanoparticles, Results Phys. 12 (2019) 1230–1237. https://doi.org/10.1016/j.rinp.2018.12.089.

[91] S. Shahabuddin, R. Khanam, M. Khalid, N.M. Sarih, J.J. Ching, S. Mohamad, R. Saidur, Synthesis of 2D boron nitride doped polyaniline hybrid nanocomposites for photocatalytic degradation of carcinogenic dyes from aqueous solution, Arabian Journal of Chemistry. 11 (2018) 1000–1016. https://doi.org/10.1016/j.arabjc.2018.05.004.

[92] Y. Yang, Z. Wu, R. Yang, Y. Li, X. Liu, L. Zhang, B. Yu, Insights into the mechanism of enhanced photocatalytic dye degradation and antibacterial activity over ternary ZnO/ZnSe/$MoSe_2$ photocatalysts under visible light irradiation, Appl Surf Sci. 539 (2021). https://doi.org/10.1016/j.apsusc.2020.148220.

[93] N. Chandel, K. Sharma, A. Sudhaik, P. Raizada, A. Hosseini-Bandegharaei, V.K. Thakur, P. Singh; Magnetically separable ZnO/$ZnFe_2O_4$ and ZnO/$CoFe_2O_4$ photocatalysts supported onto nitrogen-doped graphene for photocatalytic degradation of toxic dyes, Arabian Journal of Chemistry. 13 (2020) 4324–4340. https://doi.org/10.1016/j.arabjc.2019.08.005.

[94] A. Fouda, S.S. Salem, A.R. Wassel, M.F. Hamza, T.I. Shaheen, Optimization of green biosynthesized visible light active CuO/ZnO nano-photocatalysts for the degradation of organic methylene blue dye, Heliyon. 6 (2020). https://doi.org/10.1016/j.heliyon.2020.e04896.

[95] H. Liu, H. Liu, J. Yang, H. Zhai, X. Liu, H. Jia, Microwave-assisted one-pot synthesis of Ag decorated flower-like ZnO composites photocatalysts for dye degradation and NO removal, Ceram Int. 45 (2019) 20133–20140. https://doi.org/10.1016/j.ceramint.2019.06.279.

[96] M. Bagheri, N.R. Najafabadi, E. Borna, Removal of reactive blue 203 dye photocatalytic using ZnO nanoparticles stabilized on functionalized MWCNTs, J King Saud Univ Sci. 32 (2020) 799–804. https://doi.org/10.1016/j.jksus.2019.02.012.

[97] H.K. Sadhanala, S. Senapati, K.V. Harika, K.K. Nanda, A. Gedanken, Green synthesis of MoS_2 nanoflowers for efficient degradation of methylene blue and crystal violet dyes under natural sun light conditions, New Journal of Chemistry. 42 (2018) 14318–14324. https://doi.org/10.1039/c8nj01731j.

[98] S. Alkaykh, A. Mbarek, E.E. Ali-Shattle, Photocatalytic degradation of methylene blue dye in aqueous solution by $MnTiO_3$ nanoparticles under sunlight irradiation, Heliyon. 6 (2020). https://doi.org/10.1016/j.heliyon.2020.e03663.

[99] Y. Slimani, M.A. Almessiere, M.J.S. Mohamed, E. Hannachi, S. Caliskan, S. Akhtar, A. Baykal, M.A. Gondal, Synthesis of Ce and Sm Co-Doped TiO_2 Nanoparticles with Enhanced Photocatalytic Activity for Rhodamine B Dye Degradation, Catalysts. 13 (2023) 668. https://doi.org/10.3390/catal13040668.

[100] J. Hou, H. Yang, B. He, J. Ma, Y. Lu, Q. Wang, High photocatalytic performance of hydrogen evolution and dye degradation enabled by CeO_2 modified TiO_2 nanotube arrays, Fuel. 310 (2022). https://doi.org/10.1016/j.fuel.2021.122364.

[101] S. Fang, Y. Xia, K. Lv, Q. Li, J. Sun, M. Li, Effect of carbon-dots modification on the structure and photocatalytic activity of g-C3N4, Appl Catal B. 185 (2016) 225–232. https://doi.org/10.1016/j.apcatb.2015.12.025.

[102] H. Liu, J. Liang, S. Fu, L. Li, J. Cui, P. Gao, F. Zhao, J. Zhou, N doped carbon quantum dots modified defect-rich g-C_3N_4 for enhanced photocatalytic combined pollutions degradation and hydrogen evolution, Colloids Surf A Physicochem Eng Asp. 591 (2020). https://doi.org/10.1016/j.colsurfa.2020.124552.

[103] Z. Xu, Z. Chen, T. Ji, D. Jv, P. Guan, The critical role of surface area optimization in carbon quantum dots modified g-C_3N_4 for photocatalytic enhancement, Mater Lett. 309 (2022). https://doi.org/10.1016/j.matlet.2021.131273.

[104] H. Zhang, L. Zhao, F. Geng, L.H. Guo, B. Wan, Y. Yang, Carbon dots decorated graphitic carbon nitride as an efficient metal-free photocatalyst for phenol degradation, Appl Catal B. 180 (2016) 656–662. https://doi.org/10.1016/j.apcatb.2015.06.056.

[105] K.T. Wong, S.B. Jang, P. Saravanan, I.W. Nah, S. Park, J. Choi, C. Park, Y. Kim, Y. Yoon, M. Jang, Critical insight on the hydrothermal effects toward exfoliation of g-C_3N_4 and simultaneous in-situ deposition of carbon quantum dots, Appl Surf Sci. 471 (2019) 703–713. https://doi.org/10.1016/j.apsusc.2018.12.064.

[106] K. Prakash, J.V. Kumar, P. Latha, P.S. Kumar, S. Karuthapandian, Fruitful fabrication of CDs on GO/ g-C_3N_4 sheets layers: A carbon amalgamation for the remediation of carcinogenic pollutants, J Photochem Photobiol A Chem. 370 (2019) 94–104. https://doi.org/10.1016/j.jphotochem.2018.10.046.

[107] B. Chai, X. Liao, F. Song, H. Zhou, Fullerene modified C3N4 composites with enhanced photocatalytic activity under visible light irradiation, Dalton Transactions. 43 (2014) 982–989. https://doi.org/10.1039/c3dt52454j.

[108] L. Zhang, J. Zhang, Y. Xia, M. Xun, H. Chen, X. Liu, X. Yin, Metal-free carbon quantum dots implant graphitic carbon nitride: Enhanced photocatalytic dye wastewater purification with simultaneous hydrogen production, Int J Mol Sci. 21 (2020). https://doi.org/10.3390/ijms21031052.

[109] H. Li, G. Huang, H. Xu, Z. Yang, X. Xu, J. Li, A. Qu, Y. Chen, Enhancing photodegradation activity of $_{g\text{-}C3N4}$ via decorating with S-doped carbon nitride quantum dots by in situ polymerization, J Solid State Chem. 292 (2020). https://doi.org/10.1016/j.jssc.2020.121705.

[110] A. Aghamali, M. Khosravi, H. Hamishehkar, N. Modirshahla, M.A. Behnajady, Synthesis, and characterization of high efficient photoluminescent sunlight driven photocatalyst of N-Carbon Quantum Dots, J Lumin. 201 (2018) 265–274. https://doi.org/10.1016/j.jlumin.2018.04.061.

[111] L. Shi, L. Yao, W. Si, One step to prepare CNTs modified porous g-C_3N_4 with excellent visible-light photocatalytic performance, Journal of Materials Science: Materials in Electronics. 30 (2019) 1714–1723. https://doi.org/10.1007/s10854-018-0444-8.

[112] T. Ma, J. Bai, C. Li, Facile synthesis of g-C3N4 wrapping on one-dimensional carbon fiber as a composite photocatalyst to degrade organic pollutants, Vacuum. 145 (2017) 47–54. https://doi.org/10.1016/j.vacuum.2017.08.027.

[113] L. Ge, C. Han, Synthesis of MWNTs/ g-C_3N_4 composite photocatalysts with efficient visible light photocatalytic hydrogen evolution activity, Appl Catal B. 117–118 (2012) 268–274. https://doi.org/10.1016/j.apcatb.2012.01.021.

[114] A. Suryawanshi, P. Dhanasekaran, D. Mhamane, S. Kelkar, S. Patil, N. Gupta, S. Ogale, Doubling of photocatalytic H 2 evolution from g-C_3N_4 via its nanocomposite formation with multiwall carbon nanotubes: Electronic and morphological effects, Int J Hydrogen Energy. 37 (2012) 9584–9589. https://doi.org/10.1016/j.ijhydene.2012.03.123.

[115] Y. Chen, J. Li, Z. Hong, B. Shen, B. Lin, B. Gao, Origin of the enhanced visible-light photocatalytic activity of CNT modified g-C_3N_4 for H_2 production, Physical Chemistry Chemical Physics. 16 (2014) 8106–8113. https://doi.org/10.1039/c3cp55191a.

[116] Y.X. Zhang, K. Li, Y.X. Yu, W. De Zhang, Carbon nanotubes-modified graphitic carbon nitride photocatalysts with synergistic effect of nickel(II) sulfide and molybdenum(II) disulfide co-catalysts for more efficient H_2 evolution, J Colloid Interface Sci. 526 (2018) 374–383. https://doi.org/10.1016/j.jcis.2018.05.003.

[117] T.Y. Ma, S. Dai, M. Jaroniec, S.Z. Qiao, Graphitic carbon nitride nanosheet-carbon nanotube three-dimensional porous composites as high-performance oxygen evolution electrocatalysts, Angewandte Chemie - International Edition. 53 (2014) 7281–7285. https://doi.org/10.1002/anie.201403946.

[118] X. Lu, T.H. Tan, Y.H. Ng, R. Amal, Highly Selective and Stable Reduction of $CO_2$to CO by a Graphitic Carbon Nitride/Carbon Nanotube Composite Electrocatalyst, Chemistry - A European Journal. 22 (2016) 11991–11996. https://doi.org/10.1002/chem.201601674.

[119] C. Wang, J. Li, X. Luo, J. Hui, X. Liu, J. Tan, X. Zhao, Graphitic carbon nitride nanosheets modified multi-walled carbon nanotubes as 3D high efficient sensor for simultaneous determination of dopamine, uric acid and tryptophan, Journal of Electroanalytical Chemistry. 780 (2016) 147–152. https://doi.org/10.1016/j.jelechem.2016.09.004.

[120] B. Posha, N. Asha, N. Sandhyarani, Carbon nitride quantum dots tethered on CNTs for the electrochemical detection of dopamine and uric acid, New Journal of Chemistry. 45 (2021) 6263–6272. https://doi.org/10.1039/d1nj00555c.

[121] Y. Xu, H. Xu, L. Wang, J. Yan, H. Li, Y. Song, L. Huang, G. Cai, The CNT modified white C_3N_4 composite photocatalyst with enhanced visible-light response photoactivity, Journal of the Chemical Society. Dalton Transactions. 42 (2013) 7604–7613. https://doi.org/10.1039/c3dt32871f.

[122] J. Liu, Y. Song, H. Xu, X. Zhu, J. Lian, Y. Xu, Y. Zhao, L. Huang, H. Ji, H. Li, Non-metal photocatalyst nitrogen-doped carbon nanotubes modified mpg-C_3N_4: facile synthesis and the enhanced visible-light photocatalytic activity, J Colloid Interface Sci. 494 (2017) 38–46. https://doi.org/10.1016/j.jcis.2017.01.010.

[123] F. Ding, Z. Zhao, D. Yang, X. Zhao, Y. Chen, Z. Jiang, One-Pot Fabrication of g-C_3N_4/MWCNTs Nanocomposites with Superior Visible-Light Photocatalytic Performance, Ind Eng Chem Res. 58 (2019) 3679–3687. https://doi.org/10.1021/acs.iecr.8b05293.

[124] A. Mahmood, T. Muhmood, F. Ahmad, Carbon nanotubes heterojunction with graphene like carbon nitride for the enhancement of electrochemical and photocatalytic activity, Mater Chem Phys. 278 (2022). https://doi.org/10.1016/j.matchemphys.2021.125640.

[125] Y. Guan, J. Wu, L. Wang, C.H. Shi, K. Lv, Y. Lv, Application of g-C_3N_4/CNTs nanocomposites in energy and environment, Energy Reports. 8 (2022) 1190–1199. https://doi.org/10.1016/j.egyr.2022.02.081.

[126] G. Liu, M. Liao, Z. Zhang, H. Wang, D. Chen, Y. Feng, Enhanced photodegradation performance of Rhodamine B with g-C_3N_4 modified by carbon nanotubes, Sep Purif Technol. 244 (2020). https://doi.org/10.1016/j.seppur.2020.116618.

[127] X. Shen, T. Zhang, P. Xu, L. Zhang, J. Liu, Z. Chen, Growth of C_3N_4 nanosheets on carbon-fiber cloth as flexible and macroscale filter-membrane-shaped photocatalyst for degrading the flowing wastewater, Appl Catal B. 219 (2017) 425–431. https://doi.org/10.1016/j.apcatb.2017.07.059.

[128] Y. Li, H. Zhang, P. Liu, D. Wang, Y. Li, H. Zhao, Cross-linked g-C_3N_4/rGO nanocomposites with tunable band structure and enhanced visible light photocatalytic activity, Small. 9 (2013) 3336–3344. https://doi.org/10.1002/smll.201203135.

[129] E.J. Stobel Christy, A. Pius, Performance of metal free g-C_3N_4 reinforced graphene oxide bio-composite for the removal of persistent dyes, Environmental Chemistry and Ecotoxicology. 3 (2021) 220–233. https://doi.org/10.1016/j.enceco.2021.06.003.

[130] A. Jilani, G.U. Rehman, M.O. Ansari, M.H.D. Othman, S.Z. Hussain, M.R. Dustgeer, R. Darwesh, Sulfonated polyaniline-encapsulated graphene@graphitic carbon nitride nanocomposites for significantly enhanced photocatalytic degradation of phenol: A mechanistic study, New Journal of Chemistry. 44 (2020) 19570–19580. https://doi.org/10.1039/d0nj03684f.

[131] J. Li, Y. Tang, R. Jin, Q. Meng, Y. Chen, X. Long, L. Wang, H. Guo, S. Zhang, Ultrasonic-microwave assisted synthesis of GO/ g-C_3N_4 composites for efficient photocatalytic H2 evolution, Solid State Sci. 97 (2019). https://doi.org/10.1016/j.solidstatesciences.2019.105990.

[132] Q. Sun, P. Wang, H. Yu, X. Wang, In situ hydrothermal synthesis and enhanced photocatalytic H_2-evolution performance of suspended rGO/ g-C_3N_4 photocatalysts, J Mol Catal A Chem. 424 (2016) 369–376. https://doi.org/10.1016/j.molcata.2016.09.015.

[133] S.S. Shinde, A. Sami, J.H. Lee, Sulfur mediated graphitic carbon nitride/S-Se-graphene as a metal-free hybrid photocatalyst for pollutant degradation and water splitting, Carbon N Y. 96 (2016) 929–936. https://doi.org/10.1016/j.carbon.2015.10.050.

[134] S. Singla, S. Sharma, S. Basu, N.P. Shetti, K.R. Reddy, Graphene/graphitic carbon nitride-based ternary nanohybrids: Synthesis methods, properties, and applications for photocatalytic hydrogen production, FlatChem. 24 (2020). https://doi.org/10.1016/j.flatc.2020.100200.

[135] W.J. Ong, L.L. Tan, S.P. Chai, S.T. Yong, A.R. Mohamed, Surface charge modification via protonation of graphitic carbon nitride (g-C_3N_4) for electrostatic self-assembly construction of 2D/2D reduced graphene oxide (rGO)/ g-C_3N_4 nanostructures toward enhanced photocatalytic reduction of carbon dioxide to methane, Nano Energy. 13 (2015) 757–770. https://doi.org/10.1016/j.nanoen.2015.03.014.

[136] W.J. Ong, L.L. Tan, S.P. Chai, S.T. Yong, Graphene oxide as a structure-directing agent for the two-dimensional interface engineering of sandwich-like graphene- g-C_3N_4 hybrid nanostructures with enhanced visible-light photoreduction of CO2 to methane, Chemical Communications. 51 (2015) 858–861. https://doi.org/10.1039/c4cc08996k.

[137] L. Sun, T. Du, C. Hu, J. Chen, J. Lu, Z. Lu, H. Han, Antibacterial Activity of Graphene Oxide/ g-C_3N_4 Composite through Photocatalytic Disinfection under Visible Light, ACS

Sustain Chem Eng. 5 (2017) 8693–8701. https://doi.org/10.1021/acssuschemeng.7b01431.

[138] C. Liu, Y. Xie, Y. Jiao, Y. Du, Q. Zheng, Y. Sun, Visible-light-driven nanoscale zero-valent iron loaded rGO/ g-C_3N_4 for fluoroquinolone antibiotics degradation in water, Front Environ Sci. 10 (2022). https://doi.org/10.3389/fenvs.2022.1065770.

[139] T. Muhmood, M. Xia, W. Lei, F. Wang, M.A. Khan, Design of Graphene Nanoplatelet/Graphitic Carbon Nitride Heterojunctions by Vacuum Tube with Enhanced Photocatalytic and Electrochemical Response, Eur J Inorg Chem. 2018 (2018) 1726–1732. https://doi.org/10.1002/ejic.201800093.

[140] J. Kalaiyarasi, K. Pandian, S. Ramanathan, S.C.B. Gopinath, Graphitic carbon nitride/graphene nanoflakes hybrid system for electrochemical sensing of DNA bases in meat samples, Sci Rep. 10 (2020). https://doi.org/10.1038/s41598-020-69578-8.

[141] G. Liao, S. Chen, X. Quan, H. Yu, H. Zhao, Graphene oxide modified g-C_3N_4 hybrid with enhanced photocatalytic capability under visible light irradiation, J Mater Chem. 22 (2012) 2721–2726. https://doi.org/10.1039/c1jm13490f.

[142] K. Dai, L. Lu, Q. Liu, G. Zhu, X. Wei, J. Bai, L. Xuan, H. Wang, Sonication assisted preparation of graphene oxide/ g-C_3N_4 nanosheet hybrid with reinforced photocurrent for photocatalyst applications, Dalton Transactions. 43 (2014) 6295–6299. https://doi.org/10.1039/c3dt53106f.

[143] K. Yu, X. Hu, K. Yao, P. Luo, X. Wang, H. Wang, Preparation of an ultrathin 2D/2D rGO/ g-C_3N_4 nanocomposite with enhanced visible-light-driven photocatalytic performance, RSC Adv. 7 (2017) 36793–36799. https://doi.org/10.1039/c7ra06210a.

[144] B. Yuan, J. Wei, T. Hu, H. Yao, Z. Jiang, Z. Fang, Z. Chu, Simple synthesis of g-C_3N_4/rGO hybrid catalyst for the photocatalytic degradation of rhodamine B, Cuihua Xuebao/Chinese Journal of Catalysis. 36 (2015) 1009–1016. https://doi.org/10.1016/S1872-2067(15)60844-0.

[145] Y. Li, D. Zhang, Q. Chen, C. Chao, J. Sun, S. Dong, Y. Sun, Synthesis of rGO/ g-C_3N_4 for methyl orange degradation in activating peroxydisulfate under simulated solar light irradiation, J Alloys Compd. 907 (2022). https://doi.org/10.1016/j.jallcom.2022.164500.

[146] Y. Gu, Y. Yu, J. Zou, T. Shen, Q. Xu, X. Yue, J. Meng, J. Wang, The ultra-rapid synthesis of rGO/ g-C_3N_4 composite via microwave heating with enhanced photocatalytic performance, Mater Lett. 232 (2018) 107–109. https://doi.org/10.1016/j.matlet.2018.08.077.

Chapter 2

Experimental details:
Synthesis, characterization, and measurements

This chapter consists of a comprehensive study of the synthesis techniques adopted for the preparation of g-C_3N_4-based hybrid photocatalysts. Besides, various structural, morphological, optical, and thermal characterization techniques employed in analysing the properties of the synthesized materials are discussed. Finally, at the end of this chapter, the photocatalytic degradation studies of the prepared material are explained in detail with supporting schematics.

2.1 Materials

The following table describes the information about the raw materials and chemicals used in the present work. These chemicals are used without further processing.

Table 2.1 List of chemicals and raw materials used for synthesis and photocatalytic studies.

Chemical	**Supplier/Grade**
Graphite Flakes (GF)	Graphite India Pvt Ltd
Graphite Electrode	Nickunj Eximp Entrp Pvt Ltd
Melamine	Sigma Aldrich
Ammonium Chloride (NH_4Cl)	Sigma Aldrich
Hexagonal Boron Nitride (hBN or BN)	Industrial Grade
Hydrogen Peroxide (H_2O_2)	Merck, India
Sulphuric Acid (H_2SO_4)	Merck, India
p-Benzoquinone (BQ)	Sigma Aldrich
Ammonium Oxalate (AO)	Sigma Aldrich
Isopropanol (IPA)	Merck, India
Rhodamine B (RhB)	Sigma Aldrich
Dimethyl Sulfoxide (DMSO)	M/S Finar Ltd, India

2.2 Materials synthesis

2.2.1 Synthesis of graphitic carbon nitride (GCN):

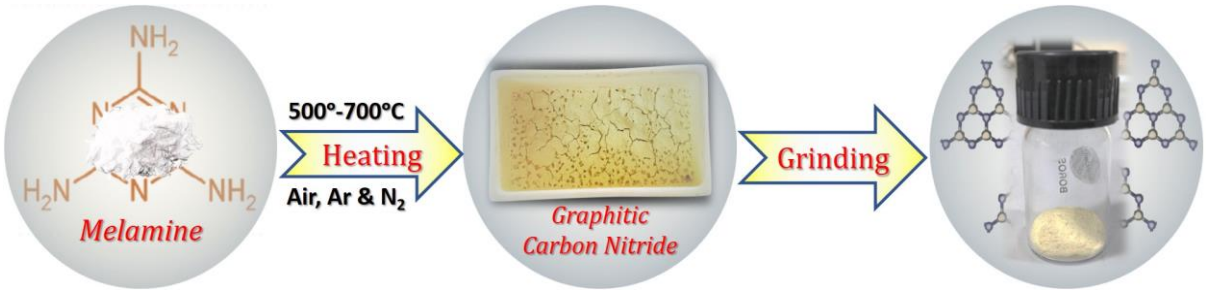

Figure 2.1 *Synthesis schematic of graphitic carbon nitride through pyrolysis of melamine.*

The GCN photocatalyst was synthesized by conventional thermal decomposition technique. Here, a certain amount of melamine was taken in an alumina crucible covered with a lid. The crucible was allowed to undergo a thermal pyrolysis process in a Muffle furnace at a slow heating rate of 2 cpm for three different temperatures i.e., 550 °C, 600 °C and 650 °C for 2 hrs. Further, different types of gaseous atmosphere were applied to study its effect on GCN synthesis. In this case, static air, argon, and nitrogen gases were used. After the reaction process was over, the crucible was allowed to cool naturally inside the furnace and was taken out afterwards and finely ground for further analysis. The schematic of synthesis and the final product obtained after the pyrolysis process are shown in Fig. 2.1.

2.2.2 Synthesis of improved graphitic carbon nitride (NGCN):

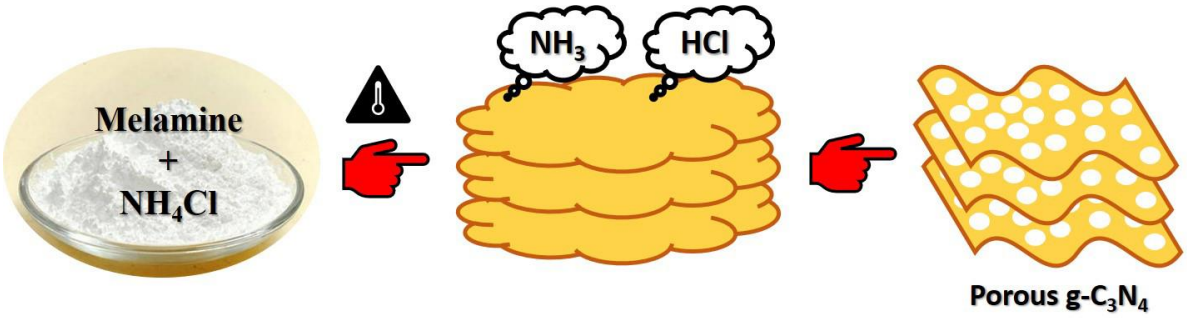

Figure 2.2 *Synthesis schematic of graphitic carbon nitride through pyrolysis of melamine and ammonium chloride.*

The synthesis parameters of GCN prepared in the above section were optimized and now, this optimized GCN is further modified for better photocatalytic performance. Here, a green templating approach was opted, wherein a bubbling agent (NH_4Cl) was incorporated along with the precursor during the pyrolysis process and was heated at 650 °C in static air for

2 hrs as shown in Fig 2.2. At elevated temperatures, NH_4Cl decomposes to produce NH_3 and HCl gases resulting in higher porosity and specific surface area. In this work, three different weight ratios of melamine and NH_4Cl were considered namely; 1:0.5, 1:1 and 1:2 which were named NGCN-1, NGCN-2, and NGCN-3 respectively.

2.2.3 Synthesis of carbon nanotubes and carbon soot via arc discharge:

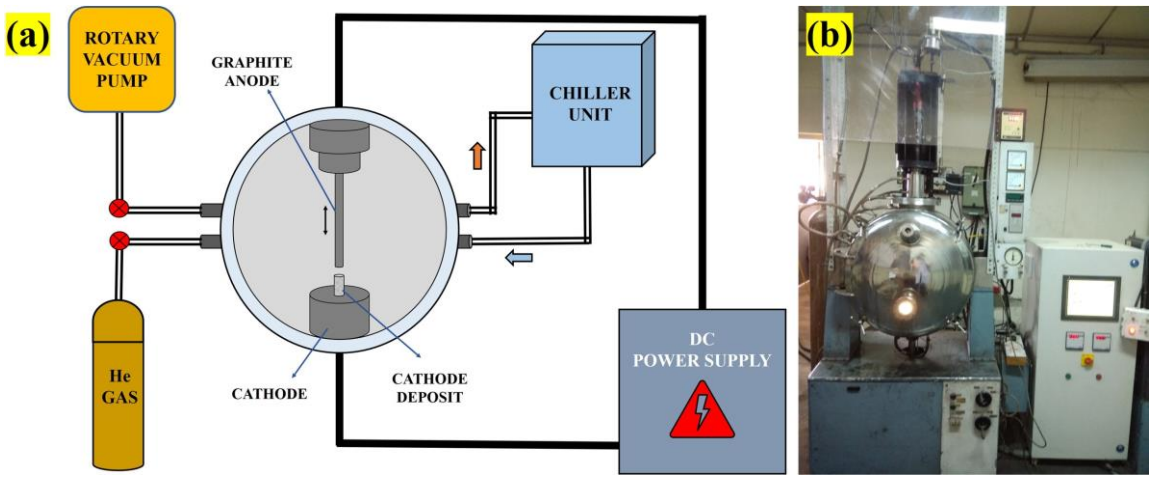

Figure 2.3 *(a) Schematic of arc discharge setup and (b) arc discharge reactor facility at ARCI.*

Arc discharge is a conventional technique to prepare carbon nanomaterials where a graphite electrode is resistively heated by applying high voltages in an inert atmosphere. The laboratory setup and the schematic are shown in Fig. 2.3. The setup consists of a stainless-steel double-walled chamber equipped with cooling water circulation and a leakproof arrangement. The setup is attached to a rotary pump to attain a vacuum and is further filled with helium gas of the required pressure before starting the experiment. A 10 mm diameter of high purity graphite electrode of an average density of 1.805 gm/cc and length of 20 cm is used as an anode and a larger diameter graphite electrode is used as a cathode. Here, the anode is a motor driven whereas the cathode is stationary. A DC voltage is applied between the electrodes and the anode is slowly moved towards the cathode. At a threshold distance of a few millimetres, an arc is struck between the electrodes. Due to the smaller diameter of the anode *w.r.t* cathode, a high current density and high temperature are generated resulting in sublimation of the anode. The temperature at the arcing point goes up to 4000 K, leading to the breakdown of the buffer gas near the electrodes in the reactor. This ionized gas results in hot plasma formation between the electrodes and the collisions of electrons and ions in the plasma emits photons which are responsible for the glow in the plasma (Fig. 2.4(a)). The role of plasma is to act as a highly conducting medium which provides the movement of carbon vapours between the electrodes.

These carbon vapours decompose and aggregate to form carbon clusters and drift towards the cathode that is relatively cooler. This temperature gradient and quenching effect of the atmosphere solidifies and crystallizes to form a stable hexagonal structure that grows along the cathode (Fig. 2.4(b, c)). Simultaneously, the walls of the reactor are covered with lightweight fluffy carbon soot that is essentially a mixture of spherical carbon nanoparticles and fullerenes. The outcomes of the arc discharge experiment are shown in Fig.2.4(d).

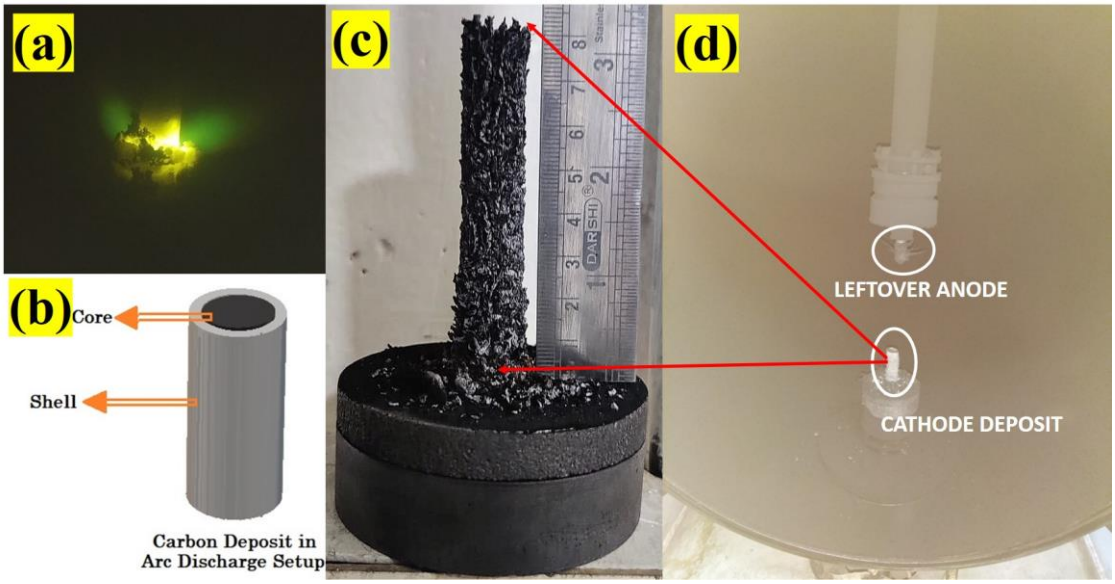

Figure 2.4 *(a) Photograph of the arcing point, (b) schematic of constituents of a typical cathode deposit, (c) photograph of cathode deposit and (d) image of the arc discharge reactor after the completion of the experiment.*

In this work, three different arc voltages and buffer gas pressure values were considered as shown in Table 2.2. The obtained cathode deposit samples were named CD1, CD2, CD3, CD4, CD5, CD6, CD7, CD8 and CD9. Similarly, the CS samples were denoted as CS1, CS2, CS3, CS4, CS5, CS6, CS7, CS8, and CS9. Here, the number in the sample nomenclature represents the corresponding voltage and pressure values given in Table 2.2. The obtained CD and CS samples were finely ground and used for further testing.

Table 2.2 Identification of matrix elements via numbering.

Pressure (Torr) → / **Voltage (V) ↓**	**200**	**400**	**600**
30	1	2	3
35	4	5	6
40	7	8	9

2.2.4 Synthesis of graphene nanoplatelets (GNP):

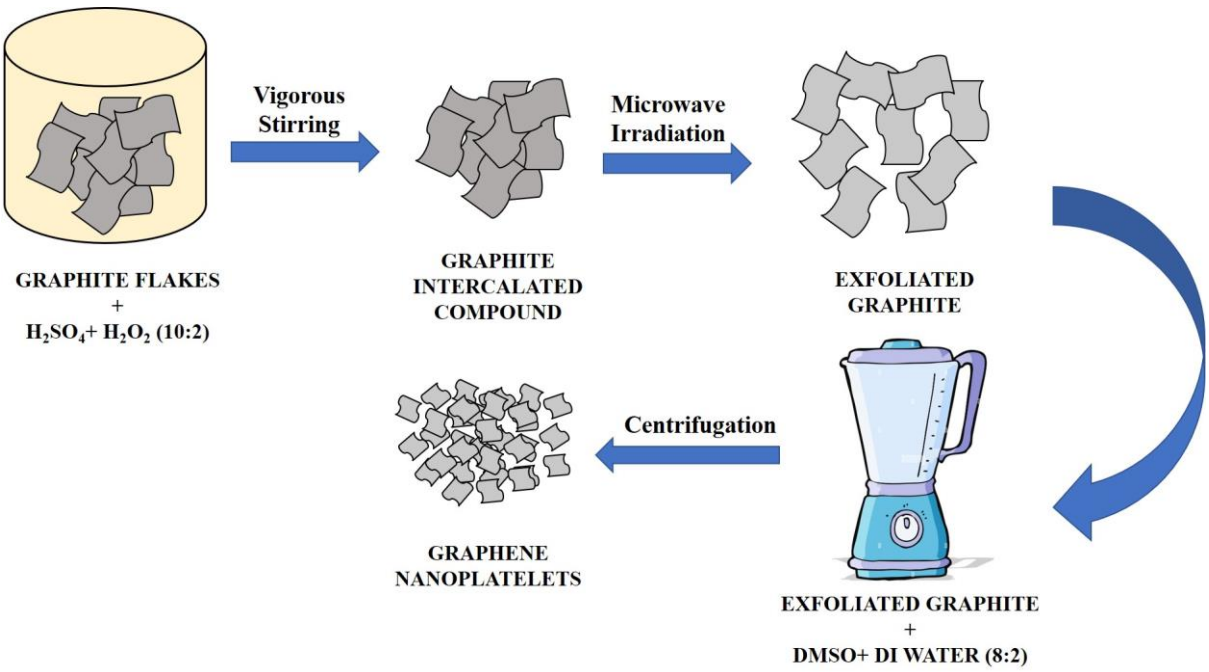

Figure 2.5 *Synthesis schematic of graphene nanoplatelets via exfoliation of graphite flakes.*

Multilayer graphene nanoplatelets (GNP) were prepared through a simple strategy of microwave exfoliation of graphite intercalation compound (GIC) followed by co-solvent mixing using a kitchen mixer (Fig. 2.5). Here, GFs were taken as raw material for the preparation of GNP. Initially, the H_2SO_4: H_2O_2 (10:2 v/v) mixture was added to 20 gm of GFs and chemically treated for 6 hrs to form GIC. This mixture was further agitated using a mechanical stirrer to attain uniform dispersion of the acid mixture and the GFs. GIC was exfoliated using a conventional microwave oven for a few seconds. Again, the obtained exfoliated graphite (EG) underwent a liquid phase exfoliation using a kitchen mixer in DMSO: Water (8:2 v/v) mixture for 1 hr. The final solution was centrifuged at 2000 rpm for 40 min to remove unexfoliated GFs based on the density separation method.

2.2.5 Synthesis of C-Soot/g-C_3N_4 hybrid photocatalyst:

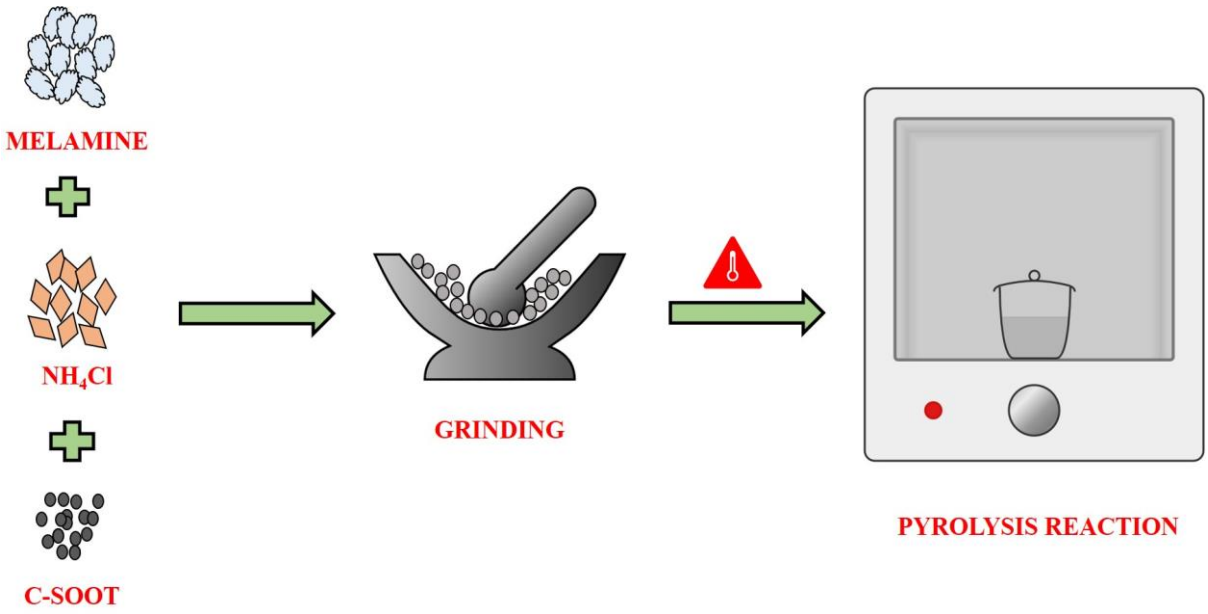

Figure 2.6 *Synthesis schematic of C-Soot/graphitic carbon nitride hybrid photocatalyst through thermal decomposition.*

This hybrid photocatalyst was prepared in a similar way as that of the modified GCN material. Here, melamine and NH_4Cl were taken in a 2:1 weight ratio and a certain amount of carbon soot was added to this mixture. These three materials were finely ground and transferred into an alumina crucible with a lid covering the top and placed in the furnace at 650 °C for 2 hrs with a slow ramping condition. In this study, four weight percentages of C-soot were considered: 0.1%, 0.3%, 0.5%, and 1% with the following reference codes: SC1, SC2, SC3 and SC4 respectively. The schematic of the synthesis is shown in Fig. 2.6.

2.2.6 Synthesis of CNT/g-C_3N_4 hybrid photocatalyst:

The CNT/GCN hybrid photocatalyst was synthesized by following a similar procedure (Fig. 2.6) as discussed in section 2.2.5. In this case, similar weight percentages of CNTs were considered during the pyrolysis process and were referred to as CC1, CC2, CC3, and CC4 respectively.

2.2.7 Synthesis of GNP/g-C_3N_4 hybrid photocatalyst:

The GNP/GCN photocatalyst was made by following the procedure employed for CNT/GCN material. Similar weight percentages and synthesis parameters were opted for and were referred to as GC1, GC2, GC3 and GC4 respectively for 0.1%, 0.3%, 0.5%, and 1% of

GNP loading in the hybrid photocatalyst. The synthesis schematic is the same as shown in Fig.2.6.

2.2.8 Synthesis of hBN/g-C_3N_4 hybrid photocatalyst:

Here, hBN used for this study was commercially procured which was synthesized by reacting boric acid with urea in nitrogen atmosphere at high temperatures and used without further modifications. Similar to the previous hybrid materials, here also similar synthesis procedure (Fig.2.6) was followed with the following weight loading percentages: 0.1%, 0.5%, 1% and 5% of hBN loading and were coded as BC1, BC2, BC3, and BC4 respectively.

2.3 Characterization Techniques

2.3.1 Scanning Electron Microscopy and Field Emission Scanning Electron Microscopy:

Scanning electron microscopy (SEM) is a fundamental technique commonly used for studying the material superficially. The basic principle of this technique involves the generation of an electron beam from a suitable source typically a tungsten filament (in SEM) or a field emission gun (for FE-SEM) [1,2]. The generated electron beam is accelerated by applying high voltages and passes through a series of apertures and electromagnetic lenses to collimate and produce a thin beam of electrons onto the surface of the specimen. The electron beam then scans the surface of the specimen and eventually electrons are emitted from the specimen surface and are finally collected by a suitably-positioned detector. There are multiple detectors for various types of electrons that are ejected after the electron beam and sample interaction such as characteristic X-rays, backscattered electrons, and secondary electrons. These detectors collect and process the emitted electrons to a signal that helps in producing an image. This image is stored and contains essential information about the sample. From this technique besides morphology, the sample's crystallographic information, composition and topography can also be found. The specimen surface must be conductive to avoid charging effects which blur the final image quality. In such cases, it is preferred to sputter the sample surface with a conductive coating of a few nanometres thick [3,4]. For this study, the Zeiss Gemini SEM500 FE-SEM instrument was used to carry out this characterization and for analysis, a few mg of powder sample was uniformly spread over a carbon tape and gold coating was done using sputtering technique.

2.3.2 Transmission Electron Microscopy:

Transmission electron microscopy (TEM) is another microscopic technique, similar to that of SEM but advanced in terms of resolution. It also uses an electron beam to produce the images of the samples. However, the major difference is that the electron beam is accelerated up to 300kV so that it can transmit across the sample to produce the image. In the TEM technique, the sample thickness must be very thin (< 100 nm) so that the electron beam can pass through the specimen. An image is formed by the interaction of electrons with the sample as the beam is transmitted through the sample. The image is thus magnified and focused onto an imaging device such as a fluorescent screen, a photographic film, or a sensor such as a charge-coupled device (CCD). There are various modes of operation depending on the user's requirements. The imaging mode provides a highly magnified view of the micro and nanostructures and ultimately results in high-resolution (HR) images. The nanoanalytical modes (X-ray and electron spectrometry) tell the user which elements are present in the tiny volume of the sample [5–7]. In this study, the JOEL JEM2100 HRTEM instrument was used to get the HR micrographs of the sample and diffraction patterns. For sample preparation, a powdered sample was dispersed in ethanol solvent by ultrasonication for a few minutes followed by drop casting on a Cu grid.

2.3.3 X-ray Diffraction:

X-ray diffraction (XRD) technique is an age-old, conventional, and non-destructive technique based on constructive interference of monochromatic X-rays ad a crystalline sample. These X-rays are produced by a cathode ray tube, filtered to generate monochromatic radiations, collimated to focus, and directed towards the sample. The interaction of incident rays with the specimen produces interference patterns when conditions satisfy Bragg's law which states that the path difference between the two x-ray beams that are diffracted from the two adjacent planes is equal to the integral multiple of the wavelength of the incident x-ray and is given by;

$$2d\,sin\theta = n\lambda \quad \text{---------- 2.1}$$

where, 'n' is an integer (n = 1,2,3, and so on), λ is the wavelength of the incident x-rays (λ= 1.5406 Å), 'd' is the interplanar spacing (nm), and θ is the angle between the incident x-ray beam and the crystal plane. These diffraction patterns contain useful information about the sample such as interplanar distance, grain or crystal orientation, and crystal structure identification and also help in measuring the shape, size, and internal stress of the small crystalline regions [8,9]. In this work, the Rigaku Smartlab 9kW powder XRD instrument producing Cu K_α radiation was used to get the diffraction pattern of the samples.

2.3.4 Thermogravimetric Analysis:

Thermogravimetric analysis (TGA) is a characterization tool that gives information about the thermal properties of a material. The main components of a TGA instrument are a heating furnace, thermobalance, temperature programmer and data acquisition system. From TGA, the user can get the following information: thermal and oxidation stability of the materials, composition of multi-component systems, decomposition kinetics of the materials, the effect of the reactive or corrosive atmosphere on materials, and moisture and volatile contents of a given sample [10]. TGA measures the changes in weight with the temperature changes. A derivative weight loss curve can be used to tell the point at which weight loss is most apparent. In the present study, the Netzsch STA 449 Jupiter simultaneous thermal analyser (STA) instrument was used for recording the TG curves. A few mg of powder sample was loaded in the alumina crucible for carrying out the studies.

2.3.5 Raman Spectroscopy:

Raman spectroscopy (RS) is a powerful tool for determining chemical species. This technique detects certain interactions of light with matter. RS was discovered by Sir CV Raman in 1928 and for which he was awarded the Noble Prize in 1930. It is a spectroscopic technique used to observe vibrational, rotational, and other low-frequency modes in a system [11,12]. When a monochromatic radiation of energy hν is incident upon a sample, inelastic scattering occurs due to the interaction of vibrational/ rotational motion of the atoms/molecules. This interaction induces a change in polarizability with respect to vibrational motion, which causes a dipole moment in the molecule. As a result, a change in the energy of the scattered light is observed. Three conditions are possible here: (1) if the scattered energy is the same as that of the incident photon energy, then it is called Rayleigh elastic scattering. (2) if this scattered energy is lower than the incident photon energy, then it is called Stokes inelastic scattering, and (3) if this scattered energy is higher than the incident energy, then it is Anti-stokes inelastic scattering. These inelastic scatterings are of great significance, as they contain major information about the chemical structure, crystallinity, and molecular interactions of the material [13]. The major components of the instrument are the laser source, sample illuminator, filter, and detector. When the sample is illuminated with the laser beam, light is scattered elastically and inelastically. The filter is used to block the elastically scattered light and passes the inelastic component to the detector which finally processes and produces a spectrum consisting of the intensity vs. Raman shift that is, change in frequency. Here in this work, the

WITec UHTS 600 Confocal Micro-Raman spectrometer with a laser excitation of 532 nm was used to obtain the Raman spectra of the samples.

2.3.6 Fourier-transform Infrared Spectroscopy:

The Fourier-transform infrared spectroscopy (FTIR) technique is also known as vibrational spectroscopy. This technique is widely used to identify unknown materials, determine the functional group existing in a given sample and calculate the amount of components in a mixture [14]. FTIR mainly consist of a simple optical device called a Michaelson Interferometer. This device produces a unique type of signal which has all the IR frequencies encoded in it. Each chemical bond or functional group has a unique characteristic vibrational frequency and hence, whenever, the incident radiation matches the vibrational frequency of a particular chemical bond or a functional group, the radiation gets absorbed. This causes a change in the vibrational states of the molecule from the ground to the excited state. As a result, the dipole moment of the molecule is also altered. It is known that when light falls on a material some part of the light is absorbed and some is transmitted. So, the transmitted light is collected by a detector and forms an interferogram which is in the time domain. To generalize the output data, it is important to convert the time domain into the frequency domain. To do that Fourier transformation is applied to the data using computer software [15,16]. Finally, the obtained FTIR spectrum is a function of transmittance or absorbance vs wavenumber. From these absorption bands, the chemical bonds or functional groups can be found easily. In this work, FTIR spectra were recorded with the help of Bruker Optics Tensor27 FTIR instrument.

2.3.7 Ultraviolet-Visible Spectroscopy:

The ultraviolet-visible spectroscopy (UVS) is a widely used characterization tool to study the absorption activity of a material in the UV and visible region of the EM spectrum. This technique is sometimes known as electronic spectroscopy because the energy is used to excite the electrons to higher energy levels. The basic components of a UVS are a UV source (Deuterium lamp) and a visible source (Sodium lamp), a filter wheel, a diffraction grating, and a detector. Essentially, a cuvette made of quartz is used as a sample holder where the liquid sample is loaded and placed before the detector. For solid samples, a different sample holder is used. Usually, a beam splitter is used to pass the incident light through the sample cuvette and a reference cuvette which contains everything except the sample. The emerging beam is compared at the detector (a photodiode) and the absorbance is obtained as a function of wavelength. The principle of working is based on Beer-Lambert's law which states that at a

given wavelength, the absorbance of a material is equal to the product of the molar absorptivity of the compound or the molecule (ε) in the solution, the path length of the cuvette (b) and the concentration of the solution (C) that is,

$$A = \varepsilon bC \quad \text{---------- 2.2}$$

A special attachment in this instrument is used for powder samples and is called diffuse reflectance spectroscopy (DRS). This method is commonly used for opaque samples that absorb too strongly to be measured in transmission mode and therefore reflectance of the sample is measured by collecting the scattered light from the sample [17,18]. For this study, a Perkin Elmer Lambda 35 UV-Visible spectrophotometer was used to study the UV-Vis behaviour of the samples.

2.3.8 Photoluminescence Spectroscopy:

Photoluminescence spectroscopy (PL) is a contactless, non-destructive method of probing the electronic structure of materials. Light is directed onto a sample where it is absorbed and imparts excess energy into the material in a process called photo-excitation. In this way, this excess energy can be dissipated by the sample either through the emission of light or by luminescence. In the case of photo-excitation, it is called photoluminescence. The intensity and spectral content of the PL curve are a direct measure of various important material properties like bandgap determination, impurity levels and defect detection, recombination mechanisms surface effects and excited states [19]. A typical emission experiment involves the selection of an excitation wavelength by one monochromator and luminescence is observed through a second monochromator positioned at a right angle to the incident light to minimise the intensity of scattered light reaching the detector. If the excitation wavelength is fixed and the emission is scanned, an emission spectrum is produced. In this work, the Horiba Scientific FL3C-21 fluorometer was used to study the PL spectra of the samples.

2.3.9 X-ray Photoelectron Spectroscopy:

X-ray photoelectron spectroscopy (XPS) also called electron spectroscopy for chemical analysis (ESCA), is an analytical method to determine the elemental composition of a material's surface. It can also be applied to determine the chemical or electronic state of these elements. XPS works on the principle of the photoelectric effect and the spectra are a result of the interaction of x-rays with the sample surface up to a few nanometres depth. When x-rays hit the

material surface, electrons are emitted from the core-shell of the atoms with a characteristic kinetic energy (KE) proportional to the energy of the radiation and is given by;

$$KE = h\nu - BE - \phi \quad \text{---------- 2.3}$$

where ϕ is the work function, $h\nu$ is the incident x-ray energy and BE is the binding energy of the electron inside the atom. To detect the emitted photoelectrons, an electron energy analyser is used. From the BE vs intensity curve, the elemental identity, chemical states, and percentage composition can be determined [20,21]. In the present work, the Thermo Scientific K-Alpha instrument was utilised to carry out the analyses.

2.3.10 Zeta Potential Analyser:

For the present work, the Malvern Zetasizer NanoZS90 instrument was used to measure the zeta potential (ZP) at various pH values thereby calculating the point of zero charge (pzc). ZP is a parameter that measures the electrochemical equilibrium at the particle-liquid interface. It measures the magnitude of electrostatic repulsion/attraction between the particles and thus it has become one of the fundamental parameters known to affect the stability of colloidal particles. Here, the ZP is measured based on the laser Doppler electrophoresis phenomenon [22]. The speed the particles move is proportional to the field strength and ZP. So, by applying the established theories and formulas and other known values ZP is calculated.

2.3.11 N_2 Adsorption-Desorption Studies:

The N_2 adsorption-desorption studies were carried out using the Quantchrome AutosorbIQ instrument. Here, the specific surface area (SSA) of the samples was calculated by using the multi-point Brunauer – Emmett – Teller (BET) model within the relative pressure range of 0.05 – 0.9. The pore volume and pore size distribution were calculated using t – plot and the total pore volume of the material was determined at a relative pressure of 0.99. The pore size distribution of the material was obtained by investigating the data under density functional theory (DFT) and Barrett – Joyner – Halenda (BJH) models [23].

The complete analysis of the sample is done by first degassing the sample above 200 °C for about 1 – 2 hrs to remove surface adsorbed impurities. The weight of the sample is measured after cooling and then subjected to N2 gas at variable pressure and fixed temperature (- 196 °C). Finally, the amount of gas adsorbed/desorbed with an increase/ decrease in the applied pressure is measured. The graph between quantity adsorbed as a function of relative pressure gives information about SSA and the pore structure of the specimen [24,25].

2.4 Photocatalytic Degradation Studies

2.4.1 Photodegradation measurements reactor setup:

A laboratory prototype was designed for carrying out photocatalytic degradation experiments. Here, a wooden box of 1ft x 1ft x 3ft dimensions was made with a door system on the front side of the box and a white LED light of 1000W was fixed on the top of the box. A magnetic stirrer was placed at a fixed place such that the distance between the surface of the beaker and the light source was 10 cm. The schematic of the reactor is shown in the figure 2.7.

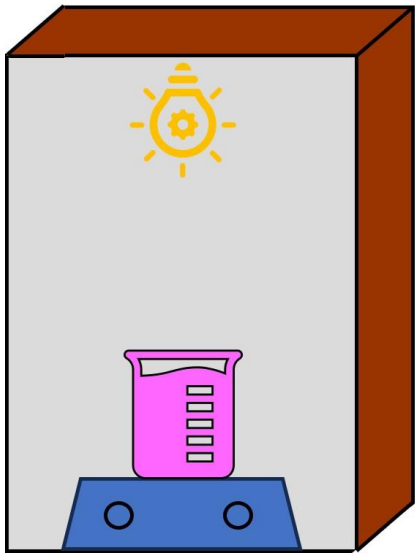

Figure 2.7 *Schematic of the reactor designed for studying photodegradation experiments.*

2.4.2 Rhodamine B photodegradation studies:

This present work discusses the photodegradation of RhB dye under a visible light source. Among several commercial dyes available in the market, RhB is highly preferred because of its cationic nature and effective activity under visible light. Also, it is considered to be a highly stable synthetic dye. Herein, a certain concentration of dye solution and some amount of photocatalyst was added and this suspension was stirred in the dark for some time to attain adsorption-desorption equilibrium before visible light irradiation. After the light source was turned on, periodic aliquots of dye solution were drawn out using a 5 mL syringe and then with the help of a syringe filter, the photocatalyst was separated from the dye. Then the filtered dye solution was scanned under a UV-Visible spectrophotometer and the absorbance intensity

at the maximum absorbance wavelength (λ_{max}) value of RhB was noted down. The amount of dye removed (%) was calculated using the following expression:

$$\eta(\%) = \frac{(C_0 - C_t)}{C_0} * \mathbf{100} \text{ ---------- } \mathbf{2.4}$$

where η (%) is the amount of dye removed (%), and C_0 and C_t are the UV- Visible absorbance intensities of RhB dye solution at time 0 minutes and 't' minutes respectively.

2.4.3 Reactive species trapping experiments:

This is a crucial study that helps in finding out the photodegradation mechanism and the active component during the degradation process. We know that the photogenerated holes, hydroxyl radicals and superoxide anions are the major reactive species that are involved during the photodegradation process. So, to find out which one has the major role during the photodegradation process, a trapping agent is added to the dye solution while starting the experiment. This chemical scavenges the generated radical species thereby affecting the overall photodegradation. In this way we can find out which is the major component responsible for photodegradation activity and a mechanism can be proposed.

In this work, three different chemicals were chosen for carrying out these studies;

(1) Ammonium Oxalate: It is a reducing agent and is used to trap photogenerated holes. A 10 mM concentration of ammonium oxalate was added to the dye solution at the beginning of the experiment. Being a reducing agent, it donates an electron to the hole and gets oxidised thus, tapping the hole.
(2) p-Benzoquinone: This chemical is used to trap superoxide anions. It traps this radical by accepting an electron from p-Benzoquinone which gets converted to hydroquinone. Thus, the superoxide anion is quenched in this process.
(3) Isopropanol: this solvent is used for hydroxyl radical trapping. Here also, 10 mM of isopropanol is added to the catalyst-loaded dye solution. In this case, the generated hydroxyl radicals react with isopropanol and convert it to propenal thereby, getting quenched in this reaction.

At the end of each experiment, the RhB degradation is noted and from this data, we can propose a mechanism and can know about the major participants during the photodegradation process.

2.5 Conclusions

In this chapter, detailed information about the chemicals and other materials used in the present work was tabulated. Followed by a detailed explanation of synthesis procedures with supporting schematics was done. Besides, the material characterization tools like FE-SEM, TEM, XRD, TGA, UV-Vis, and other techniques used in this work were discussed briefly. In the end, the photocatalytic degradation studies; experimental setup and measurement procedures were discussed with the help of schematics.

References

[1] M. De, A. Pereira-Da-Silva, F.A. Ferri, 1 - Scanning Electron Microscopy, 2017. https://doi.org/10.1016/B978-0-323-49778-7/00001-1.

[2] J.M. Bonard, K.A. Dean, B.F. Coll, C. Klinke, Field Emission of Individual Carbon Nanotubes in the Scanning Electron Microscope, Phys Rev Lett. 89 (2002). https://doi.org/10.1103/PhysRevLett.89.197602.

[3] P. Echlin, Handbook of Sample Preparation for Scanning Electron Microscopy and X-Ray Microanalysis, Springer US, 2009. https://doi.org/10.1007/978-0-387-85731-2.

[4] W.S. Werner, Related Titles Characterization of Surfaces and Nanostructures Academic and Industrial Applications Characterization of Solid Materials and Heterogeneous Catalysts From Structure to Surface Reactivity Characterization Techniques for Polymer Nanocomposites Basic Concepts of X-Ray Diffraction Advanced Characterization Techniques for Thin Film Solar Cells, 2013. http://dnb.d-nb.de.

[5] L.E. Franken, K. Grünewald, E.J. Boekema, M.C.A. Stuart, A Technical Introduction to Transmission Electron Microscopy for Soft-Matter: Imaging, Possibilities, Choices, and Technical Developments, Small. 16 (2020). https://doi.org/10.1002/smll.201906198.

[6] S.J. Pennycook, Transmission Electron Microscopy: Overview and Challenges, in: AIP Publishing, 2003: pp. 627–633. https://doi.org/10.1063/1.1622537.

[7] J. Ayache, L. Beaunier, J. Boumendil, G. Ehret, D. Laub, Sample Preparation Handbook for Transmission Electron Microscopy, Springer New York, 2010. https://doi.org/10.1007/978-0-387-98182-6.

[8] B.E. Warren, X-ray diffraction methods, J Appl Phys. 12 (1941) 375–383. https://doi.org/10.1063/1.1712915.

[9] C.G. Pope, Information • Textbooks • Media • Resources X-Ray Diffraction and the Bragg Equation, 1997.

[10] Thermogravimetric Analysis Rod Bottom, n.d.

[11] D.L. Gerrard, P.R. Graves, D. Louden, G. Turrell, S.-V. Berlin Heidelberg NewYork London Paris Tokyo, Practical Raman Spectroscopy With Contributions by, n.d.

[12] D. Roy, S. Kanojia, K. Mukhopadhyay, N. Eswara Prasad, Analysis of carbon-based nanomaterials using Raman spectroscopy: principles and case studies, (n.d.). https://doi.org/10.1007/s12034-020-02327-9S.

[13] R.S. Das, Y.K. Agrawal, Raman spectroscopy: Recent advancements, techniques and applications, Vib Spectrosc. 57 (2011) 163–176. https://doi.org/10.1016/j.vibspec.2011.08.003.

[14] The elements, n.d.

[15] Tuan. Vo-Dinh, G. (Günter) Gauglitz, Handbook of spectroscopy, Wiley-VCH, 2003.

[16] R. Bhargava, S.Q. Wang, J.L. Koenig, FTIR microspectroscopy of polymeric systems, Advances in Polymer Science. 163 (2003) 137–191. https://doi.org/10.1007/b11052.

[17] M. Picollo, M. Aceto, T. Vitorino, UV-Vis spectroscopy, Physical Sciences Reviews. 4 (2019). https://doi.org/10.1515/psr-2018-0008.

[18] Y. Guo, C. Liu, R. Ye, Q. Duan, Advances on water quality detection by uv-vis spectroscopy, Applied Sciences (Switzerland). 10 (2020) 1–18. https://doi.org/10.3390/app10196874.

[19] T. Aoki, PHOTOLUMINESCENCE SPECTROSCOPY, n.d.

[20] J.D. Andrade, X-ray Photoelectron Spectroscopy (XPS), n.d.

[21] S. Oswald, X-Ray Photoelectron Spectroscopy in Analysis of Surfaces, in: Encyclopedia of Analytical Chemistry, John Wiley & Sons, Ltd, 2013. https://doi.org/10.1002/9780470027318.a2517.pub2.

[22] C.N. Lunardi, A.J. Gomes, F.S. Rocha, J. De Tommaso, G.S. Patience, Experimental methods in chemical engineering: Zeta potential, Canadian Journal of Chemical Engineering. 99 (2021) 627–639. https://doi.org/10.1002/cjce.23914.

[23] J. Jagiello, M. Thommes, Comparison of DFT characterization methods based on N2, Ar, CO2, and H2 adsorption applied to carbons with various pore size distributions, in: Carbon N Y, Elsevier Ltd, 2004: pp. 1227–1232. https://doi.org/10.1016/j.carbon.2004.01.022.

[24] A. Galarneau, F. Villemot, J. Rodriguez, F. Fajula, B. Coasne, Validity of the t-plot method to assess microporosity in hierarchical micro/mesoporous materials, Langmuir. 30 (2014) 13266–13274. https://doi.org/10.1021/la5026679.

[25] D. Chen, A. Groenvold, H.P. Rebo, K. Moljord, A. Holmen, P. Albers, S. Bösing, H. Lansink-Rotgerink, D.K. Ross, S.F. Parker, K.S. W Sing, D.H. Everett, R.A. W Haul, L. Moscou, R.A. Pierotti, J. Rouquerol, Reporting Physisorption Data for Gas/Solid Systems, Elsevier, 1988.

Chapter 3

Part I- Synthesis of g-C_3N_4 photocatalyst: Effect of reaction atmosphere & pyrolysis temperature

3.1 Introduction

g-C_3N_4 has shown tremendous potential as a visible-radiation active photocatalyst for energy generation *as well as* pollutant removal [1]. It is a metal-free polymeric semiconductor that exhibits suitable Physico-chemical properties - as low bandgap (~2.7 eV), 2D stacked layered structure with high surface area *etc*. Structurally, it consists of triazine or heptazine motifs forming a periodic array in a stacking pattern, rendering a high density of catalytic sites. It also shows excellent thermal stability up to 600 ºC, due to its aromatic structure. Thus, g-C_3N_4-based photocatalysts have opened a new avenue in photo-catalysis research [2]. There are several reports of nitrogen-doped visible light photocatalysts [3,4] and certain g-C_3N_4 systems used for several applications ranging from environmental remediation to energy storage. Further, such nitride systems show tremendous potential for their utilization in the photo-degradation of organic toxic wastes, reduction of carbon dioxide, hydrogen evolution and in electrode material for batteries and supercapacitors [5]. There are quite a few publications on the synthesis of g-C_3N_4. In one such report by Yan S.C and others, they made g-C_3N_4 material by directly heating melamine as precursor material [6]. Whereas Zhang *et al.* prepared g-C_3N_4 through pyrolysis of thiourea at different temperatures [7]. Dong F *et al.* made graphitic carbon nitride by thermal decomposition of urea at 550 ºC [8]. Here, we exploited a simple graphitic carbon nitride preparation methodology to prepare an efficient visible light active photocatalyst.

In the present work, we have undertaken a systematic optimization of graphitic carbon nitride synthesis with parametric variation in reaction temperature and atmosphere, during melamine pyrolysis reaction. Further, we have investigated these carbon nitride systems for the photocatalytic deterioration studies of organic-dye, to achieve an efficient photocatalyst. This study is expected to improve an understanding of g-C_3N_4 photocatalyst designing and synthesis for several related applications.

3.2 Results and discussions

The melamine-derived graphitic-carbon nitride (MGCN) samples were prepared by thermal degradation of melamine at different temperatures and reaction atmospheres. Further, the obtained product was finely ground and taken for further studies. For the sake of clarity in name convention, these synthesized MGCN samples were termed according to temperature and gas atmosphere used during the reaction as tabulated below in Table 3.1.

Table 3.1 Nomenclature of the MGCN samples synthesized at various reaction temperatures and gas atmosphere.

	Air	**Ar (Argon)**	**N_2 (Nitrogen)**
550 °C	550Air	550Ar	550N_2
600 °C	600Air	600Ar	600N_2
650 °C	650Air	650Ar	650N_2

3.2.1. Effect of pyrolysis temperature

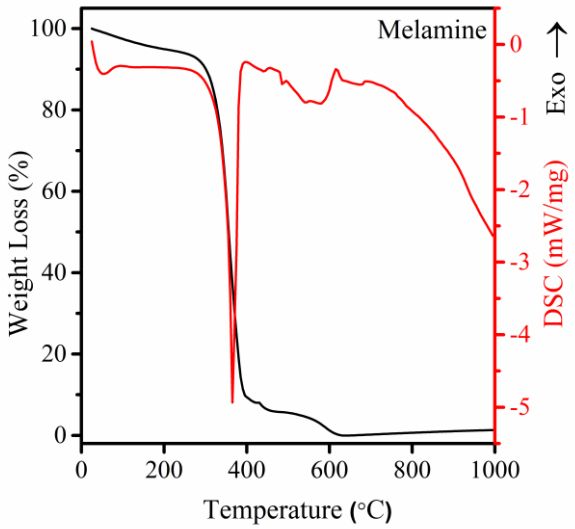

Figure 3.1 *TG-DSC curve of melamine.*

Pyrolysis temperature is a key parameter that influences C_3N_4 formation. Accordingly, melamine undergoes various intermediates reactions and finally, g-C_3N_4 is formed. Thermogravimetric studies of melamine (Fig. 3.1) indicate a temperature range of 500 - 700 °C is suitable for temperature optimization. Fig. 3.2 displays the XRD pattern of MGCN samples prepared at various temperatures and indicates the formation of C_3N_4 above 550 °C. As the temperature increases above 400 °C, structural modification of melamine occurs through forming intermediate products until 500 °C [9]. From 550 °C onwards, the significant peaks of

g-C_3N_4 were observed at around 13.1° (210) and 27.5° (002) which are attributed to the intra-planar recurring motifs of the C-N architecture and the pi-conjugated assembly of g-C_3N_4 layers, respectively [10,11].

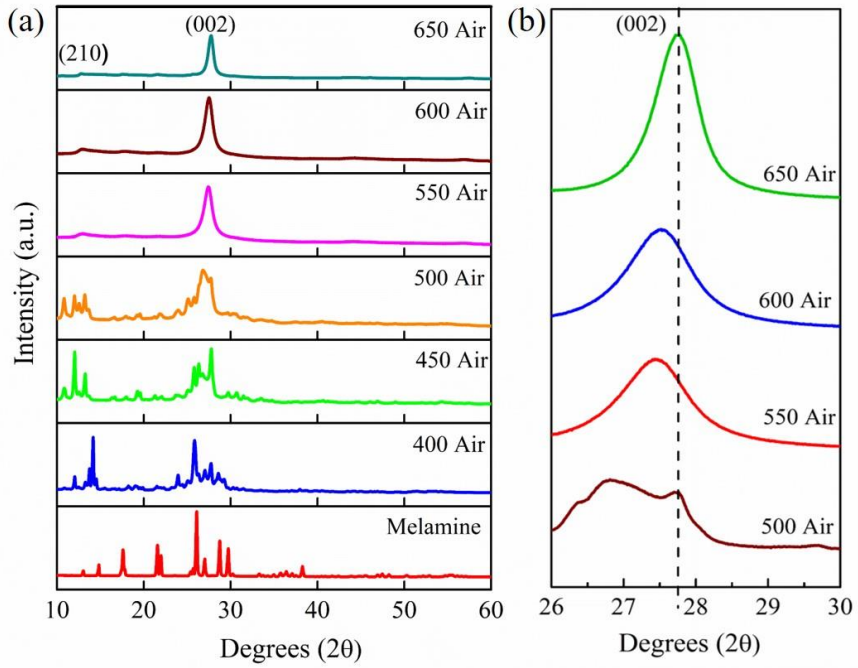

Figure 3.2 *(a)XRD diffractogram of MGCN synthesized at different temperatures and (b) magnified view of (002) peak with respect to increasing temperature.*

In-depth analyses reveal that the (002) peak shifts to higher angles, with an increase in reaction temperature, and correspondingly inter-layer distance decreases from 0.325 nm to 0.321 nm. This decrease in *d*-spacing is associated with the removal of the N- containing species from the MGCN framework [12]. Fig. 3.3 shows the FESEM micrograph of MGCN samples in the air at different temperatures, demonstrating the formation of a layered structure with an increase in pyrolysis temperature. Further, the size of the crystallites was calculated using the Scherrer equation which can be given as,

$$\boldsymbol{D = K\lambda/\beta cos\theta} \quad \text{---------- 3.1}$$

where *D* is the size of the crystallite (nm), *K* is the Scherrer's constant (~0.9), λ is the X-ray source wavelength (Cu-K_α) *i.e.,* 0.15418 nm and β is the FWHM of the (002) peak. The number of layers (*n*) in a single crystallite can be calculated using the formula: $n = \left(\frac{D}{d}\right) + 1$ where *d* is the interlayer spacing (nm) [13]. The calculated values are tabulated below (Table 3.2). It was noticed that the size of the crystallite increases with an increment in reaction temperature and so does the number of layers. For the *650Air* sample, a single crystallite contains 36 layers of

C_3N_4 stack, promoting a huge number of active locations from the sheet edges in the degradation reaction. Thus, at higher temperatures, the crystallite size increases indicating that higher pyrolysis temperature assists the nucleation and growth of MGCN [14]. Moreover, the specific surface area of the MGCN samples clearly shows an increasing trend with reaction temperature where 650 ℃ sample records the highest value among all the samples. Above 650 ℃, MGCN becomes unstable and decomposes at 700 ℃ [15].

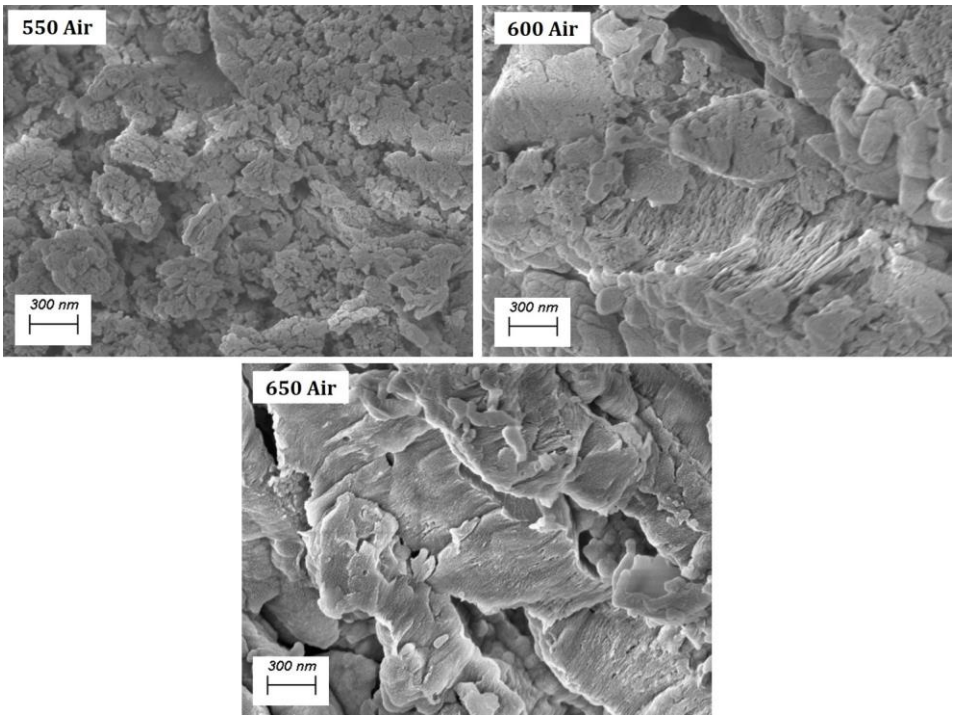

Figure 3.3 *FESEM micrographs of MGCN synthesized at different temperatures.*

Table 3.2 Interlayer spacing, crystallite size, number of layers and BET surface area of MGCN samples synthesized by varying reaction temperature and reaction atmosphere.

Sample	**Interlayer spacing d (nm)**	**Crystallite Size D (nm)**	**Number of Layers 'n'**	**S_{BET} (m^2g^{-1})**
550Air	0.324	6.32	20	14.22
600Air	0.323	7.00	23	18.49
650Air	0.321	11.39	36	42.34

Figure 3.4(a) shows the UV-DRS spectra for the MGCN samples. It shows a distinct and gradual red-shift in, the absorption band with a rise in the reaction temperature. This behaviour is ascribed to the extension of the heterocyclic pattern in the g-C_3N_4 network [16]. Fig. 3.4(b) shows the KM analyses of the corresponding absorption spectra used to estimate the indirect bandgap values, which are found to decrease from 2.78 eV to 2.73 eV, and 2.71 eV concerning an increase in temperature. These values are in accordance with past reports [6,7] and exploited here as visible light photocatalysts.

PL spectroscopy is essential to investigate the separation competency of the charge carriers. Fig. 3.4(c) shows the photoluminescence behaviour of the MGCN samples that were synthesized at different reaction temperatures. It indicates that the peak intensity gradually reduced with the steady rise in the reaction temperature, thereby implying enhancement in the lifetime of the photoinduced charge carriers and a higher charge transfer efficiency [17]. The chemical structure development of MGCN samples made at various reaction temperatures was analysed by FT-IR spectroscopy, as shown in Fig. 3.4(d). All IR peaks match with the absorption bands of the pristine g-C_3N_4 reported earlier [18]. A strong peak at 806 cm^{-1} is associated with the outward-plane bending vibrations of the CN aromatic structures. The peak at 890cm^{-1} is associated with the deformation mode of the cross-linked heptazine units. Whereas, the peaks within the range of 1200-1800 cm^{-1} are ascribed to the vibrating modes of aromatic C-N skeletons [19]. A broad band centred 3160 cm^{-1} could be attributed to the stretching modes of N - H bond vibrations [20]. No major difference could be seen in the spectra of MGCN samples prepared at 550 °C, 600 °C and 650 °C. However, the MGCN sample synthesized at 500 °C comparatively had distinguishable absorption bands indicating insufficient condensation of melamine which is consistence with the XRD results previously discussed [21]. Hence, from the observations, it can be said that 650 °C is the ideal temperature for g-C_3N_4 formation. Further, it can be noted that IR peaks of the *650Air* sample are much sharper and more intense which is due to a higher degree of polycondensation of these C-N heterocyclic systems [22].

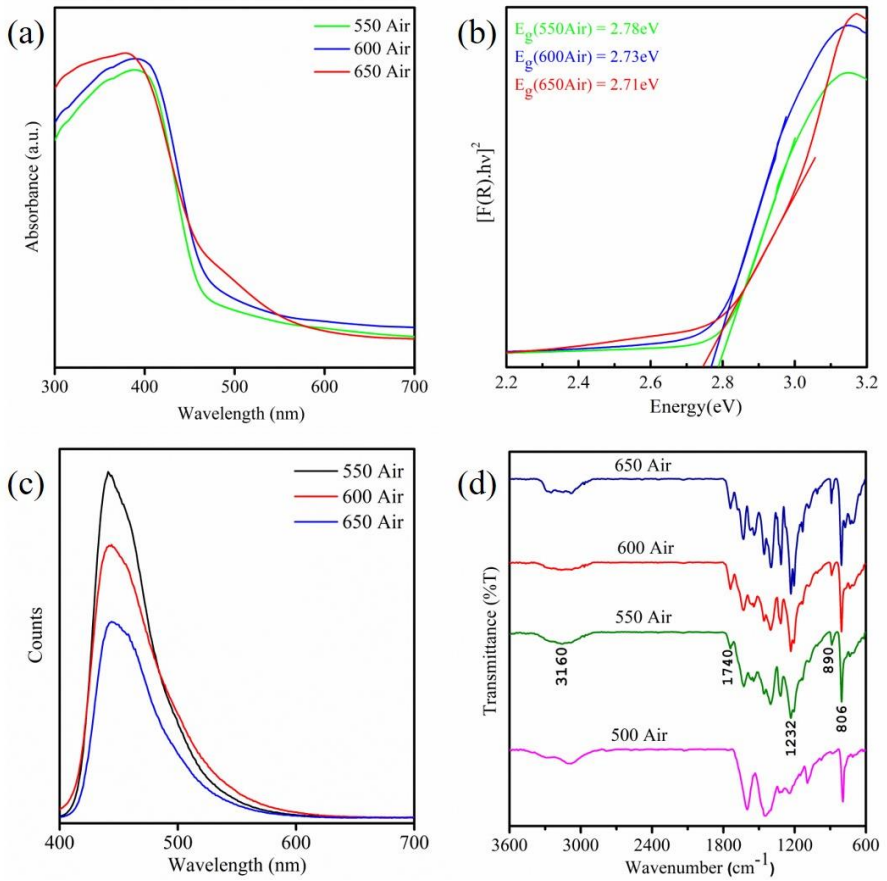

Figure 3.4 *(a) UV-DRS spectra, (b) its respective KM plot, (c) PL spectra (λ_{ext} ~365 nm) and (d) FT-IR spectra of MGCN samples.*

The elemental composition can be accurately measured using the XPS technique due to its extremely high sensitivity of valence electron spectrum to the chemical bonding environment. The survey spectra predominantly reveal that all the samples majorly contain C and N elements along with small traces of O that might be attributed to the adsorbed O_2 or H_2O on the sample surface or due to pyrolysis atmosphere. The atomic percentages and C/N ratio are tabulated in Table 3.3. It was observed that only the *650Air* sample has a C/N value near the stoichiometric value *i.e.,* 0.75. Fig. 3.6 displays the XPS spectra of MGCN samples prepared in air. For C 1s spectra, the photoelectron line is observed around 284.5 eV and for C with N compounds, these lines are observed between 283-289 eV [23]. The major peak varying between 287.01 and 287.27 eV is attributed to the sp^2-bonded carbon in nitrogen-containing triazine or heptazine rings ($(N)_2$─C=N). Whereas the peak between 287.75 and 288.62 eV can be assigned to sp^3 bonded carbon (C─$(N)_3$) [24]. Peaks between 283 and 285 eV are induced by the adventitious carbon and C─C bond [25]. The N 1s spectra mainly consist of three peaks. The main peak centred around 398 eV corresponds to pyridinic nitrogen (C=N─C) which is sp^2 hybridized N in the aromatic rings. Minor peaks around 399 and 400 eV are assigned to tertiary nitrogen N─$(C)_3$ and N─H structures respectively [16,26] The deconvoluted O 1s spectra

consist of two peaks around 531 and 533 eV. These peaks reveal the adsorbed oxygen functional groups on the surface of the samples [14].

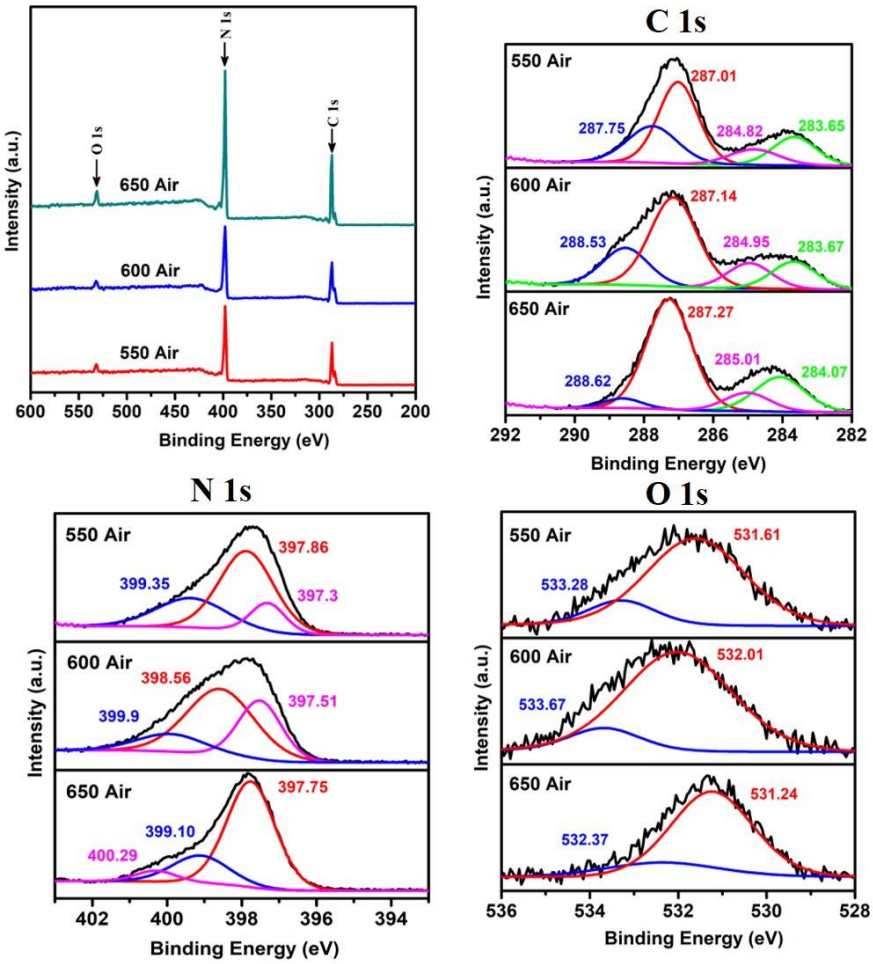

Figure 3.5 *XPS spectra of MGCN samples synthesized at different temperatures in air atmosphere.*

Table 3.3 Elemental composition and C/N ratio of MGCN samples synthesized in air atmosphere.

Sample	C (%)	N (%)	O (%)	C/N
550Air	45.76	50.72	3.52	0.9
600Air	50.27	47.65	2.08	1.05
650Air	40.41	55.82	3.77	0.72

3.2.2. Effect of reaction atmosphere

The reaction atmosphere in the pyrolysis process can be a major factor that can influence the final product. It may act as a carrier agent in the process or as a protective gear from excessive oxidation at elevated temperatures. Lack of such a controlled protective atmosphere could lead to partial or overreactions resulting in deformed or defective chemical structure. Thus, it is important to observe the effect of the reaction atmosphere on the formation of graphitic carbon nitride. Here three types of atmospheres have been taken into consideration: first is oxidative (air), second and third is an inert atmosphere of argon and nitrogen. The following studies have been made to observe the effect of each gas type in the synthesis process.

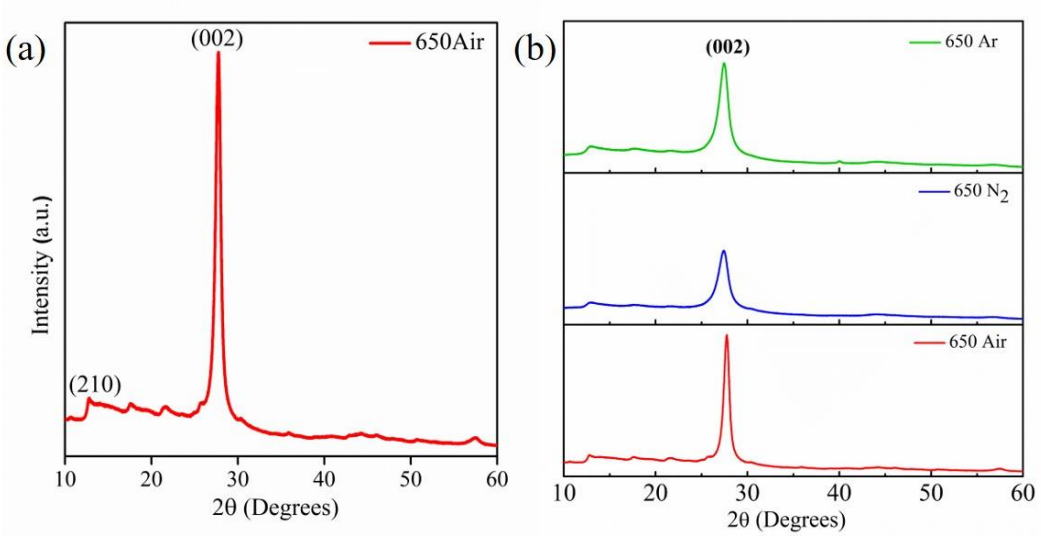

Figure 3.6 *XRD diffractogram of (a) MGCN 650Air sample, (b) MGCN synthesized in different reaction atmospheres at 650 °C.*

Figure 3.6 shows the XRD pattern of the *650Air* sample and other MGCN samples prepared under various reacting atmospheres of N_2, Ar and Air. All MGCN samples show analogous XRD patterns. The reaction atmosphere exhibits a significant effect on the crystal structure as shown in Fig. 3.6(b). The inter-planar spacing, graphitic stack size, specific surface area and other relevant information are tabulated below (Table 3.4). The (002) peak intensity enhanced from N_2 to Air in different reaction atmospheres. This indicated that inter-layer distance decreased synchronously as the reaction atmosphere changed from nitrogen to argon and air. This decrease is probably because of the elimination of nitrogen-containing species from MGCN architectures [27] which is obstructed in the case of nitrogen and argon atmospheres. Besides, the morphology of these samples observed under FESEM (Fig. 3.7) confirms that the air sample has a large number of stacking formations as compared to that of the other two samples. In addition, the obtained BET surface area value of the air sample stands out as compared to that of the N_2 and Ar samples. These numbers directly correlate with the

extent of polymerization developed during the pyrolysis reaction [24]. Thus, the air sample has the highest degree of polymerization as compared to other samples.

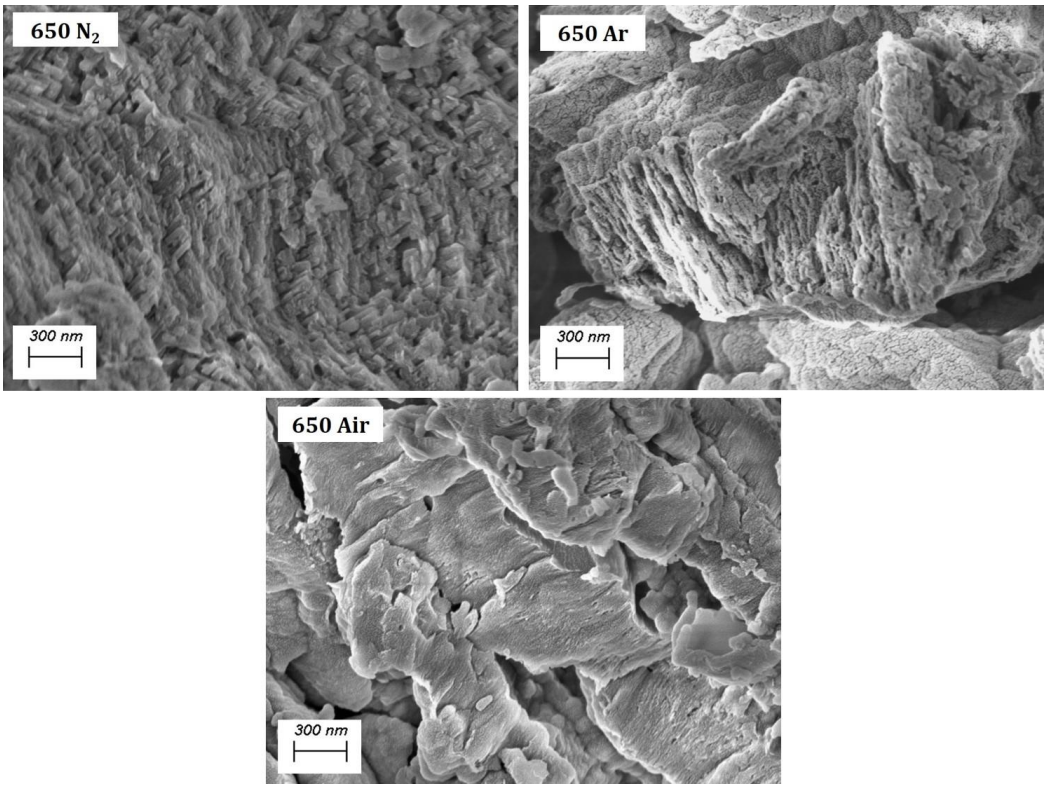

Figure 3.7 *FESEM Micrographs of MGCN synthesized in different reaction atmospheres at 650°C.*

Table 3.4 Variation of crystallite size(D), number of layers(n) and SSA of MGCN samples synthesized by the change in reaction atmosphere at 650 °C.

Sample	Interlayer spacing d (nm)	Crystallite Size D (nm)	Number of layers 'n'	S_{BET} (m^2g^{-1})
650 N_2	0.323	5.48	18	6.07
650 Ar	0.325	6.21	20	8.43
650 Air	0.321	11.39	36	42.34

Figure 3.8(a, b) displays the optical absorption bands of the as-prepared MGCN samples in argon and nitrogen atmospheres respectively. From the KM plot, the calculated energy bandgap values are 2.73 eV, 2.65 eV and 2.51 eV for nitrogen samples whereas 2.7 eV, 2.6 eV and 2.55 eV for argon samples with respect to increasing temperature. At 650 °C, the obtained indirect energy gap values for nitrogen, argon and air samples are 2.51 eV, 2.55 eV and 2.71 eV

respectively. From this, it is evident that the lower value of the energy gap was seen for the nitrogen sample whereas the air sample shows the highest energy gap. The reason for this is the ratio of the defect generated in nitrogen and argon samples as compared to that in air samples.

As depicted in Fig. 3.8(c), the PL spectra of the MGCN samples in argon and nitrogen atmospheres showed similar behaviour as that of the one in the air. However, the peaks obtained were broader and less intense than those of the air samples. Theoretically, these samples should be highly photoactive, but in reality, this was not true [28]. The reason for this could be the presence of structural defects due to ineffective polycondensation of melamine in argon and nitrogen atmospheres which falsely decrease the PL intensity in these samples. From Fig. 3.9(d) all the samples showed similar IR spectra with notable intensity variation. But in the case of nitrogen and argon samples, these peaks were moderately strong implying that there could be a structural deviation in both cases due to the low degree of polymerization, which in turn led to low photodegradation activity [24]. However, all the MGCN samples showed similar bands as described in the previous section implying clear evidence for graphitic carbon nitride formation [29].

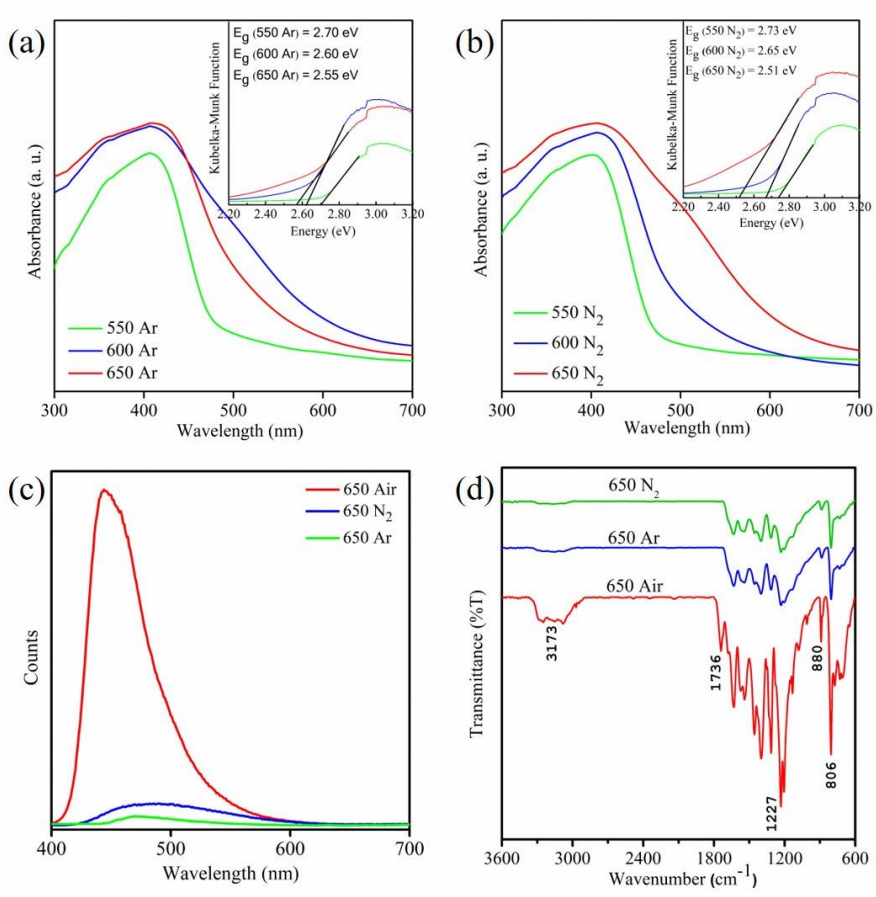

Figure 3.8 *(a, b) UV-DRS spectra and inset shows respective KM plots, (c) PL spectra (λ_{ext} ~365 nm) and (d) FT-IR spectra of MGCN samples in argon and nitrogen atmospheres.*

Figure 3.9 shows the XPS spectra of MGCN samples in different reaction atmospheres. All the peaks are relevant to the significant lines of the constituent elements. However, in the case of the argon atmosphere sample, the intensities of the major peak in C 1s and N 1s spectra are lower as compared to air and nitrogen atmospheres implying a lower degree of polymerization in this case. Moreover, from the N 1s spectrum of the nitrogen atmosphere sample, a minor peak at 400 eV disappears probably suggesting the lack of N─H structures in the architecture which further implies the stoichiometric deviation of the graphitic carbon nitride structure formation. Also, the atomic percentages of the constituent elements are shown in Table 5. Like in the previous section here also *650Air* sample holds the C/N ratio near the stoichiometric value suggesting g-C_3N_4 structure formation.

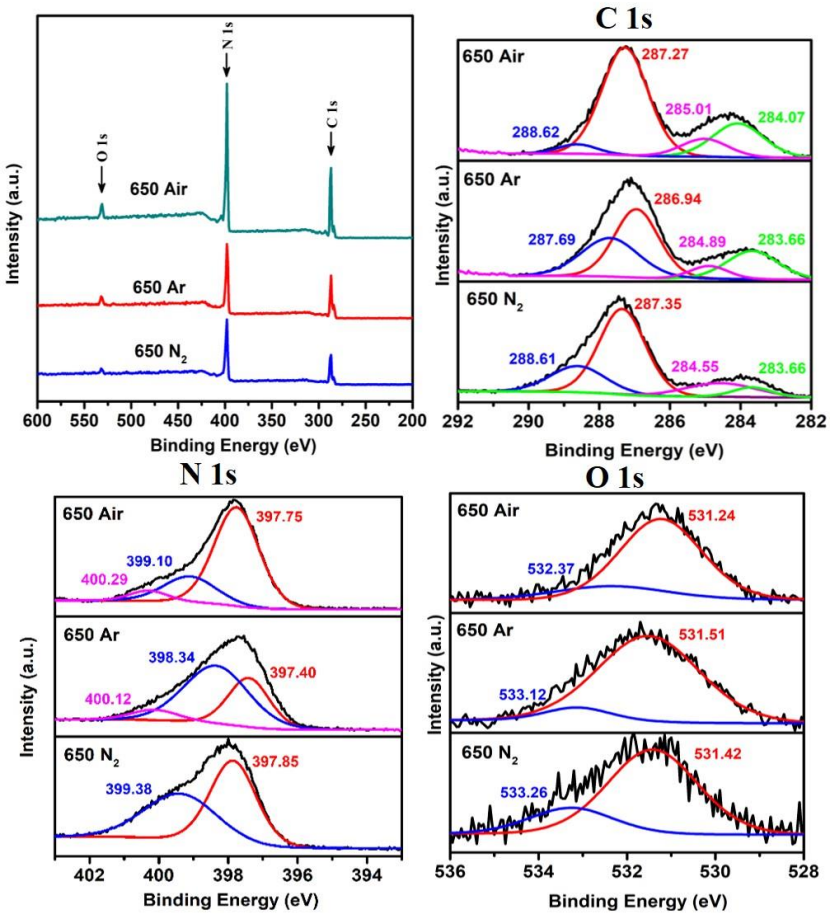

Figure 3.9 *XPS spectra of MGCN samples synthesized in different atmospheres at 650 °C.*

Table 3.5 Elemental composition and C/N ratio of MGCN samples synthesized in different atmospheres.

Sample	C (%)	N (%)	O (%)	C/N
650 AIR	40.41	55.82	3.77	0.72
650 Ar	48.29	47.73	3.98	1.01
650 N_2	44.89	53.13	1.98	0.84

3.2.3. Photodegradation studies

The photodegradation efficiency of the as-prepared MGCN samples in the air was examined by studying the photodegradation of RhB dye (concentration = 5 mg/L) under visible light illumination as shown in Fig. 3.10. The UV-Vis absorption spectra of RhB show a maximum at 554 nm in water, which is generally considered for decolouration studies. Prolonged illumination of the dye solution creates a blue shift in the intensity of the absorption maximum. This behaviour is due to the de-ethylation of the RhB dye molecule leading to chromophore cleavage in the end [30]. All the MGCN samples degraded consistently under a longer irradiation time. However, the *650Air* sample showed excellent activity by degrading about 94% of the dye in just 45 minutes and a total of 96% in 90 minutes. Whereas *550Air* and *600Air* samples showed moderate efficiency of 88% and 81% respectively as shown in Fig. 3.10(a). The experimental values were fitted in first-order kinetics reaction *i.e.,* $\ln\left(\frac{C}{C_0}\right) = -kt$ (Fig. 3.10(b)), where C_0 is the original concentration of the pollutant suspension, C_t is the concentration at time t and k is the apparent rate constant of the first-order degradation reaction whose value can be calculated using the expression: $k = \frac{\ln(2)}{t_{1/2}}$ where $t_{1/2}$ is the half-time value when the concentration of the dye becomes half of its initial concentration [31]. The apparent rate constant of RhB degradation is shown in Table 3.6. It can be noticed that the photocatalytic activity of the *650Air* sample is 4 times faster than that of the *550Air* and *600Air* samples.

Table 3.6 Rate constant values of MGCN samples with their respective half-time values.

Sample	Half time $t_{1/2}$ (min^{-1})	Rate constant K (min^{-1})
550 Air	45.89	0.015
600 Air	62.68	0.011
650 Air	15.66	0.044
650 Ar	36.84	0.018
650 N_2	26.46	0.026

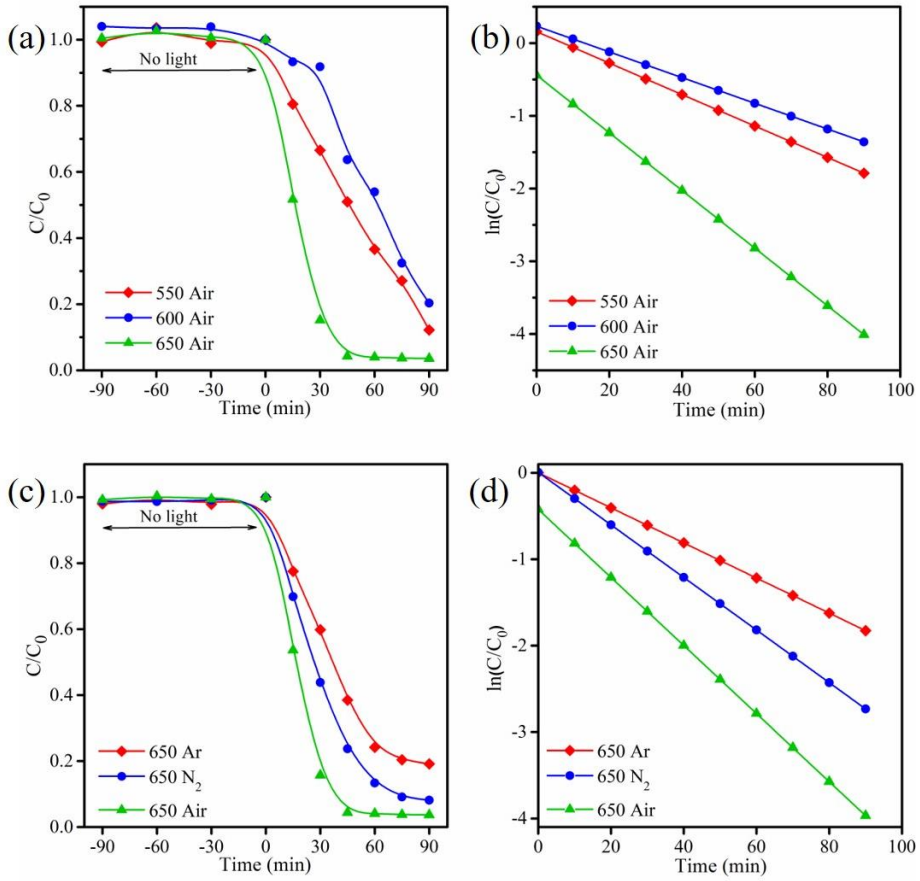

Figure 3.10 *Photodegradation studies of MGCN samples (a) prepared at different temperatures in air, (b) its respective first-order kinetics curve, (c) prepared in different atmospheres at 650 °C, and (d) its respective first-order kinetics curve.*

The degradation studies of MGCN samples prepared in argon, nitrogen, and air are shown in Fig. 3.10(c). It was observed that argon samples showed nominal decolouration *i.e.,* around 79% whereas nitrogen samples showed good efficiency of 92%. Above all, the air

sample showed the highest activity of 96% in 90 min. From Table 3.6 it was observed that the photodegradation activity followed this order: Air > N_2 > Ar (Fig. 3.10(d)). The reason for *650Ar* showing lesser activity even after having a higher surface area from *650N₂* is due to the lower average lifetime of the photoinduced charge carriers in the case of the *650Ar* sample. Overall characterization and testing indicate that 650ºC temperature and Air atmosphere are the optimum process parameters for the formation of g-C_3N_4 and superior photocatalytic activity.

To understand the degradation mechanism, it is crucial to know the isoelectric point (IEP) of the photocatalyst material as it is an important physicochemical property of many compounds. By knowing this value one can interpret the adsorption ability of the material. IEP is estimated by measuring the zeta potential at different pH values and the pH value resulting in zero net charge is called the isoelectric point. The zeta potential of *650Air* as a function of pH value is shown in Fig. 3.11. The IEP value of *650Air* was obtained to be 2.43 which means the MGCN particles are positively charged below this pH value whereas negatively charged above this point. The interactions of hydrogen and hydroxyl ions with MGCN surface groups under different pH conditions result in various zeta potentials and surface charges. As we know graphitic carbon nitride structure consists of primary (CNH_2), secondary (C_2NH) and tertiary (C_3N) amine groups and in aqueous suspensions, ionization of these groups on the surface takes place as amine groups due to their lone pair of electrons acts as proton acceptor and acquire positive surface charges [32] and at the same time, primary and secondary amine groups can react with hydroxyl ions and acquire negative surface charges. According to Zhu *et al* [33], the number of amine groups on the carbon surface and the pH of the MGCN suspension determine the chemical equilibrium and thereby resulting in diverse zeta potentials. Two significant factors can enhance the adsorption activity *i.e.,* higher surface areas and negative zeta potentials. *650Air* has both a negative zeta potential value as well a higher surface area. Hence, *650Air* shows a higher adsorption capability of Rhodamine B dye than other MGCN samples.

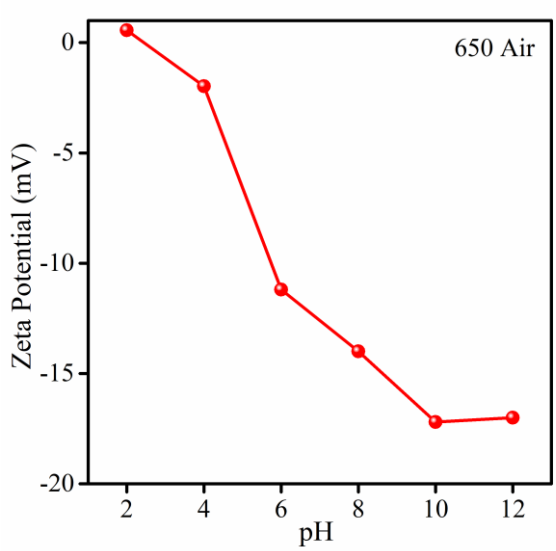

Figure 3.11 *Zeta potential of 650 Air as a function of the pH value of the suspension.*

To understand the RhB degradation process by MGCN samples, it is very important to know the fundamental processes, that take place during the photodegradation of organic pollutants. Fig. 3.12 explains the heterogenous photocatalysis phenomenon in detail. The first step in this phenomenon is the exposure of the photocatalyst material with an appropriate light energy source which leads to the generation of photoinduced electron-hole (e^{-}/h^{+}) pairs. Some of the generated charge carriers drift to the surface (holes near the valence band (VB) and electrons near the conduction band (CB)) and initiate a chain of chemical reactions with the adsorbed pollutant species [34]. Meanwhile, a large percentage of electrons recombine with the holes due to the electrostatic force of interactions either through radiative or non-radiative ways [35]. Photocatalytic reactions involve three main dynamic species: h^{+}, •OH and $O_2^{\bullet -}$ radicals. Each of these plays a typical role in the oxidation-reduction reactions as discussed in section 1.3.4.1.

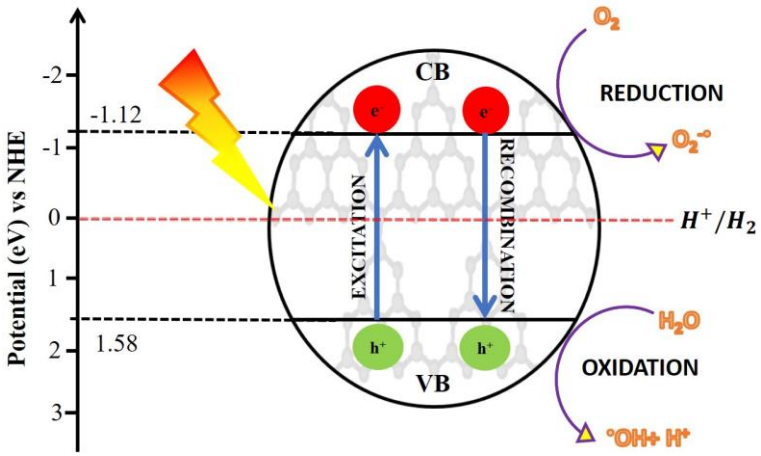

Figure 3.12 Photodegradation mechanism in MGCN.

The overall performance of the photocatalyst depends on the energy levels of the VB and CB. The surface oxidation and reduction reactions by photogenerated h^+ and e^- respectively are only possible when their reduction and oxidation potentials lie between the CB and VB potentials. These values can be analytically found using the equations given below [36]:

$$E_{VB} = X - E_e + 0.5E_g \quad \text{----------3.2}$$

$$E_{CB} = E_{VB} - E_g \quad \text{---------- 3.3}$$

where E_{VB} is the potential band-edge of the VB, X is the absolute semiconductor electronegativity, E_e is the free-electron energy on the normal hydrogen energy (NHE) scale (~4.5eV) and E_g is the semiconductor energy gap. The E_{VB} and E_{CB} values of the *650Air* sample calculated from the above equations (6 & 7) are 1.58 eV and -1.12 eV, respectively which are essentially higher than the oxidation potential of water (1.23eV vs. *NHE*) and lower than the reduction potential of oxygen (-0.33eV vs *NHE*) [37]. Moreover, RhB being a cationic dye can easily be adsorbed on the photocatalyst surface as the photocatalyst possesses a negative surface charge in water above 2.43 pH as discussed earlier [33]. Hence, the photodegradation of RhB by MGCN follows the reaction sequence as given in equations (2-5) thereby clearly indicating that MGCN is suitable for the decomposition of RhB and can find potential applications in pollutant removal.

Part II- Synthesis of improved g-C_3N_4 photocatalyst for enhanced photodegradation performance

3.3 Introduction

g-C_3N_4 is a novel material that has become the epitome of visible light photocatalysis for a few years and continues to explore its potential in multiple aspects. Due to its remarkable features like visible light activity corresponding to a wavelength of around 460 nm, low bandgap (~2.7 eV), appropriate band edge potentials required for photo-oxidation and reduction of organic pollutants, two-dimensional layered stacking consisting of C-N aromatic architecture providing higher specific surface areas and high thermal stability up to 600 °C. g-C_3N_4 has a wide band of applications in energy and environmental remediation sectors such as wastewater decontamination, CO_2 reduction, hydrogen/oxygen evolution via water splitting, electrode material in battery or supercapacitor, deodorization of toxic gases and many more [1,2,5,38–41].

However, this super material also has some drawbacks like low specific surface area and rapid charge carrier recombination which are mainly due to its bulk structure resulting in a relatively low photocatalytic degradation efficiency. Hence, there is an urgent need to encounter these issues and enhance its photocatalytic efficiency. In this connection, few research groups have come up with a green templating technique wherein, a bubbling material *i.e.,* ammonium chloride (NH_4Cl) is incorporated along with the precursor material during the thermal decomposition process where NH_3 and HCl gases are liberated resulting in bubbling action leaving behind a porous structure [42–46]. The main idea behind adapting such an approach is to delaminate the layers of the bulk structure and obtain a highly porous material resulting in a greater number of surface sites for pollutant adsorption thereby increasing the photodegradation efficiency. However, out of the reported literature on the subject, the concept is not extensively investigated to attain its full potential.

In the present work, we report this novel synthesis approach with an in-depth investigation to prove the bubbling material concept during the thermal decomposition process. The amount of NH_4Cl loading during the melamine decomposition process is optimized systematically. Herein, we observe a remarkable increase in the interlayer spacing with the addition of NH_4Cl and denote this material as expanded g-C_3N_4. The expanded g-C_3N_4 has exhibited high surface area and volume expansion leading to enhanced photodegradation performance of RhB under visible light, confirmed with relevant supporting experimental pieces of evidence.

3.4 Results and discussions

GCN was synthesized through the thermal pyrolysis method as discussed in the earlier section. Besides, for obtaining higher surface areas, a bubbling agent (NH_4Cl) was incorporated along with the precursor during the pyrolysis process. At higher temperatures, NH_4Cl decomposes to liberate NH_3 and HCl gases resulting in higher porosity and specific surface areas. In this study, three different weight ratios of melamine and NH_4Cl are considered *viz*, 2:1, 1:1 and 1:2 which are named NGCN-1, NGCN-2, and NGCN-3, respectively.

Figure 3.13(a) shows the XRD pattern of the GCN and NGCN samples. It can be noticed that NGCN samples possess a similar XRD pattern as that of the GCN sample which essentially means that the original structure of the g-C_3N_4 material has been retained irrespective of NH_4Cl presence during the pyrolysis process. The XRD pattern typically matches with the ICDD PDF: 00-066-0183 pattern assuming orthorhombic crystal structure [47]. It was also observed that there was a peak broadening and shift in the (002) peak in NGCN samples implying an increase

in d-spacing value (Table 3.7) as shown in Fig. 3.13(b, c) and suggesting shortened-range stacking order of layers along the c-axis [44]. However, this increase in the d-spacing showed a reverse trend with an increase in the amount of NH_4Cl loading. This is attributed to the incomplete polycondensation of melamine caused by an excessive amount of ammonium chloride, supported by an earlier report [45]. Similar results were observed in the FTIR spectra as well which will be discussed later.

Table 3.7 Interlayer spacing calculated using Bragg's law, $2d\sin\theta=n\lambda$, n=1, full-width half maxima (FWHM) and crystallite size calculated using Scherrer's formula, $D=K\lambda/\beta\cos\theta$, K=0.9 of GCN and NGCN samples.

Sample	Interlayer spacing 'd'(nm)	FWHM (β)	Crystallite Size (nm)
NGCN-1	0.325	0.0187	7.60
NGCN-2	0.325	0.0178	7.99
NGCN-3	0.323	0.0170	8.35
GCN	0.322	0.0151	9.47

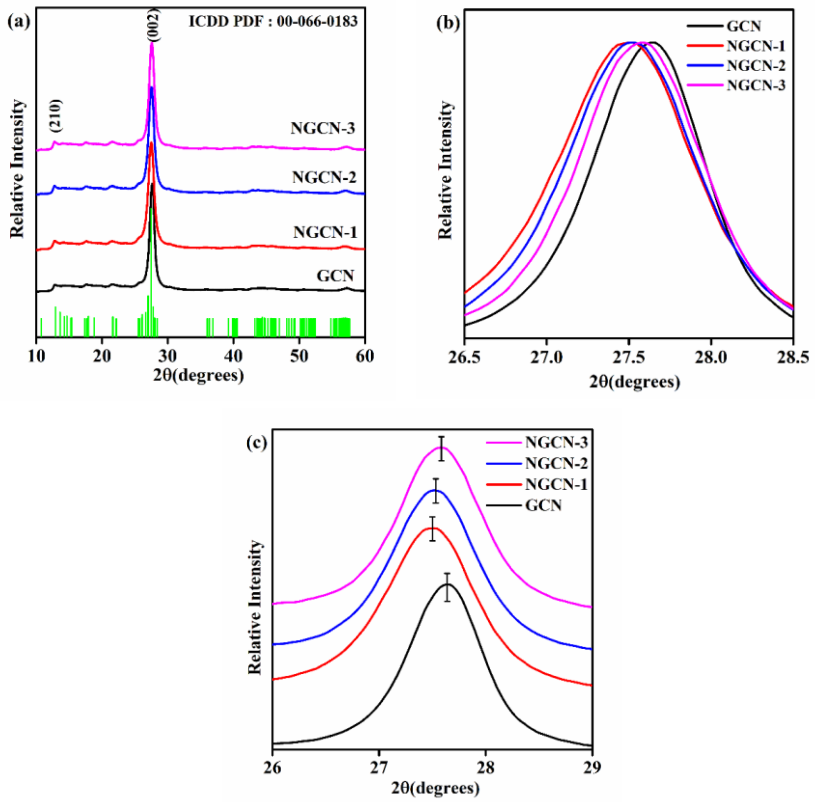

Figure 3.13 *(a) X-ray diffractogram pattern, (b) the (002) peak broadening and (c) the (002) peak shift of NGCN and GCN samples.*

The morphology and microstructure of the synthesized GCN and NGCN-1 samples were observed under FESEM and TEM as shown in Fig. 3.14. The GCN sample possesses a bulk structure having thick and dense sheets which are closely packed [Fig. 3.14 (d, e & f)]. However, the NGCN-1 sample unlike GCN bears a completely distinct morphology with a reduced particle size as shown in Fig. 3.14 (a, b & c). It can be seen that the NGCN-1 sample possesses a flaky structure containing irregular-shaped hollow spaces caused by the decomposition of NH_4Cl leading to the liberation of NH_3 and HCl gases during the pyrolysis process, supported by a similar phenomenon reported earlier [48,49]. These hollow spaces are attributed to the porous nature of the material leading to elevated specific surface areas.

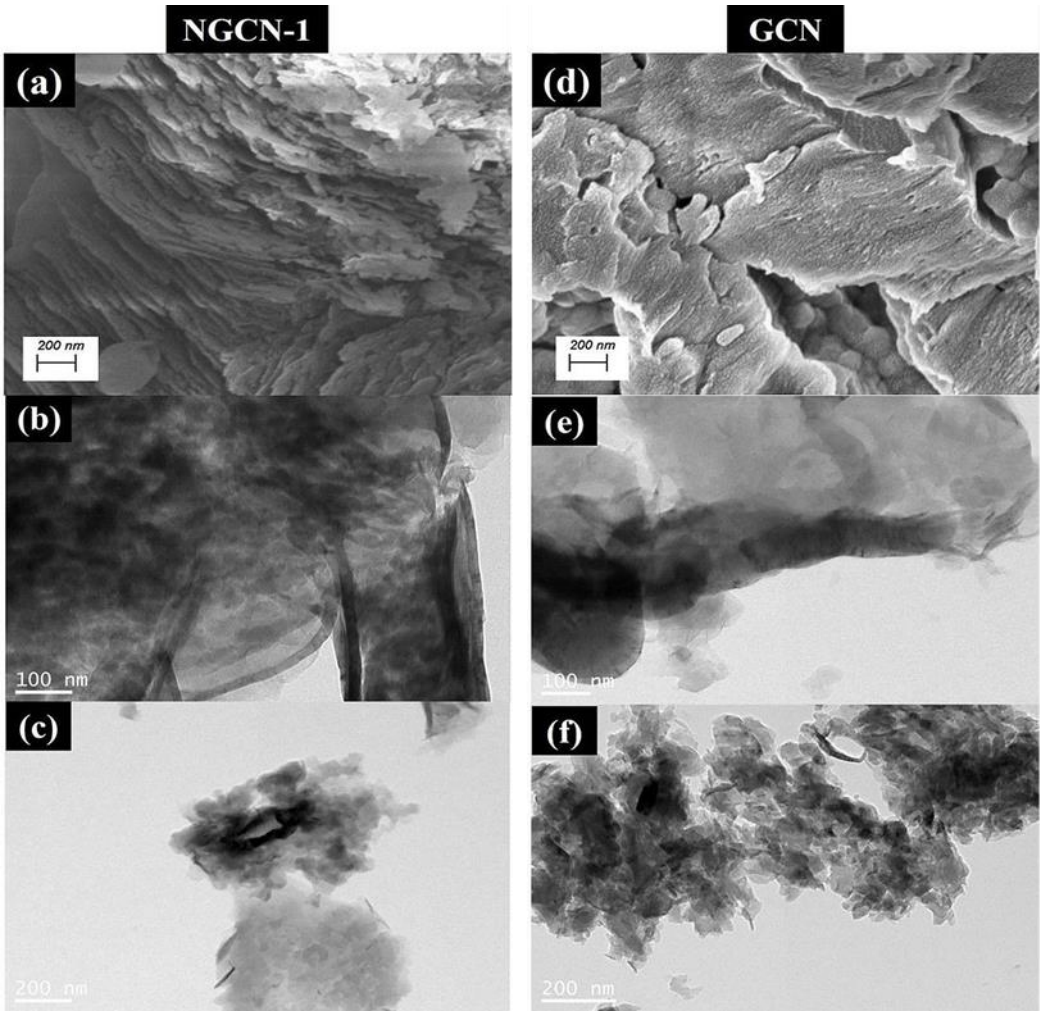

Figure 3.14 *(a, b & c) FE-SEM images of NGCN-1 and GCN samples respectively; (d, e & f) TEM micrographs of NGCN-1 and GCN samples, respectively*.

The optical properties of a photocatalyst material are a very crucial factor that governs the photodegradation performance. To analyse its properties, UV-DRS and PL studies were carried out as shown in Fig. 3.15. From the UV-DRS spectra [Fig. 3.15 (a)], it was discovered that all the NGCN samples have a wider absorption edge in the visible region of the

electromagnetic spectrum with respect to the GCN sample. Besides, the Kubelka-Munk (KM) plot of these samples shows a substantial raise in the energy bandgap (E_g) of the NGCN samples as depicted in Fig. 3.15 (b) which is mainly due to the size confinement effect where electrons and holes are confined to CB and VB respectively [50]. Moreover, the flat-band potentials of all the samples were calculated using the following equations 3.6 and 3.7. The calculated values are plotted as shown in Fig. 3.15(c) where the CB minimum and VB maximum of all NGCN samples have widened in opposite directions. Apart from this, the photoluminescence data has interesting observations as shown in Fig. 3.15(d) where at an excitation wavelength of 365 nm, NGCN samples have lower PL intensity than GCN samples which essentially implies that NGCN samples have a relatively higher charge carrier lifetime than GCN sample [17,51].

The structural information was reconfirmed with the help of infrared (IR) studies. As displayed in Fig. 3.16, all the vibrational bands have characteristic peak positions related to g-C_3N_4 material [18]. The broad peak around 3173 cm^{-1} is due to the vibrations of N-H groups at the edges of the g-C_3N_4 sheet [20], the bands between 1200-1800 cm^{-1} belong to the stretching vibrations of the C-N aromatic architecture and the peaks below 900 cm^{-1} are due to the out-of-plane bending vibrations of triazine units [19]. The IR results are evident and supplement the structural analysis and formation of g-C_3N_4.

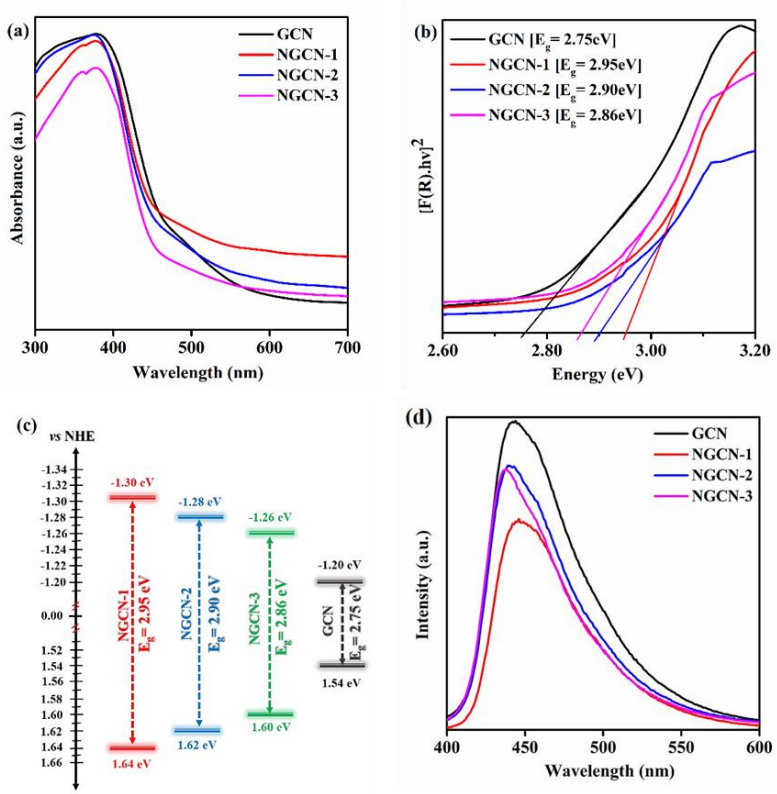

Figure 3.15 (*a) UV-Visible absorbance spectra, (b) its respective Kubelka-Munk plot, (c) the shift in the VB and CB potentials and (d) the PL spectra of NGCN and GCN samples.*

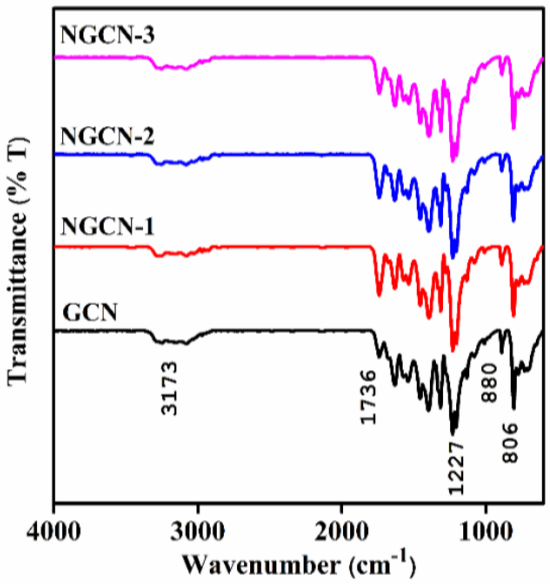

Figure 3.16 *FTIR spectra of NGCN and GCN samples.*

The XPS is a surface-sensitive quantitative spectroscopic technique widely used for identifying the elemental composition of a material. From Fig. 3.17, it can be observed that the XPS spectra of GCN and NGCN-1 samples essentially contain C and N elements with minute traces of O that could be attributed to the surface adsorbed oxygen or water molecules. Clearly, there is no signal related to the Cl element in NGCN-1 thus indicating the absence of Cl incorporation during the pyrolysis process in C-N architecture. The atomic composition in percentages is tabulated in Table 3.8 where it can be observed that the C/N ratio remains unaltered irrespective of NH4Cl addition during the synthesis process. The elemental composition and C/N ratio of GCN and NGCN-1 samples are presented in Table 3.8.

Table 3.8 Elemental composition and C/N ratio of GCN and NGCN-1 samples.

Sample	C (%)	N (%)	O (%)	C/N
GCN	45.98	50.2	3.82	0.91
NGCN-1	45.77	50.54	3.69	0.90

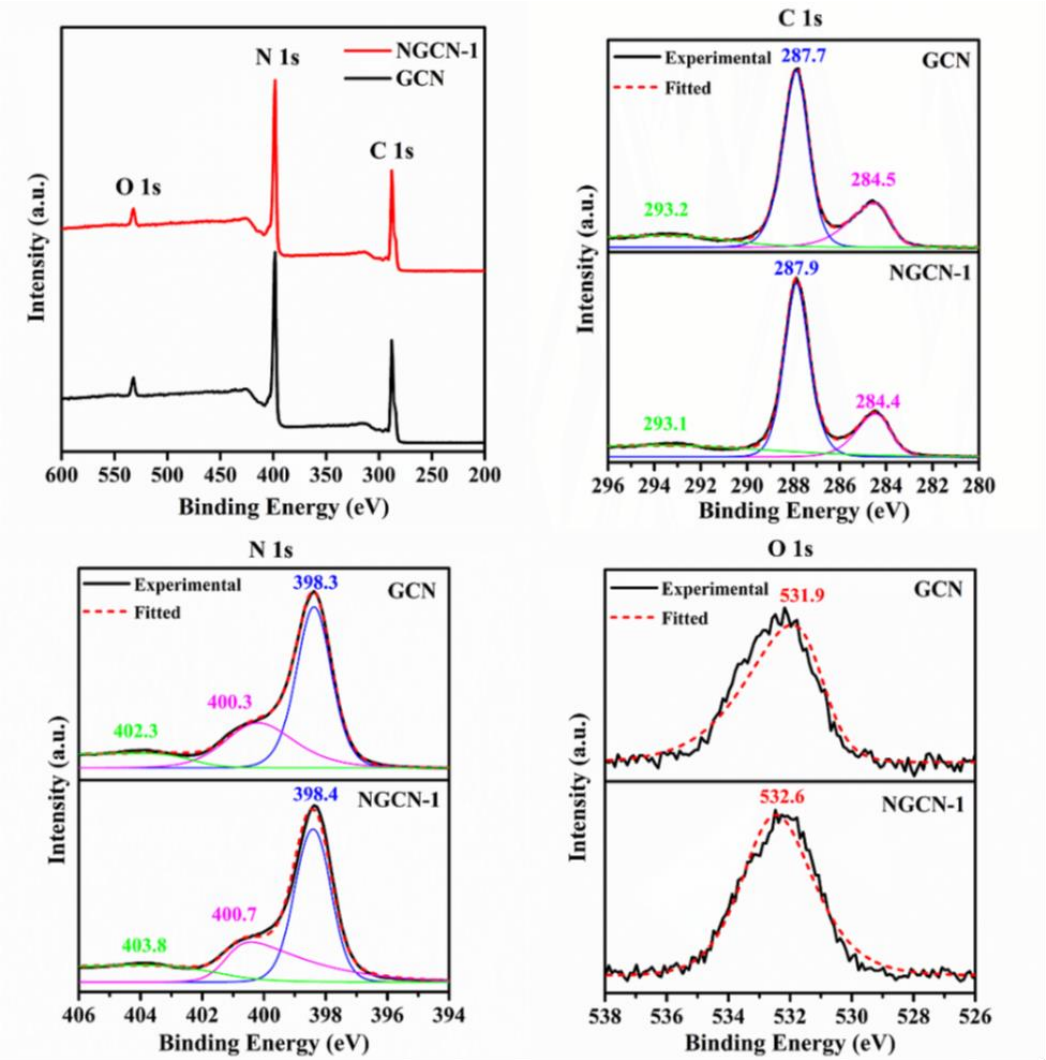

Figure 3.17 *XPS spectra of GCN and NGCN-1 samples.*

In XPS spectra for C1s spectrum, its significant photoelectron line is observed around 284 eV and the signal around 287 eV is attributed to sp^2 bound C in N- containing ring architecture. Besides, the carbon attached to uncondensed -NH_2 groups shows a signal around 293 eV [24]. The high–resolution N1s spectrum shows three peaks around 398, 400 and 402 eV which are attributed to pyridinic-N [C – N = C], tertiary nitrogen-containing groups [N – $(C)_3$] and N – H species respectively [25,26]. The deconvoluted O1s spectrum consists of one peak around 531 eV which is due to surface adsorbed oxygen groups on the material [14].

The nitrogen adsorption-desorption isotherms of GCN and NGCN samples were investigated in Fig. 3.18. All the samples typically reflect type IV isotherm following the H3 hysteresis loop essentially containing porous morphology [52]. It was observed that all the NGCN samples showed elevated specific surface area values and decreased average pore size concerning the GCN sample as summarized in Table 3.9. Further, the crystallite size of NGCN samples was relatively lower which is also responsible for higher surface availability providing

an increased number of potential active sites over the surface for carrying out photodegradation reactions [44].

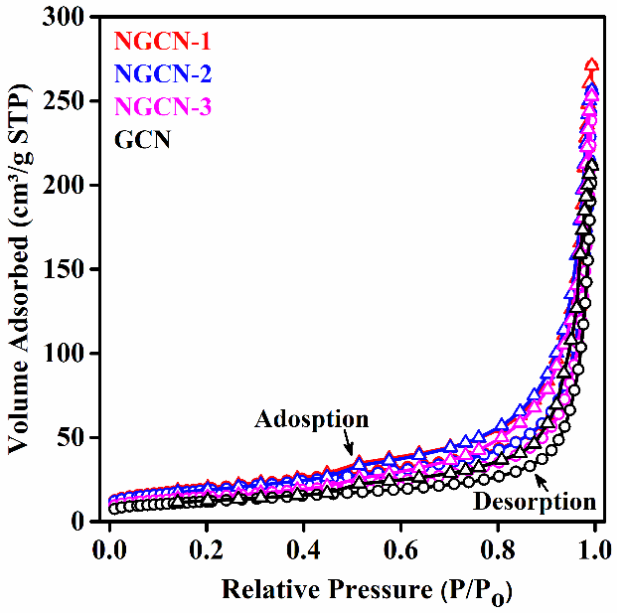

Figure 3.18 *Nitrogen adsorption-desorption isotherms of NGCN and GCN samples.*

Table 3.9 Specific surface area, pore size and pore volume of GCN and NGCN samples.

Sample	S_{BET} (m^2/g)	Pore Size (nm)	Pore Volume (cc/g)
NGCN-1	69	21.3	0.39
NGCN-2	66	23.5	0.39
NGCN-3	51	28.8	0.36
GCN	42	29.2	0.30

The zeta potential measurement is a quantitative study to identify the electrostatic charge on the surface of the photocatalyst material in an aqueous phase at a given pH value [53]. The zeta potential at various pH values provides an outline of the material surface-charge conditions which is a very crucial factor that directly influences the photodegradation performance [54]. To understand the surface-charge phenomenon on photodegradation performance, one needs to estimate the IEP. In general, the material possesses a negative charge below IEP and a positive charge above this value. In g-C_3N_4, the interactions of surface groups with the hydrogen and hydroxyl ions determine the variation in the surface charge, the phenomenon is explained in detail in our earlier report [55]. From Fig. 3.19, it can be observed that GCN and NGCN samples have IEPs between 2 and 5 which implies that at pH 7 (pH of the dye solution during

photodegradation), the surface of the photocatalyst possesses negative charges and hence, the target pollutant must have a net positive surface charge. Therefore, we choose RhB as the target pollutant since it is a cationic dye and can easily be adsorbed onto the photocatalyst surface.

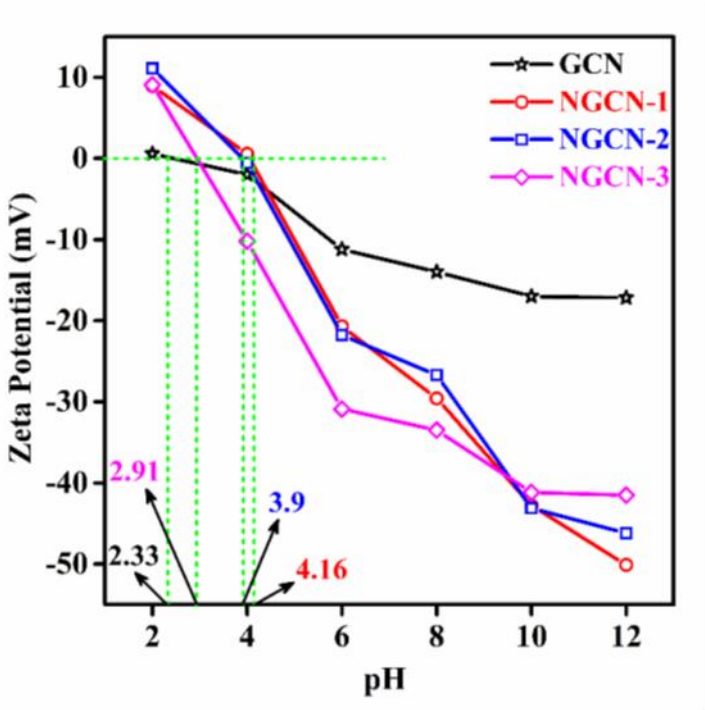

Figure 3.19 *Isoelectric points of NGCN and GCN samples*.

The photodegradation efficiency of the samples was investigated by taking RhB as a target pollutant (concentration = 10 mg/L) under visible light source irradiation for 30 minutes. It was observed that all the NGCN samples have higher degradation efficiencies than the GCN sample as shown in Fig. 3.20(a). Besides, the photo-deterioration reaction followed first-order reaction kinetics as shown in Fig. 3.20(b), the degradation experimental details are summarized in Table 3.10. The reaction mechanism involves the investigation of the role of major reactive species responsible for photo oxidation-reduction of the target pollutant [56]. For this, reactive species trapping experiments were performed by adding a certain amount of each of the scavenging agents during the photodegradation process. In this study, equal amounts of isopropanol (IPA), p-Benzoquinone (p-BQ) and ammonium oxalate (AO) were incorporated as scavenging agents for $\boldsymbol{HO^{\bullet}}$, $\bullet\, \boldsymbol{O_2^-}$ and h^+ respectively [57]. By adding IPA to the dye solution during the experiment, the IPA gets reduced by generated hydroxyl radicals to propenal thereby scavenging the hydroxyl reactive species. Similarly, p-BQ takes an electron from the superoxide radical and gets oxidised to hydroquinone and AO being a reducing agent, loses an electron to the photo-generated holes thereby acting as a trapping agent. The degradation performance after adding each of the scavenging chemicals individually effected in the following manner as shown in Fig. 3.20(c). From Table 3.11 it can be predicted that each of the reactive species has

a definite role in the decomposition process. Among all, photogenerated holes majorly affected the photo-degradation however, we cannot rule out the influence of other reactive species which rendered an almost equal role during the photodecomposition process. Apart from this, the effect of only light (photolysis) and only photocatalyst (adsorption) was also carried out to find out its influence during the dye degradation process.

Table 3.10 Reaction rate constant 'k (min^{-1})' and percentage (%) of RhB degradation of GCN and NGCN samples.

Sample	k (min^{-1})	RhB Degradation (%)
GCN	0.015	35
NGCN-1	0.036	94
NGCN-2	0.026	55
NGCN-3	0.023	49

Table 3.11 RhB photodegradation experiments with different radical scavenging agents, without photocatalyst (photolysis) and light irradiation (adsorption) for the NGCN-1 sample.

Experimental detail	RhB Degradation (%)
Photolysis (Only Light)	2
Adsorption (Only Photocatalyst)	5
Hole Scavenger	30
Hydroxyl Scavenger	45
Superoxide Scavenger	53
No Scavenger	94

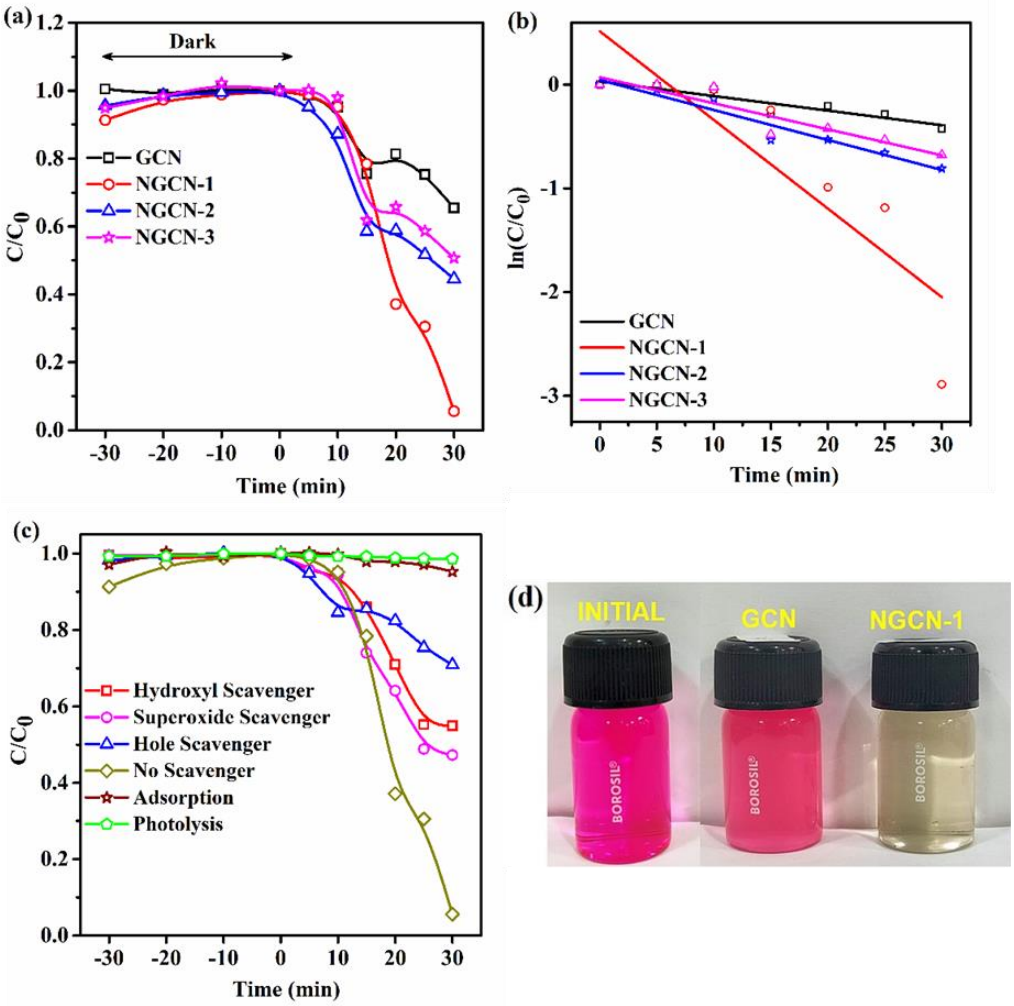

Figure 3.20 (*a) Dye degradation studies, (b) first-order kinetics curve of NGCN and GCN samples, (c) reactive species trapping experiment of NGCN-1 sample using different scavenging agents and (d) RhB dye solution images of initial concentration and post photodegradation concentrations of GCN and NGCN-1 samples.*

3.5 Conclusions

In summary, the first part deals with the synthesis of graphitic carbon nitride by a facile template-free technique through the thermal decomposition of melamine at various temperatures and reaction atmospheres. The superior photocatalytic activity was achieved in the *650Air* sample due to its large specific surface area (42 m^2g^{-1}), the suitable position of the band edge potentials and higher degradation rate constant (0.044 min^{-1}). More importantly, the present photocatalyst is prepared from an economical and eco-friendly method which can be easily produced in bulk. These optimized process parameters can be used as a standard recipe for the synthesis of g-C_3N_4 and could be further extended in making g-C_3N_4-based composites.

Further, the second part discusses synthesis of expanded g-C_3N_4 using this single-step cost-effective approach. The amount of NH_4Cl required for the porous structure was optimized and found to be adequate in the NGCN-1 sample. The XRD and FTIR results confirm the structural integrity of g-C_3N_4 irrespective of NH_4Cl addition during synthesis which implies that NH_4Cl does not alter the structure of g-C_3N_4 and only generates porosity in the sample as confirmed based on TEM analysis. The structural and morphological modifications in g-C3N4 by the present process inherently enhanced the photodegradation efficiency rate by 2.4 times. This can be adapted as the standard synthesizing process for porous g-C_3N_4 which can be further applied while making g-C_3N_4-based composites.

References

[1] G. Dong, Y. Zhang, Q. Pan, J. Qiu, A fantastic graphitic carbon nitride (g-C3N4) material: Electronic structure, photocatalytic and photoelectronic properties, Journal of Photochemistry and Photobiology C: Photochemistry Reviews. 20 (2014) 33–50. https://doi.org/10.1016/j.jphotochemrev.2014.04.002.

[2] S. Cao, J. Low, J. Yu, M. Jaroniec, Polymeric Photocatalysts Based on Graphitic Carbon Nitride, Advanced Materials. 27 (2015) 2150–2176. https://doi.org/10.1002/adma.201500033.

[3] R. Asahi, T. Morikawa, H. Irie, T. Ohwaki, Nitrogen-doped titanium dioxide as visible-light-sensitive photocatalyst: Designs, developments, and prospects, Chem Rev. 114 (2014) 9824–9852. https://doi.org/10.1021/cr5000738.

[4] B. Padya, P.K. Jain, G. Padmanabham, M. Ravi, K.S. Bhat, Highly-ordered nitrogen doped carbon nanotube novel structures of aligned carpet for enhanced field emission properties, in: AIP Conf Proc, 2013: pp. 196–199. https://doi.org/10.1063/1.4810056.

[5] L. Kong, J. Wang, F. Ma, M. Sun, J. Quan, Graphitic carbon nitride nanostructures: Catalysis, Appl Mater Today. 16 (2019) 388–424. https://doi.org/10.1016/j.apmt.2019.06.003.

[6] S.C. Yan, Z.S. Li, Z.G. Zou, Photodegradation performance of g-C3N4 fabricated by directly heating melamine, Langmuir. 25 (2009) 10397–10401. https://doi.org/10.1021/la900923z.

[7] G. Zhang, J. Zhang, M. Zhang, X. Wang, Polycondensation of thiourea into carbon nitride semiconductors as visible light photocatalysts, J Mater Chem. 22 (2012) 8083–8091. https://doi.org/10.1039/c2jm00097k.

[8] F. Dong, Z. Wang, Y. Sun, W.K. Ho, H. Zhang, Engineering the nanoarchitecture and texture of polymeric carbon nitride semiconductor for enhanced visible light photocatalytic activity, J Colloid Interface Sci. 401 (2013) 70–79. https://doi.org/10.1016/j.jcis.2013.03.034.

[9] H. May, Pyrolysis of melamine, Journal of Applied Chemistry. 9 (2007) 340–344. https://doi.org/10.1002/jctb.5010090608.

[10] D.L. Yu, J.L. He, Z.Y. Liu, B. Xu, D.C. Li, Y.J. Tian, Phase transformation of melamine at high pressure and temperature, in: J Mater Sci, 2008: pp. 689–695. https://doi.org/10.1007/s10853-007-2148-y.

[11] X. Wang, K. Maeda, A. Thomas, K. Takanabe, G. Xin, J.M. Carlsson, K. Domen, M. Antonietti, A metal-free polymeric photocatalyst for hydrogen production from water under visible light, Nat Mater. 8 (2009) 76–80. https://doi.org/10.1038/nmat2317.

[12] P. Niu, G. Liu, H.M. Cheng, Nitrogen vacancy-promoted photocatalytic activity of graphitic carbon nitride, Journal of Physical Chemistry C. 116 (2012) 11013–11018. https://doi.org/10.1021/jp301026y.

[13] R. Sharma, N. Chadha, P. Saini, Determination of defect density, crystallite size and number of graphene layers in graphene analogues using X-ray diffraction and Raman spectroscopy, 2017.

[14] H.Y. Xu, L.C. Wu, H. Zhao, L.G. Jin, S.Y. Qi, Synergic Effect between Adsorption and Photocatalysis of Metal-Free g-C3N4 Derived from Different Precursors, PLoS One. 10 (2015). https://doi.org/10.1371/journal.pone.0142616.

[15] Z. Mo, X. She, Y. Li, L. Liu, L. Huang, Z. Chen, Q. Zhang, H. Xu, H. Li, Synthesis of g-C3N4 at different temperatures for superior visible/UV photocatalytic performance and photoelectrochemical sensing of MB solution, RSC Adv. 5 (2015) 101552–101562. https://doi.org/10.1039/c5ra19586a.

[16] I. Papailias, T. Giannakopoulou, N. Todorova, D. Demotikali, T. Vaimakis, C. Trapalis, Effect of processing temperature on structure and photocatalytic properties of g-C 3 N 4, in: Appl Surf Sci, Elsevier B.V., 2015: pp. 278–286. https://doi.org/10.1016/j.apsusc.2015.08.097.

[17] L. Jiang, X. Yuan, G. Zeng, X. Chen, Z. Wu, J. Liang, J. Zhang, H. Wang, H. Wang, Phosphorus- and Sulfur-Codoped g-C3N4: Facile Preparation, Mechanism Insight, and Application as Efficient Photocatalyst for Tetracycline and Methyl Orange Degradation under Visible Light Irradiation, ACS Sustain Chem Eng. 5 (2017) 5831–5841. https://doi.org/10.1021/acssuschemeng.7b00559.

[18] H. Zou, X. Yan, J. Ren, X. Wu, Y. Dai, D. Sha, J. Pan, J. Liu, Photocatalytic activity enhancement of modified g-C3N4 by ionothermal copolymerization, Journal of Materiomics. 1 (2015) 340–347. https://doi.org/10.1016/j.jmat.2015.10.004.

[19] X. Chen, D.H. Kuo, D. Lu, Nanonization of g-C3N4 with the assistance of activated carbon for improved visible light photocatalysis, RSC Adv. 6 (2016) 66814–66821. https://doi.org/10.1039/c6ra10357j.

[20] W.J. Ong, L.L. Tan, S.P. Chai, S.T. Yong, Heterojunction engineering of graphitic carbon nitride (g-C3N4) via Pt loading with improved daylight-induced photocatalytic reduction of carbon dioxide to methane, Dalton Transactions. 44 (2014) 1249–1257. https://doi.org/10.1039/c4dt02940b.

[21] F. Dong, L. Wu, Y. Sun, M. Fu, Z. Wu, S.C. Lee, Efficient synthesis of polymeric g-C3N4 layered materials as novel efficient visible light driven photocatalysts, J Mater Chem. 21 (2011) 15171–15174. https://doi.org/10.1039/c1jm12844b.

[22] Q. Guo, Y. Xie, X. Wang, S. Lv, T. Hou, X. Liu, Characterization of well-crystallized graphitic carbon nitride nanocrystallites via a benzene-thermal route at low temperatures, Chem Phys Lett. 380 (2003) 84–87. https://doi.org/10.1016/j.cplett.2003.09.009.

[23] J.F. Moulder, W.F. Stickle, P.E.' Sobol, K.D. Bomben, J. Chastain, Handbook of X-ray Photoelectron Spectroscopy AReference Book of Standard Spectra for Identification and Interpretation of XPS Data, n.d.

[24] J. Zou, Y. Yu, W. Yan, J. Meng, S. Zhang, J. Wang, A facile route to synthesize boron-doped g-C 3 N 4 nanosheets with enhanced visible-light photocatalytic activity, J Mater Sci. 54 (2019) 6867–6881. https://doi.org/10.1007/s10853-019-03384-0.

[25] Y. Chai, Q. Liu, L. Zhang, J. Ren, W.L. Dai, Structure Engineered g-C3N4 Nano-Sheets by Switching the Pyrolysis Gas Atmosphere for Enhanced Photo-Catalytic Degradation, Chin J Chem. 35 (2017) 173–182. https://doi.org/10.1002/cjoc.201600608.

[26] G. Song, Z. Chu, W. Jin, H. Sun, Enhanced performance of g-C3N4/TiO2 photocatalysts for degradation of organic pollutants under visible light, Chin J Chem Eng. 23 (2015) 1326–1334. https://doi.org/10.1016/j.cjche.2015.05.003.

[27] J. Xu, L. Zhang, R. Shi, Y. Zhu, Chemical exfoliation of graphitic carbon nitride for efficient heterogeneous photocatalysis, J Mater Chem A Mater. 1 (2013) 14766–14772. https://doi.org/10.1039/c3ta13188b.

[28] R. Mohini, N. Lakshminarasimhan, Coupled semiconductor nanocomposite g-C3N4/TiO2 with enhanced visible light photocatalytic activity, Mater Res Bull. 76 (2016) 370–375. https://doi.org/10.1016/j.materresbull.2015.12.034.

[29] P. Jiménez-Calvo, C. Marchal, T. Cottineau, V. Caps, V. Keller, Influence of the gas atmosphere during the synthesis of g-C3N4 for enhanced photocatalytic H2 production from water on Au/g-C3N4 composites, J Mater Chem A Mater. 7 (2019) 14849–14863. https://doi.org/10.1039/c9ta01734h.

[30] M. Pica, S. Calzuola, A. Donnadio, P.L. Gentili, M. Nocchetti, M. Casciola, De-ethy lation and cleavage of rhodamine b by a zirconium phosphate/silver bromide composite photocatalyst, Catalysts. 9 (2019). https://doi.org/10.3390/catal9010003.

[31] S. Kumar, A. Baruah, S. Tonda, B. Kumar, V. Shanker, B. Sreedhar, Cost-effective and eco-friendly synthesis of novel and stable N-doped ZnO/g-C3N4 core-shell nanoplates with excellent visible-light responsive photocatalysis, Nanoscale. 6 (2014) 4830–4842. https://doi.org/10.1039/c3nr05271k.

[32] B.P. Singh, S. Gaydardzhiev, P. Ay, Stabilization of aqueous silicon nitride suspension with Dolapix A88, J Dispers Sci Technol. 27 (2006) 91–97. https://doi.org/10.1081/DIS-200066756.

[33] B. Zhu, P. Xia, W. Ho, J. Yu, Isoelectric point and adsorption activity of porous g-C 3 N 4, Appl Surf Sci. 344 (2015) 188–195. https://doi.org/10.1016/j.apsusc.2015.03.086.

[34] X. Li, J. Yu, M. Jaroniec, Hierarchical photocatalysts, Chem Soc Rev. 45 (2016) 2603–2636. https://doi.org/10.1039/c5cs00838g.

[35] S.M. Lam, J.C. Sin, A.R. Mohamed, A review on photocatalytic application of g-C3N4/semiconductor (CNS) nanocomposites towards the erasure of dyeing wastewater, Mater Sci Semicond Process. 47 (2016) 62–84. https://doi.org/10.1016/j.mssp.2016.02.019.

[36] Y. Li, J. Wang, H. Yao, L. Dang, Z. Li, Efficient decomposition of organic compounds and reaction mechanism with BiOI photocatalyst under visible light irradiation, J Mol Catal A Chem. 334 (2011) 116–122. https://doi.org/10.1016/j.molcata.2010.11.005.

[37] M.R. Hoffmann, S.T. Martin, W. Choi, D.W. Bahnemann1', W.M. Keck, Environmental Applications of Semiconductor Photocatalysis, 1995.

[38] L. Liang, L. Shi, F. Wang, H. Wang, P. Yan, Y. Cong, L. Yao, Z. Yang, W. Qi, g-C3N4 nano-fragments as highly efficient hydrogen evolution photocatalysts: Boosting effect of nitrogen vacancy, Appl Catal A Gen. 599 (2020). https://doi.org/10.1016/j.apcata.2020.117618.

[39] L. Liang, L. Shi, F. Wang, L. Yao, Y. Zhang, W. Qi, Synthesis and photo-catalytic activity of porous g-C3N4: Promotion effect of nitrogen vacancy in H2 evolution and pollutant degradation reactions, Int J Hydrogen Energy. 44 (2019) 16315–16326. https://doi.org/10.1016/j.ijhydene.2019.05.001.

[40] J. Wen, J. Xie, X. Chen, X. Li, A review on g-C 3 N 4 -based photocatalysts, Appl Surf Sci. 391 (2017) 72–123. https://doi.org/10.1016/j.apsusc.2016.07.030.

[41] L. Liang, L. Shi, F. Wang, H. Wang, W. Qi, The improvement of photocatalytic performance for hydrogen evolution over mesoporous g-C3N4modified with nitrogen defects, Sustain Energy Fuels. 4 (2020) 5179–5187. https://doi.org/10.1039/d0se01012j.

[42] Y. Dang, Q. Hu, P. He, T. Ren, Tailoring the ratio of ammonium chloride and graphitic carbon nitride for high photocatalytic activity, J Mol Struct. 1209 (2020). https://doi.org/10.1016/j.molstruc.2020.127961.

[43] B. Fei, Y. Tang, X. Wang, X. Dong, J. Liang, X. Fei, L. Xu, Y. Song, F. Zhang, One-pot synthesis of porous g-C3N4 nanomaterials with different morphologies and their superior photocatalytic performance, Mater Res Bull. 102 (2018) 209–217. https://doi.org/10.1016/j.materresbull.2018.02.041.

[44] W. Iqbal, C. Dong, M. Xing, X. Tan, J. Zhang, Eco-friendly one-pot synthesis of well-adorned mesoporous g-C3N4 with efficiently enhanced visible light photocatalytic activity, Catal Sci Technol. 7 (2017) 1726–1734. https://doi.org/10.1039/c7cy00286f.

[45] D. Zhang, Y. Guo, Z. Zhao, Porous defect-modified graphitic carbon nitride via a facile one-step approach with significantly enhanced photocatalytic hydrogen evolution under visible light irradiation, Appl Catal B. 226 (2018) 1–9. https://doi.org/10.1016/j.apcatb.2017.12.044.

[46] B. Babu, J. Shim, A.N. Kadam, K. Yoo, Modification of porous g-C3N4 nanosheets for enhanced photocatalytic activity: In-situ synthesis and optimization of NH4Cl quantity, Catal Commun. 124 (2019) 123–127. https://doi.org/10.1016/j.catcom.2019.01.009.

[47] F. Fina, S.K. Callear, G.M. Carins, J.T.S. Irvine, Structural investigation of graphitic carbon nitride via XRD and neutron diffraction, Chemistry of Materials. 27 (2015) 2612–2618. https://doi.org/10.1021/acs.chemmater.5b00411.

[48] Z. Huang, H. Chen, L. Zhao, W. Fang, X. He, W. Li, P. Tian, In suit inducing electron-donating and electron-withdrawing groups in carbon nitride by one-step NH4Cl-assisted route: A strategy for high solar hydrogen production efficiency, Environ Int. 126 (2019) 289–297. https://doi.org/10.1016/j.envint.2019.02.030.

[49] J. Xiao, Y. Xie, C. Li, J.H. Kim, K. Tang, H. Cao, Enhanced hole-dominated photocatalytic activity of doughnut-like porous g-C3N4 driven by down-shifted valance band maximum, Catal Today. 307 (2018) 147–153. https://doi.org/10.1016/j.cattod.2017.02.024.

[50] C. Zhang, J. Liu, X. Huang, D. Chen, S. Xu, Multistage Polymerization Design for g-C3N4 Nanosheets with Enhanced Photocatalytic Activity by Modifying the Polymerization Process of Melamine, ACS Omega. 4 (2019) 17148–17159. https://doi.org/10.1021/acsomega.9b01510.

[51] G. Liu, L. Shi, L. Yao, L. Cui, In-situ synthesis of defects modified mesoporous g-C3N4 with enhanced photocatalytic H2 evolution performance, Int J Energy Res. 45 (2021) 10478–10488. https://doi.org/10.1002/er.6535.

[52] Y. Zheng, Y. Jiao, J. Chen, J. Liu, J. Liang, A. Du, W. Zhang, Z. Zhu, S.C. Smith, M. Jaroniec, G.Q. Lu, S.Z. Qiao, Nanoporous graphitic-C 3N 4@carbon metal-free electrocatalysts for highly efficient oxygen reduction, J Am Chem Soc. 133 (2011) 20116–20119. https://doi.org/10.1021/ja209206c.

[53] M.J. Arlos, M.M. Hatat-Fraile, R. Liang, L.M. Bragg, N.Y. Zhou, S.A. Andrews, M.R. Servos, Photocatalytic decomposition of organic micropollutants using immobilized TiO

2 having different isoelectric points, Water Res. 101 (2016) 351–361. https://doi.org/10.1016/j.watres.2016.05.073.

[54] F. Azeez, E. Al-Hetlani, M. Arafa, Y. Abdelmonem, A.A. Nazeer, M.O. Amin, M. Madkour, The effect of surface charge on photocatalytic degradation of methylene blue dye using chargeable titania nanoparticles, Sci Rep. 8 (2018). https://doi.org/10.1038/s41598-018-25673-5.

[55] V.P. Madhurima, P.H. Borse, K. Kumari, T.N. Rao, P.K. Jain, Improved photocatalytic activity of carbon-based polymeric semiconductor for efficient decontamination of wastewater: Effect of reaction atmosphere and pyrolysis temperature, Opt Mater (Amst). 110 (2020). https://doi.org/10.1016/j.optmat.2020.110523.

[56] T. Liu, L. Wang, X. Lu, J. Fan, X. Cai, B. Gao, R. Miao, J. Wang, Y. Lv, Comparative study of the photocatalytic performance for the degradation of different dyes by ZnIn2S4: adsorption, active species, and pathways, RSC Adv. 7 (2017) 12292–12300. https://doi.org/10.1039/c7ra00199a.

[57] M. Sharma, S. Vaidya, A.K. Ganguli, Enhanced photocatalytic activity of g-C3N4-TiO2 nanocomposites for degradation of Rhodamine B dye, J Photochem Photobiol A Chem. 335 (2017) 287–293. https://doi.org/10.1016/j.jphotochem.2016.12.002.

Chapter 4

Synthesis of carbon nanomaterials through arc discharge method

4.1 Introduction

The state-of-the-art material, carbon nanotubes (CNTs) was first made by Sumio Iijima in 1991 by simple arc-plasma ablation of pure graphite electrodes in an inert atmosphere [1]. Since then, this new class of material has been tremendously explored and today after three decades of its discovery, still this material is studied and applied in various sectors of application around the globe. Besides, the formation of CNTs, the arc discharge technique is also utilized to synthesise carbon soot which essentially consists of fullerenes [2]. However, the separation and extraction of fullerenes from carbon soot is a laborious task and requires a special extraction setup and toxic solvents [3]. Therefore, in this work, the as-produced carbon soot is employed. The arc discharge is a conventional physical technique used to synthesise different carbon nanomaterials (CNMs) like nanotubes, fullerenes, carbon onions, etc. through a simple sublimation of graphite rods in an inert atmosphere. The major drawback of this method is the presence of an excess of graphitic nanoparticles along with CNMs. However, the quality of CNTs obtained from this technique is higher compared to other techniques due to their length and shape. In this case, sharp needle-like CNTs are obtained whereas in the chemical vapour deposition (CVD) technique, entangled and curly CNTs are observed.

CNTs due to their excellent electrical, mechanical, thermal, optical, and physicochemical properties [4] are widely explored in several fields of applications like automobile and aerospace industries [5], electrochemical devices [6], display panels, discharge tubes, and X-rays and microwave generators [7] and many more. Besides, CNTs are also actively used as adsorbents in water purification systems due to their surface properties [8]. Among these, the adsorption of toxic textile dyes from wastewater has always been a matter of concern and rigorous research has been done in the last decades [9–11]. Furthermore, the carbon soot obtained from various sources has been extensively used for pollutant adsorption studies [12–15].

Herein, we report a systematic approach for the optimization of process parameters for higher yields of carbon nanomaterial synthesis through the arc discharge method. The as-prepared samples were characterized using various techniques and discussed in this work.

4.2 Results and discussions

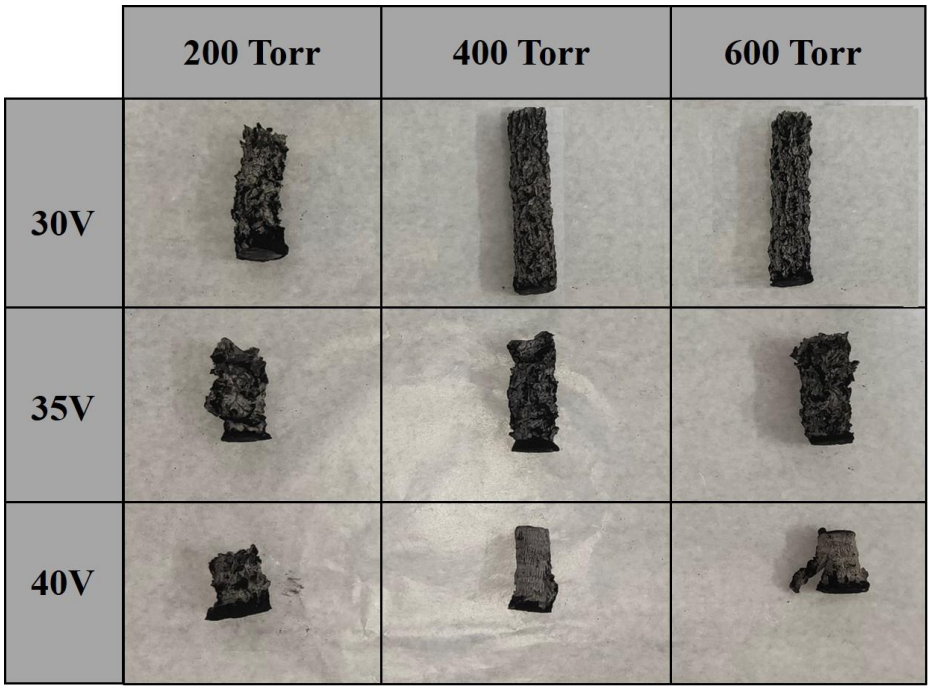

Figure 4.1 *Images of cathode deposits obtained at different pressure and voltage values.*

Figure 4.1 shows the image of the cathode deposits obtained at different voltages and pressure values. From this image few observations can be drawn: (1) at fixed voltage conditions, cathode deposit length initially increased with an increase in buffer gas pressure and beyond 400 Torr, a slight decrease in the length was observed. This could be ascribed to the function of gas pressure which is to facilitate momentum to the gaseous particles and to channelize the flow of ions between the electrodes. At low pressure, the yield is low because the ion density is low eventually leading to unstable plasma. However, at higher pressure, a greater amount of ions were involved in the plasma formation thereby blocking the movement of carbon vapours between the electrodes [16–18]. Therefore, the optimum range of He gas pressure for higher yields of CNTs synthesis was noticed to be ranging between 300 to 500 Torr. (2) At a given pressure condition, the deposit length showed inverse proportionality with applied voltage. The arc voltage is a crucial parameter as it is responsible for the electrical breakdown of the buffer gas. The applied voltage directly affects the arc current which is one of the significant process parameters in the arc discharge technique. The overall yield and quality of the nanotubes depend on the arc current. It results in electron emission from the cathode which travels with high velocity and sputter the target carbon source from the anode. The applied current generates

resistive heating of electrodes which leads to high temperatures. Due to this, the carbon source sublimes to form carbon vapours and nucleates at the cathode which is relatively cooler due to the cooling water supply and thus, results in nanotubes formation. Higher arc voltages lead to instability and frequent fluctuations of arc current values due to faster consumption of anode thus forming shorter deposits [19]. Below 30V, discontinuous arcing was noticed due to low ion density leading to unstable plasma resulting in lower yield and quality of nanotubes [20]. Therefore, an arc voltage of 30V could be optimum for higher yields of CNTs. Besides the formation of deposits during the arcing process, a notable amount of carbon soot was also generated. However, a very low yield (a few milligrams) of soot was produced at lower voltages (30 and 35V). But at 40V, soot yield was remarkably increased with pressure. This could be essentially due to the faster rates of anode erosion at higher arc currents thus resulting in higher amounts of soot generation than cathode deposit [21,22].

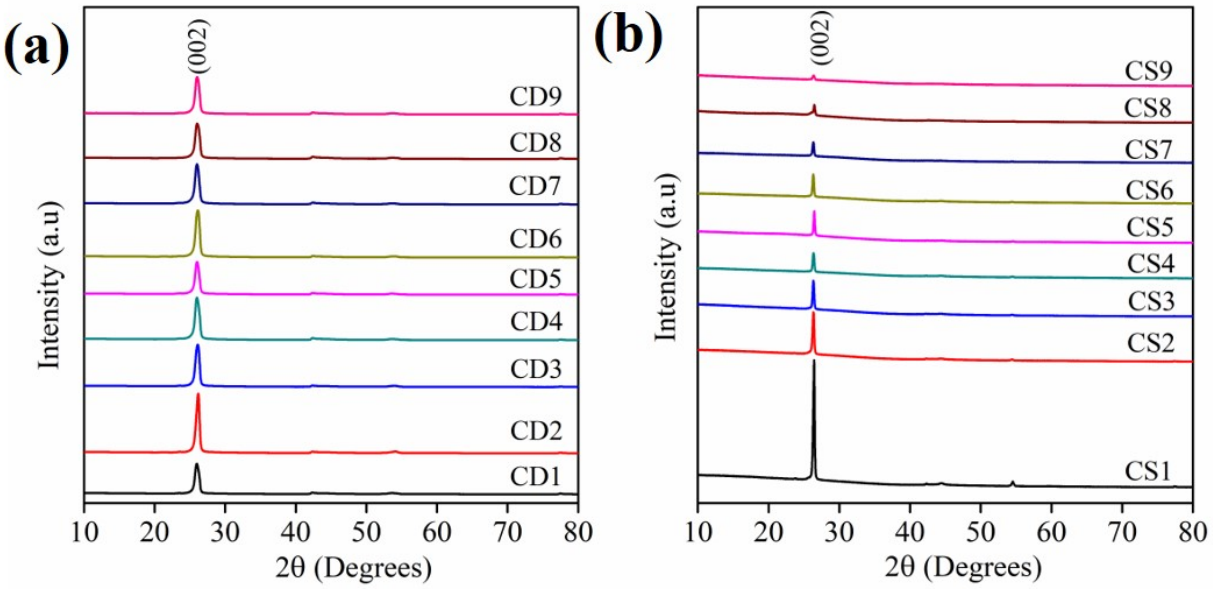

Figure 4.2 *XRD diffractogram pattern of (a) CD samples and (b) CS9 sample.*

The as-prepared samples were further analysed under XRD, Raman, FESEM and HRTEM to validate the above observations. Fig. 4.2(a) shows the XRD diffractogram of all the *CD* samples. It was noticed that all the samples displayed similar XRD patterns pertaining to MWNTs. However, the (002) peak intensity for the *CD2* sample was the highest among the set thus indicating higher orderliness of nanotubes stacking layers [23]. The XRD pattern of the *CD2* sample with peaks distributed around 26° (002), 42° (100), 44° (101), 54° (004) and 77° (006) attributed to the stacking of graphitic sheets, honeycomb lattice structure, in-plane regularities, and reflection from parallel basal hexagonal planes respectively [24]. The interlayer spacing (d) and the particle size (D) were calculated using Bragg's law and Debye-

Scherrer's formula respectively and were found to be 0.341 nm and 12.28 nm respectively for the *CD2* sample. Fig. 4.2(b) shows the stacking of XRD patterns of all *CS* samples. It was observed that one sharp intense peak around 26° associated with (002) hkl plane obtained due to the stacking of lamellar benzoic lattice decreased gradually with raise in voltage and pressure values [25] and the yield increased inversely. The XRD pattern of the *CS9* sample where two broad peaks at 26.5° (002) and 43.1° (100) were associated with graphitic peaks as discussed above and having a d-spacing of 0.337 nm and crystallite size of 1.82 nm. The broadness of the (002) peak can be ascribed to the amorphous nature of the arc soot [26]. Table 4.1 shows the FWHM of all the CD and CS samples. It can be observed that CD2 sample has lowest value which means the diameter of the nanotubes is higher in this case [27]. Further, all the CS samples showed lower FWHM values however, CS9 sample showed highest value which was attributed to the lower degree of crystallinity of the carbon soot material [28].

Table 4.1 Full width half maximum (FWHM) of CD & CS samples.

Sample	FWHM (β°)	Sample	FWHM (β°)
CD1	0.012	CS1	0.006
CD2	0.009	CS2	0.004
CD3	0.011	CS3	0.005
CD4	0.012	CS4	0.004
CD5	0.011	CS5	0.005
CD6	0.011	CS6	0.005
CD7	0.012	CS7	0.006
CD8	0.013	CS8	0.007
CD9	0.012	CS9	0.016

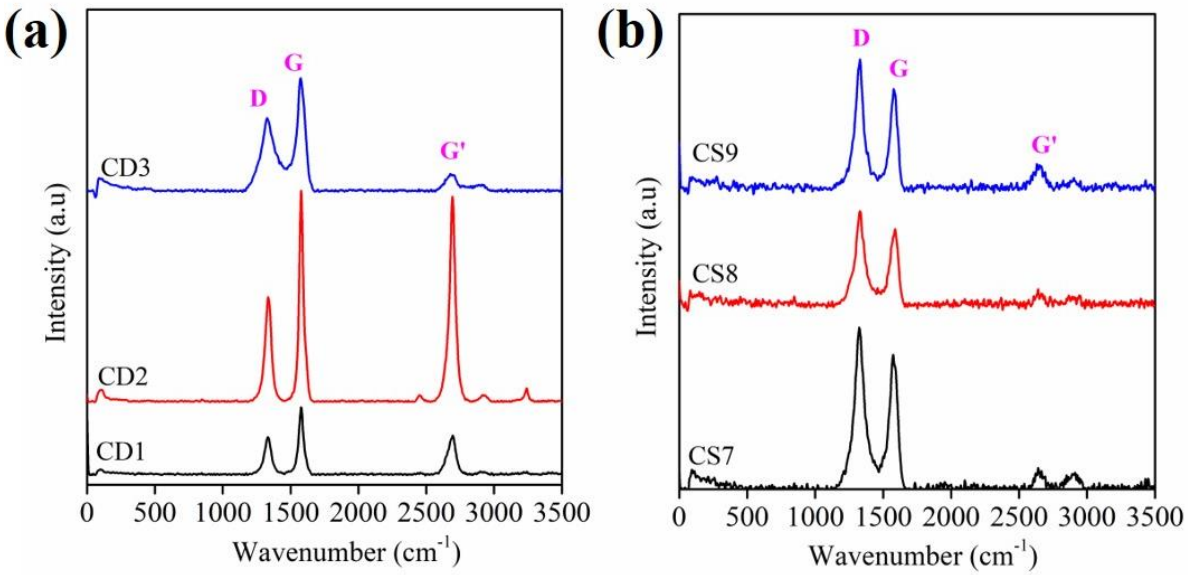

Figure 4.3 *Raman spectra of (a) CD1, CD2, and CD3 samples; (b) CS7, CS8, and CS9 samples.*

The Raman spectra of any of the carbon nanomaterial (Fig. 4.3) can be associated with three characteristic peaks obtained at 1335 cm^{-1}, 1579 cm^{-1}, and 2696 cm^{-1} which can be ascribed to; D-peak: the disorder peak connected with structural defects, G-peak: the graphitic resulted due to the vibration of sp^2 carbon atoms, and G' or 2D-peak: corresponds to the second overtone of the D peak respectively [29]. For *CD1, CD2*, and *CD3* samples (Fig. 4.3(a)), the ratio of the intensities of D peak to G peak (I_D/I_G) which is the measure of the graphitization index was lowest for the *CD2* sample as shown in Table 4.2. Similarly, the high I_{2D}/I_D ratio which is the measure of the overall crystalline quality of the graphite network and the high I_{2D}/I_G ratio which represents the long-range ordering of the graphite network are favourable for greater quality of nanotubes [30]. The new bands around G' peak can be attributed to the combination of D+G which corresponds to a defect-generated double resonance scattering process [31] or D+D' which is allowed via a defect-generated triple resonance process [32]. From Fig. 4.3(b), the comparable intensities of D and G peaks reveal that the arc soot consists of significant quantities of both graphitized and amorphous structures [33]. For all the samples, the I_D/I_G ratio was greater than 1 leading to strong disordering which was attributed to nano porosity [34].

Table 4.2 I_D/I_G, I_{2D}/I_G, and I_{2D}/I_D ratios of CD samples.

Sample	I_D/I_G	I_{2D}/I_G	I_{2D}/I_D
CD1	0.556	1.042	0.58
CD2	0.493	1.966	0.968
CD3	0.649	0.226	0.147

The microstructural and morphological studies of cathode deposits were carried out under FESEM and HRTEM. Fig. 4.4(a, b, and c) shows the FESEM micrographs of *CD1*, *CD2*, and *CD3* samples respectively. It was visible that the cathode deposit essentially contained a lot of impurities in the form of graphitic carbon particles [35]. This is a major drawback of arc discharge CNTs. However, the *CD2* sample had relatively higher amounts of CNTs. The length of the nanotubes was in the order of a few hundred microns and were highly crystalline having needle-like sharp tips. This is one of the advantages of arc discharge CNTs. Fig. 4.4(d, e, and f) shows the HRTEM images of the *CD2* sample displaying agglomerated clusters of carbon nanoparticles embedded with the CNTs and removing it has always been a tedious task. The CNTs structure observed in HRTEM very well supports the FESEM results. The SAED pattern shows blurred rings with bright spots on it depicting the polycrystalline nature of arc discharge CNTs. Fig. 4.5 shows the nanoscopic images of the *CS9* arc soot sample. The soot contained spherical nanocarbon particles with an average size between 50-100 nm that are highly amorphous as noticed from SAED diffused ring pattern [36].

The N_2 adsorption-desorption studies were done to investigate the specific surface area (SSA), pore size, and ore volume of the CNMs produced by arc discharge as shown in Fig. 4.6. All the samples possessed type IV isotherm essentially having abundant mesoporosity and followed H4 hysteresis [37,38]. The *CD* samples showed smaller SSA and pore volume as shown in Table 4.3 resulting in lower volume adsorption (Fig. 4.6(a)). Moreover, the *CS* samples showed remarkably high SSA values resulting in higher pore volumes and thereby better adsorption ability. Further, the pore size distribution curves (Fig. 4.6(Inset)) typically showed mesoporous richness in the case of both cathode deposit and carbon soot samples. However, slight microporosity can be observed in *CS* samples.

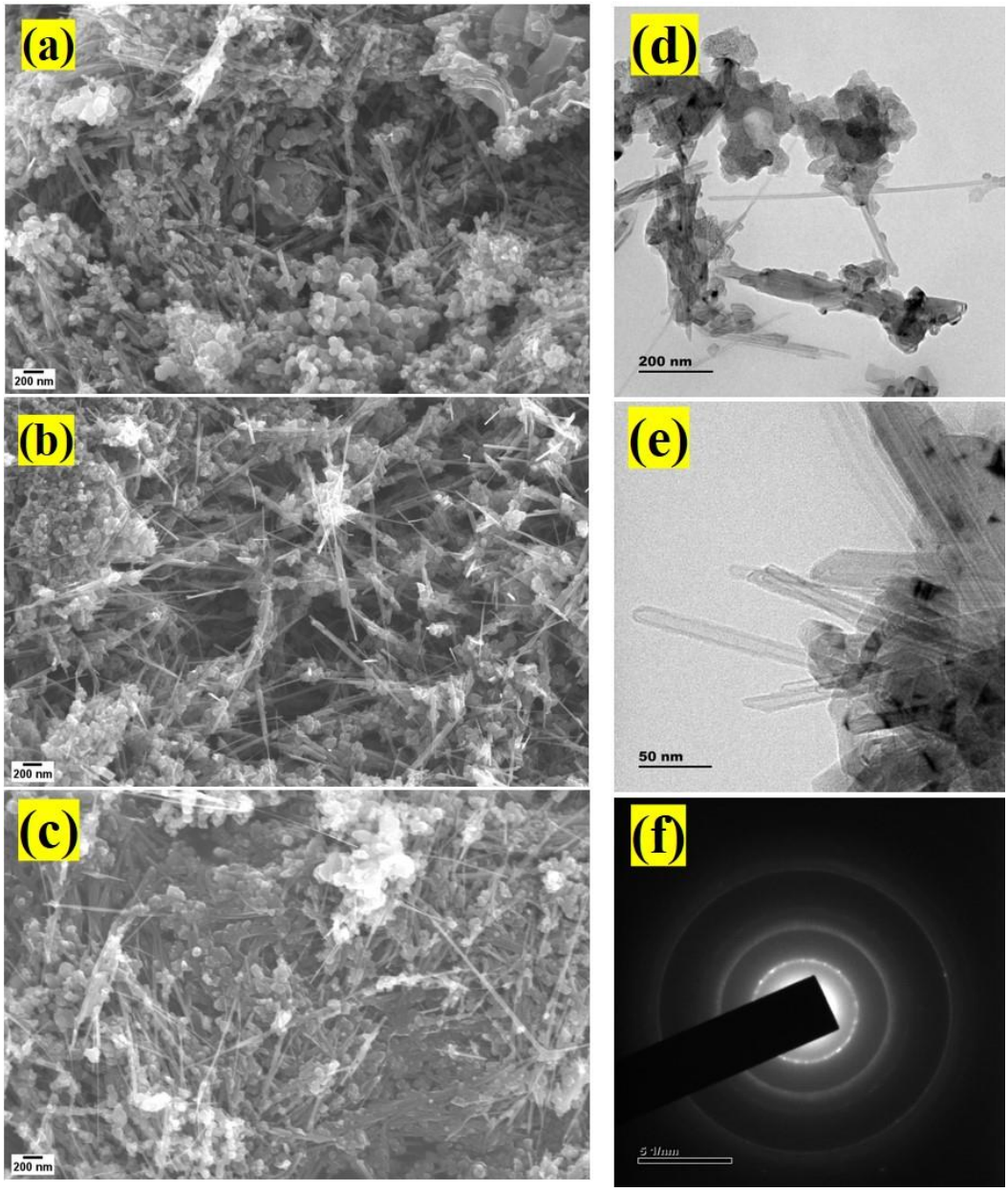

Figure 4.4 *FESEM micrographs of (a) CD1, (b) CD2, (c) CD3; (d & e) HR-TEM micrographs of CD2 sample and (f) SAED pattern of CD2 sample.*

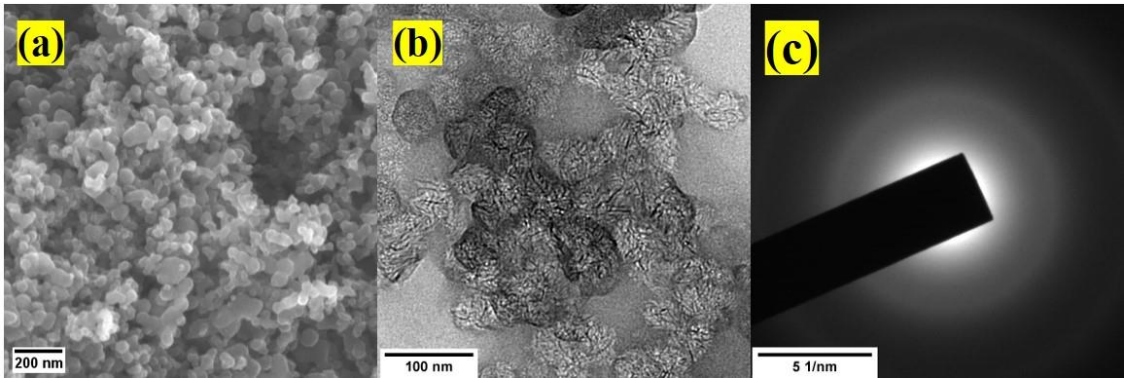

Figure 4.5 *(a)FESEM, (b) HRTEM, and (c) SAED pattern of CS9 sample.*

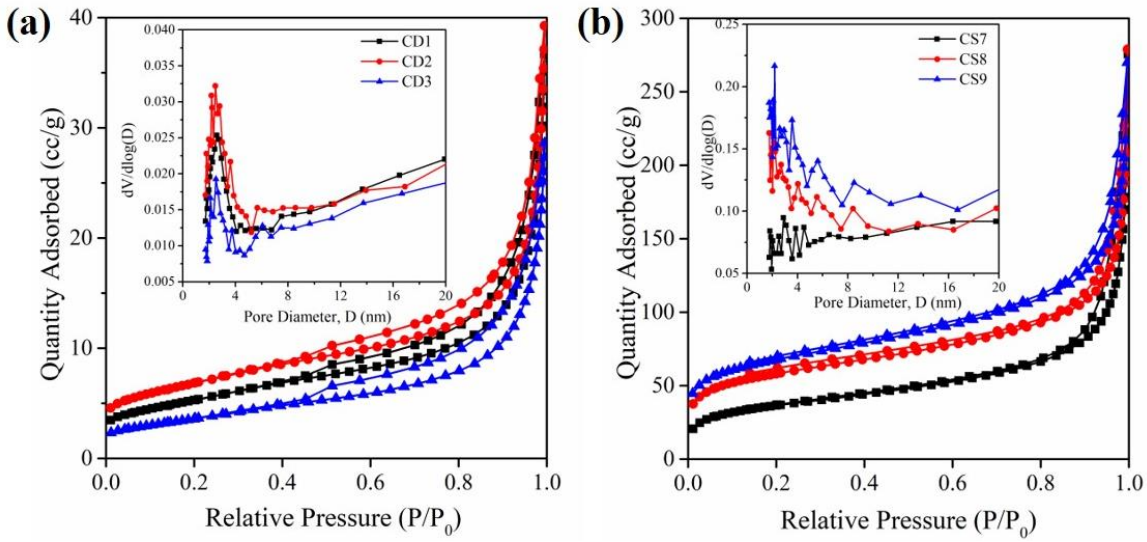

Figure 4.6 *N_2 adsorption-desorption isotherms and the insets showing the pore size distribution of (a) CD samples and (b) CS samples.*

Table 4.3 SSA, pore size and pore volume of CD and CS samples.

Sample	SSA (m^2/g)	Pore Size (nm)	Pore Volume (nm)
CD1	19	11.64	0.054
CD2	24	10.39	0.056
CD3	13	12.33	0.042
CS7	131	13.32	0.269
CS8	204	9.29	0.280
CS9	237	10.06	0.378

4.3 Conclusions

In summary, the present work focuses on the optimization of process parameters of the arc discharge technique for the synthesis of higher yield and quality of carbon nanotubes and carbon soot. Here, buffer gas pressure and arc voltage were optimized to [400 Torr, 30 V] and [600 Torr, 40 V] for obtaining higher yields of nanotubes and of carbon soot nanoparticles respectively with the help of various techniques like XRD, FESEM, HRTEM, Raman and BET.

References

[1] Y. Ando, X. Zhao, Y. Ando, X. Zhao, Synthesis of Carbon Nanotubes by Arc-Discharge Method, 2006.

[2] L.D. Lamb, D.R. Huffman, Fullerene production, Journal of Physics and Chemistry of Solids 54 (1993) 1635–1643. https://doi.org/10.1016/0022-3697(93)90277-X.

[3] D.H. Parker, K. Chatterjee, P. Wurz, K.R. Lykke, M.J. Pellin, L.M. Stock, J.C. Hemminger, Fullerenes and giant fullerenes: Synthesis, separation, and mass spectrometric characterization, Carbon N Y 30 (1992) 1167–1182. https://doi.org/10.1016/0008-6223(92)90060-A.

[4] R.B. Mathur, Carbon nanomaterials: Synthesis, structure, properties and applications, 2016. https://doi.org/10.1201/9781315371849.

[5] B. Ribeiro, E.C. Botelho, M.L. Costa, C.F. Bandeira, Carbon nanotube buckypaper reinforced polymer composites: A review, Polimeros 27 (2017) 247–255. https://doi.org/10.1590/0104-1428.03916.

[6] C. Gao, Z. Guo, J.H. Liu, X.J. Huang, The new age of carbon nanotubes: An updated review of functionalized carbon nanotubes in electrochemical sensors, Nanoscale 4 (2012) 1948–1963. https://doi.org/10.1039/c2nr11757f.

[7] Y. Saito, S. Uemura, Field emission from carbon nanotubes and its application to electron sources, Carbon N Y 38 (2000) 169–182. https://doi.org/10.1016/S0008-6223(99)00139-6.

[8] F.S.A. Khan, N.M. Mubarak, M. Khalid, Y.H. Tan, E.C. Abdullah, M.E. Rahman, R.R. Karri, A comprehensive review on micropollutants removal using carbon nanotubes-based adsorbents and membranes, J Environ Chem Eng 9 (2021). https://doi.org/10.1016/j.jece.2021.106647.

[9] T. Ahamad, M. Naushad, G.E. Eldesoky, S.I. Al-Saeedi, A. Nafady, N.S. Al-Kadhi, A.H. Al-Muhtaseb, A.A. Khan, A. Khan, Effective and fast adsorptive removal of toxic cationic dye (MB) from aqueous medium using amino-functionalized magnetic multiwall carbon nanotubes, J Mol Liq 282 (2019) 154–161. https://doi.org/10.1016/j.molliq.2019.02.128.

[10] O.A. Shabaan, H.S. Jahin, G.G. Mohamed, Removal of anionic and cationic dyes from wastewater by adsorption using multiwall carbon nanotubes, Arabian Journal of Chemistry 13 (2020) 4797–4810. https://doi.org/10.1016/j.arabjc.2020.01.010.

[11] M. Saxena, N. Sharma, R. Saxena, Highly efficient and rapid removal of a toxic dye: Adsorption kinetics, isotherm, and mechanism studies on functionalized multiwalled carbon nanotubes, Surfaces and Interfaces 21 (2020). https://doi.org/10.1016/j.surfin.2020.100639.

[12] Gunture, J. Kaushik, A.K. Garg, D. Saini, P. Khare, S.K. Sonkar, Pollutant Diesel Soot Derived Onion-like Nanocarbons for the Adsorption of Organic Dyes and Environmental Assessment of Treated Wastewater, Ind Eng Chem Res 59 (2020) 12065–12074. https://doi.org/10.1021/acs.iecr.0c01267.

[13] V.P. Singh, R. Vaish, Adsorption of dyes onto candle soot: Equilibrium, kinetics and thermodynamics, Eur Phys J Plus 133 (2018). https://doi.org/10.1140/epjp/i2018-12212-x.

[14] V.P. Singh, R. Singhal, R. Vaish, Optimization of dye removal by diesel exhaust emission soot using response surface methodology, Environ Prog Sustain Energy 39 (2020). https://doi.org/10.1002/ep.13419.

[15] H.F. El-Gamal, F.K.M. Wali, K.H. Khalil, Thermodynamic Parameters For Adsorption of Some Disperse Dyes From Industrial Wastewater on Carbon Soot, 2014. http://www.journalijar.com.

[16] E.I. Waldorff, A.M. Waas, P.P. Friedmann, M. Keidar, Characterization of carbon nanotubes produced by arc discharge: Effect of the background pressure, J Appl Phys 95 (2004) 2749–2754. https://doi.org/10.1063/1.1642737.

[17] T. Zhao, Y. Liu, J. Zhu, Gas and pressure effects on the synthesis of amorphous carbon nanotubes, Chinese Science Bulletin 49 (2004) 2569–2571. https://doi.org/10.1360/04we0132.

[18] H.H. Kim, H.J. Kim, Preparation of carbon nanotubes by DC arc discharge process under reduced pressure in an air atmosphere, Mater Sci Eng B Solid State Mater Adv Technol 133 (2006) 241–244. https://doi.org/10.1016/j.mseb.2006.06.017.

[19] S. Scalese, V. Scuderi, S. Bagiante, F. Simone, P. Russo, L. D'Urso, G. Compagnini, V. Privitera, Controlled synthesis of carbon nanotubes and linear C chains by arc discharge in liquid nitrogen, J Appl Phys 107 (2010). https://doi.org/10.1063/1.3275500.

[20] S. Scalese, V. Scuderi, S. Bagiante, S. Gibilisco, G. Faraci, V. Privitera, Order and disorder of carbon deposit produced by arc discharge in liquid nitrogen, J Appl Phys 108 (2010). https://doi.org/10.1063/1.3475726.

[21] M. Caraman, G. Lazar, M. Stamate, I. Lazar, Arc discharge instalation for fullerene production, Romanian Reports of Physics 53 (2008) 273–278.

[22] G.N. Churilov, Synthesis of fullerenes and other nanomaterials in arc discharge, in: Fullerenes Nanotubes and Carbon Nanostructures, 2008: pp. 395–403. https://doi.org/10.1080/15363830802281641.

[23] T. Belin, F. Epron, Characterization methods of carbon nanotubes: A review, Mater Sci Eng B Solid State Mater Adv Technol 119 (2005) 105–118. https://doi.org/10.1016/j.mseb.2005.02.046.

[24] R. Das, S. Hamid, Md. Ali, S. Ramakrishna, W. Yongzhi, Carbon Nanotubes Characterization by X-ray Powder Diffraction – A Review, Curr Nanosci 11 (2014) 23–35. https://doi.org/10.2174/15734137106661408182100 43.

[25] J.C. Scanlon, L.B. Ebert, X-ray diffraction study of fullerene soot, Journal of Physical Chemistry 97 (1993) 7138–7140. https://doi.org/10.1021/j100130a004.

[26] N. Komatsu, T. Ohe, K. Matsushige, A highly improved method for purification of fullerenes applicable to large-scale production, Carbon N Y 42 (2004) 163–167. https://doi.org/10.1016/j.carbon.2003.10.009.

[27] D.K. Singh, P.K. Iyer, P.K. Giri, Diameter dependence of interwall separation and strain in multiwalled carbon nanotubes probed by X-ray diffraction and Raman scattering studies, Diam Relat Mater 19 (2010) 1281–1288. https://doi.org/10.1016/j.diamond.2010.06.003.

[28] Y.C. Chiang, W.H. Lin, Y.C. Chang, The influence of treatment duration on multi-walled carbon nanotubes functionalized by H 2 SO 4 /HNO 3 oxidation, Appl Surf Sci 257 (2011) 2401–2410. https://doi.org/10.1016/j.apsusc.2010.09.110.

[29] L. Bokobza, J.-L. Bruneel, M. Couzi, Raman Spectra of Carbon-Based Materials (from Graphite to Carbon Black) and of Some Silicone Composites, C (Basel) 1 (2015) 77–94. https://doi.org/10.3390/c1010077.

[30] S. Santangelo, G. Messina, G. Faggio, M. Lanza, C. Milone, Evaluation of crystalline perfection degree of multi-walled carbon nanotubes: Correlations between thermal kinetic analysis and micro-Raman spectroscopy, Journal of Raman Spectroscopy 42 (2011) 593–602. https://doi.org/10.1002/jrs.2766.

[31] R. Saito, M. Hofmann, G. Dresselhaus, A. Jorio, M.S. Dresselhaus, Raman spectroscopy of graphene and carbon nanotubes, Adv Phys 60 (2011) 413–550. https://doi.org/10.1080/00018732.2011.582251.

[32] A.C. Ferrari, D.M. Basko, Raman spectroscopy as a versatile tool for studying the properties of graphene, Nat Nanotechnol 8 (2013) 235–246. https://doi.org/10.1038/nnano.2013.46.

[33] G. Xu, H. Niwa, T. Imaizumi, H. Takikawa, T. Sakakibara, K. Yoshikawa, A. Kondo, S. Itoh, Carbon nanoballoon produced by thermal treatment of arc soot, New Diamond and Frontier Carbon Technology 15 (2005) 73–81. chrome-extension://efaidnbmnnnibpcajpcglclefindmkaj/https://myukk.xsrv.jp/free_journal/download.php?fn=NDFCT476_full.pdf.

[34] Y. Raitses, C.H. Skinner, F. Jiang, T.S. Duffy, Raman spectroscopy of carbon dust samples from NSTX, Journal of Nuclear Materials 375 (2008) 365–369. https://doi.org/10.1016/j.jnucmat.2008.01.012.

[35] Y.A. Iijima, Preparation of Carbon Nanotubes by Arc-Discharge Evaporation, Jpn J Appl Phys 32 (1993) L107. https://doi.org/10.1143/JJAP.32.L107.

[36] D. Zhang, K. Ye, Y. Yao, F. Liang, T. Qu, W. Ma, B. Yang, Y. Dai, T. Watanabe, Controllable synthesis of carbon nanomaterials by direct current arc discharge from the inner wall of the chamber, Carbon N Y 142 (2019) 278–284. https://doi.org/10.1016/j.carbon.2018.10.062.

[37] K.S.W. Sing, Reporting physisorption data for gas/solid systems with special reference to the determination of surface area and porosity (Recommendations 1984), Pure and Applied Chemistry 57 (1985) 603–619. https://doi.org/10.1351/pac198557040603.

[38] J.C. Groen, L.A.A. Peffer, J. Pérez-Ramírez, Pore size determination in modified micro- and mesoporous materials. Pitfalls and limitations in gas adsorption data analysis, Microporous and Mesoporous Materials 60 (2003) 1–17. https://doi.org/10.1016/S1387-1811(03)00339-1.

Chapter 5

Arc discharge-derived carbon nanomaterials-based hybrid photocatalysts for RhB dye photodegradation studies

5.1 Introduction

Among all the known photocatalytic materials, graphitic carbon nitride (g-C_3N_4 or CN) has emerged as a star performer due to its visible-light activity, metal-free composition, 2D layered morphology, ideal band gap value (~ 2.7 eV), and large surface area [1–3]. Due to these outstanding properties, g-C_3N_4 photocatalyst is used in water splitting, energy storage, environmental remediation, H_2 evolution, CO_2 reduction and several other applications [4–6]. Unfortunately, the performance of g-C_3N_4 is majorly restricted by fast recombination rates of photo-generated charges thus limiting its practical application [7]. To overcome this situation, the construction of semiconductor heterostructures has proven to be an effective way. Several binary or ternary heterostructures have been developed and tested. However, the metal ions or other harmful elements doped in these structures are likely to be released into water during photodegradation experiments [8]. Meanwhile, CNMs due to their non-toxicity and exceptional properties have gained widespread attention. CNMs have excellent electron affinity and high chemical inertness which makes them good electron acceptor species and this nature can be effectively utilised to achieve greater charge separation efficiencies in the g-C_3N_4 hybrid photocatalyst materials [9]. Several carbon-based photocatalyst materials are available commercially thus, proving their significance in enhancing photocatalytic performance [10][11].

In this work, CNMs (Carbon Soot and MWCNTs) exclusively made from the conventional arc discharge method are utilized in making g-C_3N_4-based hybrid photocatalysts. Carbon soot is a non-crystalline CNM with remarkably high surface area and pore volume which is mainly exploited in this study. Some of the works focusing on sphere-like CNMs based on g-C_3N_4 materials used in heterogenous photocatalysis are discussed here. Martinez J.P.C and group [12], have prepared g-C_3N_4/ Carbon Sphere composite through hydrothermal synthesis having a visible region band gap for removal of Chromium [Cr (VI)] from water. After 4 hrs of light irradiation, 82% (100 ppm conc.) of the metal ions were removed from the water (pH2). Another group [13], fabricated a g-C_3N_4/C_{60} hybrid photocatalyst via a solid-state

mechanochemical route and used it for hydrogen production. It was observed that the hybrid photocatalyst has produced 4 times higher amounts of H_2 than that of the pristine g-C_3N_4 photocatalyst. On the other hand, CNT is a 1D CNM having an outstanding aspect ratio, extremely good surface area to volume ratio, abundant surface reactive sites for electron trapping and good chemical stability [14]. Thus, CNT stands out to be an appropriate filler material that meets the requirements as discussed earlier. Many research groups across the world have worked on CNT-based g-C_3N_4 photocatalysts for wastewater detoxification studies. Ding. F and co-workers, fabricated CNT/ g-C_3N_4 nanocomposite using melamine-cyanuric acid precursor via a one-pot method. Here, 2% weight loading of CNTs showed complete degradation in 1 hour under visible light. The target pollutant used in this case was Rhodamine B (RhB) solution (30 mL, 10 mg/L) with 30 mg of photocatalyst loaded in it [15]. Another group Wang. C, *et. al*., developed a novel electrochemical sensor consisting of CNTs and g-C_3N_4 on a glassy carbon electrode [16]. The fabricated electrode exhibited excellent response in the detection of dopamine, uric acid, and tryptophan levels.

Herein, we address a systematic approach in preparing the g-C_3N_4/CS and g-C_3N_4/MWCNT hybrid photocatalysts with varying weight loading percentages of CS and MWCNTs in g-C_3N_4 from 0.1 to 1% separately. The as-prepared hybrid samples showed lower PL intensity, thus resulting in effective charge separation, and achieving higher photodegradation efficiency under visible light.

5.2 Results and discussions

5.2.1 C-Soot/g-C_3N_4 hybrid photocatalyst for RhB photodegradation studies

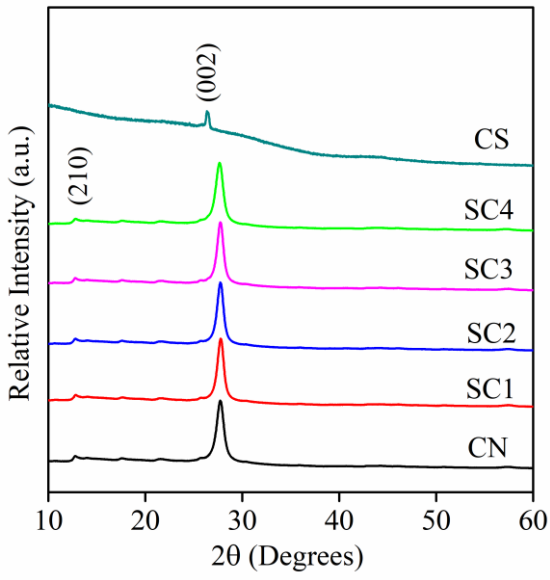

Figure 5.1 *XRD diffractograms of CN, CS, and SC samples.*

The structural properties and phase information of the as-synthesized materials were investigated by studying the X-ray diffractogram (Fig. 5.1). It was observed that all the *SC* samples retained a similar diffraction pattern as that of the pristine *CN* sample maintaining two significant peaks around 12.8° and 27.7° associated with the in-plane distance between the heptazine moieties, (210) plane and inter-plane distance between the stacking structure, (002) plane respectively matching with the ICDD PDF: 00-066-0183 pattern [17]. The *CS* sample showed a small peak at 26.3° associated with the (002) plane arising due to the stacking of a lamellar benzoid lattice, a commonly found signature peak in all graphitic carbon materials [18]. The interlayer distance, d (nm) and crystallite size, D (nm) were calculated using Bragg's law and Scherrer's formula respectively. The 'd' and 'D' values for the *CS* sample were calculated to be 0.338 nm and 18.75 nm whereas for the *CN* sample, it was found to be 0.325 nm and 7.6 nm respectively for the (002) plane. Moreover, it was noticed that the average 'd' and 'D' values of all the *SC* samples were obtained to be 0.321 nm and 10.02 nm respectively. This increase in the crystallite size was evident because of the incorporation of soot nanoparticles however, it did not alter the primary structure of the g-C_3N_4 material.

The surface morphology and microstructure information were evaluated using FESEM and HRTEM (Fig. 5.2). From the FESEM micrograph of the *CN* sample, a large flake-like surface was observed. However, HRTEM gave a clearer image where a thin sheet-like structure with folded edges was noticed and possessed a diffused SAED ring pattern (Fig. 5.2(a, b)) implying weak crystallinity [19]. Fig .5.2(c, d) shows the SEM and TEM micrographs of carbon soot particles. Huge clusters of spherical particles were observed in SEM whereas crushed paper-ball-like morphology was seen under HRTEM which were highly non-crystalline as confirmed by the SAED pattern [20]. The average particle size was typically between 50-100 nm as observed from these micrographs. Fig. 5.2(e, f) shows the micrograph of the *SC1* sample. Here, the FESEM image was similar to that of the *CN* sample showing platelet-like layered morphology however, TEM showed high-resolution images where tiny soot particles were evenly embedded in the g-C_3N_4 sheets as observed in the similar report [21].

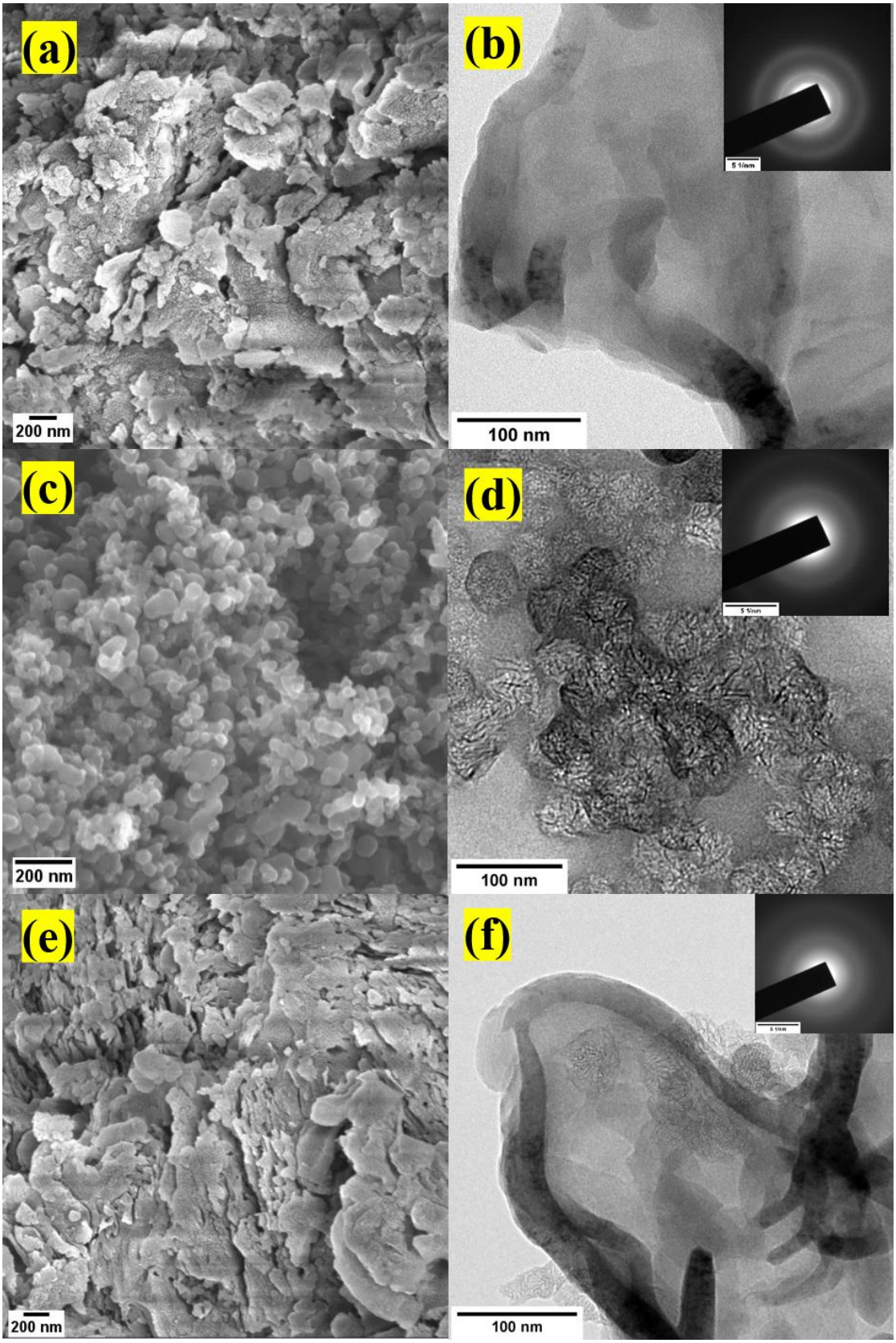

Figure 5.2 *FESEM and HRTEM micrographs with SAED pattern (inset) of CN (a, b), CS (c, d) and SC1 (e, f), respectively.*

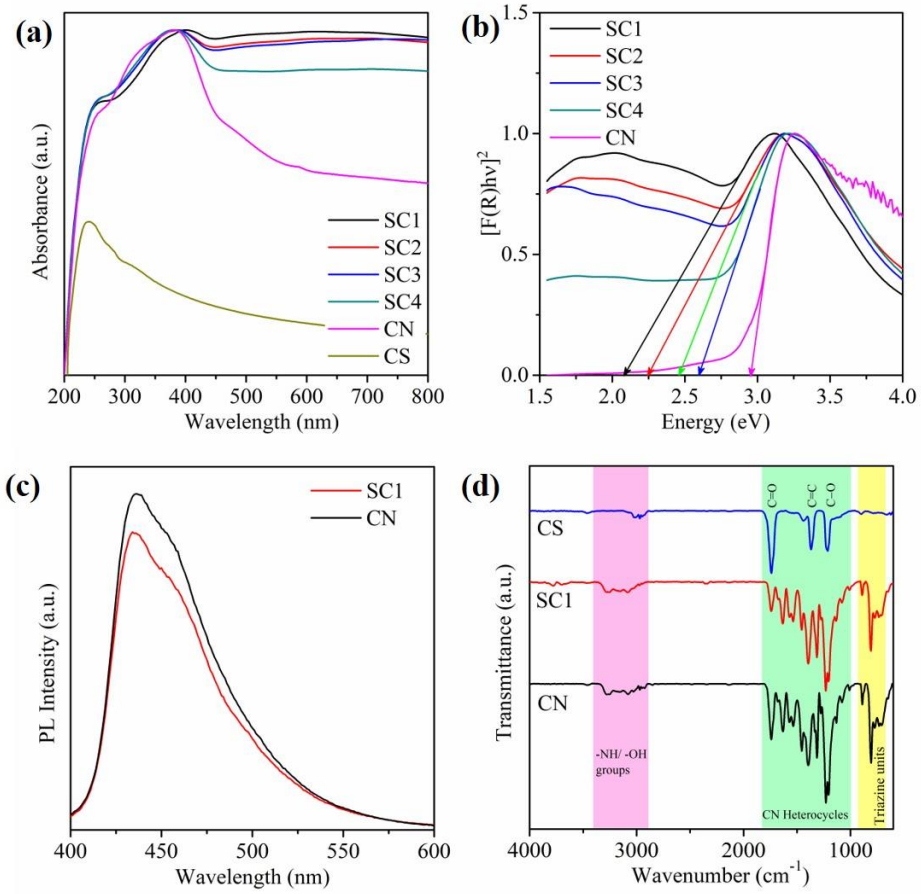

Figure 5.3 *(a) UV-DRS spectra, (b) the KM plot, (c) the PL spectra and (d) the FTIR spectra of CN, CS, and SC samples.*

The UV-DRS studies of all the as-prepared samples (Fig. 5.3(a)) revealed that the addition of carbon soot increased the absorbance edge in the visible region which is evident with the slight red shift in the absorbance spectra of the *SC* samples [22]. Besides, the bare *CS* sample has maximum absorbance in the ultraviolet region and extends into the visible region. The energy band gap of all the photocatalyst material was obtained by drawing the KM Plot as shown in Fig. 5.3(b). The energy band gap values of *SC1* and *CN* samples were estimated to be 2.08 eV and 2.96 eV respectively. The lower band gap values in all the *SC* samples than the pristine *CN* sample were due to the increased crystallite size that resulted from the addition of soot nanoparticles [23]. The photogenerated charge carrier behaviour was examined with the help of PL spectroscopy (Fig. 5.3(c)). It was seen that the nanocomposite sample *SC1* showed reduced PL intensity than the *CN* sample. This was essentially due to the incorporation of soot nanoparticles which generate intermediate metastable states resulting in increased lifetime of the charge carriers [24]. The FTIR spectra of *CN*, *SC1*, and *CS* samples are shown in Fig. 5.3(d). The pure g-C_3N_4 sample showed strong vibrational bands around 800 cm^{-1} attributed to out-of-plane bending vibrations of triazine units [25], bands between 1000 – 1800 cm^{-1} were assigned to stretching modes of CN heterocyclic structures [26] and the bands around 3200 cm^{-1} were designated to adsorbed -OH and uncondensed -NH groups [27]. Meanwhile, the FTIR spectrum

of the *CS* sample displayed three moderate peaks around 1223 cm^{-1}, 1370 cm^{-1}, and 1738 cm^{-1} which could be assigned to C – O, C = C, and C = O respectively [28]. Due to the minute addition of carbon soot, the hybrid photocatalyst essentially retained the original vibrational band structure of the pristine *CN* sample [29].

The XPS studies were carried out to obtain the elemental composition and chemical bonding information of *CN*, *CS*, and *SC1* samples (Fig. 5.4). From the wide scan spectra, it was discovered that the *CN* and *SC1* samples essentially contained C, N, and O elements only (Fig. 5.4(a)) and *CS* sample contained C and O elements. The deconvoluted C1s spectra (Fig. 5.4(b)) of *CN* and *SC1* samples showed three similar peaks at ~ 284 eV, ~ 288 eV, and ~ 293 eV assigned to the C – C bond (photoelectronic line of C), C = N – C (sp^2 carbon in CN network), and C – NH_2 (carbon attached to the uncondensed amine groups) respectively [30]. Furthermore, the deconvoluted N1s spectra (Fig. 5.4(c)) of *CN* and *SC1* samples displayed three similar peaks at ~ 398 eV, ~ 400 eV, and ~ 404 eV typically attributed to sp^2 hybridised 'N' bonded to 'C' (N – C = N, pyridinic N), sp^3 hybridised N in CN architecture (N – (C)3), and terminal –NH groups respectively [31]. For the *CS* sample, the C1s spectrum had two peaks, one at ~ 284 eV attributed to graphitic carbon, (C=C) and a minor peak due to π – π* interactions. All the samples showed a small peak at ~ 532 eV due to surface-adsorbed moisture or oxygen (Fig. 5.4(d)) [32]. From Table 5.1, it can be confirmed that no substantial changes were manifested with the addition of carbon soot nanoparticles. As the C/N ratio is essentially constant for the hybrid photocatalyst.

Table 5.1 Elemental composition of CN, CS and SC1 samples.

Sample	C1s (%)	N1s (%)	C/N Ratio	O1s (%)
CN	44.48	53.01	0.83	2.51
SC1	44.03	52.6	0.83	3.37
CS	85.34	-	-	14.66

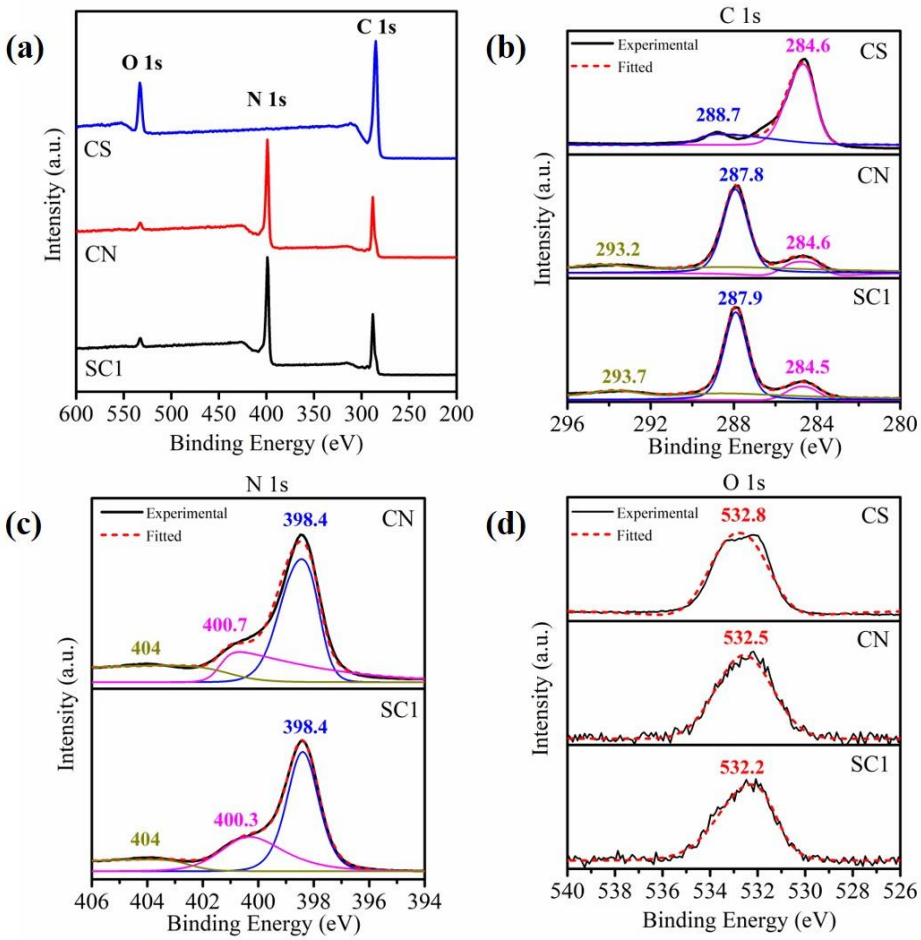

Figure 5.4 *XPS spectra of CN, CS, and SC1 samples.*

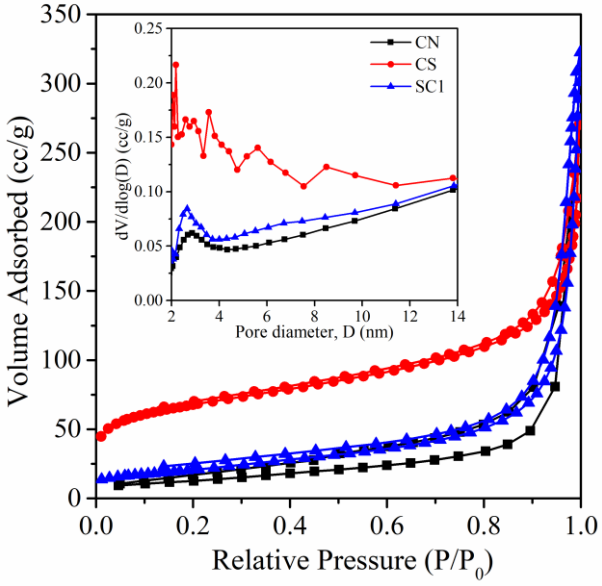

Figure 5.5 *N_2 adsorption-desorption isotherms with the inset showing pore radii distribution of CN, CS, and SC1 samples.*

The BET surface area and pore size distribution of *CN*, *SC1*, and *CS* samples were calculated by studying the N_2 adsorption-desorption equilibrium behaviour (Fig. 5.5). It was

perceived that all the samples typically contained mesoporous structures which was evident by the Type – IV isotherm and followed H4 hysteresis loop [33]. The pore size distribution also confirms the mesoporosity of the samples (Fig. 4.11 Inset) where the *CS* sample has a majority of mesoporous structures [34]. The specific surface area (SSA), pore width and volume values are tabulated in Table 5.2. Due to the high SSA of *CS*, just by adding 0.1 % weight percentage of soot, the SSA remarkably increased to 75 m^2/g (*SC1*). Thus, larger surface areas promote better photocatalytic activity [35].

Table 5.2 SSA, average pore width and volume of CN, CS, and SC1 samples.

Sample	SSA, (m^2/g)	Pore Width D (nm)	Pore Volume V (cc/g)
CN	69	21.35	0.365
SC1	75	20.55	0.378
CS	237	10.06	0.426

The zeta potential (ZP) studies are used to find the surface charge potential on the photocatalyst material which essentially decides the target pollutant adsorption and thereby degradation efficiency. The net surface charge on g-C_3N_4 material is determined based on the interactions between photogenerated charges and the primary, secondary, and ternary amine groups present in the g-C_3N_4 structure [36]. The ZP vs pH curve gives information about the effect of pH on the surface charge polarity [37]. From Fig. 5.6, it can be commented that with an increase in the pH of the solution, the surface charge changes from positive to negative potential. At neutral pH, essentially *CN* and *SC1* samples have negative ZP which implies that the surface of the photocatalyst is negatively charged. Therefore, a cationic pollutant can be easily degraded in this case.

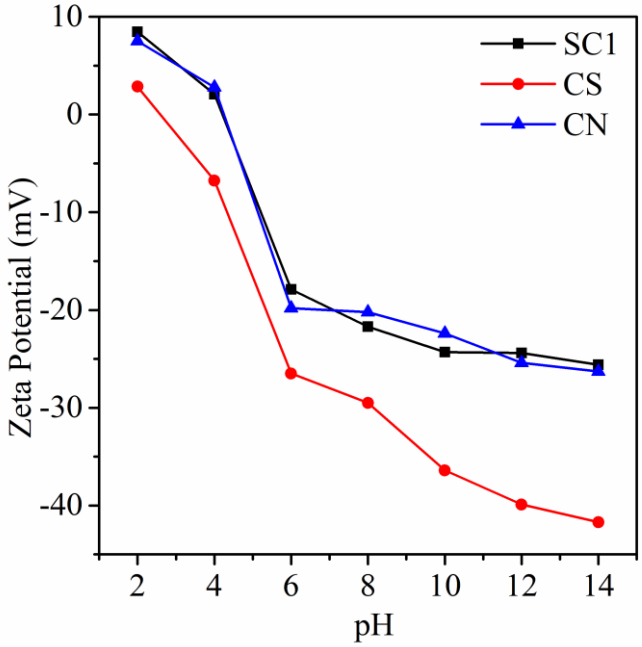

Figure 5.6 *Zeta potential values at various pH values of CN, CS, and SC1 samples.*

The photocatalytic performance was evaluated by studying RhB photodegradation as shown in Fig. 5.7(a). The removal efficiencies of *SC1, SC2, SC3, SC4, CN*, and *CS* samples were 97 %, 58 %, 28 %, 31 %, 88 %, and 72 % respectively in 90 minutes of light illumination. The 0.1% loaded sample showed maximum photodegradation among all the samples. However, the gradual increase in carbon soot content drastically decreased the performance. This was attributed to the limited exposure of light on the photocatalyst due to the presence of excess soot particles in the nanocomposite material [35]. Besides, the *CS* sample showed notable efficiency which was basically due to the high SSA value that resulted in the adsorption of dye molecules on the soot particles. The rate of reaction of all the photocatalyst samples was obtained by applying pseudo – 1^{st} order kinetics equation [$\ln C/C_0 = -kt$, where k (min^{-1}) is the rate constant] as shown in Fig. 5.7(b). It was noticed that the *SC1* sample degradation rate was 1.44 times faster than the pristine *CN* sample. This was due to the addition of carbon soot nanoparticles. The present work has been compared with some of the previously reported works using different pollutants as given in Table 5.3.

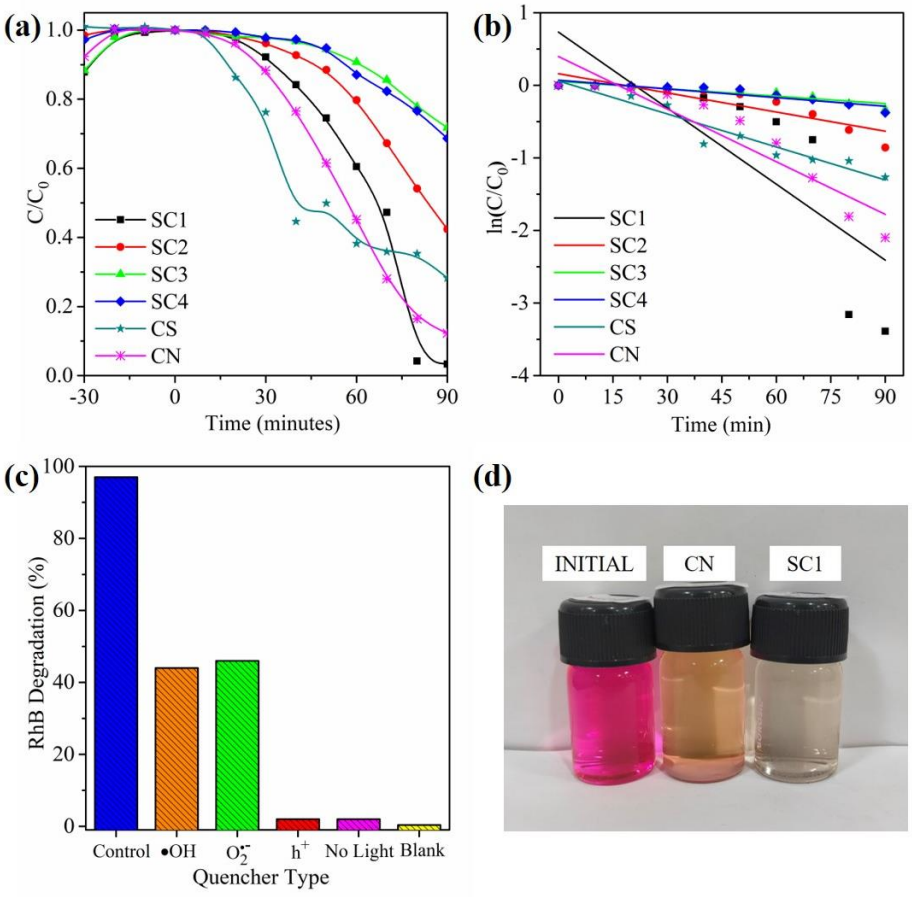

Figure 4.13 *(a) Dye degradation studies of all the samples, (b) 1st-order reaction kinetics curve of all the samples, (c) radical trapping experiment of SC1 sample using different trapping agents, and (d) RhB dye solution images post photodegradation experiment.*

Table 5.3 Comparative study of present work with some of the C/ g-C_3N_4 published literature.

S. No.	Spherical CNMs Loading (%)	Target Pollutant	Target Conc. (mg/L)	Time (Minutes)	Degradation (%)	Ref. No.
1	-	Cr (IV)	75	240	~100	[46]
2	0.3	RhB	10	60	~100	[53]
3	2	RhB	5	40	91	[66]
4	1	RhB	5	60	97	[69]
5	0.03	MB	3	300	-	[70]
6	**0.1**	**RhB**	**20**	**90**	**97**	**This Work**

The degradation mechanism was further explored by conducting radical quenching experiments (Fig. 5.7(c)). Here, 10 mM each of Ammonium Oxalate, (AO) p-Benzoquinone (pBQ), and Isopropanol (IPA) were added to the dye solution to quench the photogenerated

holes (h^+), superoxide anion ($\bullet O_2^-$), and hydroxyl radical (•OH) respectively. It was discovered that with the addition of a h^+ scavenger, the removal efficiency dropped to 2 % whereas when $\bullet O_2^-$ and •OH scavenging agents were added, and the removal percentage dropped to 46 % and 44 % respectively. On this note, it can be said that h^+ majorly influenced the photodegradation process followed by superoxide and hydroxyl radicals. The image of the final colour of *CN* and *SC1* sample solutions after the photodegradation experiment is shown in Fig. 5.7(d). Clearly, the solution treated with *SC1* became colourless whereas *CN* treated solution was slightly coloured.

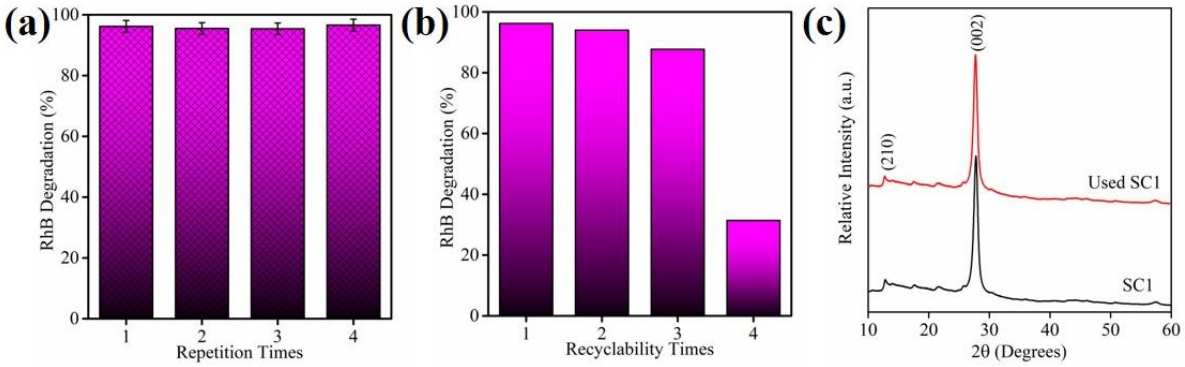

Figure 5.8 *(a, b) Repeatability and recyclability of CC1 photocatalyst sample for RhB degradation and (c) XRD pattern of SC1 sample before and after photodegradation experiments.*

The consistency and stability of the material were studied by doing repeatability and reusability tests as displayed in Fig. 5.8(a, b). For four times consecutively, the degradation efficiency remained constant and during the reusability study, up to three cycles, there was a minute drop in the overall efficiency however, in the fourth cycle the efficiency dropped to 30 %. This could be majorly due to the loss of material during the collection and drying process. Furthermore, the XRD pattern of the used *SC1* sample showed an identical pattern to that of the fresh *SC1* sample (Fig. 5.8(c)) which implies that the structural characteristics were essentially unperturbed post-experiment.

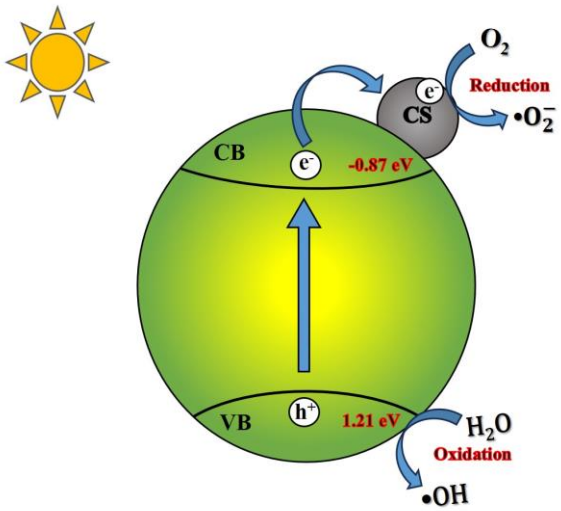

Figure 5.9 *A possible mechanism for RhB degradation in the SC1 sample.*

Based on the above results, a plausible degradation mechanism is proposed as shown in Fig. 5.9. In general, when the light of required energy is incident on the photocatalyst material, electron-hole pairs ($e^- - h^+$) are generated and the e^- gets excited to conduction band (CB) from the valence band (VB) leaving behind a hole void in the VB which eventually participate in photo redox reactions. Simultaneously, a large portion of charge carriers are recombined resulting in low performance. To overcome this problem, nanocomposites are developed that contain a small fraction of electron-accepting species like carbon nanomaterials. Due to the incorporation of carbon soot nanoparticles in this case, the photoelectrons are easily delocalised in the honeycomb structure of the soot nanoparticles facilitating a synergistic charge separation and transportation [38]. The transferred electrons will presumably migrate towards the surface and capture the surface-bound oxygen molecules to produce superoxide radicals and thus participate in photocatalytic reactions [39].

5.2.2 MWCNTs/g-C_3N_4 hybrid photocatalyst for RhB photodegradation studies

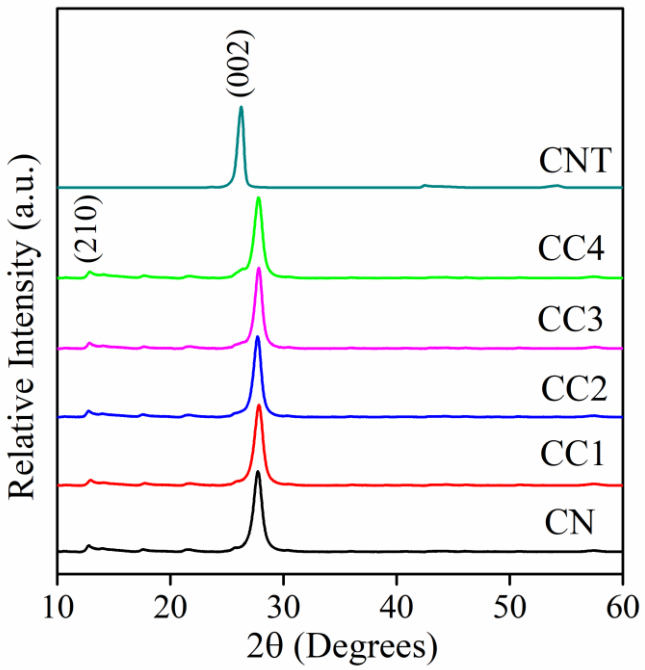

Figure 5.10 *XRD diffractograms of CN, CNT, and CC samples.*

The crystallographic structural information was investigated via XRD studies as shown in Fig. 5.10. It was noticed that the raw *CN* sample showed significant fingerprint peaks at 12.8° and 27.7° designated to (210) and (002) planes and typically matches the reference ICDD PDF: 00-066-0183 pattern and assumes orthorhombic crystal structure [40]. Further, the *CNT* sample possessed one prominent peak at 26.2° corresponding to the (002) plane which was due to the rolling up of graphene sheets in concentric formation [41]. With the incorporation of CNTs in the g-C_3N_4 network, no major alterations in phase information were observed. This could be plausibly due to the infinitesimal loading of CNTs in the g-C_3N_4 network [42]. Besides, the crystallite size (D) and the inter-layer distance (d) were calculated using Scherrer's expression and Bragg's law respectively. The values are tabulated in Table 5.4. The values are almost near to that of the pristine *CN* sample. Thus, the inclusion of CNTs did not manipulate the primary structure of g-C_3N_4 thereby maintaining the structural stability of the carbon nitride.

Table 5.4 The interplanar distance, d and the crystallite size, D, of the as-prepared CN, CNT, and CC samples.

Sample	Interplanar distance d (nm)	Crystallite dimension D (nm)
CN	0.325	7.6
CC1	0.320	9.40
CC2	0.322	10.28
CC3	0.320	10.83
CC4	0.320	9.65
CNT	0.339	12.95

The morphological inspection was carried out under FESEM and HRTEM as shown in Fig. 5.11. The pristine CN sample (Fig. 5.11(a, b)) showed a flake-like structure in FESEM whereas clear layered morphology was observed under HRTEM [43]. The SAED pattern essentially pointed towards the amorphous nature of g-C_3N_4. The arc discharge fabricated MWCNTs (Fig. 5.11(c, d)) were typically embedded with a huge number of graphitic carbon nanoparticles which is a major drawback of these CNTs [44]. The SAED rings indicated the polycrystalline nature of these nanotubes. The hybrid nanostructure of CNTs and g-C_3N_4 (Fig. 5.11(e, f)) showed a similar structure as that of pure CN in FESEM due to smaller loading amounts of CNTs. However, TEM micrographs showed random diffusion of CNTs into the g-C_3N_4 sheets [45]. Thus, confirming the composite formation.

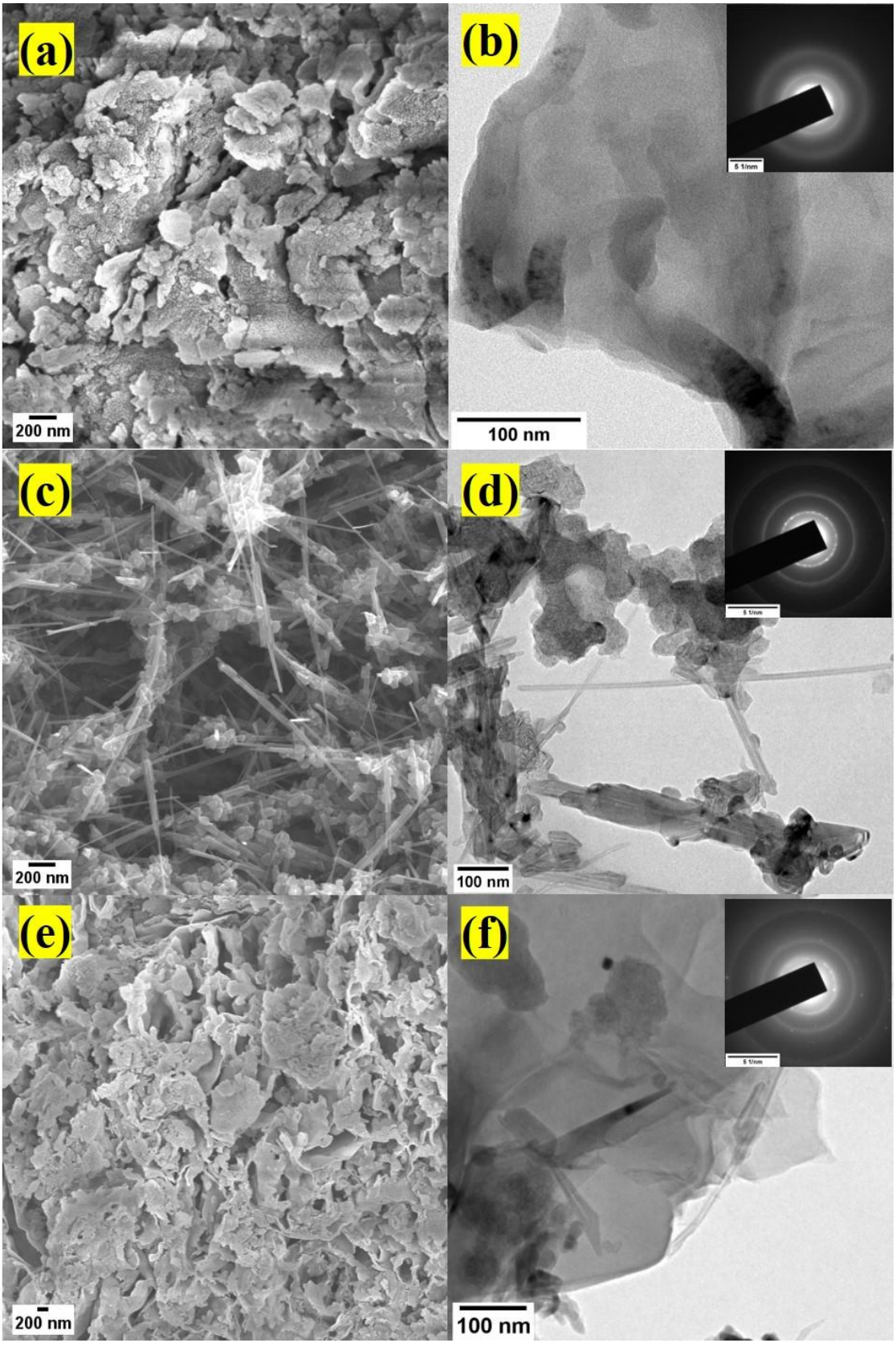

Figure 5.11 *FESEM micrograph and HRTEM image with SAED pattern (inset) of CN (a, b), CNT (c, d) and CC1 (e, f), respectively.*

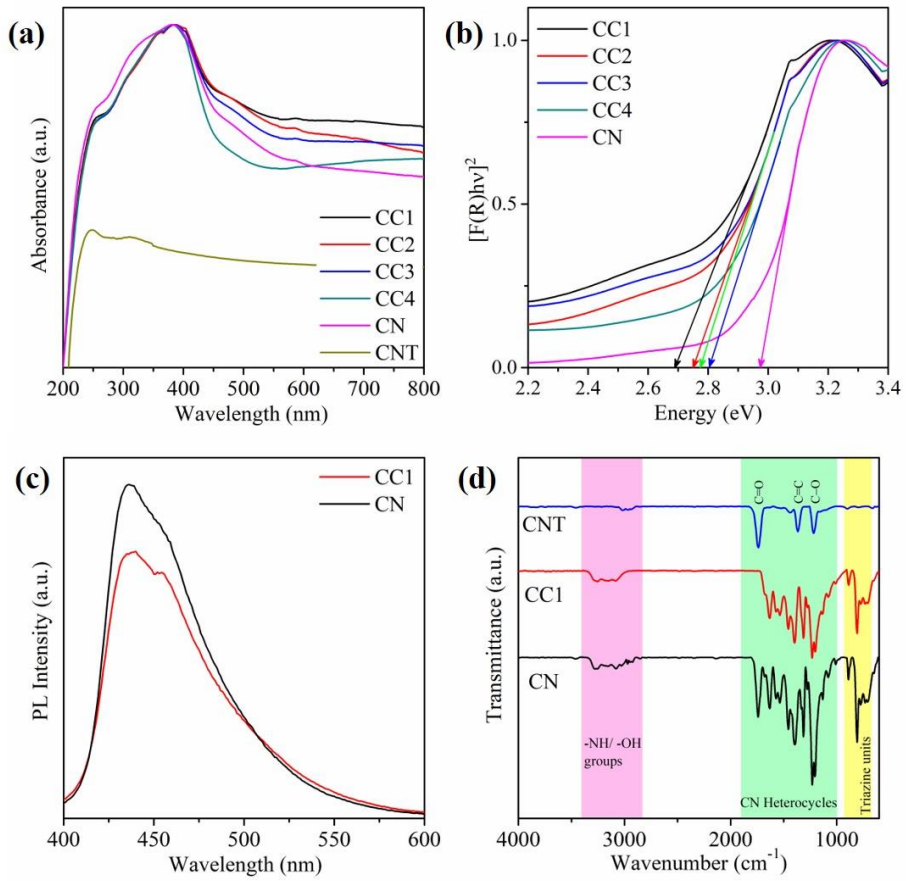

Figure 5.12 *(a) UV-DRS absorbance spectra, (b) the KM curve, (c) the PL spectra and (d) the FTIR spectra of CN, CNT, and CC samples.*

The optical behaviour of the samples was investigated with the assistance of UV-DRS, PL, and FTIR spectroscopic techniques as displayed in Fig. 5.12. The UV-DRS spectra (Fig. 5.12(a)) of all the *CC* samples showed a greater absorption edge in the visible region as compared to the pristine *CN* sample. Besides, the *CNT* sample showed low absorbance in the visible range as expected [46]. This enhanced visible light absorption resulted in the decrease of the energy bandgap of the hybrid photocatalyst from 2.96 eV (*CN*) to 2.68 eV (*CC1*) as displayed in the KM plot (Fig. 5.12(b)). However, a gradual increment in the CNT addition resulted in a decrease in the visible light activity of the hybrid photocatalysts. This could be attributed to the black colour of the CNTs which minimized the overall optical absorption of the samples [47].

The charge carrier lifetime was evaluated by studying the photoluminescence property of all the as- samples at an excitation wavelength of 365 nm. As shown in Fig. 5.12(c), the *CC1* sample has lower PL intensities than the pure *CN* sample. This could be surely associated with the charge carrier separation phenomenon that happened due to the incorporation of CNTs into

the g-C_3N_4 network [48]. The chemical bonding and other functional group information were obtained by examining the FTIR spectra of *CN, CC1*, and *CNT* samples (Fig. 5.12(d)). *CN* and *CC1* samples displayed similar absorption bands [49–51] pertaining to the g-C_3N_4 fingerprint structure. Thereby confirming that no substantial changes in the skeletal structure of g-C_3N_4 occurred with the addition of CNTs [15]. The FTIR spectrum of *CNT* showed three weak bands between 1000 and 2000 cm^{-1} which are the fingerprint peaks relevant to the sp^2 and sp^3 carbons [52].

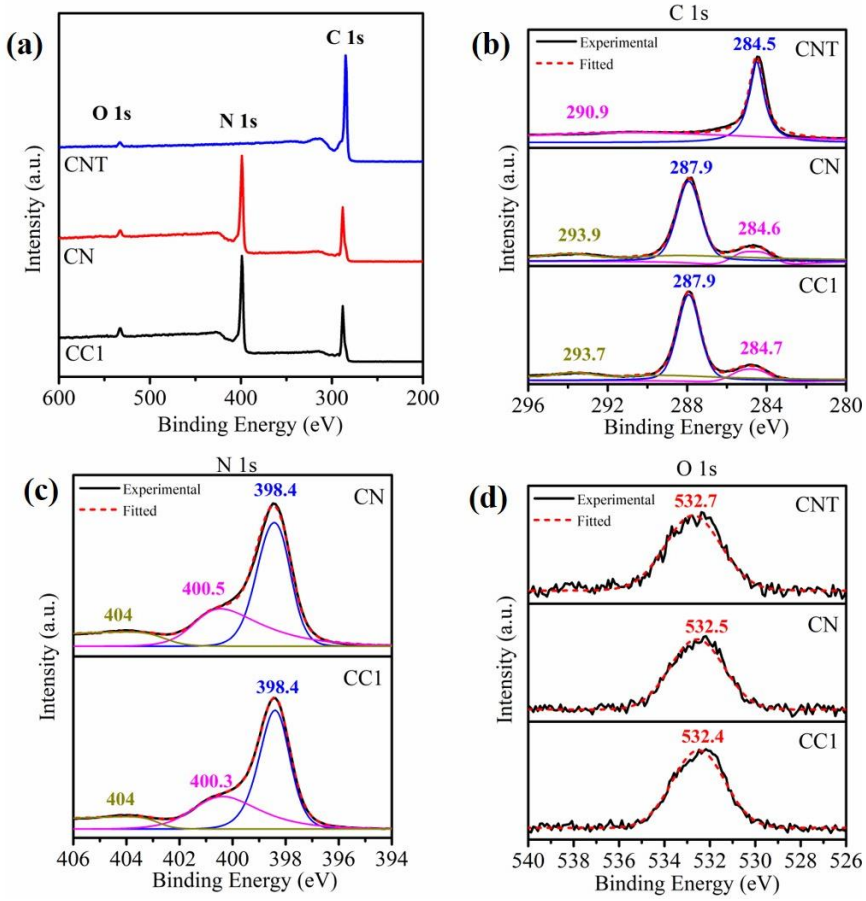

Figure 5.13 *XPS spectra of CN, CNT, and CC1 samples.*

The elemental and chemical analyses of the as-synthesized samples were investigated through XPS as shown in Fig. 5.13. The wide scan spectra (Fig. 5.13(a)) of *CN*, *CC1*, and *CNT* samples confirmed the existence of C, N, and O elements with the percentage compositions as shown in Table 5.5. The deconvoluted C1s spectra of all the samples are given in Fig. 5.13(b). *CN* and *CC1* samples were deconvoluted into three peaks roughly located at ~284 eV, ~287 eV, and ~293 eV attributed to the photoelectron line of C, sp^2 bonded carbon in CN architecture, and carbon attached to amine groups respectively [53]. Similarly, the N1s deconvoluted spectra of *CN* and *CC1* samples (Fig. 5.13(c)) showed three peaks around ~398 eV, ~400 eV, and ~ 404 eV designated to sp^2 bonded N in aromatic rings (N─C=N), also called pyridinic N, tertiary N-

containing species [N−(C)$_3$], and − NH groups respectively [54,55]. In the case of *CNT*, the C1s spectrum showed one intense peak at ~ 284 eV attributed to the graphitic carbon, (C=C) and a small hump at ~ 291 eV due to $\pi-\pi^*$ interactions [56]. Further, all the samples showed a minor peak at ~ 532 eV due to the surficial oxygen (Fig. 5.13(d)) [57]. Due to lower loading portions of CNTs (~ 0.1%, w/w), there was negligible change in the C/N ratio as shown in Table 5.5.

Table 5.5 Elemental composition of CN, CNT and CC1 samples.

Sample	C1s (%)	N1s (%)	C/N Ratio	O1s (%)
CN	44.48	53.01	0.83	2.51
CC1	43.58	52.93	0.82	3.5
CNT	97.99	-	-	2.01

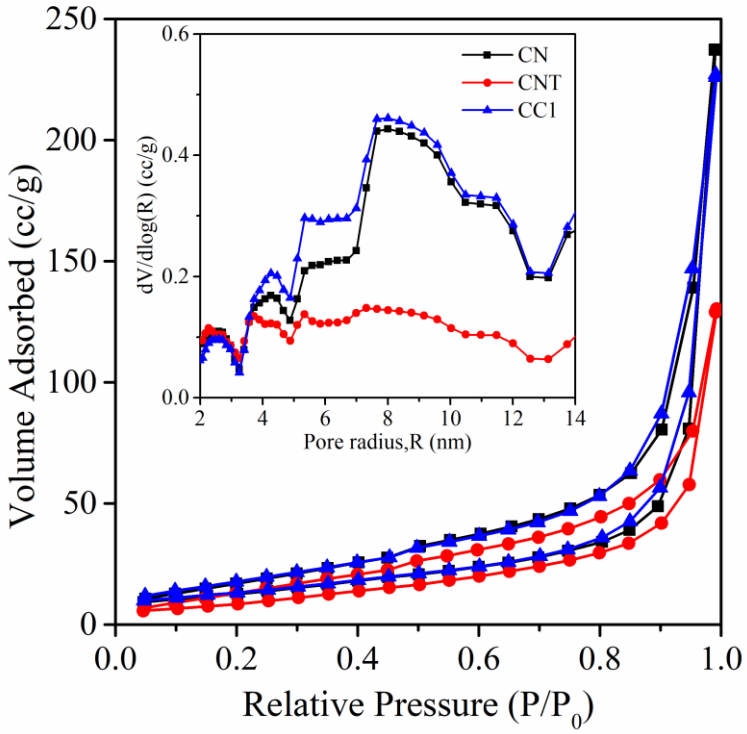

Figure 5.14 *BET surface area isotherms with the inset showing pore radii distribution of CN, CNT, and CC1 samples.*

The N_2 adsorption-desorption studies were done to evaluate the specific surface area (SSA), pore width and capacity as shown in Fig. 5.14. Essentially, all the samples possessed mesoporosity which was evident from its Type-IV isotherm following the H4 hysteresis loop [58]. The pore distribution (Fig. 5.14(Inset)) displayed a broad spectrum of mesoporous

structures [59]. But there was a slight decrease in the surface area was seen after CNT incorporation (Table 5.6). However, the photocatalytic activity was not affected due to the lower SSA value of the heterostructure, which means that the surface area was not the major parameter for the enhanced photodegradation performance [47].

Table 5.6 SSA, average pore radius and volume of CN, CNT, and CC1 samples.

Sample	SSA, (m^2/g)	Pore Radius R (nm)	Pore Volume V (cc/g)
CN	69	15.32	0.367
CNT	37	14.31	0.349
CC1	49	10.85	0.201

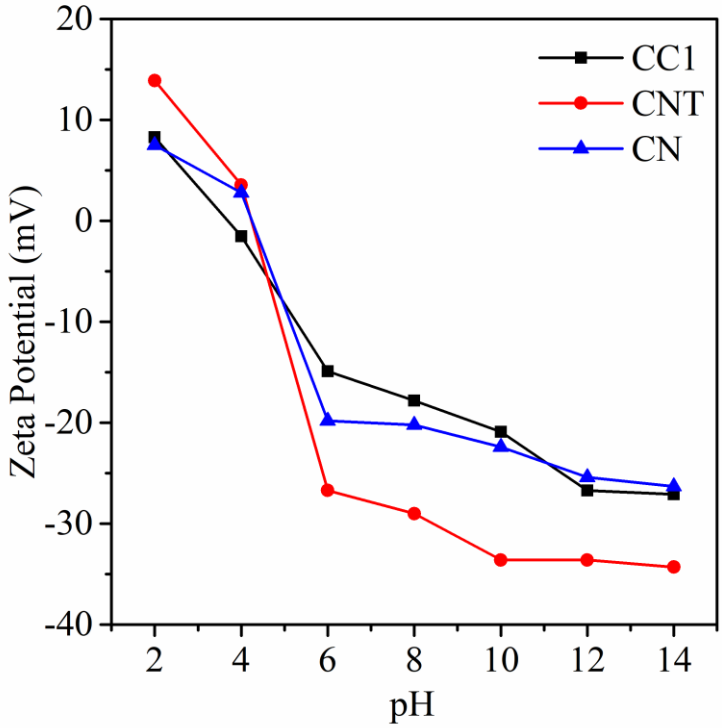

Figure 5.15 *Zeta potential values at various pH values of CN, CNT, and CC1 samples.*

The zeta potential (ZP) calculations play an essential role in deciding the target pollutant. Fig. 5.15 shows the ZP vs pH curve, from which one can get information about overall electrostatic charges on the surface at different pH values [60]. At pH7, both the *CN* and *CC1* samples possessed a net negative charge which means the target contaminant must possess a total positive charge for better electrostatic attractions resulting in surface adsorption of the pollutant to the catalyst. In the g-C_3N_4 network, the overall surface polarity usually depends on

the synergistic interactions between the primary, secondary, and tertiary amine groups present in the lattice and the photogenerated charge carriers [61].

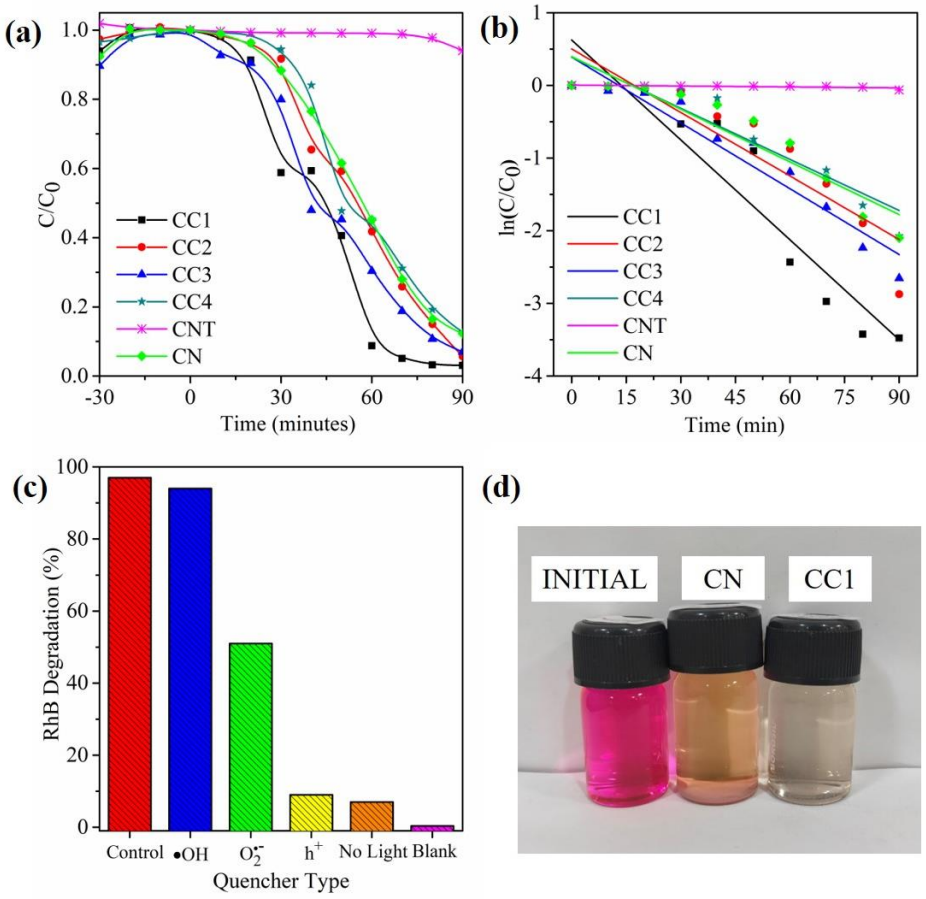

Figure 5.16 *(a) Dye degradation studies of all the samples, (b) 1st-order reaction kinetics curve of all the samples, (c) radical scavenging experiments of CC1 sample, and (d) RhB dye solution images post photodegradation experiment.*

The photocatalytic performance of all the CC samples was assessed by studying the photodegradation performance of RhB dye under visible light illumination (Fig. 5.16(a)). For comparison, CN and CNT samples were also tested under similar conditions. The degradation efficiency and reaction rate constant are displayed in Table 5.7. It was observed that the CC1 sample showed near complete degradation in 90 minutes. The dye degradation performance decreased beyond pristine CN when the CNT loading percentage reached 1% w/w of g-C_3N_4 (CC4 sample). This gradual decrease in the performance can be attributed to the presence of an excess amount of CNT sheets blocking the surface and thus preventing the absorption of visible light [62]. However, the overall performance was improved by the successful separation of photo-induced charges due to the addition of CNTs in g-C_3N_4 [63]. The present work has been compared with some of the previously reported works using different pollutants as given in Table 5.8.

Table 5.7 RhB degradation percentage and reaction rate constant values of CN, CNT, and CC samples after 90 minutes of light illumination.

Sample	RhB Degradation (%)	Rate Constant, k (min^{-1})
CC1	97	0.0458
CC2	94	0.0291
CC3	93	0.0301
CC4	87	0.0234
CN	88	0.0241
CNT	6	0.0004

Table 5.8 Comparative study of present work with some of the CNT/ g-C_3N_4 published literature.

S. No.	CNT Loading (%)	Target Pollutant	Target Conc. (mg/L)	Time (Minutes)	Degradation (%)	Ref. No.
1	0.1	RhB	-	300	91.7	[42]
2	1	RhB	10	60	98.1	[45]
3	2.3	RhB	5	40	99	[48]
4	2	RhB	10	60	100	[15]
5	0.2	RhB	15	80	~100	[62]
6	**0.1**	**RhB**	**20**	**90**	**97**	**This Work**

The reaction rate constant was estimated by employing a pseudo-1st order reaction equation [ln (C/C0) = -kt, where k (min-1) is the rate of reaction] as shown in Fig. 5.16(b). From Table 5.7, it can be noticed that the degradation rate of CC1 was double that of the CN sample. Also, except CC4, all the CC samples showed higher degradation rates. The degradation procedure was further analysed by studying the reactive species scavenging experiments. Here, 10 mM of para-Benzoquinone (p-BQ), ammonium oxalate (AO) and isopropanol (IPA) were added separately at the beginning of the light irradiation to trap the photogenerated holes (h^+), superoxide anion ($\bullet O_2^-$), and hydroxyl radical (•OH) respectively. From Fig. 5.16(c), it was clear that h^+ was mainly responsible for the photodegradation of RhB (η= 9%). Similarly, $\bullet O_2^-$ and •OH radicals also affected the overall degradation efficiency (η = 54% and 94% respectively). Based on the above discussions, a theoretical degradation mechanism can be proposed in the upcoming section. the images of the final colour of the dye

solution after 90 minutes of light exposure for CN and CC1 samples can be seen in Fig. 5.16(d) along with the image of the initial solution.

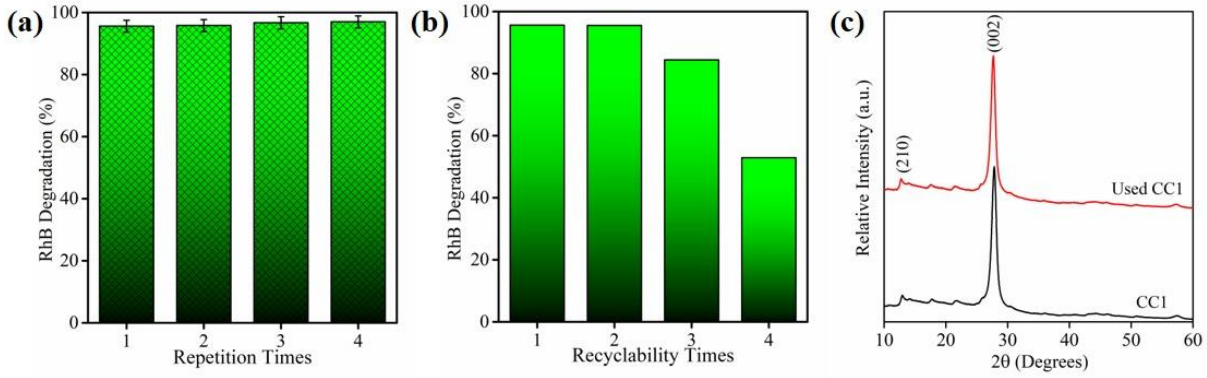

Figure 5.17 *(a, b) Repeatability and recyclability of CC1 photocatalyst sample for RhB degradation and (c) XRD pattern of CC1 sample before and after photodegradation experiments.*

The repeatability and recyclability of the CC1 sample were studied as shown in Fig. 5.17(a, b). For 4 times consecutively, the degradation efficiency was unaltered thus confirming the consistency of the synthesized material. Besides, the recyclability of the sample was greatly affected after 3rd cycle which could be majorly due to the loss of material during the collection process. The post-experiment material was tested for its structural stability (Fig. 5.17(c)). and it was noticed that the photocatalyst material has shown an unaltered structure in its XRD pattern post-photodegradation experiment.

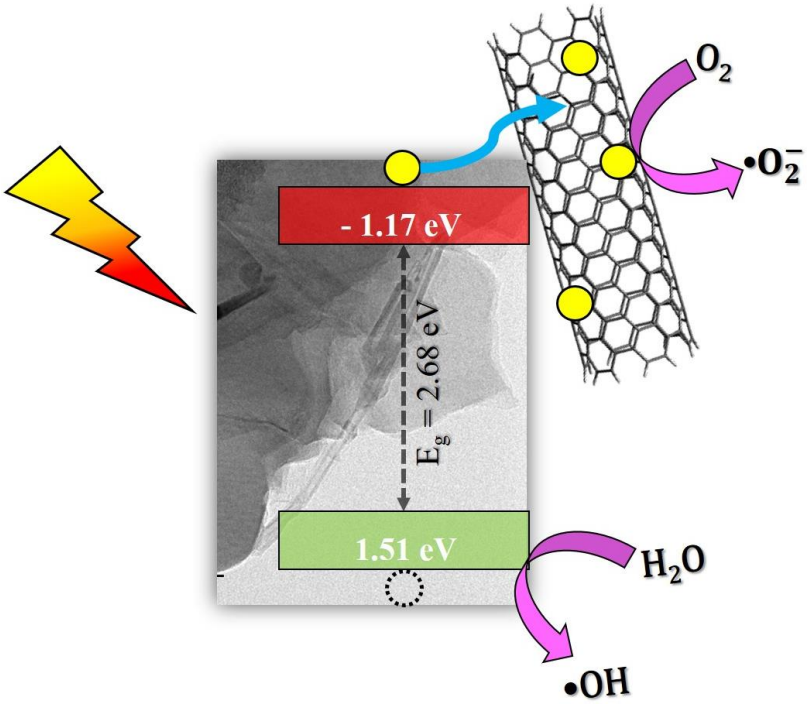

Figure 5.18 *A possible mechanism for RhB degradation in the CC1 sample.*

A possible photodegradation mechanism can be predicted based on the above results and discussions (Fig. 5.18). When the light of suitable energy is exposed to the material, electrons (e^-) are excited from the stable energy states, valance band (VB) to the excited states, conduction band (CB) creating a charge vacancy, hole (h^+) in the VB. Here, in a pristine *CN* sample, some of the photogenerated charges quickly recombine resulting in lower photodegradation efficiencies. However, in the case of composite photocatalyst, strong interaction between the carbon nitride and carbon nanotube forms a barrier junction due to close contact between the constituent materials and offers an effective pathway for minimizing e^- — h^+ recombination by facilitating intrusion of electrons into the nanotube [64]. In this way, CNTs promote interfacial electron transfer by acting as electron acceptors while the semiconductor acts as an electron donor under light irradiation.

5.3 Conclusions

In summary, a hybrid photocatalyst was successfully prepared using a one-pot synthesis approach where, melamine, CNMs, and ammonium chloride were mixed physically and allowed to undergo a pyrolysis reaction at 650 °C for 2 hrs. The as-prepared samples were tested under XRD, SEM, TEM, FTIR, PL, BET, XPS, UV-DRS, etc to study the optical, structural, morphological, chemical bonding and other crucial information. All the hybrid photocatalyst samples were applied to study the RhB photodegradation performance. It was observed that under visible light, 0.1 % of carbon soot loading showed a remarkable degradation performance of 97 % of the dye in 90 minutes whereas 0.1 % of CNT loading showed the height photodegradation performance by scrapping 92 % of RhB dye in 60 minutes. However, the pristine g-C_3N_4 sample could degrade only 88 % and 55 % in 90 and 60 minutes respectively under visible light illumination. This enhanced performance can be attributed to high SSA and pore volume, longer lifetime of charge carriers and appropriate band edge potentials which implies efficient charge separation.

References

[1] S. Cao, J. Low, J. Yu, M. Jaroniec, Polymeric Photocatalysts Based on Graphitic Carbon Nitride, Advanced Materials. 27 (2015) 2150–2176. https://doi.org/10.1002/adma.201500033.

[2] J. Zhu, P. Xiao, H. Li, S.A.C. Carabineiro, Graphitic carbon nitride: Synthesis, properties, and applications in catalysis, ACS Appl Mater Interfaces. 6 (2014) 16449–16465. https://doi.org/10.1021/am502925j.

[3] J. Wen, J. Xie, X. Chen, X. Li, A review on g-C 3 N 4 -based photocatalysts, Appl Surf Sci. 391 (2017) 72–123. https://doi.org/10.1016/j.apsusc.2016.07.030.

[4] M. Tan, C. Yu, J. Li, Y. Li, C. Tao, C. Liu, H. Meng, Y. Su, L. Qiao, Y. Bai, Engineering of g-C3N4-based photocatalysts to enhance hydrogen evolution, Adv Colloid Interface Sci. 295 (2021). https://doi.org/10.1016/j.cis.2021.102488.

[5] Q. Xu, Z. Xia, J. Zhang, Z. Wei, Q. Guo, H. Jin, H. Tang, S. Li, X. Pan, Z. Su, S. Wang, Recent advances in solar-driven CO2 reduction over g-C3N4-based photocatalysts, Carbon Energy. 5 (2023). https://doi.org/10.1002/cey2.205.

[6] G. Mamba, A.K. Mishra, Graphitic carbon nitride (g-C3N4) nanocomposites: A new and exciting generation of visible light driven photocatalysts for environmental pollution remediation, Appl Catal B. 198 (2016) 347–377. https://doi.org/10.1016/j.apcatb.2016.05.052.

[7] X. Yang, F. Qian, G. Zou, M. Li, J. Lu, Y. Li, M. Bao, Facile fabrication of acidified g-C3N4/g-C3N4 hybrids with enhanced photocatalysis performance under visible light irradiation, Appl Catal B. 193 (2016) 22–35. https://doi.org/10.1016/j.apcatb.2016.03.060.

[8] P. Ahuja, S.K. Ujjain, R. Kanojia, P. Attri, Transition metal oxides and their composites for photocatalytic dye degradation, Journal of Composites Science. 5 (2021). https://doi.org/10.3390/jcs5030082.

[9] K.D. Sattler, Carbon nanomaterials sourcebook. Volume 1, Graphene, fullerenes, nanotubes, and nanodiamonds, n.d.

[10] H. Yi, D. Huang, L. Qin, G. Zeng, C. Lai, M. Cheng, S. Ye, B. Song, X. Ren, X. Guo, Selective prepared carbon nanomaterials for advanced photocatalytic application in environmental pollutant treatment and hydrogen production, Appl Catal B. 239 (2018) 408–424. https://doi.org/10.1016/j.apcatb.2018.07.068.

[11] H. Yi, D. Huang, L. Qin, G. Zeng, C. Lai, M. Cheng, S. Ye, B. Song, X. Ren, X. Guo, Selective prepared carbon nanomaterials for advanced photocatalytic application in environmental pollutant treatment and hydrogen production, Appl Catal B. 239 (2018) 408–424. https://doi.org/10.1016/j.apcatb.2018.07.068.

[12] J.P. Castrejón Martínez, M. Casales-Díaz, J.J. Ramos-Hernández, T. Kar, S. Godavarthi, M. Calixto Rodríguez, M.K. Kesarla, g-C3N4/Carbon spheres composite for efficient photoreduction and simultaneous removal of chromium, Mater Lett. 310 (2022). https://doi.org/10.1016/j.matlet.2021.131486.

[13] X. Chen, H. Chen, J. Guan, J. Zhen, Z. Sun, P. Du, Y. Lu, S. Yang, A facile mechanochemical route to a covalently bonded graphitic carbon nitride (g-C3N4) and fullerene hybrid toward enhanced visible light photocatalytic hydrogen production, Nanoscale. 9 (2017) 5615–5623. https://doi.org/10.1039/c7nr01237c.

[14] L. Cheng, H. Zhang, X. Li, J. Fan, Q. Xiang, Carbon–Graphitic Carbon Nitride Hybrids for Heterogeneous Photocatalysis, Small. 17 (2021). https://doi.org/10.1002/smll.202005231.

[15] F. Ding, Z. Zhao, D. Yang, X. Zhao, Y. Chen, Z. Jiang, One-Pot Fabrication of g-C3N4/MWCNTs Nanocomposites with Superior Visible-Light Photocatalytic Performance, Ind Eng Chem Res. 58 (2019) 3679–3687. https://doi.org/10.1021/acs.iecr.8b05293.

[16] C. Wang, J. Li, X. Luo, J. Hui, X. Liu, J. Tan, X. Zhao, Graphitic carbon nitride nanosheets modified multi-walled carbon nanotubes as 3D high efficient sensor for simultaneous determination of dopamine, uric acid and tryptophan, Journal of Electroanalytical Chemistry. 780 (2016) 147–152. https://doi.org/10.1016/j.jelechem.2016.09.004.

[17] F. Fina, S.K. Callear, G.M. Carins, J.T.S. Irvine, Structural investigation of graphitic carbon nitride via XRD and neutron diffraction, Chemistry of Materials. 27 (2015) 2612–2618. https://doi.org/10.1021/acs.chemmater.5b00411.

[18] J.C. Scanlon'9t, L.B. Ebertg, X-ray Diffraction Study of Fullerene Soot, 1993.

[19] J. Liu, T. Zhang, Z. Wang, G. Dawson, W. Chen, Simple pyrolysis of urea into graphitic carbon nitride with recyclable adsorption and photocatalytic activity, J Mater Chem. 21 (2011) 14398–14401. https://doi.org/10.1039/c1jm12620b.

[20] D. Zhang, K. Ye, Y. Yao, F. Liang, T. Qu, W. Ma, B. Yang, Y. Dai, T. Watanabe, Controllable synthesis of carbon nanomaterials by direct current arc discharge from the inner wall of the chamber, Carbon N Y. 142 (2019) 278–284. https://doi.org/10.1016/j.carbon.2018.10.062.

[21] L. Song, T. Li, S. Zhang, Fullerenes/graphite carbon nitride with enhanced photocatalytic hydrogen evolution ability, Journal of Physical Chemistry C. 121 (2017) 293–299. https://doi.org/10.1021/acs.jpcc.6b09064.

[22] Y. Wang, H. Cai, F. Qian, Y. Li, J. Yu, X. Yang, M. Bao, X. Li, Facile one-step synthesis of onion-like carbon modified ultrathin g-C3N4 2D nanosheets with enhanced visible-light photocatalytic performance, J Colloid Interface Sci. 533 (2019) 47–58. https://doi.org/10.1016/j.jcis.2018.08.039.

[23] G. Liu, M. Xue, Q. Liu, H. Yang, Y. Zhou, Facile synthesis of C-doped hollow spherical g-C3N4 from supramolecular self-assembly for enhanced photoredox water splitting, Int J Hydrogen Energy. 44 (2019) 25671–25679. https://doi.org/10.1016/j.ijhydene.2019.08.056.

[24] Y. Ding, Z. Lin, J. Deng, Y. Liu, L. Zhang, K. Wang, S. Xu, S. Cao, Construction of carbon dots modified hollow g-C3N4 spheres via in situ calcination of cyanamide and glucose for highly enhanced visible light photocatalytic hydrogen evolution, Int J Hydrogen Energy. 47 (2022) 1568–1578. https://doi.org/10.1016/j.ijhydene.2021.10.108.

[25] H. Li, Y. Jing, X. Ma, T. Liu, L. Yang, B. Liu, S. Yin, Y. Wei, Y. Wang, Construction of a well-dispersed Ag/graphene-like g-C3N4 photocatalyst and enhanced visible light photocatalytic activity, RSC Adv. 7 (2017) 8688–8693. https://doi.org/10.1039/c6ra26498k.

[26] W. Bing, Z. Chen, H. Sun, P. Shi, N. Gao, J. Ren, X. Qu, Visible-light-driven enhanced antibacterial and biofilm elimination activity of graphitic carbon nitride by embedded Ag nanoparticles, Nano Res. 8 (2015) 1648–1658. https://doi.org/10.1007/s12274-014-0654-1.

[27] T. Narkbuakaew, P. Sujaridworakun, Synthesis of Tri-S-Triazine Based g-C3N4 Photocatalyst for Cationic Rhodamine B Degradation under Visible Light, Top Catal. 63 (2020) 1086–1096. https://doi.org/10.1007/s11244-020-01375-z.

[28] A.B. Siddique, A.K. Pramanick, S. Chatterjee, M. Ray, Amorphous Carbon Dots and their Remarkable Ability to Detect 2,4,6-Trinitrophenol, Sci Rep. 8 (2018). https://doi.org/10.1038/s41598-018-28021-9.

[29] Z. Chen, T.T. Fan, X. Yu, Q.L. Wu, Q.H. Zhu, L.Z. Zhang, J.H. Li, W.P. Fang, X.D. Yi, Gradual carbon doping of graphitic carbon nitride towards metal-free visible light photocatalytic hydrogen evolution, J Mater Chem A Mater. 6 (2018) 15310–15319. https://doi.org/10.1039/c8ta03303j.

[30] G. Song, Z. Chu, W. Jin, H. Sun, Enhanced performance of g-C3N4/TiO2 photocatalysts for degradation of organic pollutants under visible light, Chin J Chem Eng. 23 (2015) 1326–1334. https://doi.org/10.1016/j.cjche.2015.05.003.

[31] Y. Chai, Q. Liu, L. Zhang, J. Ren, W.L. Dai, Structure Engineered g-C3N4 Nano-Sheets by Switching the Pyrolysis Gas Atmosphere for Enhanced Photo-Catalytic Degradation, Chin J Chem. 35 (2017) 173–182. https://doi.org/10.1002/cjoc.201600608.

[32] H.Y. Xu, L.C. Wu, H. Zhao, L.G. Jin, S.Y. Qi, Synergic Effect between Adsorption and Photocatalysis of Metal-Free g-C3N4 Derived from Different Precursors, PLoS One. 10 (2015). https://doi.org/10.1371/journal.pone.0142616.

[33] INTERNATIONAL UNION OF PURE AND APPLIED CHEMISTRY PHYSICAL CHEMISTRY DIVISION COMMISSION ON COLLOID AND SURFACE CHEMISTRY INCLUDING CATALYSIS* REPORTING PHYSISORPTION DATA FOR GAS/SOLID SYSTEMS with Special Reference to the Determination of Surface Area and Porosity Reporting physisorption data for gas/solid systems-with special reference to the determination of surface area and porosity, 1985.

[34] J.C. Groen, L.A.A. Peffer, J. Pérez-Ramírez, Pore size determination in modified micro- and mesoporous materials. Pitfalls and limitations in gas adsorption data analysis, Microporous and Mesoporous Materials. 60 (2003) 1–17. https://doi.org/10.1016/S1387-1811(03)00339-1.

[35] L. Shi, F. Wang, J. Zhang, J. Sun, Onion-like carbon modified porous graphitic carbon nitride with excellent photocatalytic activities under visible light, Ceram Int. 42 (2016) 18116–18123. https://doi.org/10.1016/j.ceramint.2016.08.124.

[36] V.P. Madhurima, P.H. Borse, K. Kumari, T.N. Rao, P.K. Jain, Improved photocatalytic activity of carbon-based polymeric semiconductor for efficient decontamination of wastewater: Effect of reaction atmosphere and pyrolysis temperature, Opt Mater (Amst). 110 (2020). https://doi.org/10.1016/j.optmat.2020.110523.

[37] F. Azeez, E. Al-Hetlani, M. Arafa, Y. Abdelmonem, A.A. Nazeer, M.O. Amin, M. Madkour, The effect of surface charge on photocatalytic degradation of methylene blue dye using chargeable titania nanoparticles, Sci Rep. 8 (2018). https://doi.org/10.1038/s41598-018-25673-5.

[38] B. Chai, X. Liao, F. Song, H. Zhou, Fullerene modified C3N4 composites with enhanced photocatalytic activity under visible light irradiation, Dalton Transactions. 43 (2014) 982–989. https://doi.org/10.1039/c3dt52454j.

[39] X. Bai, L. Wang, Y. Wang, W. Yao, Y. Zhu, Enhanced oxidation ability of g-C3N4 photocatalyst via C60 modification, Appl Catal B. 152–153 (2014) 262–270. https://doi.org/10.1016/j.apcatb.2014.01.046.

[40] F. Fina, S.K. Callear, G.M. Carins, J.T.S. Irvine, Structural investigation of graphitic carbon nitride via XRD and neutron diffraction, Chemistry of Materials. 27 (2015) 2612–2618. https://doi.org/10.1021/acs.chemmater.5b00411.

[41] R. Das, S. Hamid, Md. Ali, S. Ramakrishna, W. Yongzhi, Carbon Nanotubes Characterization by X-ray Powder Diffraction – A Review, Curr Nanosci. 11 (2014) 23–35. https://doi.org/10.2174/15734137106661408182100 43.

[42] Y. Guan, J. Wu, L. Wang, C.H. Shi, K. Lv, Y. Lv, Application of g-C3N4/CNTs nanocomposites in energy and environment, Energy Reports. 8 (2022) 1190–1199. https://doi.org/10.1016/j.egyr.2022.02.081.

[43] Y. Xu, H. Xu, L. Wang, J. Yan, H. Li, Y. Song, L. Huang, G. Cai, The CNT modified white C3N4 composite photocatalyst with enhanced visible-light response photoactivity, Journal of the Chemical Society. Dalton Transactions. 42 (2013) 7604–7613. https://doi.org/10.1039/c3dt32871f.

[44] 19. Preparation_of_carbon_nanotubes_by_arc-d, (n.d.).

[45] G. Liu, M. Liao, Z. Zhang, H. Wang, D. Chen, Y. Feng, Enhanced photodegradation performance of Rhodamine B with g-C3N4 modified by carbon nanotubes, Sep Purif Technol. 244 (2020). https://doi.org/10.1016/j.seppur.2020.116618.

[46] L. Ge, C. Han, Synthesis of MWNTs/g-C 3N 4 composite photocatalysts with efficient visible light photocatalytic hydrogen evolution activity, Appl Catal B. 117–118 (2012) 268–274. https://doi.org/10.1016/j.apcatb.2012.01.021.

[47] J. Liu, Y. Song, H. Xu, X. Zhu, J. Lian, Y. Xu, Y. Zhao, L. Huang, H. Ji, H. Li, Non-metal photocatalyst nitrogen-doped carbon nanotubes modified mpg-C3N4: facile synthesis and the enhanced visible-light photocatalytic activity, J Colloid Interface Sci. 494 (2017) 38–46. https://doi.org/10.1016/j.jcis.2017.01.010.

[48] L. Shi, L. Yao, W. Si, One step to prepare CNTs modified porous g-C3N4 with excellent visible-light photocatalytic performance, Journal of Materials Science: Materials in Electronics. 30 (2019) 1714–1723. https://doi.org/10.1007/s10854-018-0444-8.

[49] T. Narkbuakaew, P. Sujaridworakun, Synthesis of Tri-S-Triazine Based g-C3N4 Photocatalyst for Cationic Rhodamine B Degradation under Visible Light, Top Catal. 63 (2020) 1086–1096. https://doi.org/10.1007/s11244-020-01375-z.

[50] W. Bing, Z. Chen, H. Sun, P. Shi, N. Gao, J. Ren, X. Qu, Visible-light-driven enhanced antibacterial and biofilm elimination activity of graphitic carbon nitride by embedded Ag nanoparticles, Nano Res. 8 (2015) 1648–1658. https://doi.org/10.1007/s12274-014-0654-1.

[51] H. Li, Y. Jing, X. Ma, T. Liu, L. Yang, B. Liu, S. Yin, Y. Wei, Y. Wang, Construction of a well-dispersed Ag/graphene-like g-C3N4 photocatalyst and enhanced visible light photocatalytic activity, RSC Adv. 7 (2017) 8688–8693. https://doi.org/10.1039/c6ra26498k.

[52] F.A. Azri, R. Sukor, R. Hajian, N.A. Yusof, F.A. Bakar, J. Selamat, Modification strategy of screen-printed carbon electrode with functionalized multi-walled carbon nanotube and chitosan matrix for biosensor development, Asian Journal of Chemistry. 29 (2017) 31–36. https://doi.org/10.14233/ajchem.2017.20104.

[53] J. Zou, Y. Yu, W. Yan, J. Meng, S. Zhang, J. Wang, A facile route to synthesize boron-doped g-C 3 N 4 nanosheets with enhanced visible-light photocatalytic activity, J Mater Sci. 54 (2019) 6867–6881. https://doi.org/10.1007/s10853-019-03384-0.

[54] Y. Chai, Q. Liu, L. Zhang, J. Ren, W.L. Dai, Structure Engineered g-C3N4 Nano-Sheets by Switching the Pyrolysis Gas Atmosphere for Enhanced Photo-Catalytic Degradation, Chin J Chem. 35 (2017) 173–182. https://doi.org/10.1002/cjoc.201600608.

[55] G. Song, Z. Chu, W. Jin, H. Sun, Enhanced performance of g-C3N4/TiO2 photocatalysts for degradation of organic pollutants under visible light, Chin J Chem Eng. 23 (2015) 1326–1334. https://doi.org/10.1016/j.cjche.2015.05.003.

[56] Y.R. Son, S.J. Park, Green preparation and characterization of graphene oxide/carbon nanotubes-loaded carboxymethyl cellulose nanocomposites, Sci Rep. 8 (2018). https://doi.org/10.1038/s41598-018-35984-2.

[57] H.Y. Xu, L.C. Wu, H. Zhao, L.G. Jin, S.Y. Qi, Synergic Effect between Adsorption and Photocatalysis of Metal-Free g-C3N4 Derived from Different Precursors, PLoS One. 10 (2015). https://doi.org/10.1371/journal.pone.0142616.

[58] INTERNATIONAL UNION OF PURE AND APPLIED CHEMISTRY PHYSICAL CHEMISTRY DIVISION COMMISSION ON COLLOID AND SURFACE CHEMISTRY INCLUDING CATALYSIS* REPORTING PHYSISORPTION DATA FOR GAS/SOLID SYSTEMS with Special Reference to the Determination of Surface Area and Porosity Reporting physisorption data for gas/solid systems-with special reference to the determination of surface area and porosity, 1985.

[59] J.C. Groen, L.A.A. Peffer, J. Pérez-Ramírez, Pore size determination in modified micro- and mesoporous materials. Pitfalls and limitations in gas adsorption data analysis, Microporous and Mesoporous Materials. 60 (2003) 1–17. https://doi.org/10.1016/S1387-1811(03)00339-1.

[60] F. Azeez, E. Al-Hetlani, M. Arafa, Y. Abdelmonem, A.A. Nazeer, M.O. Amin, M. Madkour, The effect of surface charge on photocatalytic degradation of methylene blue dye using chargeable titania nanoparticles, Sci Rep. 8 (2018). https://doi.org/10.1038/s41598-018-25673-5.

[61] V.P. Madhurima, P.H. Borse, K. Kumari, T.N. Rao, P.K. Jain, Improved photocatalytic activity of carbon-based polymeric semiconductor for efficient decontamination of wastewater: Effect of reaction atmosphere and pyrolysis temperature, Opt Mater (Amst). 110 (2020). https://doi.org/10.1016/j.optmat.2020.110523.

[62] A. Mahmood, T. Muhmood, F. Ahmad, Carbon nanotubes heterojunction with graphene like carbon nitride for the enhancement of electrochemical and photocatalytic activity, Mater Chem Phys. 278 (2022). https://doi.org/10.1016/j.matchemphys.2021.125640.

[63] S. Yousefzadeh, B. Fathi, Construction of carbon nanotube-g-C3N4 nanocomposite photoanode for the enhanced photoelectrochemical activity in water splitting, Journal of Electroanalytical Chemistry. 878 (2020). https://doi.org/10.1016/j.jelechem.2020.114580.

[64] T. A., The Role of Carbon Nanotubes in Enhancement of Photocatalysis, in: Syntheses and Applications of Carbon Nanotubes and Their Composites, InTech, 2013. https://doi.org/10.5772/51050.

Chapter 6

2D/2D g-C_3N_4 based hybrid photocatalyst materials for photodegradation of RhB dye

6.1 Introduction

Recently, graphene and graphene analogous materials have picked tremendous attention due to their unique outstanding structural and electronic properties. One such material, graphitic-carbon nitride (g-C_3N_4), a non-metallic organic polymeric semiconducting material having an ideal bandgap of 2.7 eV, essentially existing in the visible region of the solar spectrum, is an incredible and assuring photocatalyst material. However, bulk g-C_3N_4 consists of a few demerits, like lower specific surface area and faster recombination rates of photogenerated charge carriers, which majorly limits its photocatalytic performance [1]. Therefore, various strategies have been deployed to overcome these shortcomings. It is known that g-C_3N_4 is a 2D material, and coupling with another 2D structure has some merits: (a) it can provide a larger area of contact for charge transfer and separation [2], (b) layered structure can be easily brought together to form a composite with the help of Van Der Waals forces of attraction thus, reducing the contact resistance [3]. Therefore, 2D/2D coupling can become a promising strategy to further enhance the photocatalytic activity of g-C_3N_4.

Special attention on graphene-based nanomaterials has been generated by researchers due to their exceptional thermo-mechanical properties, honeycomb-lattice structure, remarkable charge carrier ability, high surface area, low noise and vast applications in catalysis, energy, and composites fields [4]. Graphene-coupled nanocomposites have been widely used for fabricating electrochemical devices [5], pollutant degradation [6], aerospace applications [7], and optoelectronic devices [8], etc. which implies that incorporation of graphene enhances the overall performance of the composite materials. Therefore, the above discussion suggests that the g-C_3N_4 and GNP would be a great choice for making a hybrid system. There are only a few reported literature related to GNP-based g-C_3N_4 nanocomposites for pollutant degradation studies. For example, Li. Y and group reported methyl orange (MO) degradation using reduced graphene oxide (rGO) and g-C_3N_4 composite prepared via thermal polymerization followed by

a hydrothermal method. Here, they removed 92.3% of MO (15 mg/L) within 120 minutes under simulated solar light irradiation [9]. Another research group [10], reported a novel synthesis method for rGO/ protonated g-C_3N_4 (rGO/pCN) nanocomposite where they have joined ultrasonic dispersion and electrostatic self-assembly approach followed by a reduction process. In this work, the optimized rGO/pCN exhibited 5.4 times enhanced CH_4 evolution than that of pristine pCN. Another work [11], explains the development of GNP and g-C_3N_4 heterojunction synthesized via vacuum vaporization/condensation method and was applied for studying the photodegradation performance of tetracycline hydrochloride under visible light. Gu. Y and co-workers [12] prepared rGO/ g-C_3N_4 through microwave irradiation technique and applied it for studying RhB degradation. After 30 minutes of illumination of visible light, 97.2% dye was removed whereas pristine g-C_3N_4 showed only 70% degradation.

Another new class of metal-free, few-layered material having a similar structure to that of graphite has come into the spotlight due to its magnificent structural, thermal, and chemical properties. This new material is called hexagonal-boron nitride (*hBN* or *BN*) or white graphene due to its similarities with graphene but white. The *hBN*-based composites have been extensively researched for the last few years [13]. A small amount of *hBN* incorporation into the photocatalyst material leads to a high surface area that facilitates charge transfer and, eventually, separation [14]. Various *hBN*/semiconductor-based photocatalyst systems have been designed and studied for several applications [15]. Almost all this research explains that the significant role of *hBN* is to provide active surface sites for pollutant adsorption, altering the behaviour of photo-induced holes or passivation of surface barriers.

Herein, we report systematic and detailed studies regarding the effect of GNP and hBN loading percentage individually on the overall photodegradation performance. The preparation method involves a single-step simple polycondensation strategy. The prepared heterostructure showed a higher carrier lifetime as observed through PL spectroscopy resulting in efficient charge separation and ultrafast degradation of RhB under visible radiation.

6.2 Results and discussions

6.2.1 GNP/g-C_3N_4 hybrid photocatalyst for RhB photodegradation studies

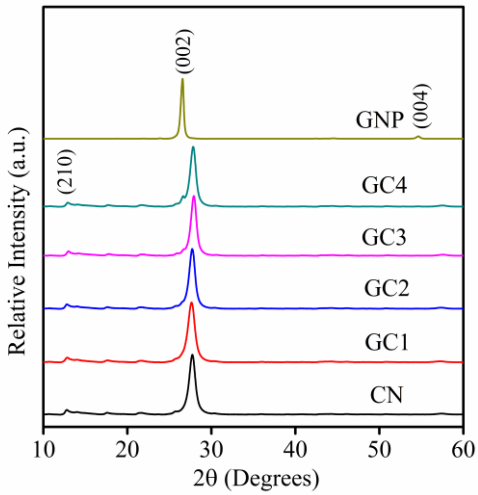

Figure 6.1 *XRD diffractograms of CN, GNP and GC samples.*

Figure 6.1 shows the typical XRD patterns of *CN*, *GNP*, and *GC* samples. The bare *CN* sample showed two significant peaks around 12.8° (210) and 27.7° (002) representing the intra-planar distance between heptazine moieties and inter-planar distance between the stacking layers respectively assuming rhombohedral structure [16]. The XRD pattern of *GNP* showed one major peak at 26.6° (002) and a minor peak at 54.6° (004) which corresponds to the reflections of graphene materials [17]. With the incorporation of *GNP* into the g-C_3N_4 structure, no significant peaks were detected pertaining to graphene structure at lower weight loading. This could be due to the smaller amounts of the added *GNP* material that inhibit the detection during XRD studies or that could also be due to the good coverage of g-C_3N_4 over the *GNP* material [18]. However, when the loading amount further increased to 1%, a slight shoulder peak was observed at 26.6° related to the (002) peak of *GNP* material. The crystallite dimension of all the *GC* samples was slightly larger than the bare *CN* sample as shown in Table 6.1. This was due to the incorporation of graphene in the g-C_3N_4 architecture. From XRD studies, it can be propounded that no major structural deformation or internal lattice stress is generated due to the incorporation of *GNP* into the g-C_3N_4 structure.

Table 6.1 The interlayer distance, d and the crystallite size, D, of the as-prepared CN, GNP, and GC samples.

Sample	Interlayer Spacing d(nm)	Crystallite dimension D(nm)
CN	0.325	7.6
GC1	0.322	8.40
GC2	0.321	9.85
GC3	0.319	10.59
GC4	0.320	10.06
GNP	0.335	20.08

The surface morphological and structural studies were carried out by observing the samples under FESEM and HRTEM (Fig. 6.2). The bare *CN* sample consisted of agglomerated flaky structures that are densely packed together (Fig. 6.2(a)). Besides, the HRTEM micrograph showed an identical layered structure that was uniformly spread throughput (Fig. 5.2(b)) with an indisputable diffused ring pattern (Fig. 6.2(b) Inset) implying the amorphous nature of the material and thereby confirming the g-C_3N_4 structure formation via thermal decomposition method [19]. The microscopic structure of *GNP* essentially possessed a large laminar structure in the order of a few microns and contained large-sized grains as shown in Fig. 6.2(c) [20]. However, the HRTEM image displayed thin translucent layered morphology acquiring a semi-crystalline nature as shown in the SAED pattern (Fig. 6.2(d) Inset). The hybrid sample *GC1* morphology approximately retained similarities to that of the bare *CN* sample (Fig. 6.2 (e)) when observed under FESEM. This could be due to the lower weight loading of *GNP* in the nanocomposite. While the HRTEM image revealed the intimate fusion of C_3N_4 and graphene sheets where the dark dense area represents the *CN* sheets and the semi-transparent region displays the *GNP* sheets (Fig. 6.2 (f)). A close investigation of diffraction rings unveils the semi-crystalline framework of the hybrid material.

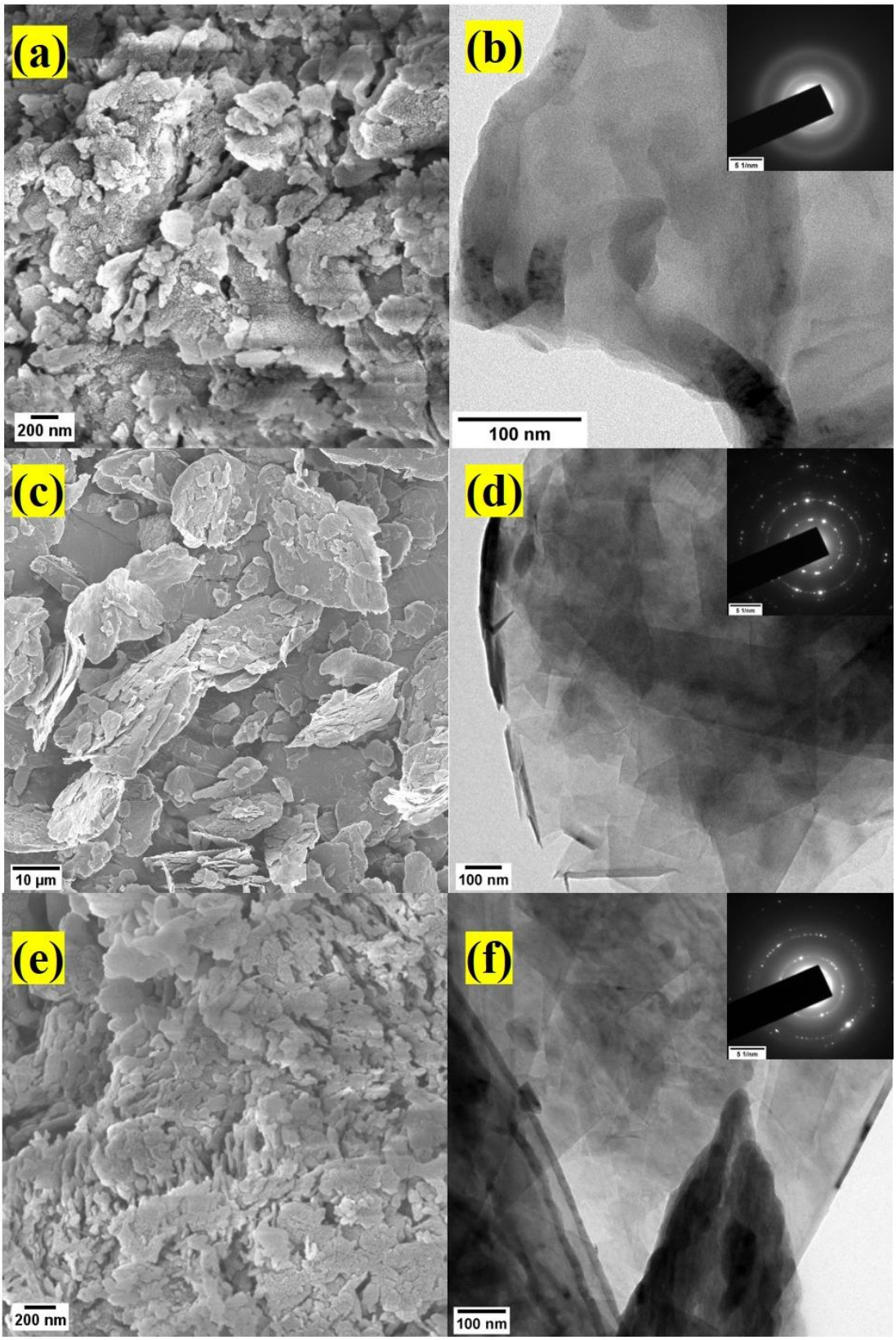

Figure 6.2 *FESEM micrograph and HRTEM image with SAED pattern (inset) of CN (a, b), GNP (c, d) and GC1 (e, f), respectively.*

The optical absorbance of the samples was measured through the UV-DRS technique (Fig. 6.3(a)). From the graph, it was observed that the incorporation of *GNP* has manifested exceptional absorbance in the visible zone as compared to the conventional g-C_3N_4 sample. Furthermore, pristine graphene does not possess a bandgap due to its symmetrical structure of non-equivalent carbon atoms [21]. To overcome this problem and create an energy band gap in graphene, it is usually coupled with other 2D materials forming heterostructures [22]. From Fig. 6.3(b), the bandgap energies of *CN*, *GC1*, *GC2*, *GC3,* and *GC4* are 2.96 eV, 2.92 eV, 2.89 eV, 2.87 eV, and 2.85 eV respectively. The incorporation of GNP has resulted in the reduction of the energy bandgap of *GC* samples. This is attributed to the large crystallite size of *GNP* as discussed in the previous section [23]. Apart from this, there also exists an intrinsic imbalance in the charges at the interface, thus resulting in band-bending and electrostatic charge adsorption onto any of the constituent materials in the composite sample [24].

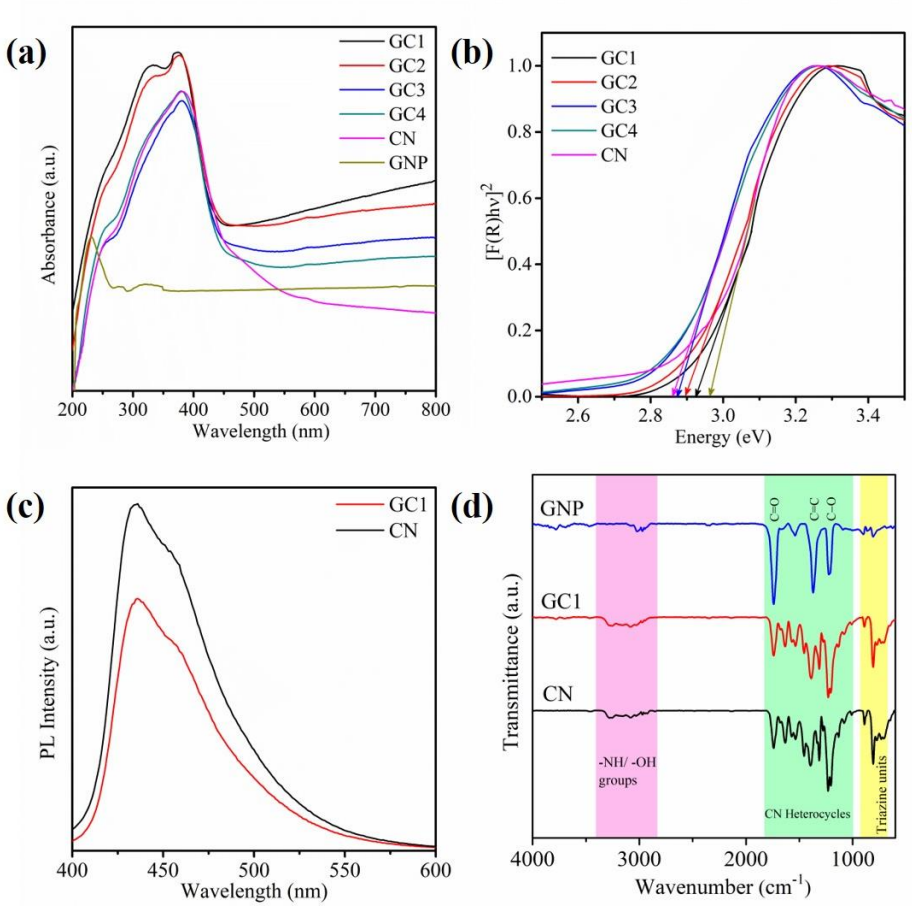

Figure 6.3 *(a) UV-DRS spectra, (b) the KM plot, (c) the PL spectra and (d) the FTIR spectra of CN, GNP, and GC samples.*

The photogenerated carrier's behaviour was analysed using a PL spectrometer. From Fig. 6.3(c) it was observed that under 365 nm of excitation, the *GC1* sample showed lower PL intensity as compared to that of the neat *CN* material. This implies that photogenerated charge carriers have longer lifetimes in the hybrid photocatalyst than the pristine g-C_3N_4 because of the presence of *GNP* which helps in delaying the recombination process by acting as a trap to these photogenerated charges [11].

The chemical structure analysis of *CN*, *GNP*, and *GC1* samples was examined using the FTIR technique (Fig. 6.3(d)). The *CN* sample showed the characteristic significant strong peaks between 1000 -1800 cm^{-1} related to the aromatic structure of CN heterocycles [25]. A strong peak around 810 cm^{-1} is assigned to the triazine blocks present in the C_3N_4 architecture [26]. The weaker peaks at longer wavenumbers are attributed to the uncondensed amino groups or hydroxyl groups present on the edges of this aromatic architecture [27]. On the other hand, the *GNP* showed three strong bands at 1735 cm^{-1}, 1368 cm^{-1}, and 1218 cm^{-1} which are ascribed to the C=O, C=C, and C—O bonds respectively. These chemical bonds could have resulted during the intercalation process [28,29]. It was observed that the amalgamation of *GNP* and *CN* did not modify the chemical structure of the pure g-C_3N_4. This could be due to the smaller portion of *GNP* loading in the nanocomposite [30].

The XPS studies of *CN*, *GNP*, and *GC1* samples are displayed in Fig. 6.4. The wide scan survey spectra of *CN* and *GC1* show an identical pattern and affirm the presence of C, N, and O elements [31]. Besides, *GNP* majorly consists of C elements and around 5.7% of O. This could be possibly due to the oxygen functional groups as discussed earlier. The deconvoluted C1s spectra of *CN* and *GC1* samples show 3 peaks around ~284 eV, ~287 eV, and ~293 eV which are attributed to the characteristic graphitic C(sp^2), C – $(N)_3$ in the CN aromatic skeleton, and C attached to the -NH_2 groups respectively [32]. Further, the N1s deconvoluted spectra of *CN* and *GC1* samples also showed 3 peaks at ~398 eV, ~400 eV, and ~404 eV which are designated peaks for pyridinic N (C=N—C) that is, N (sp^2) in aromatic rings, tertiary N-containing groups [N—$(C)_3$], and N—H species respectively [33,34]. Apart from this, the O1s spectra show a single peak at 532.5 eV for all the samples which in the case of *CN* and *GC1* was assigned to surface adsorbed oxygen [35] whereas for *GNP* this was due to the existence of oxygen groups attached to the graphene structure [20]. Due to lower amounts of *GNP* loading, there was no substantial change in the C/N ratio for *CN* and *GC1* samples (Table 6.2) [18].

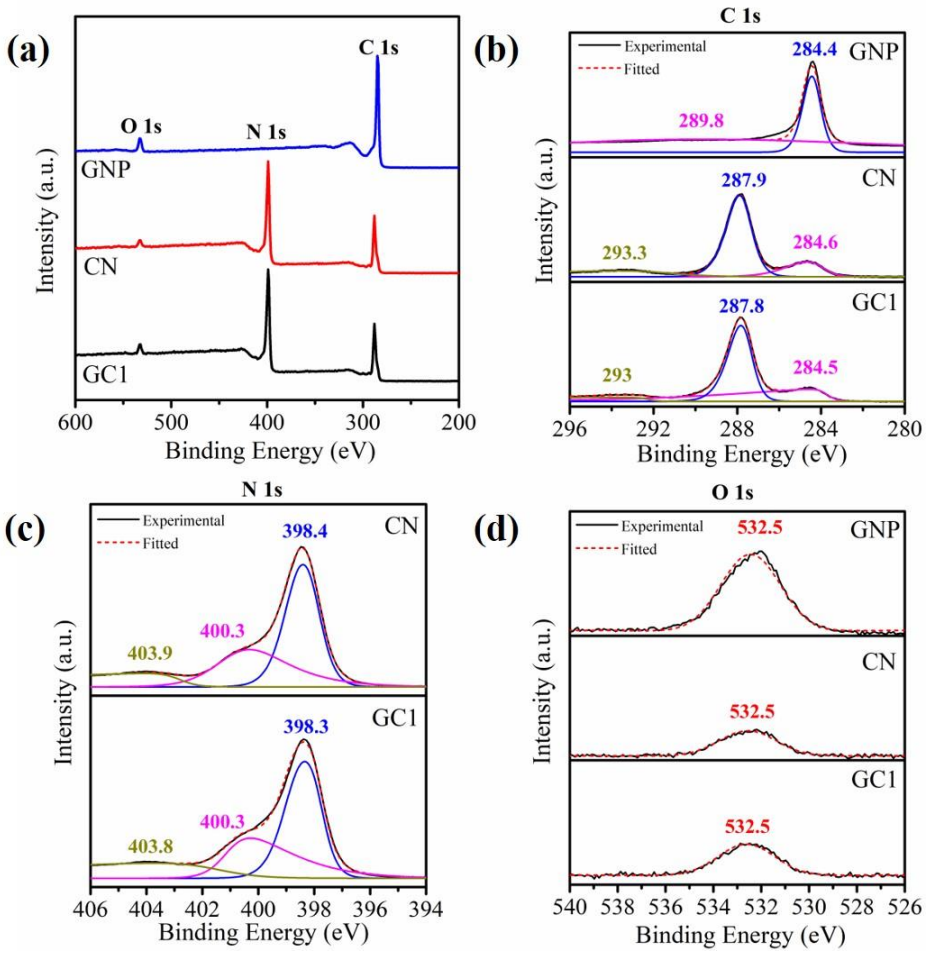

Figure 6.4 *XPS spectra of CN, GNP, and GC1 samples.*

Table 6.2 Elemental composition of CN, GNP and GC1 samples.

Sample	C1s (%)	N1s (%)	C/N Ratio	O1s (%)
CN	44.48	53.01	0.83	2.51
GC1	42.56	53.62	0.79	3.82
GNP	94.3	-	-	5.7

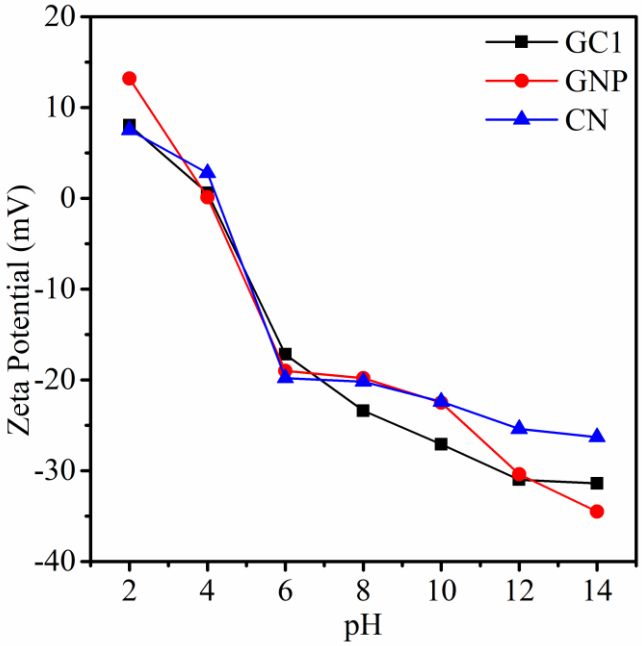

Figure 6.5 *Zeta potential values at various pH values of CN, GNP, and GC1 samples.*

Zeta potential studies are crucial and help in finding the electrostatic charge polarity on the surface of the photocatalyst in an aqueous phase [36]. For this, one must calculate the isoelectric point (IEP) [37], which is known as the point of zero surface charge *i.e.,* the value of the pH of the solution where the total surface charge is zero. Typically, all the material possesses a net positive surface charge below the IEP and a net negative charge above this point. This value helps in choosing the target pollutant *i.e.*, the target pollutant must possess an opposite charge as that of the photocatalyst to develop electrostatic forces of attraction between the photocatalyst and the pollutant. Fig. 6.5 shows the IEP measurements for *CN*, *GC1*, and *GNP* samples. It was noticed that all the samples possessed zero surface charge when the pH of the solution was around 4. This means the photocatalyst will attain a negative charge in the solution having a pH value greater than 4 and vice-versa. In g-C_3N_4, the synergy between the primary, secondary, and ternary amine groups with photogenerated carriers decides the overall surface charge for a given pH value [38]. Therefore, the target pollutant must have an overall positive charge for efficient photodegradation (Since the pH of the solution is neutral during the experiments).

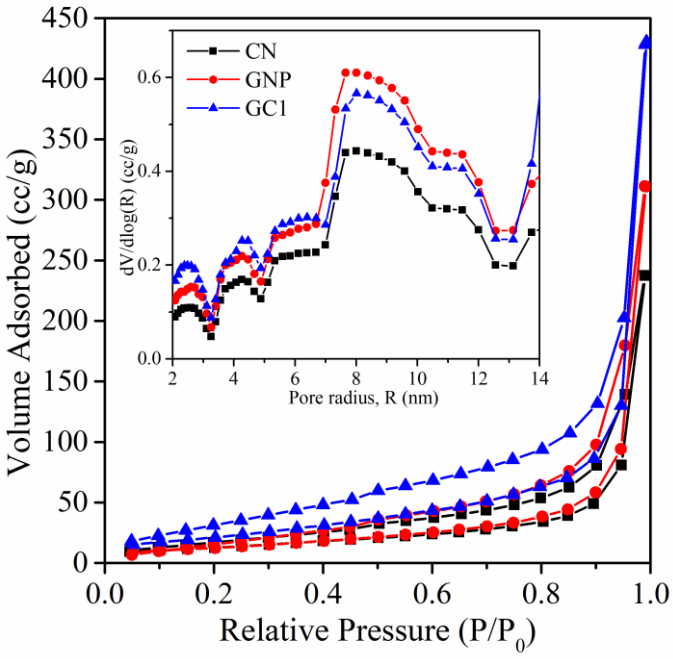

Figure 6.6 *N_2 adsorption-desorption isotherms with the inset showing pore radii distribution of CN, GNP and GC1 samples.*

The N_2 adsorption-desorption studies were carried out to calculate the specific surface area (SSA), average pore size and volume of *CN*, *GNP*, and *GC1* samples. From Fig. 6.6, it can be realised that all the samples obey Type-IV isotherm, under the IUPAC classification following the H4 hysteresis loop which is mainly recognised to the predominance of mesoporous structure [39]. From Table 6.3, it can be noticed that with the addition of *GNP* to *CN*, the SSA remarkably increased leading to a larger pore volume. This could be possibly due to a large number of mesopores as shown in the pore size distribution plot (Fig 6.6(Inset)). Therefore, higher SSA renders higher surface sites for pollutant adsorption thus leading to faster degradation [40].

Table 6.3 SSA (Specific surface area), average pore radius and pore volume of CN, GNP, and GC1 samples.

Sample	SSA, (m^2/g)	Pore Radius R (nm)	Pore Volume V (cc/g)
CN	69	15.32	0.367
GNP	48	19.97	0.480
GC1	83	16.03	0.665

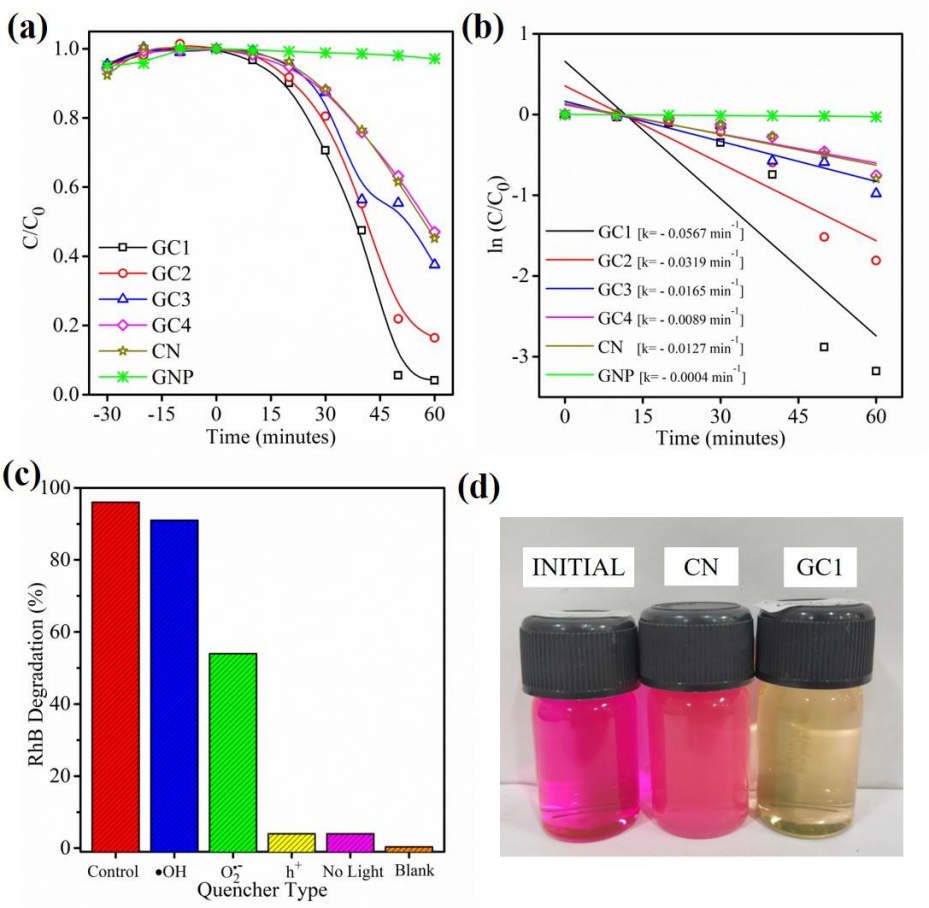

Figure 6.7 *(a) Dye degradation studies of all the samples, (b) 1st-order reaction kinetics curve of all the samples, (c) radical trapping experiment of GC1 sample using different trapping agents, and (d) RhB dye solution images post photodegradation experiment.*

The photocatalytic activity of *GC* samples was inspected by mineralizing RhB dye under visible light and studied with the help of degradation curves (Fig. 6.7(a)). For reference, the photodegradation performance of *CN* and *GNP* was also carried out under similar experimental conditions. The dye removal efficiencies of *GC1*, *GC2*, *GC3*, *GC4*, *CN*, and *GNP* after 60 minutes of visible light illumination were 96%, 84%, 62%, 53%, 55%, and 3% respectively. Thus, indicating high photodegradation activity by the *GC1* sample. So, the infinitesimal addition of *GNP* showed remarkably almost complete degradation of RhB within 60 minutes. However, the pristine *CN* sample displayed minimal performance. The increase in loading of *GNP* showed a gradual decrease in the degradation efficiency which could be ascribed to the excess of *GNP* sheets over the *CN* sheets thereby blocking its surface from absorbing the visible light [41]. However, the modification with *GNP* has favoured the charge separation conditions [42]. The present work has been compared with some of the previously reported works using different pollutants as given in Table 6.4.

The photocatalytic reaction rate was calculated by applying pseudo-1st order reaction kinetics (Fig. 6.7(b)) [ln (C/C_0) = -kt, here k (min^{-1}) is the reaction rate const.] where *GC1* possessed 4.5 times higher rate const. (k= 0.0567 min^{-1}) than that of pristine *CN* (k= 0.0127 min^{-1}). Moreover, the reactive species quenching experiments were carried out to further investigate the degradation mechanism (Fig. 6.7(c)). For this study, 10 mM of Ammonium Oxalate, p-Benzoquinone (p-BQ), and Isopropanol (IPA) (Sigma Aldrich, Purity < 95%) was added separately at the beginning of the experiment to quench the photogenerated superoxide anion ($\bullet O_2^-$), holes (h^+), and hydroxyl radical (•OH) species respectively. It was noticed that photogenerated holes majorly influenced the photodegradation process (η=4%) as compared to other reactive species whose influence was moderate. Besides, during adsorption and photolysis experiments, a negligible amount of dye degradation happened. On this note, a theoretical mechanism was proposed in the later section. The images of the final solution are shown in Fig. 6.7(d) where it is visible that the *GC1* sample has completely eradicated the dye whereas, the pristine sample has merely performed.

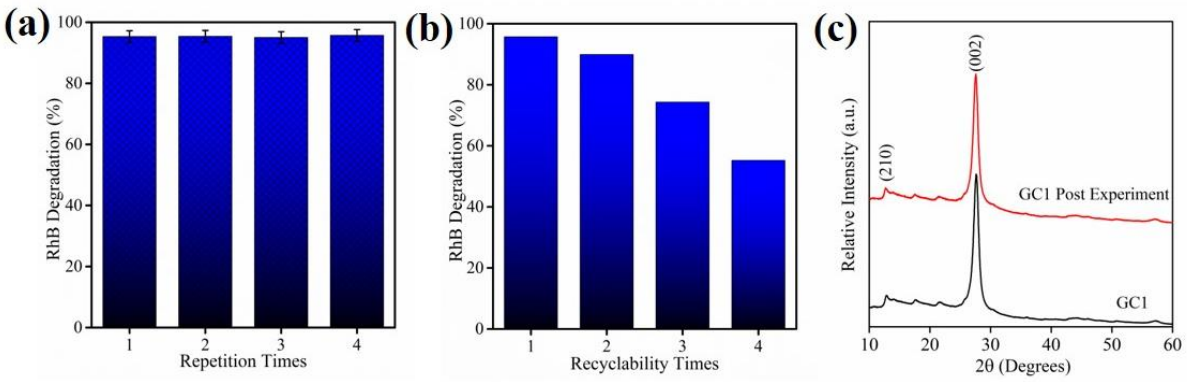

Figure 6.8 *(a, b) Repeatability and recyclability of GC1 photocatalyst sample for RhB degradation and (c) XRD pattern of GC1 sample before and after photodegradation experiments.*

The consistency of the prepared photocatalyst material was tested consecutively for 4 times and it was seen that the material holds great repeatability against RhB degradation (Fig. 6.8(a)). The reusability of the *GC1* sample was carried out for 4 times and it was noticed that after each cycle there was a notable amount of decrease in the overall degradation efficiency (Fig. 6.8(b)). This could be mainly due to the loss of material during the collection and drying process. The crystal structure of the *GC1* sample post-experiment was studied under XRD (Fig. 6.8(c)) and was found that there was no sign of any structural modifications after the photodegradation experiment implying material stability against external environments.

Table 6.4 Comparative study of present work with some of the published literature.

S. No.	Graphene Loading (%)	Target Pollutant	**Target Conc.** (mg/L)	**Time** (Minutes)	**Degradation** (%)	Ref. No.
1	0.5	TCH (Tetracycline hydrochloride)	15	120	~ 100	[11]
2	0.25	BPA (Bisphenol A)	5	45	~ 92.2	[18]
3	N/A	MB (Methylene Blue)	0.2	51	87	[30]
4	5	Nizatidine	5	20	85	[43]
5	**0.1**	**RhB**	**20**	**60**	**96**	**This work**

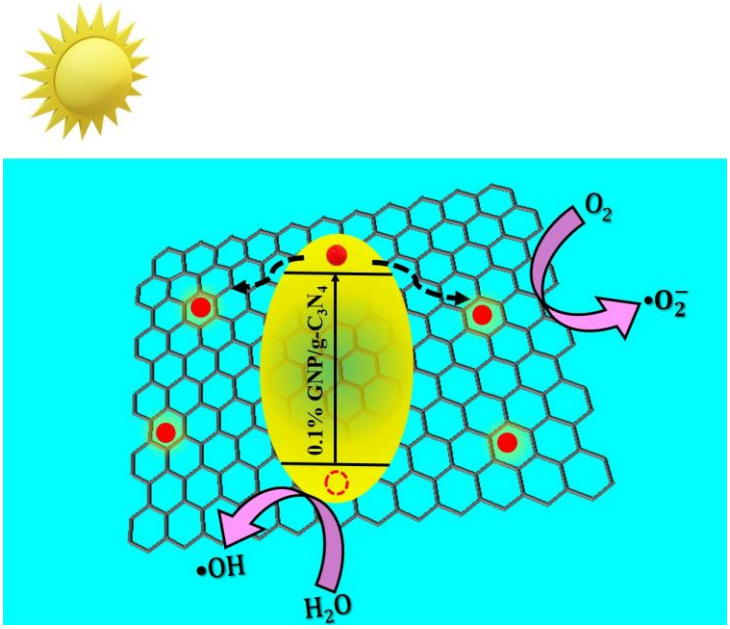

Figure 6.9 *Possible mechanism for RhB degradation in GC1 sample.*

From the earlier discussions, a probable photodegradation mechanism has been realized as shown in Fig. 6.9. When the energy of suitable wavelength is incident on the material, electron-hole pairs are generated where photogenerated electrons travel through the energy gap to reach the conduction band (CB) and holes stay back in the valence band (VB). In pristine g-C_3N_4, after this step, a major amount of photogenerated carriers are recombined resulting in poor photodegradation performance. However, due to the addition of *GNP*, the charge

recombination issue was effectively counter-attacked. In this case, the photogenerated electron after reaching the CB immediately gets migrated towards the *GNP* sheets due to its remarkable conductivity and electron storing capability [44]. Besides, the flat band potentials were slightly lowered with the inclusion of *GNP*. From the electronegativity equations [45], the flat band potentials for *CN* were found to be: E_{CBM} = -1.31 eV; E_{VBM} = 1.65 eV and for *GC1* it was: E_{CBM} = -1.29 eV; E_{VBM} = 1.67 eV where E_{CBM} and E_{VBM} are CB minimum and VB maximum respectively. The slight shift of VB towards the positive direction greatly influences the photo-oxidation process thereby enhancing the overall efficiency [46]. Therefore, the enhanced performance of the nanocomposite can be accredited to the remarkable SSA, greater visible light absorption, better carrier lifetime and efficient charge separation.

6.2.2 hBN/g-C_3N_4 hybrid photocatalyst for RhB photodegradation studies

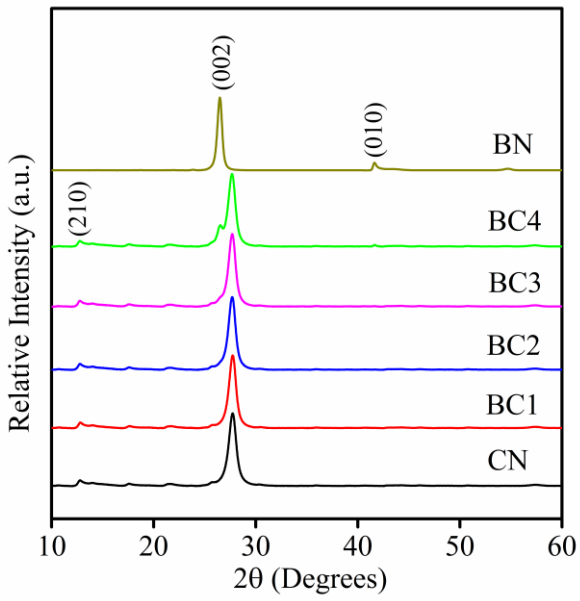

Figure 6.10 *XRD diffractogram patterns of as-prepared BN, CN and BC samples.*

The crystal structure and phase information of the as-prepared *CN*/*BN* nanocomposites were investigated by studying the XRD diffractogram as shown in Fig. 6.10. The pristine *CN* sample showed two significant peaks at 12.8° and 27.7° corresponding to (210) and (002) planes typically matching the ICDD PDF: 00-066-0183 pattern and presuming orthorhombic structure [47]. Besides, the pristine *BN* sample XRD pattern fits well with the ICDD PDF: 98-016-8894 pattern possessing a hexagonal crystal structure containing one prominent peak at 26.4°, attributing to the (002) plane. No substantial variation in the diffraction pattern was observed

for all the *BC* samples. However, a small shoulder peak was observed at 26.5° in the *BC*4 sample, attributed to the pristine *BN* (002) phase. The average crystallite size of *BC* samples was slightly larger than the pristine *CN* sample which was typically due to the addition of *BN* (Table 6.5). Besides, the interplanar distance of *BC* samples decreased infinitesimally than that of *CN* samples due to the presence of BN. These results propound that incorporating *BN* did not influence the phase information and crystal structure of *BC* samples, and that could be plausibly due to the infinitesimal loading amounts of *BN* material [48].

Table 6.5 The interlayer distance, d and the crystallite size, D, of the as-prepared CN, BN, and BC samples.

Sample	Interplanar spacing d (nm)	Crystallite Size D(nm)
CN	0.325	7.6
***BC*1**	0.321	10.06
BC2	0.322	9.92
***BC*3**	0.322	10.06
***BC*4**	0.322	9.72
BN	0.336	15.16

The morphological studies of *CN*, *BN* and *BC2* were carried out using FESEM and HRTEM techniques. The FESEM micrograph of *CN* (Fig. 6.11(a)) showed flake-like structures closely packed together, resulting in aggregation. Similarly, the HRTEM image (Fig. 6.11(b)) revealed thin layers with curled edges with obvious diffused fringe patterns (Fig. 6.11(b), Inset), indicating the amorphous nature of the material and thus, confirming the bulk g-C_3N_4 morphology formation by polycondensation method [49]. From 6.11(c, d), it was understood that the *BN* structure consists of small stackings of platelet-like design arranged compactly, resulting in aggregation of *hBN* sheets. The selected area electron diffraction (SAED) pattern exhibited a semi-crystalline nature of the material (Fig. 6.11(d) Inset) [50]. The FESEM technique could not find the hybrid structure in the case of the *BC2* sample, as shown in Fig. 6.11(e). This could probably be due to the selected area dependency of the characterization technique. However, the HRTEM image showed the hybrid structure formation with slight semi-crystallinity, as shown in the SAED pattern. A close observation of Fig. 6.11(f) discovered that the *BN* sheets were nicely ingrained onto the *CN* sheets, clearly showing the 2D-2D interactions between the *hBN* and g-C_3N_4 [51,52].

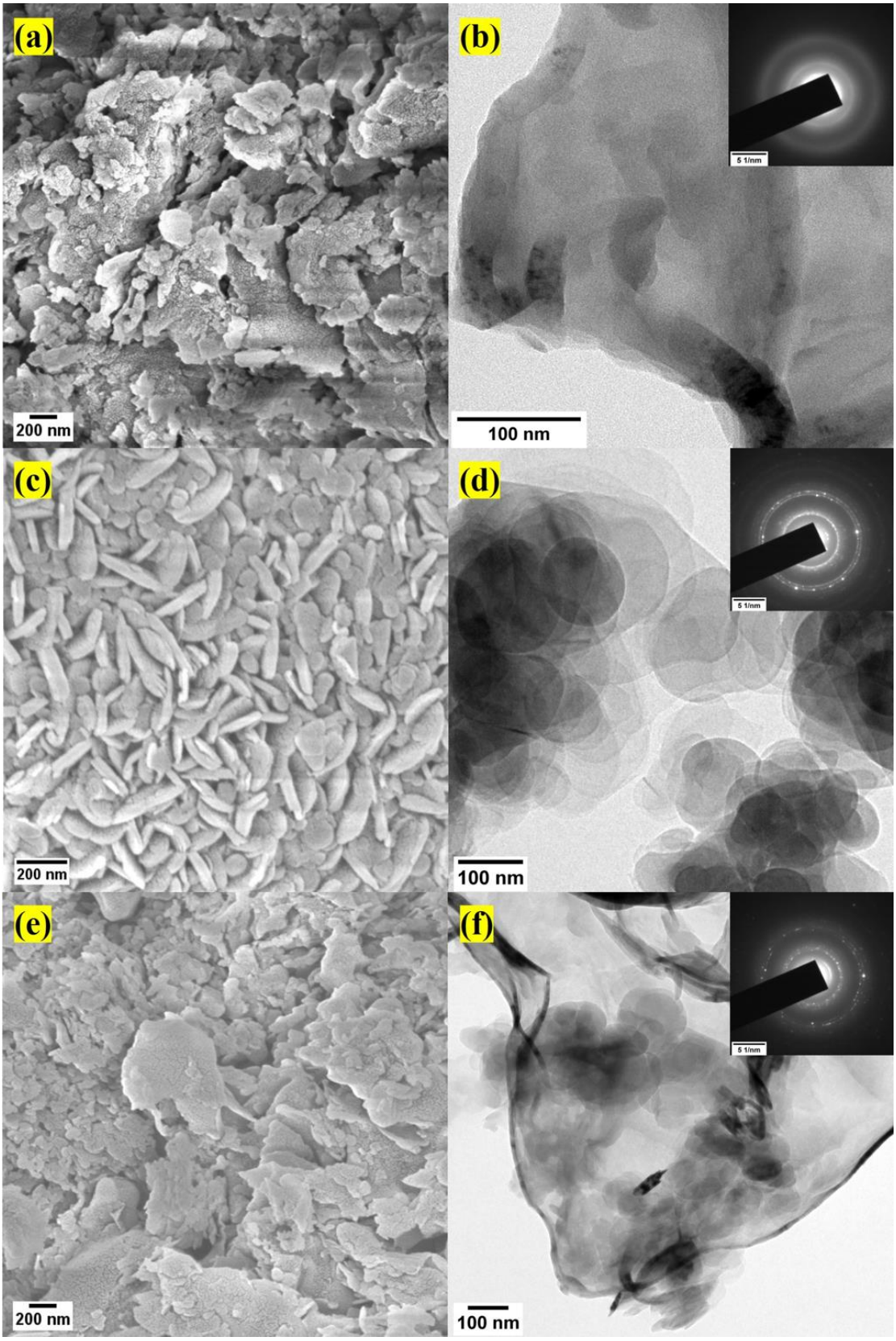

Figure 6.11 *FESEM micrograph and HRTEM image with SAED pattern (inset) of CN (a, b), BN (c, d) and BC2 (e, f), respectively.*

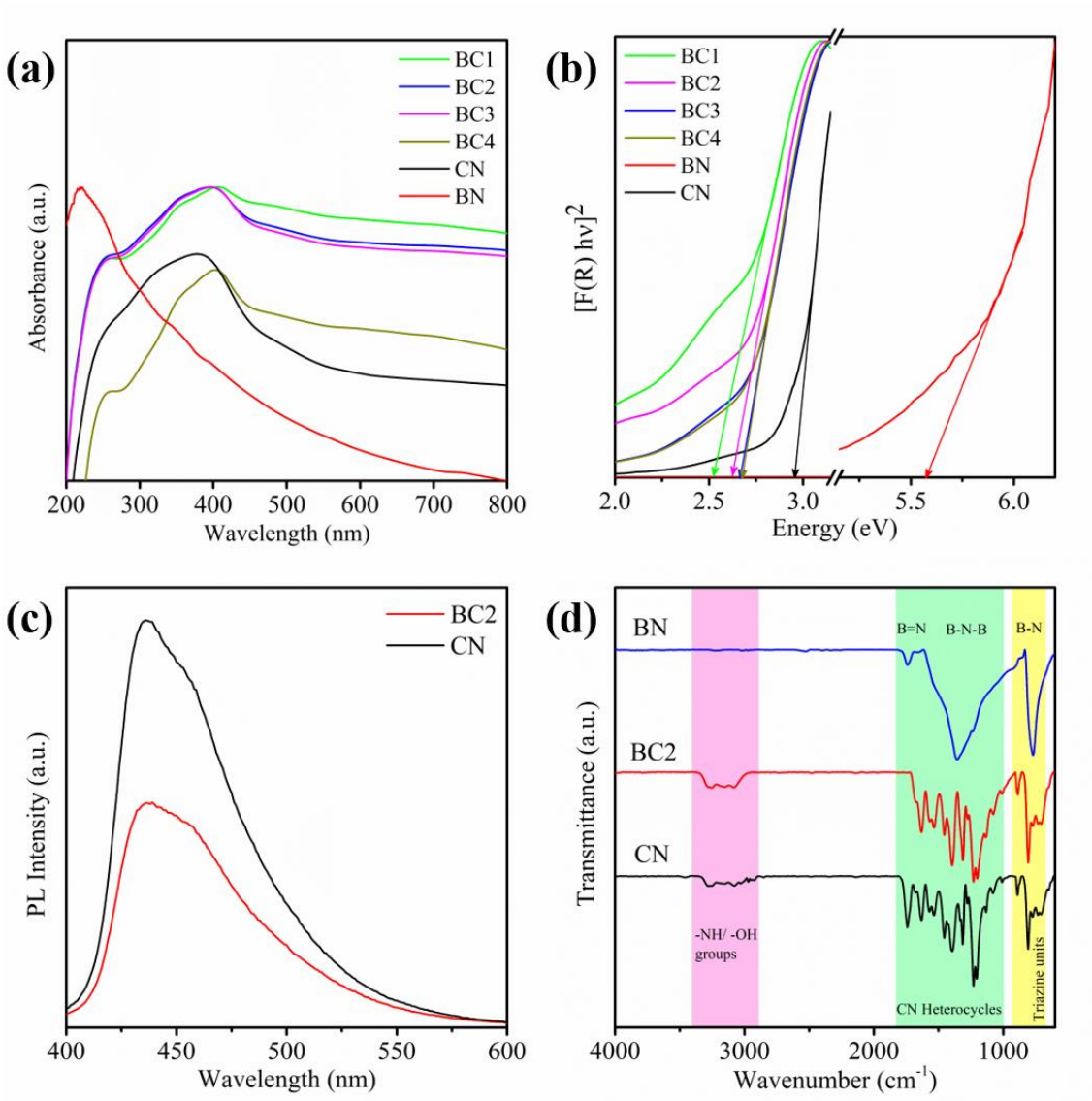

Figure 6.12 *(a) UV-DRS spectra, (b) the K-M plot, (c) the PL spectra and (d) the FTIR spectra of CN, BN, and BC samples.*

The optical behaviour of all the samples was initially investigated using the UV-DRS technique (Fig. 6.12(a)). All the *BC* samples have manifested remarkably enhanced light-harvesting capability across the visible region compared to that of the pristine *CN*. As evident, the *BN* sample exhibited minimal absorbance in the visible spectrum. The optical bandgap (E_g) of the *BC* samples was slightly lower as compared to the *CN* sample. This could be due to the size of the *BC* samples, as discussed in the earlier section [52]. Another possible reason could be attributed to the local imbalance in the charge neutrality at the interface, causing band-bending or electrostatic charges adsorbed to *BN* or *CN* components in the composite samples [53]. The calculated bandgap values of *BC*1, *BC2*, *BC*3, *BC*4, *CN* and *BN* from the KM plot were 2.52 eV, 2.62 eV, 2.66 eV, 2.67 eV, 2.95 eV and 5.57 eV, respectively (Fig. 6.12(b)). The

E_g values in the *BC* samples suggest good interaction of the *BN* with *CN* which may be due to the structural and morphological modifications between these materials at optimal ratio [54].

The photogenerated charge carrier efficiency was examined by analysing the samples under a fluorimeter Fig. 6.12(c) shows the PL spectra of the *CN* and *BC2* sample under an excitation wavelength of 365 nm. A low PL intensity usually implies a reduced photo-induced electron-hole pair recombination rate. Clearly, the *BN*-modified photocatalyst showed significantly lowered PL intensity relative to the pristine *CN*, thus suggesting a notable drop in the charge recombination rate [55].

The chemical structure of the samples was studied under an FTIR spectrophotometer (Fig. 6.12(d)). Strong absorption peaks in the *CN* and *BC2* samples revealed their molecular structure. Multiple intense bands at 810 cm^{-1}, between 100-1700 cm^{-1} and 3000-3300 cm^{-1} attributed to the breathing modes of triazine units, stretching modes of C-N heterocyclic structures and the vibrational modes of O-H and N-H bonds of the uncondensed amino groups in the C_3N_4 network [56,57]. Besides, the pure *BN* sample showed two significant sharp peaks at around 773 cm^{-1} and 1360 cm^{-1}, corresponding to B-N-B out-of-plane bending vibrational mode and B-N in-plane stretching vibrational modes, respectively [58]. Due to the infinitesimal incorporation of *BN* in *BC* samples, no additional peaks induced by *BN* loading were detected, suggesting that the g-C_3N_4 structure was well preserved [59].

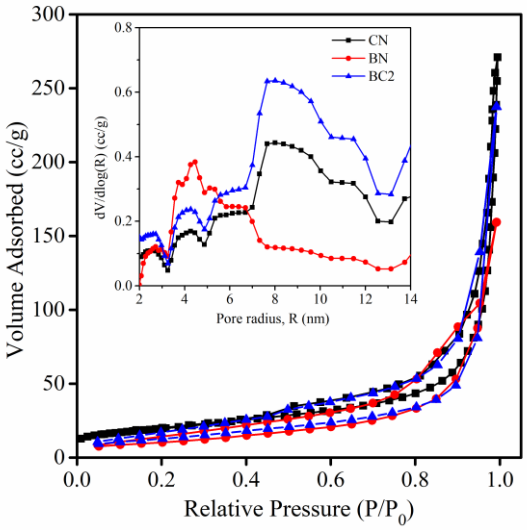

Figure 6.13 *N_2 adsorption-desorption isotherms with the inset showing the pore size distribution of CN, BN and BC2 samples.*

The N_2 adsorption-desorption isothermal studies were carried out for *CN*, *BN* and *BC2* samples, as shown in Fig. 6.13. All three samples showed mesoporous morphology with an average pore size between 2-50 nm (Table 6.6). However, the specific surface area of the *BC2* sample was slightly lower than the pristine CN sample, the pore volume was relatively higher than pristine CN due to the presence of smaller pores as shown in the distribution curve (Fig.6.13 inset). Lower specific surface area could be attributed to the blockage of pores due to the addition of *hBN* to g-C_3N_4 [60]. Nevertheless, the overall specific surface area value was still notable in providing abundant active sites on the surface of the photocatalyst. All the samples possessed type IV isotherm adhering to the H4 hysteresis loop [61].

Table 6.6 SSA, average pore radius and pore volume of CN, BN, and BC2 samples.

Sample	S_{BET}, (m^2/g)	Pore Radius R (nm)	Pore Volume V (cc/g)
CN	69	15.32	0.36
BN	39	12.73	0.24
BC2	64	17.43	0.55

The elemental composition, chemical structure, and oxidation states of the as-synthesized *BN*, *CN* and *BC2* samples were analysed using the XPS technique. As shown in Fig. 6.14(a), the wide scan spectra of these samples confirmed the presence of C, N, B and O elements. The survey scan also noticed that the *BC2* sample did not contain any traces of B element. However, a narrow scan showed a small peak at the energy position corresponding to the photoelectron line of the B element, thus, confirming the presence of boron in the composite samples.

The C1s spectra (Fig. 6.14(b)) of these samples showed one expected peak at 284 eV designated to the pristine C element. The peaks around 288 eV and 293 eV are attributed to the sp^2 hybridized C in triazine or heptazine moieties in the C_3N_4 network and the carbon attached to the uncondensed $–NH_2$ groups [62]. The N1s spectrum (Fig. 6.14(c)) of *BN* contained one sharp peak at 398 eV corresponding to the N–B bond in the *BN* structure. In the case of *CN* and *BC2*, the N1s spectra were deconvoluted into three peaks situated at 398 eV, 400 eV and 404 eV assigned to pyridinic N (C=N–C) that is sp^2 bonded N in C-N aromatic rings, tertiary N ($N–C_3$) and N–H species respectively in the C_3N_4 architecture [63,64]. From the B1s

spectrum (Fig. 6.14(d)), it was noticed that one sharp, intense peak at 190 eV was assigned to the B-N bond, and the *BC2* sample, too, showed a low-intensity peak at the same position [65]. The O1s spectra (Fig. 6.14(e)) showed a less intense peak at 532 eV due to the surface adsorbed moisture or dust during the analyses [66]. Table 6.7 shows the elemental composition of all the samples. It was observed that the C/N ratio remained unchanged in the case of the *BC2* sample, which could be due to the small amounts of BN addition.

Table 6.7 Elemental composition of BN, CN and BC2 samples.

Sample	C1s (%)	N1s (%)	C/N Ratio	O1s (%)	B1s (%)
BN	7.75	40.33	-	4.49	47.43
CN	44.48	53.01	0.83	2.51	-
BC2	42.84	52.66	0.83	3.84	0.66

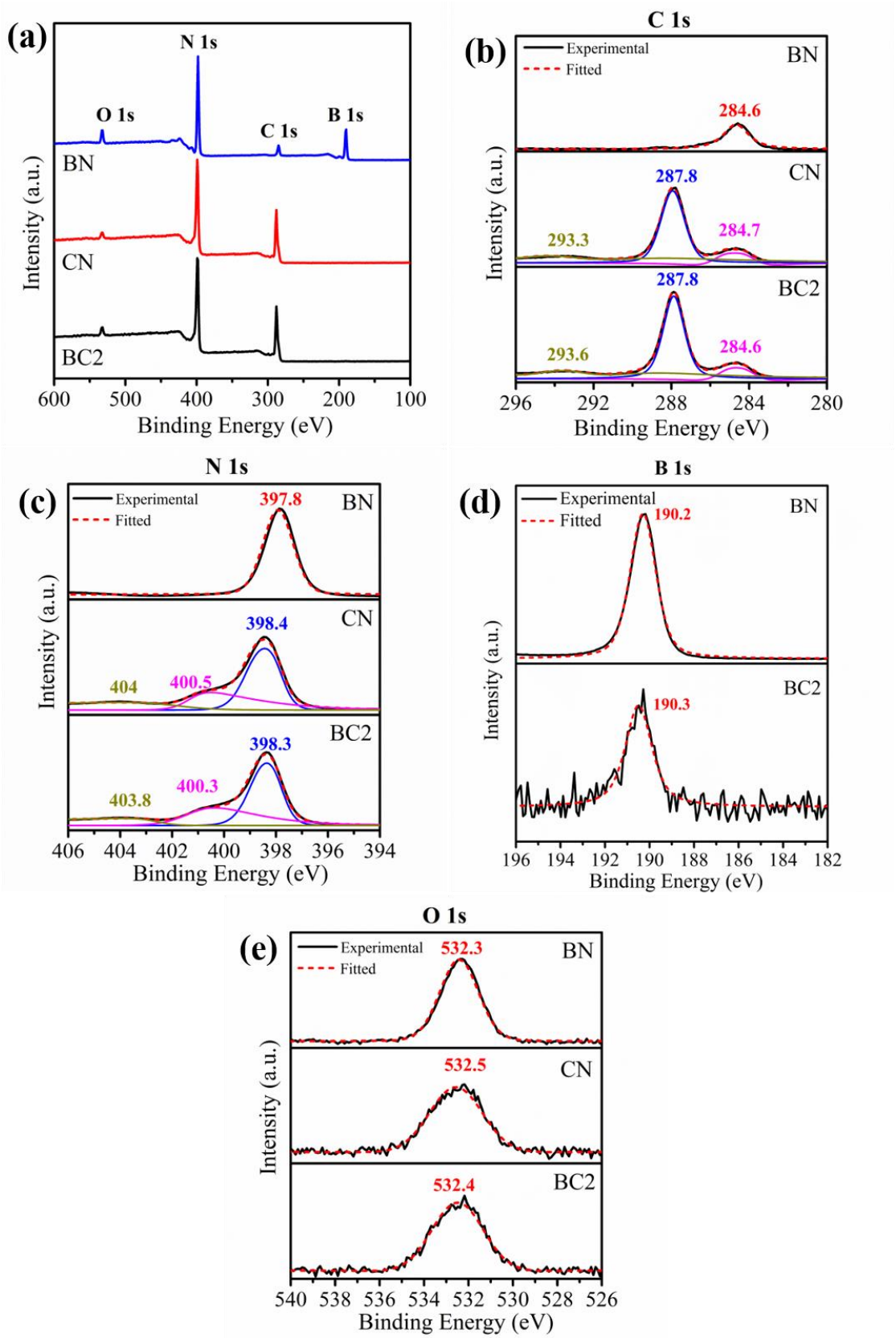

Figure 6.14 *XPS spectra of BN, CN, and BC2 samples.*

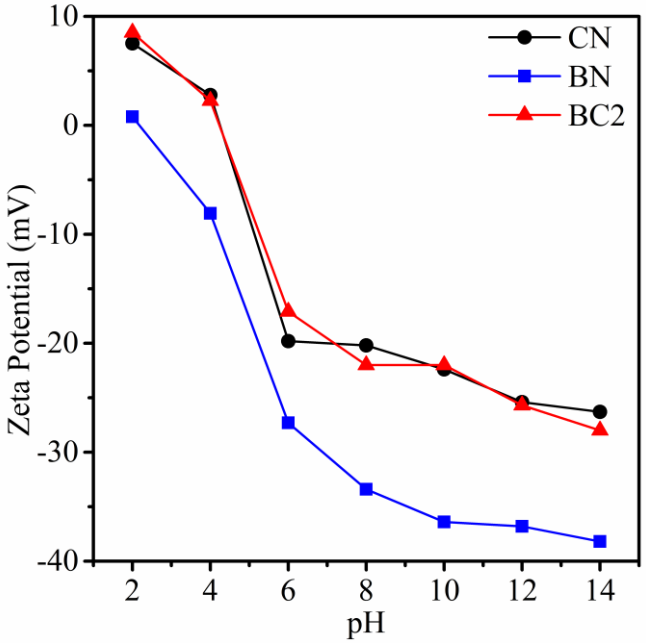

Figure 6.15 *Zeta potential values at various pH values of BN, CN, and BC2 samples.*

The overall photocatalytic performance of a material also depends on the net electrostatic charge on the photocatalyst surface. To understand better, it is crucial to calculate a critical physicochemical property called the isoelectric point (IEP) of the material. IEP is the pH value of the solution for a given solute where the net surface charge is zero [67]. It is obtained by measuring the zeta potential by varying the pH values. From the graph (Fig. 6.15), the IEP values for *BN*, *CN* and *BC2* were found to be 2.14, 4.23 and 4.22, respectively, meaning that the material holds a net positive charge below a net negative charge above this point. For better adsorption, the target pollutant must possess an opposite surface charge with respect to the photocatalyst material at a given pH value. Hence, zeta potential studies are crucial in deciding the target contaminant. In the g-C_3N_4 network, the interactions of the primary, secondary, and tertiary amine groups with the photogenerated electron-hole pairs determine the overall surface charge at a given pH value [68].

The photocatalytic degradation activity of *BC* samples was investigated by neutralising RhB (Conc. 20 mg/L) under visible light irradiation. For reference, the photodegradation performance of *BN* and *CN* was also evaluated under identical experimental conditions. The solution, including the pollutant and the photocatalyst, was stirred in aphotic conditions for about 30 minutes to attain adsorption-desorption equilibrium. From Fig. 6.16(a), the photodegradation efficiency of *hBN*-loaded samples showed better performance than the

pristine g-C_3N_4. *BC2* sample showed the highest degradation efficiency and removed 91% of RhB in 60 minutes. However, with the increase in the *hBN* loading, the performance decreased gradually. This could be attributed to the overloading of the *hBN* sheets onto g-C_3N_4, thus, shielding its surface from absorbing the visible light. Although the modification with *BN* favoured the charge separation phenomenon, the lower light harvesting condition would reduce the generation of electron-hole pairs [69]. The reaction kinetics of all the samples for RhB photodegradation were examined (Fig. 6.16(b)). All the samples fit well with the pseudo-first-order kinetics, that is, ln (C/C_0) = -kt, where C_0 is the initial concentration, C is the final concentration in mg/L at time t, and k is the apparent first-order rate constant (min^{-1}). From Table 6.8, it can be observed that there was a gradual increase in the degradation performance initially followed by a decline with further *BN* addition. A comparative study with some of the previous works has been included in Table 6.9 where similar photocatalyst material performance is compared with the present work.

Table 6.8 RhB degradation (%) and reaction rate constant 'k (min^{-1})' of as-prepared samples.

Sample	RhB Degradation (%)	Rate Constant, k (min^{-1})
***BC*1**	75	0.0239
BC2	91	0.0412
***BC*3**	90	0.0309
***BC*4**	43	0.0096
CN	55	0.0127
BN	32	0.0069

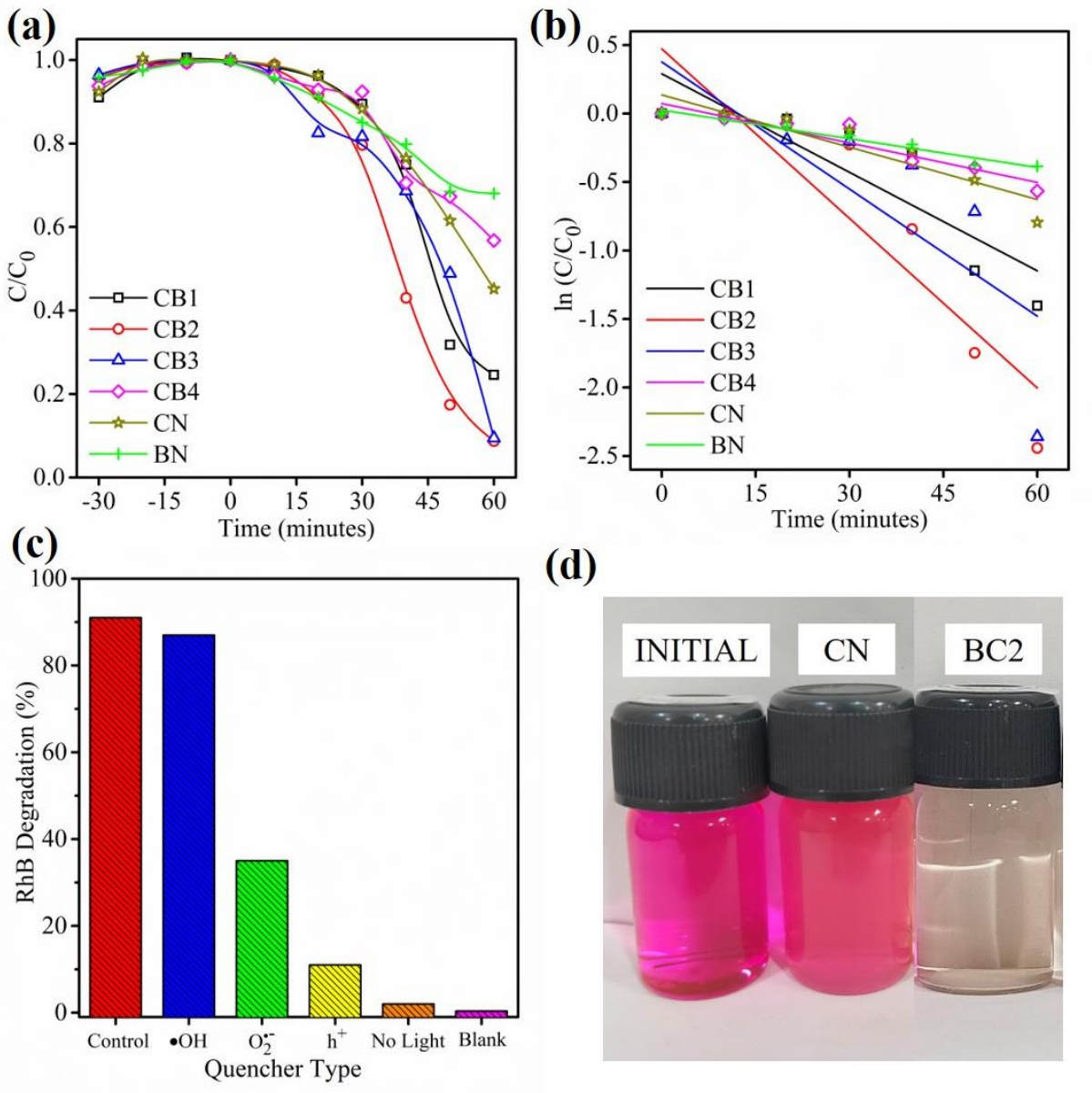

Figure 6.16 *(a) Dye degradation studies of all the prepared samples, (b) first-order reaction kinetics curve of all the prepared samples, (c) radical trapping experiment of BC2 sample using different trapping agents, and (d) RhB dye solution images post photodegradation experiment.*

Photo-induced reactive species trapping studies were carried out to explore the degradation mechanism further. It is a known fact that the photogenerated holes (h^+), superoxide anions ($\bullet O_2^-$) and hydroxyl radicals (•OH), are the exclusive participants in the photodegradation process. To probe the predominant active species, p-Benzoquinone (BQ), Ammonium Oxalate (AO) and Isopropanol (IPA) were employed as the trapping agents of $\bullet O_2^-$, h^+ and •OH reactive species, respectively. From Fig. 6.16(c), it was discovered that for the hole scavenging experiment, the photodegradation efficiency of RhB drastically dropped from 91%

to 11%, indicating that holes are the primary active species. Similarly, a considerable amount of degradation loss was observed when BQ was added, thus, verifying the superoxide radical's active role in the photodegradation mechanism. However, minor losses were noticed during IPA addition, indicating minor business of hydroxyl radicals during the experiment. The colour of the final solution of *BN*, *CN* and *BC2* is shown in Fig. 6.16(d). From the above discussion, a plausible mechanism is picturized in the later section. The repeatability and reusability experiments for the *BC2* sample were performed (Fig. 6.17 (a, b)), and it was observed that the degradation result was consistent throughout the repetitions; however, the reusability performance dropped after two runs. This could be majorly due to material loss while collecting samples for measurements. Further, the post-experimental characterization was carried out for the BC2 sample as shown in Fig. 6.17(c). It was observed that the crystal structure of the photocatalyst material was stable even after the photodegradation experiments. Thus, proving the material stability.

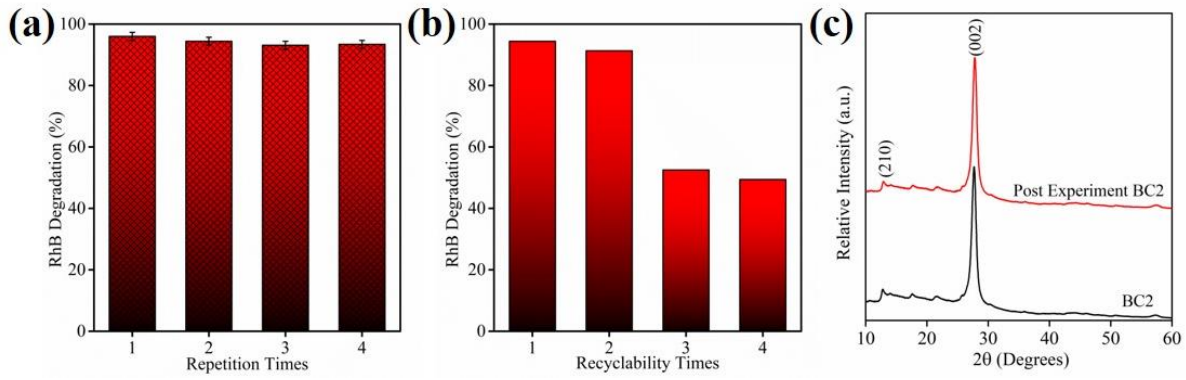

Figure 6.17 *(a, b) Repeatability and recyclability of BC2 photocatalyst sample for RhB degradation and (c) XRD pattern of BC2 sample before and after photodegradation experiments.*

Table 6.9 Comparative study of present work with some of the published literature.

S. No.	Boron Nitride Loading (%)	Target Pollutant	Target Conc. (mg/L)	Time (Minutes)	Degradation (%)	Ref. No.
1	0.5	RhB	10	120	98.2	[49]
2	0.48	TC (Tetracycline)	10	60	79.7	[50]
3	1.5	TCH (Tetracycline Hydrochloride)	40	60	91	[52]

4	3	ENFX (Enrofloxacin)	8	60	100	[54]
5	0.9	BPA	10	150	91.9	[55]
6	**0.5**	**RhB**	**20**	**60**	**91**	**This work**

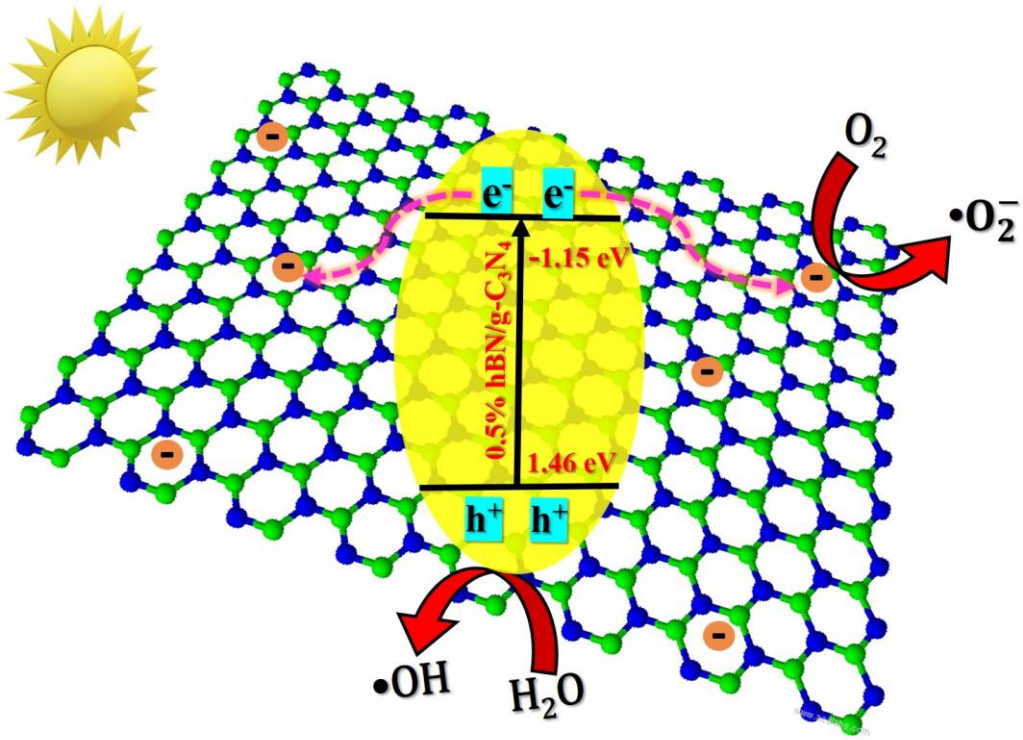

Figure 6.18 *Possible mechanism for RhB degradation in BC2 sample.*

The above discussion leads to the explanation of a possible photocatalytic degradation mechanism (Fig. 6.18). When the *BN*/*CN* hybrid is irradiated with visible light, the g-C_3N_4 gets excited and generates exciton pairs in the semiconductor photocatalyst material. The conduction and valence band edges for *CN* and *BC2* were calculated using equations 3.2 and 3.3. The conduction band edges for *CN* and *BC2* were -1.30 eV and -1.15 eV, respectively, whereas the valence band edges were 1.64 eV and 1.46 eV, respectively, for *CN* and *BC2*. After photoexcitation, the electrons in the conduction band migrate towards its surface and get rapidly transferred into the *hBN* layers due to the intrinsic nature of the boron nitride, which makes it a kind of surface passivation material to alter the behaviour of photogenerated electrons [70]. This leads to efficient charge separation and thus restricts charge recombination. At the conduction band, electrons react with the dissolved oxygen forming superoxide radicals,

thereby mineralizing the RhB. Hence, it can be acknowledged that a good surface area, better visible light absorption, higher carrier lifetime and efficient charge separation are beneficial for increasing the performance efficiency of a photocatalyst.

6.3 Conclusions

In summary, 2D/2D g-C_3N_4-based hybrid photocatalyst materials were successfully prepared using GNP and hBN by employing a one-pot thermal decomposition synthesis technique. The structural and morphological construction of the hybrid photocatalysts were validated by XRD, FESEM, and HRTEM techniques. The photocatalytic performance of the nanocomposites was applied to study RhB photodegradation under visible light irradiation for 60 minutes. It was observed that 0.1% loading of GNP showed the highest degradation performance when compared with other samples. The hybrid sample showed 4.5 times faster degradation than the pristine g-C_3N_4 sample. However, the 0.5% h-BN loading sample displayed the highest photocatalytic RhB degradation under visible light illumination for 60 minutes. Meanwhile, pristine g-C_3N_4 showed 55% of dye removal under similar experimental conditions. This enhanced photodegradation can be ascribed to the higher SSA, better visible light absorbance, and higher carrier lifetime of the hybrid material. These observations were validated by BET, UV-DRS, and PL studies respectively. Further, radical trapping experiments were conducted to propose a degradation mechanism. Moreover, the photocatalyst reusability and repeatability were also checked 4 times. This work resulted in the development of a new class of multifunctional 2D/2D visible-light active photocatalyst material and exposed a new dimension to further explore the advancements in visible-light-driven photocatalysis.

References

[1] Y. Zhang, T. Mori, L. Niu, J. Ye, Non-covalent doping of graphitic carbon nitride polymer with graphene: Controlled electronic structure and enhanced optoelectronic conversion, Energy Environ Sci. 4 (2011) 4517–4521. https://doi.org/10.1039/c1ee01400e.

[2] X. Zhang, X. Yuan, L. Jiang, J. Zhang, H. Yu, H. Wang, G. Zeng, Powerful combination of 2D g-C3N4 and 2D nanomaterials for photocatalysis: Recent advances, Chemical Engineering Journal. 390 (2020) 124475. https://doi.org/10.1016/j.cej.2020.124475.

[3] Y. Liu, H. Xiao, W.A. Goddard, Schottky-Barrier-Free Contacts with Two-Dimensional Semiconductors by Surface-Engineered MXenes, J Am Chem Soc. 138 (2016) 15853–15856. https://doi.org/10.1021/jacs.6b10834.

[4] S. Dutta, S.K. Pati, Novel properties of graphene nanoribbons: A review, J Mater Chem. 20 (2010) 8207–8223. https://doi.org/10.1039/c0jm00261e.

[5] W. Hooch Antink, Y. Choi, K.D. Seong, J.M. Kim, Y. Piao, Recent Progress in Porous Graphene and Reduced Graphene Oxide-Based Nanomaterials for Electrochemical

Energy Storage Devices, Adv Mater Interfaces. 5 (2018). https://doi.org/10.1002/admi.201701212.

[6] M. Al Kausor, D. Chakrabortty, Graphene oxide based semiconductor photocatalysts for degradation of organic dye in waste water: A review on fabrication, performance enhancement and challenges, Inorg Chem Commun. 129 (2021). https://doi.org/10.1016/j.inoche.2021.108630.

[7] A. Kausar, I. Ahmad, M.H. Eisa, M. Maaza, Graphene Nanocomposites in Space Sector—Fundamentals and Advancements, C (Basel). 9 (2023) 29. https://doi.org/10.3390/c9010029.

[8] S. Sagadevan, M.M. Shahid, Z. Yiqiang, W.C. Oh, T. Soga, J. Anita Lett, S.F. Alshahateet, I. Fatimah, A. Waqar, S. Paiman, M.R. Johan, Functionalized graphene-based nanocomposites for smart optoelectronic applications, Nanotechnol Rev. 10 (2021) 605–635. https://doi.org/10.1515/ntrev-2021-0043.

[9] Y. Li, D. Zhang, Q. Chen, C. Chao, J. Sun, S. Dong, Y. Sun, Synthesis of rGO/g-C3N4 for methyl orange degradation in activating peroxydisulfate under simulated solar light irradiation, J Alloys Compd. 907 (2022). https://doi.org/10.1016/j.jallcom.2022.164500.

[10] W.J. Ong, L.L. Tan, S.P. Chai, S.T. Yong, A.R. Mohamed, Surface charge modification via protonation of graphitic carbon nitride (g-C3N4) for electrostatic self-assembly construction of 2D/2D reduced graphene oxide (rGO)/g-C3N4 nanostructures toward enhanced photocatalytic reduction of carbon dioxide to methane, Nano Energy. 13 (2015) 757–770. https://doi.org/10.1016/j.nanoen.2015.03.014.

[11] T. Muhmood, M. Xia, W. Lei, F. Wang, M.A. Khan, Design of Graphene Nanoplatelet/Graphitic Carbon Nitride Heterojunctions by Vacuum Tube with Enhanced Photocatalytic and Electrochemical Response, Eur J Inorg Chem. 2018 (2018) 1726–1732. https://doi.org/10.1002/ejic.201800093.

[12] Y. Gu, Y. Yu, J. Zou, T. Shen, Q. Xu, X. Yue, J. Meng, J. Wang, The ultra-rapid synthesis of rGO/g-C3N4 composite via microwave heating with enhanced photocatalytic performance, Mater Lett. 232 (2018) 107–109. https://doi.org/10.1016/j.matlet.2018.08.077.

[13] W. Wang, M. Chen, D. Huang, G. Zeng, C. Zhang, C. Lai, C. Zhou, Y. Yang, M. Cheng, L. Hu, W. Xiong, Z. Li, Z. Wang, An overview on nitride and nitrogen-doped photocatalysts for energy and environmental applications, Compos B Eng. 172 (2019) 704–723. https://doi.org/10.1016/j.compositesb.2019.05.097.

[14] K. Zhang, Y. Feng, F. Wang, Z. Yang, J. Wang, Two dimensional hexagonal boron nitride (2D-hBN): Synthesis, properties and applications, J Mater Chem C Mater. 5 (2017) 11992–12022. https://doi.org/10.1039/c7tc04300g.

[15] C. Zhou, C. Lai, C. Zhang, G. Zeng, D. Huang, M. Cheng, L. Hu, W. Xiong, M. Chen, J. Wang, Y. Yang, L. Jiang, Semiconductor/boron nitride composites: Synthesis, properties, and photocatalysis applications, Appl Catal B. 238 (2018) 6–18. https://doi.org/10.1016/j.apcatb.2018.07.011.

[16] F. Fina, S.K. Callear, G.M. Carins, J.T.S. Irvine, Structural investigation of graphitic carbon nitride via XRD and neutron diffraction, Chemistry of Materials. 27 (2015) 2612–2618. https://doi.org/10.1021/acs.chemmater.5b00411.

[17] S. Hossain, W.S. Chu, C.S. Lee, S.H. Ahn, D.M. Chun, Photocatalytic performance of few-layer Graphene/WO 3 thin films prepared by a nano-particle deposition system,

Mater Chem Phys. 226 (2019) 141–150. https://doi.org/10.1016/j.matchemphys.2019.01.026.

[18] Y.H. Chen, B.K. Wang, W.C. Hou, Graphitic carbon nitride embedded with graphene materials towards photocatalysis of bisphenol A: The role of graphene and mediation of superoxide and singlet oxygen, Chemosphere. 278 (2021). https://doi.org/10.1016/j.chemosphere.2021.130334.

[19] Y. Zhang, J. Liu, G. Wu, W. Chen, Porous Graphitic Carbon Nitride Synthesized via Directly Polymerization of Urea for Efficient Sunlight-driven Photocatalytic Hydrogen Production Received (in XXX, XXX) Xth XXXXXXXXX 20XX, Accepted Xth XXXXXXXXX 20XX, (n.d.). https://doi.org/10.1039/b000000x.

[20] P. Selvarajan, M. Fawaz, C. Sathish, M. Li, D. Chu, X. Yu, M.B.H. Breesec, J. Yi, A. Vinu, Activated Graphene Nanoplatelets Decorated with Carbon Nitrides for Efficient Electrocatalytic Oxygen Reduction Reaction, Advanced Energy and Sustainability Research. 2 (2021) 2100104. https://doi.org/10.1002/aesr.202100104.

[21] X. Cao, J.J. Shi, M. Zhang, X.H. Jiang, H.X. Zhong, P. Huang, Y.M. Ding, M. Wu, Band Gap Opening of Graphene by Forming Heterojunctions with the 2D Carbonitrides Nitrogenated Holey Graphene, g-C3N4, and g-CN: Electric Field Effect, Journal of Physical Chemistry C. 120 (2016) 11299–11305. https://doi.org/10.1021/acs.jpcc.6b03308.

[22] X. Li, Y. Dai, Y. Ma, S. Han, B. Huang, Graphene/g-C3N4 bilayer: Considerable band gap opening and effective band structure engineering, Physical Chemistry Chemical Physics. 16 (2014) 4230–4235. https://doi.org/10.1039/c3cp54592j.

[23] R.E. Marotti, P. Giorgi, G. Machado, E.A. Dalchiele, Crystallite size dependence of band gap energy for electrodeposited ZnO grown at different temperatures, Solar Energy Materials and Solar Cells. 90 (2006) 2356–2361. https://doi.org/10.1016/j.solmat.2006.03.008.

[24] D. Voigt, L. Sarpong, M. Bredol, Tuning the optical band gap of semiconductor nanocomposites-A case study with ZnS/carbon, Materials. 13 (2020). https://doi.org/10.3390/ma13184162.

[25] T. Narkbuakaew, P. Sujaridworakun, Synthesis of Tri-S-Triazine Based g-C3N4 Photocatalyst for Cationic Rhodamine B Degradation under Visible Light, Top Catal. 63 (2020) 1086–1096. https://doi.org/10.1007/s11244-020-01375-z.

[26] W. Bing, Z. Chen, H. Sun, P. Shi, N. Gao, J. Ren, X. Qu, Visible-light-driven enhanced antibacterial and biofilm elimination activity of graphitic carbon nitride by embedded Ag nanoparticles, Nano Res. 8 (2015) 1648–1658. https://doi.org/10.1007/s12274-014-0654-1.

[27] H. Li, Y. Jing, X. Ma, T. Liu, L. Yang, B. Liu, S. Yin, Y. Wei, Y. Wang, Construction of a well-dispersed Ag/graphene-like g-C3N4 photocatalyst and enhanced visible light photocatalytic activity, RSC Adv. 7 (2017) 8688–8693. https://doi.org/10.1039/c6ra26498k.

[28] A.A. Kadhem, A. Al-Nayili, Dehydrogenation of Formic Acid in Liquid Phase over Pd Nanoparticles Supported on Reduced Graphene Oxide Sheets, Catalysis Surveys from Asia. 25 (2021) 324–333. https://doi.org/10.1007/s10563-021-09332-w.

[29] M. Andrade-Guel, C. Cabello-Alvarado, V.J. Cruz-Delgado, P. Bartolo-Perez, P.A. De León-Martínez, A. Sáenz-Galindo, G. Cadenas-Pliego, C.A. ávila-Orta, Surface

modification of graphene nanoplatelets by organic acids and ultrasonic radiation for enhance uremic toxins adsorption, Materials. 12 (2019). https://doi.org/10.3390/ma12050715.

[30] Q. Yu, S. Guo, X. Li, M. Zhang, One-step fabrication and high photocatalytic activity of porous graphitic carbon nitride/graphene oxide hybrid by direct polymerization of cyanamide without templates, Russian Journal of Physical Chemistry A. 88 (2014) 1643–1649. https://doi.org/10.1134/S003602441410029X.

[31] J. Kalaiyarasi, K. Pandian, S. Ramanathan, S.C.B. Gopinath, Graphitic carbon nitride/graphene nanoflakes hybrid system for electrochemical sensing of DNA bases in meat samples, Sci Rep. 10 (2020). https://doi.org/10.1038/s41598-020-69578-8.

[32] J. Zou, Y. Yu, W. Yan, J. Meng, S. Zhang, J. Wang, A facile route to synthesize boron-doped g-C 3 N 4 nanosheets with enhanced visible-light photocatalytic activity, J Mater Sci. 54 (2019) 6867–6881. https://doi.org/10.1007/s10853-019-03384-0.

[33] Y. Chai, Q. Liu, L. Zhang, J. Ren, W.L. Dai, Structure Engineered g-C3N4 Nano-Sheets by Switching the Pyrolysis Gas Atmosphere for Enhanced Photo-Catalytic Degradation, Chin J Chem. 35 (2017) 173–182. https://doi.org/10.1002/cjoc.201600608.

[34] G. Song, Z. Chu, W. Jin, H. Sun, Enhanced performance of g-C3N4/TiO2 photocatalysts for degradation of organic pollutants under visible light, Chin J Chem Eng. 23 (2015) 1326–1334. https://doi.org/10.1016/j.cjche.2015.05.003.

[35] H.Y. Xu, L.C. Wu, H. Zhao, L.G. Jin, S.Y. Qi, Synergic Effect between Adsorption and Photocatalysis of Metal-Free g-C3N4 Derived from Different Precursors, PLoS One. 10 (2015). https://doi.org/10.1371/journal.pone.0142616.

[36] M.J. Arlos, M.M. Hatat-Fraile, R. Liang, L.M. Bragg, N.Y. Zhou, S.A. Andrews, M.R. Servos, Photocatalytic decomposition of organic micropollutants using immobilized TiO 2 having different isoelectric points, Water Res. 101 (2016) 351–361. https://doi.org/10.1016/j.watres.2016.05.073.

[37] F. Azeez, E. Al-Hetlani, M. Arafa, Y. Abdelmonem, A.A. Nazeer, M.O. Amin, M. Madkour, The effect of surface charge on photocatalytic degradation of methylene blue dye using chargeable titania nanoparticles, Sci Rep. 8 (2018). https://doi.org/10.1038/s41598-018-25673-5.

[38] V.P. Madhurima, P.H. Borse, K. Kumari, T.N. Rao, P.K. Jain, Improved photocatalytic activity of carbon-based polymeric semiconductor for efficient decontamination of wastewater: Effect of reaction atmosphere and pyrolysis temperature, Opt Mater (Amst). 110 (2020). https://doi.org/10.1016/j.optmat.2020.110523.

[39] INTERNATIONAL UNION OF PURE AND APPLIED CHEMISTRY PHYSICAL CHEMISTRY DIVISION COMMISSION ON COLLOID AND SURFACE CHEMISTRY INCLUDING CATALYSIS* REPORTING PHYSISORPTION DATA FOR GAS/SOLID SYSTEMS with Special Reference to the Determination of Surface Area and Porosity Reporting physisorption data for gas/solid systems-with special reference to the determination of surface area and porosity, 1985.

[40] W. Iqbal, C. Dong, M. Xing, X. Tan, J. Zhang, Eco-friendly one-pot synthesis of well-adorned mesoporous g-C3N4 with efficiently enhanced visible light photocatalytic activity, Catal Sci Technol. 7 (2017) 1726–1734. https://doi.org/10.1039/c7cy00286f.

[41] B. Yuan, J. Wei, T. Hu, H. Yao, Z. Jiang, Z. Fang, Z. Chu, Simple synthesis of g-C3N4/rGO hybrid catalyst for the photocatalytic degradation of rhodamine B, Cuihua

Xuebao/Chinese Journal of Catalysis. 36 (2015) 1009–1016. https://doi.org/10.1016/S1872-2067(15)60844-0.

[42] G. Liao, S. Chen, X. Quan, H. Yu, H. Zhao, Graphene oxide modified g-C 3N 4 hybrid with enhanced photocatalytic capability under visible light irradiation, J Mater Chem. 22 (2012) 2721–2726. https://doi.org/10.1039/c1jm13490f.

[43] F. Al Marzouqi, R. Selvaraj, Surface Plasmon Resonance Induced Photocatalysis in 2D/2D Graphene/g-C3N4 Heterostructure for Enhanced Degradation of Amine-Based Pharmaceuticals under Solar Light Illumination, Catalysts. 13 (2023) 560. https://doi.org/10.3390/catal13030560.

[44] K. Yu, X. Hu, K. Yao, P. Luo, X. Wang, H. Wang, Preparation of an ultrathin 2D/2D rGO/g-C3N4 nanocomposite with enhanced visible-light-driven photocatalytic performance, RSC Adv. 7 (2017) 36793–36799. https://doi.org/10.1039/c7ra06210a.

[45] Y. Li, J. Wang, H. Yao, L. Dang, Z. Li, Efficient decomposition of organic compounds and reaction mechanism with BiOI photocatalyst under visible light irradiation, J Mol Catal A Chem. 334 (2011) 116–122. https://doi.org/10.1016/j.molcata.2010.11.005.

[46] Y. Li, H. Zhang, P. Liu, D. Wang, Y. Li, H. Zhao, Cross-linked g-C3N4/rGO nanocomposites with tunable band structure and enhanced visible light photocatalytic activity, Small. 9 (2013) 3336–3344. https://doi.org/10.1002/smll.201203135.

[47] F. Fina, S.K. Callear, G.M. Carins, J.T.S. Irvine, Structural investigation of graphitic carbon nitride via XRD and neutron diffraction, Chemistry of Materials. 27 (2015) 2612–2618. https://doi.org/10.1021/acs.chemmater.5b00411.

[48] E. Budak, Ç. Bozkurt, Synthesis of hexagonal boron nitride with the presence of representative metals, Physica B Condens Matter. 405 (2010) 4702–4705. https://doi.org/10.1016/j.physb.2010.08.067.

[49] J. Gu, J. Yan, Z. Chen, H. Ji, Y. Song, Y. Fan, H. Xu, H. Li, Construction and preparation of novel 2D metal-free few-layer BN modified graphene-like g-C3N4 with enhanced photocatalytic performance, Dalton Transactions. 46 (2017) 11250–11258. https://doi.org/10.1039/c7dt02092a.

[50] L. Jiang, X. Yuan, G. Zeng, Z. Wu, J. Liang, X. Chen, L. Leng, H. Wang, H. Wang, Metal-free efficient photocatalyst for stable visible-light photocatalytic degradation of refractory pollutant, Appl Catal B. 221 (2018) 715–725. https://doi.org/10.1016/j.apcatb.2017.09.059.

[51] K. Harikrishnan, G. Singh, A. Kushwaha, V.P. Singh, U.K. Gaur, M. Sharma, 2D/2D heterojunction of graphitic carbon nitride and hexagonal boron nitride nanosheets mediated electrochemical detection of hazardous hydroquinone with high selectivity and sensitivity, J Environ Chem Eng. 10 (2022) 108717. https://doi.org/10.1016/j.jece.2022.108717.

[52] L. Acharya, S.P. Pattnaik, A. Behera, R. Acharya, K. Parida, Exfoliated Boron Nitride (e-BN) Tailored Exfoliated Graphitic Carbon Nitride (e-CN): An Improved Visible Light Mediated Photocatalytic Approach towards TCH Degradation and H2Evolution, Inorg Chem. 60 (2021) 5021–5033. https://doi.org/10.1021/acs.inorgchem.1c00062.

[53] D. Voigt, L. Sarpong, M. Bredol, Tuning the optical band gap of semiconductor nanocomposites-A case study with ZnS/carbon, Materials. 13 (2020) 4162. https://doi.org/10.3390/ma13184162.

[54] T. Chen, Q. Zhang, Z. Xie, C. Tan, P. Chen, Y. Zeng, F. Wang, H. Liu, Y. Liu, G. Liu, W. Lv, Carbon nitride modified hexagonal boron nitride interface as highly efficient blue LED light-driven photocatalyst, Appl Catal B. 238 (2018) 410–421. https://doi.org/10.1016/j.apcatb.2018.07.053.

[55] H. Xu, Z. Wu, Y. Wang, C. Lin, Enhanced visible-light photocatalytic activity from graphene-like boron nitride anchored on graphitic carbon nitride sheets, J Mater Sci. 52 (2017) 9477–9490. https://doi.org/10.1007/s10853-017-1167-6.

[56] X. Chen, D.H. Kuo, D. Lu, Nanonization of g-C3N4 with the assistance of activated carbon for improved visible light photocatalysis, RSC Adv. 6 (2016) 66814–66821. https://doi.org/10.1039/c6ra10357j.

[57] H. Zou, X. Yan, J. Ren, X. Wu, Y. Dai, D. Sha, J. Pan, J. Liu, Photocatalytic activity enhancement of modified g-C3N4 by ionothermal copolymerization, Journal of Materiomics. 1 (2015) 340–347. https://doi.org/10.1016/j.jmat.2015.10.004.

[58] S. Li, X. Zeng, H. Chen, W. Fang, X. He, W. Li, Z. hui Huang, L. Zhao, Porous hexagonal boron nitride nanosheets from g-C3N4 templates with a high specific surface area for CO2 adsorption, Ceram Int. 46 (2020) 27627–27633. https://doi.org/10.1016/j.ceramint.2020.07.257.

[59] D. Li, Y. Liu, C. Wen, J. Huang, R. Li, H. Liu, J. Zhong, P. Chen, W. Lv, G. Liu, Construction of dual transfer channels in graphitic carbon nitride photocatalyst for high-efficiency environmental pollution remediation: Enhanced exciton dissociation and carrier migration, J Hazard Mater. 436 (2022) 129171. https://doi.org/10.1016/j.jhazmat.2022.129171.

[60] Y. Wu, X. Jin, H. Liu, W. Lv, G. Liu, Synergistic effects of boron nitride quantum dots and reduced ultrathin g-C3N4: dual-channel carrier transfer and band structure regulation boost the photodegradation of fluoroquinolone, Sep Purif Technol. 303 (2022) 122185. https://doi.org/10.1016/j.seppur.2022.122185.

[61] Y. Zheng, Y. Jiao, J. Chen, J. Liu, J. Liang, A. Du, W. Zhang, Z. Zhu, S.C. Smith, M. Jaroniec, G. Qing, M. Lu, S.Z. Qiao, Yao Zheng, † Yan Jiao, ‡ , § Jun Chen, || Jian Liu, † Ji Liang, † Aijun Du, ‡ Weimin Zhang, || Zhonghua Zhu, § Sean C. Smith, ‡ Mietek Jaroniec, ^ Gao Qing (Max) Lu, † and Shi Zhang Qiao* , † †, Jacs. 133 (2011) 20116–20119.

[62] J. Zou, Y. Yu, W. Yan, J. Meng, S. Zhang, J. Wang, A facile route to synthesize boron-doped g-C 3 N 4 nanosheets with enhanced visible-light photocatalytic activity, J Mater Sci. 54 (2019) 6867–6881. https://doi.org/10.1007/s10853-019-03384-0.

[63] Y. Chai, Q. Liu, L. Zhang, J. Ren, W.L. Dai, Structure Engineered g-C3N4 Nano-Sheets by Switching the Pyrolysis Gas Atmosphere for Enhanced Photo-Catalytic Degradation, Chin J Chem. 35 (2017) 173–182. https://doi.org/10.1002/cjoc.201600608.

[64] G. Song, Z. Chu, W. Jin, H. Sun, Enhanced performance of g-C3N4/TiO2 photocatalysts for degradation of organic pollutants under visible light, Chin J Chem Eng. 23 (2015) 1326–1334. https://doi.org/10.1016/j.cjche.2015.05.003.

[65] X. Lv, J. Wang, Z. Yan, D. Jiang, J. Liu, Design of 3D h-BN architecture as Ag3VO4 enhanced photocatalysis stabilizer and promoter, J Mol Catal A Chem. 418–419 (2016) 146–153. https://doi.org/10.1016/j.molcata.2016.03.036.

[66] H.Y. Xu, L.C. Wu, H. Zhao, L.G. Jin, S.Y. Qi, Synergic Effect between Adsorption and Photocatalysis of Metal-Free g-C3N4 Derived from Different Precursors, PLoS One. 10 (2015) 1–20. https://doi.org/10.1371/journal.pone.0142616.

[67] V.P. Madhurima, P.H. Borse, K. Kumari, T.N. Rao, P.K. Jain, Improved photocatalytic activity of carbon-based polymeric semiconductor for efficient decontamination of wastewater: Effect of reaction atmosphere and pyrolysis temperature, Opt Mater (Amst). 110 (2020) 110523. https://doi.org/10.1016/j.optmat.2020.110523.

[68] B. Zhu, P. Xia, W. Ho, J. Yu, Isoelectric point and adsorption activity of porous g-C 3 N 4, Appl Surf Sci. 344 (2015) 188–195. https://doi.org/10.1016/j.apsusc.2015.03.086.

[69] J. Di, J. Xia, M. Ji, B. Wang, S. Yin, Q. Zhang, Z. Chen, H. Li, Advanced photocatalytic performance of graphene-like BN modified BiOBr flower-like materials for the removal of pollutants and mechanism insight, Appl Catal B. 183 (2016) 254–262. https://doi.org/10.1016/j.apcatb.2015.10.036.

[70] J. Yan, J. Gu, X. Wang, Y. Fan, Y. Zhao, J. Lian, Y. Xu, Y. Song, H. Xu, H. Li, Design of 3D WO3/h-BN nanocomposites for efficient visible-light-driven photocatalysis, RSC Adv. 7 (2017) 25160–25170. https://doi.org/10.1039/c7ra02929b.

Chapter 7

Summary and conclusions

In this chapter, an overall summary and detailed conclusions of the present thesis work are discussed. The future scope for this work to explore multiple fields of research has also been suggested.

7.1 Summary of the thesis work

The main aim of the present work was to investigate the role of multi-dimensional carbon nanomaterials coupled with graphitic carbon nitride towards visible-light photocatalytic purification of wastewater. The pristine 2D g-C_3N_4 gave limited activity for the photodegradation of RhB under visible light due to the rapid recombination of photo-generated charge carriers. Therefore, research was extended to investigate the reasons why the material did not perform as expected based on the literature reports. Some evidence of improved charge separation led to the use of carbon nanomaterials for the photocatalytic decomposition of RhB. To achieve this aim, the objective decided at the beginning of the research was accomplished and was addressed in detail in chapters 3 to 5. A cost-effective, eco-friendly, and easy synthesis process was adapted to develop visible-light photocatalyst material that showed good photodegradation performance. Improved specific surface area and overall efficiency were successfully achieved for graphitic carbon nitride-based hybrid materials. The overall summary of the thesis work is framed in Table 7.1.

Table 7.1 Summary of the thesis work.

S. No.	Photocatalyst Material	Synthesis Method	Target Pollutant	Degradation (%)
1	Graphitic Carbon Nitride (GCN)	Polycondensation of melamine	Rhodamine B (Conc. 5 mg/L)	95% in 45 min
2	Improved g-C_3N_4 (g-C_3N_4)	Polycondensation of melamine and NH_4Cl (2:1 ratio)	Rhodamine B (Conc. 10 mg/L)	94% in 30 min
3	CS/g-C_3N_4	Arc Discharge synthesis of CS nanoparticles followed by thermal decomposition of melamine, NH_4Cl and CS	Rhodamine B (Conc. 20 mg/L)	97% in 90 min
4	MWCNT/ g-C_3N_4	Arc Discharge synthesis of MWCNTs followed by thermal decomposition of	Rhodamine B (Conc. 20 mg/L)	92% in 60 min

		melamine, NH_4Cl and MWCNTs		
5	GNP/ g-C_3N_4	Microwave-assisted synthesis of GNP followed by thermal decomposition of melamine, NH_4Cl and GNP	Rhodamine B (Conc. 20 mg/L)	96% in 60 min
6	hBN/g-C_3N_4	Thermal decomposition of melamine, NH_4Cl and commercial-grade hBN	Rhodamine B (Conc. 20 mg/L)	91% in 60 min

7.2 Conclusions

The following conclusions have been drawn from the present thesis work:

- In Chapter 3, 2D g-C_3N_4 photocatalyst material was synthesized and the process parameters like reaction temperature (550 – 650 °C) and atmosphere (air, nitrogen, and argon) were optimized.
- The morphology of the as-prepared samples was studied under FESEM, and XRD to understand the structural and crystalline properties of the samples. FESEM confirmed the 2D layered structure formation and XRD results also supported these observations.
- The optical studies revealed that the sample synthesized at 650 °C in air showed near the ideal bandgap of 2.71 eV.
- The BET-specific surface area of this sample was observed to be 42 m^2/g and was the highest among all the samples. Also, the PL intensity was lower thus implying these process parameters to be optimum for the formation of g-C_3N_4.
- These results were also backed by favouring FTIR and XPS data. Besides, the zeta potential studies were carried out to find the surface charge potential of the sample.
- All the synthesized samples were applied to study the photodegradation of RhB (Conc. 5 mg/L). It was observed that the sample synthesized at 650 °C in the air atmosphere removed 95% of the dye in 45 minutes whereas other samples moderately performed.
- Further, this performance was enhanced by undertaking some modifications in the synthesis process. Here, a green templating technique was approached where a bubbling agent like NH_4Cl was included along with the precursor melamine during the pyrolysis reaction. Three different ratios of melamine and NH_4Cl were considered (2:1, 1:1, and 1:2).
- All three samples were characterized using various techniques like XRD, SEM, TEM, UV-DRS, PL, FTIR, XPS, BET and ZETA to study their structural, morphological, optical, chemical composition, surface area and surface charge behaviours.

- The d-spacing of the modified sample (2:1 ratio) increased more than the pristine g-C_3N_4 sample. This was essentially due to the incorporation of NH_4Cl during the synthesis process. However, the structural integrity was maintained irrespective of NH_4Cl addition.
- The optical band gap increased from 2.71 eV to 2.95 eV due to the reduction in the crystallite size. Similarly, low PL intensity and high BET surface area were also observed for the (2:1 ratio) sample. XPS results also confirmed that no traces of NH_4Cl were left over after the pyrolysis reaction.
- All the samples were applied to study the photodecomposition of RhB (Conc. 10 mg/L). it was noticed that (2:1 ratio) prepared g-C_3N_4 sample degraded 94% in 30 minutes whereas pristine g-C_3N_4 could remove only 35%. This enhanced performance was due to the increased specific surface area and porosity of the photocatalyst material.
- Therefore, at 650 °C in the air atmosphere, the addition of NH_4Cl (1 part) to melamine (2 parts) during the pyrolysis process produced an efficient g-C_3N_4 photocatalyst material.
- In Chapter 4, the synthesis of carbon nanomaterials through arc discharge was studied in the first part. Here MWCNTs and CS nanoparticles were synthesized by fine-tuning buffer gas pressure and arc voltage.
- Different pressure values (200 Torr, 400 Torr, and 600 Torr) and arc voltages (30V, 35V, and 40V) were considered. XRD, SEM, TEM and Raman characterizations were conducted to study the structural and morphological properties of the carbon samples.
- It was observed that 30V and 400 Torr favoured the formation of MWCNTs whereas 40V and 600 Torr showed higher amounts of carbon soot deposits which essentially contained these spherical carbon nanoparticles.
- Further, the 2^{nd} and 3^{rd} parts of Chapter 4 deal with the development of the hybrid photocatalyst with the synthesized carbon nanomaterials and the g-C_3N_4 materials. Here four different weight ratios of carbon nanomaterial wrt to g-C_3N_4 were considered namely: 0.1%, 0.3%, 0.5% and 1%.
- The CS loaded in g-C_3N_4 samples were named SC1, SC2, SC3, and SC4 respectively whereas, the MWCNTs loaded in g-C_3N_4 samples were coded as CC1, CC2, CC3, and CC4 respectively.
- All these samples were characterized under SEM, TEM, XRD, UV-DRS, PL, FTIR, BET, XPS, and ZETA to study their structural, optical, morphological, chemical composition, surface area and charge properties.
- It was discovered that all these hybrid samples showed smaller bandgaps than pristine g-C_3N_4 and also low PL intensities. The hybrid photocatalyst materials essentially preserved

the fundamental g-C_3N_4 structure. This was confirmed by XRD, FTIR, and XPS. However, TEM confirmed the formation of hybrid structures.

- The photodegradation of RhB (Conc. 20 mg/L) was performed to study the photocatalytic activity of the hybrid samples. It was noticed that the 0.1% loading of CS in g-C_3N_4 (SC1 sample) showed the highest degradation performance i.e., 97% in 90 minutes.
- Similarly, 0.1% loaded MWCNTs in g-C_3N_4 (CC1 sample) also showed 97% degradation in 90 minutes whereas pristine g-C_3N_4 showed 88% efficiency in similar experimental conditions. This enhanced performance was typically due to the effective charge carrier separation phenomenon.
- In Chapter 5, 2D/2D hybrid nanostructures were developed using GNP and hBN separately. Here, four different weight ratios were considered namely: 0.1%, 0.3%, 0.5%, and 1% of GNP in g-C_3N_4 coded as GC1, GC2, GC3, and GC4 respectively and 0.1%, 0.5%, 1%, and 5% of hBN in g-C_3N_4 coded as BC1, BC2, BC3, and BC4 respectively.
- GNP was prepared by microwave exfoliation of graphite intercalated compound followed by shear mixing of the obtained exfoliated graphite in DMSO & DI water mixture and finally centrifuged to remove unexfoliated particles.
- The obtained GNP was mixed with melamine and NH_4Cl and kept in a Muffle furnace at 650 °C in air. Similarly, hBN was procured commercially and used to prepare hybrid material through the thermal condensation method as discussed earlier.
- All the synthesized samples were studied using different characterization tools like XRD, SEM, TEM, XPS, UV-DRS, PL, FTIR, BET, etc. to know their structural, optical, morphological, chemical, and other essential properties.
- The hybrid photocatalyst materials showed lower PL intensity and low optical bandgap than the pristine g-C_3N_4 sample. Also, there was no substantial change in the structure of the photocatalyst by adding either GNP or hBN. This was confirmed through XRD, FTIR, and XPS analyses.
- The photocatalytic activity of as-prepared samples was studied by degrading RhB (Conc. 20 mg/L) under a visible light source. It was observed that the GC1 sample removed 96% of the dye whereas the BC2 sample removed 91% of the dye in 60 minutes. However, the pristine g-C_3N_4 sample removed only 55% of RhB under similar experimental conditions.
- In 2D/2D hybrid photocatalyst, the charge carrier separation was more effective as compared to previous models due to which faster degradation was possible. This was definitely due to the morphology of the coupled material.
- Nevertheless, the interesting finding from the RhB photo decomposition was the potential role of carbon nanomaterials in g-C_3N_4 hybrid photocatalyst material. This work makes a

significant contribution to our knowledge concerning carbon nanomaterial morphology and its effective charge carrier separation in photocatalytic decontamination of wastewater.

7.3 Scope of the future work

The present work has addressed the synthesis and parameter optimization of g-C_3N_4 followed by hybrid structure formation using different carbon nanomaterials via a detailed study of the synthesis, structural, optical, and chemical properties of photocatalytic degradation activity. This work can be further extended to study the photocatalytic performance in real time under direct sunlight. Also, different types of pollutants can be explored and studied with these developed materials. Besides carbon nanomaterials, other 2D materials like Metal oxides, MXenes, Metal chalcogenides, etc. can be explored for the development of binary and ternary hybrid structures. Meanwhile, these hybrid materials can be explored and experimented with in different applications like CO_2 reduction, H_2 evolution and many more.

List of publications

Papers Published in International Journals (SCI):

1. **V.P. Madhurima** [a, b], P.H. Borse [c], Kusum Kumari [b], T.N. Rao [a], P.K. Jain[a*]. Improved photocatalytic activity of carbon-based polymeric semiconductor for efficient decontamination of wastewater: Effect of reaction atmosphere and pyrolysis temperature. Optical Materials, 110, 2020, 110523. https://doi.org/10.1016/j.optmat.2020.110523
2. **V.P. Madhurima** [a, b], Kusum Kumari [b *], P.K. Jain[a *]. A facile single-step approach to achieve in-situ expanded g-C3N4 for improved photodegradation performance. Polymers for Advanced Technologies, 34, 2023, 578 – 586. https://doi.org/10.1002/pat.5908
3. **V.P. Madhurima** [a, b], Kusum Kumari [b *], P.K. Jain[a *]. "Synthesis and study of carbon nanomaterials through arc discharge technique for efficient adsorption of organic dyes". Daimond and related materials, 141, 2024, 110538. https://doi.org/10.1016/j.diamond.2023.110538

Papers communicated in International Journals (SCI):

1. **V.P. Madhurima** [a, b], Kusum Kumari [b *], P.K. Jain[a *]. Unravelling the uniqueness of white graphene anchored on g-C_3N_4 for ultrafast detoxification of wastewater. Submitted to Journal of Applied Polymer Science (2023).
2. **V.P. Madhurima** [a, b], Kusum Kumari [b *], P.K. Jain[a *]. Construction of 2D/2D GNP/g-C_3N_4 hybrid photocatalyst for synergistic charge separation and rapid photodegradation of organic pollutant. Submitted to Colloids and Surfaces A: Physicochemical and Engineering Aspects (2023).
3. **V.P. Madhurima** [a, b], Kusum Kumari [b *], P.K. Jain[a *]. Engineering of novel g-C_3N_4 photocatalyst using arc-discharge synthesized sphere-like carbon nanoparticles for enhanced photocatalytic activity. Submitted to Materials Science in Semiconductor Processing (2023).
4. **V.P. Madhurima** [a, b], Kusum Kumari [b *], P.K. Jain[a *]. Highly efficient 1D/2D nanohybrid photocatalyst made from arc discharge synthesized MWCNTs and g-C_3N_4 for visible-light photocatalysis. Submitted to Daimond and Related Materials (2023).

Papers Presented in National/ International Conferences

1. **V.P. Madhurima**, Balaji Padya, Kusum Kumari, and P.K. Jain, "*Carbon-based 2D/2D GNP/g-C3N4 nanocomposite for heterogeneous photodegradation of organic pollutants under visible light irradiation*", Advances in Science and Technology of Graphene-2022 held from 1st to 2nd, November, 2022 through virtual mode.
2. **V.P. Madhurima**, Kusum Kumari, T.N. Rao, and P.K. Jain, "*Carbon-based polymeric semiconductor for organic pollutant degradation: synthesis, properties and photocatalytic performance*," Conference on Carbon Materials-2019, held from 20th to 21st November, 2019, at New Delhi.
3. **V.P. Madhurima**, Kusum Kumari, Supriya Chakrabarti, Balaji Padyaa, T.N. Rao, and P.K. Jain, "*Optimization of buffer gas pressure and arc voltage for carbon nanotubular structures growth and their energy storage studies*," ICAFMD-2019 held from 26th to 28th February, 2019 at NIT Warangal.
4. **V.P. Madhurima**, Supriya Chakrabarti, Kusum Kumari, Balaji Padya, E Prasanth Kumar, M. Sagar and P.K. Jain, "*Synthesis of Concentric-shelled Carbon Nanostructures produced by Arc Discharge for Energy Storage Application*," NCMfEE-2018, held from 29th to 30th April 2018 at Dept. of Physics, Osmania University, Hyderabad.